

# Morphologically Complex Protostellar Envelopes: Structure and Kinematics

by

John J. Tobin

A dissertation submitted in partial fulfillment  
of the requirements for the degree of  
Doctor of Philosophy  
(Astronomy and Astrophysics)  
in The University of Michigan  
2011

Doctoral Committee:

Professor Lee W. Hartmann, Co-Chair

Professor Edwin A. Bergin, Co-Chair

Professor Fred C. Adams

Professor Nuria P. Calvet

Associate Professor Leslie W. Looney (University of Illinois)

Copyright © John J. Tobin 2011  
All Rights Reserved

*To my son Sean, a new star shining brightly in the world.*

## ACKNOWLEDGMENTS

My journey toward the completion of this thesis really started about seven years ago while still an undergraduate at the University of Illinois. I was sitting in the Extra-Terrestrial Life class taught by Leslie Looney and on that day we were briefly reviewing the star formation process. I remember seeing the images of the Orion Proplyds, proto-planetary disks viewed in shadow against the nebula, and thinking to myself “that is so freaking cool.” After that, I was hooked on star formation. I must thank both Leslie Looney and Brian Fields for their enthusiasm for teaching and doing much to shape my early interest in astronomy. In addition to being my teachers, they were also my first colleagues and I must thank them for their mentorship during my first research project. Leslie also guided me on my second research project where I learned many of the basic data analysis skills that I still use today. I must also thank Robert Gruendl and Shiya Wang for helping me out when I got stuck with IRAF and various other stumbling blocks. I also must thank You-Hua Chu for being a source of stimulating discussions/stories, encouragement, and ability to offer ideas on most any problem.

I am enormously indebted to my thesis advisor Lee Hartmann for his guidance and patience over the past five years. He has been an excellent mentor over the past 5 years, helping to direct my research in the proper direction, while still giving me the freedom to run with whatever interesting things I found. My co-advisor Ted Bergin has been a great help over the years as I learned how to interpret molecular line observations and he was the only other source of knowledge on GILDAS. Nuria Calvet, also on my thesis committee, has been extremely helpful over the years, her knowledge on radiative transfer modeling has been invaluable. Also, a big thanks goes out to Fred Adams for being my Cognate committee member, and often providing a

fresh perspective on my research.

As this thesis was taking shape, Leslie Looney's guidance was again invaluable, teaching me to basics of reducing interferometry data. Hsin-Fang Chiang and Woojin Kwon also provided me with invaluable help in this area. A big thanks goes to Claire Chandler for teaching me how to reduce VLA data with CASA during my visit to Socorro, Sebastien Maret for help reducing data from the IRAM 30m and PdBI, Barbara Whitney for making her radiative transfer model available and discussions about extending its use. I am also indebted to Hsin-Fang Chiang and Josep Maria Masque for covering an observing run at the IRAM 30m over Christmas break that I unfortunately could not attend.

The observations taken for this thesis would not have been possible without the assistance and dedication of the staff and observers at the IRAM 30m radio telescope, MDM Observatory, Las Campanas Observatory, IRAM Plateau de Bure Interferometer, Cerro Tololo Inter-American Observatory, Gemini Observatory, the Very Large Array, and the Combined Array for Research in Millimeter Astronomy.

This thesis has been supported by the *Spitzer Space Telescope* archival research program 50668, HST-GO-11548.04, and the University of Michigan Rackham Dissertation Fellowship. Chapters 2,3,4 are based on publications in the *Astrophysical Journal* and *Astrophysical Journal Letters* (Tobin et al., 2008, 2010b,a). Chapter 5 and 6 are based an articles to appear in the *Astrophysical Journal* (Tobin et al. 2011 submitted) and (Tobin et al. 2011 in preparation).

Last but not least, a big thanks to my wife Alice for her support during my thesis work and help editing the introduction, conclusions, fellowship proposals, and my GeminiFocus article. Also a big thanks to my new son Sean for not being too much of a handful and letting me finish in time!

# CONTENTS

DEDICATION . . . . .	ii
ACKNOWLEDGMENTS . . . . .	iii
LIST OF FIGURES . . . . .	x
LIST OF TABLES . . . . .	xiv
ABSTRACT . . . . .	xv
CHAPTER	
1 <b>Introduction</b> . . . . .	1
1.1 Observationally Constraining Star Formation . . . . .	1
1.1.1 Infrared and Sub/Millimeter . . . . .	2
1.1.2 Molecular Line Studies of Protostars and Dense Cores . .	3
1.2 Core Shapes and Initial Conditions of Core formation . . . . .	5
1.2.1 Formation Conditions of Pre- and Protostellar Cores . . .	5
1.2.2 Observed Core Shapes . . . . .	7
1.3 Protostellar Collapse . . . . .	8
1.3.1 Observations of Infall . . . . .	9
1.3.2 Constraining Envelope Parameters with SEDs . . . . .	10
1.3.3 Modeling Beyond the SED . . . . .	11
1.4 Formation of Multiple Systems and Disks . . . . .	12
1.4.1 Observing Core/Envelope Rotation . . . . .	14
1.4.2 Velocity Gradients from Infall? . . . . .	15
1.5 Termination of Infall . . . . .	16
1.6 Thesis Overview . . . . .	17

<b>2</b>	<b>Constraining the Envelope Structure of L1527 IRS: Infrared Scattered Light Modeling</b>	<b>23</b>
2.1	Introduction	23
2.2	Observations and data reduction	25
2.2.1	Spitzer Space Telescope Data	25
2.2.2	Near-Infrared Observations	26
2.2.3	Additional Infrared Data	27
2.2.4	Photometry	27
2.3	Observed Morphology	28
2.3.1	Asymmetry	29
2.3.2	Variability	30
2.3.3	Local Extinction	30
2.4	Modeling	33
2.4.1	Envelope and Disk Structure	33
2.4.2	Dust Properties	36
2.4.3	Model Fitting	37
2.5	Results	38
2.5.1	Reproducing the Scattered Light Morphology	38
2.5.2	SED Fitting: Disk Emission	40
2.6	Discussion	43
2.6.1	Comparison to Previous Models	43
2.6.2	Envelope Neck	45
2.6.3	Variability and Asymmetry	46
2.6.4	Interpretation of Physical Parameters	48
2.6.5	Class 0 versus I	49
2.6.6	General Applicability of the Model	50
2.6.7	Dust Properties and Emission Processes	51
2.6.8	Predictions	53
2.7	Conclusions	53

<b>3</b>	<b>The Inner Envelope and Disk of L1527 Revealed: Gemini L/-band Scattered Light Imaging</b>	74
3.1	Introduction	74
3.2	Observations and Data Reduction	75
3.3	Results	76
3.3.1	Models	77
3.4	Discussion	79
3.4.1	Conclusions	81
<b>4</b>	<b>Complex Structure in Class 0 Protostellar Envelopes</b>	86
4.1	Introduction	86
4.2	Observations and Data Reduction	87
4.2.1	<i>Spitzer</i> IRAC Observations	88
4.2.2	Near-IR Observations	89
4.3	Results	91
4.4	Optical Depth Maps	92
4.5	Quantitative Results	94
4.5.1	Non-Axisymmetric Structure	94
4.5.2	Flattened Structure	95
4.5.3	Mass Estimates	98
4.6	Discussion	99
4.6.1	Outflow-induced structure	99
4.6.2	Dense Non-axisymmetric Structure	100
4.6.3	Implications of Non-Axisymmetric Collapse	102
4.6.4	Turbulent formation	103
4.6.5	Relationship with Larger Structures	105
4.7	Conclusions	107
4.8	Appendix	109
<b>5</b>	<b>Kinematic Structure of Complex Class 0 Protostellar Envelopes: Single-Dish and Interferometric Molecular Line Mapping</b>	128
5.1	Introduction	128

5.2	Observations and Data Reduction . . . . .	131
5.2.1	The Sample . . . . .	131
5.2.2	IRAM 30m Observations . . . . .	132
5.2.3	CARMA Observations . . . . .	133
5.2.4	VLA Observations . . . . .	135
5.2.5	Plateau de Bure Interferometer Observations . . . . .	137
5.2.6	Data Analysis . . . . .	138
5.2.7	Extended Structure Sensitivity . . . . .	140
5.3	Results . . . . .	141
5.3.1	Similarity of $N_2H^+$ and $NH_3$ Emission Properties . . . . .	141
5.3.2	Velocity Gradients . . . . .	142
5.3.3	Description of Individual Sources . . . . .	144
5.4	Discussion . . . . .	164
5.4.1	Large-Scale Velocity Field . . . . .	164
5.4.2	Small-scale Velocity Structure . . . . .	167
5.4.3	Outflow Induced Kinematic Structure . . . . .	170
5.4.4	Linewidths . . . . .	172
5.4.5	Chemical Effects on Molecular Tracers . . . . .	173
5.5	Summary . . . . .	175
5.6	Appendix: Continuum Data . . . . .	176
6	<b>Velocity Gradients in Non-Axisymmetric Envelopes, Infall or Rotation?</b> . . . . .	222
6.1	Introduction . . . . .	222
6.2	Kinematic Models . . . . .	224
6.2.1	Rotating Collapse Model . . . . .	225
6.3	Observational and Model Results . . . . .	228
6.3.1	L1527 . . . . .	228
6.3.2	L1157 . . . . .	229
6.3.3	L1165 . . . . .	231
6.3.4	CB230 . . . . .	232

6.4	Discussion . . . . .	233
6.4.1	Velocity Gradients as Rotation . . . . .	234
6.4.2	Velocity Gradients from Projected Infall? . . . . .	235
6.4.3	Linewidth Constraints on Infall . . . . .	236
6.5	Summary and Conclusions . . . . .	237
<b>7</b>	<b>Summary and Conclusions . . . . .</b>	<b>253</b>
7.1	Initial Conditions of Core/Envelope Formation . . . . .	253
7.2	Infall and Rotation in Protostellar Systems . . . . .	255
7.3	Outflows Effects on Envelope Kinematics . . . . .	256
7.4	Constraints on Protostellar Structure from Radiative Transfer Modeling . . . . .	257
7.5	Future Work . . . . .	259
	<b>BIBLIOGRAPHY . . . . .</b>	<b>263</b>

# LIST OF FIGURES

## Figure

1.1	Spectral Energy Distributions of young stars spanning Classes I to III .	19
1.2	Molecular line maps showing complex shapes of dense cores . . . . .	20
1.3	Plots of H <sub>2</sub> CO line profiles presumably tracing infall. . . . .	21
1.4	Model SEDs of protostars showing effects of inclination . . . . .	22
2.1	False-color IRAC image of L1527 IRS (IRAS 04368+2557) . . . . .	55
2.2	Near-infrared and <i>Spitzer</i> images of L1527 . . . . .	56
2.3	L1527 and model 3.6 $\mu$ m images zooming in on center . . . . .	57
2.4	Wide-field view of L1527 region at 8.0 $\mu$ m . . . . .	58
2.5	SCUBA 850 $\mu$ m data overlaid compared with model 850 $\mu$ m data . . . . .	59
2.6	Variability of mid-infrared nebulosity in L1527 . . . . .	60
2.7	Radial profile of outflow cavity brightness in 2 epochs . . . . .	61
2.8	Dust albedo and opacity curves . . . . .	62
2.9	Radial profile of outflow cavity brightness compared to models . . . . .	63
2.10	Schematic representation of modeled cavity and envelope structure . . .	64
2.11	SED of L1527 compared to model . . . . .	65
2.12	Model images from single-cavity model . . . . .	66
2.13a	L1527 observed images compared to best fitting dual-cavity model . . .	67
2.13b	. . . . .	68
2.14	SEDs of best fitting model at multiple inclinations . . . . .	69
2.15	High resolution simulated images of inner envelope scattered light . . .	70
3.1	Gemini <i>L'</i> and <i>Spitzer</i> 3.6 $\mu$ m images of L1527. . . . .	82
3.2	Comparison of models with L1527 observations . . . . .	83

3.3	Model SEDs compared with observations . . . . .	84
3.4	L' image of L1527 with 7mm dust continuum contours overlaid . . . . .	85
4.1	Filamentary envelopes (BHR71, L723, HH108, L673, Serpens MMS3, L1157) . . . . .	113
4.2	One-sided envelopes (Perseus 5, L1527, HH270 VLA1, CB230) . . . . .	115
4.3	Approximately spherical envelopes (IRAM 04191, L1521F, IRAS 16253- 2429) . . . . .	116
4.4	Binary cores (CB244, L1152) . . . . .	117
4.5	Irregular envelopes (L1448 IRS2, IRAS 03282+3035, IRAS 05295+1247, IRAS 09449-5052, L483, L1165) . . . . .	118
4.6	Ks-band images of BHR71 and L483 with $8\mu\text{m}$ extinction contours . . .	120
4.7	Vertical structure of filamentary envelopes . . . . .	121
4.8	Optical image of CB230 region with $8\mu\text{m}$ contours overlaid . . . . .	122
4.9	L1165 region in $8\mu\text{m}$ extinction with H-K extinction map . . . . .	123
4.10	Uncorrected extinction at $8\mu\text{m}$ compared to background stars . . . . .	123
4.11	Corrected extinction at $8\mu\text{m}$ compared to background stars . . . . .	124
5.1	L1157 $\text{N}_2\text{H}^+$ data from the IRAM 30m and PdBI . . . . .	178
5.2	L1157 $\text{NH}_3$ data from the VLA and $\text{N}_2\text{H}^+$ from CARMA. . . . .	179
5.3	L1157 $\text{N}_2\text{H}^+$ data highlight outflow entrained material . . . . .	180
5.4	L1165 $\text{N}_2\text{H}^+$ data from IRAM 30m and CARMA . . . . .	181
5.5	L1165 $\text{HCO}^+$ data showing high velocity emission from the inner en- velope . . . . .	182
5.6	CB230 $\text{N}_2\text{H}^+$ data from the IRAM 30m and $\text{NH}_3$ data from the VLA .	183
5.7	HH108IRS data from the IRAM 30m and CARMA . . . . .	184
5.8	HH108MMS data from the IRAM 30m and CARMA . . . . .	185
5.9	Serpens MMS3 $\text{N}_2\text{H}^+$ data from the IRAM 30m and $\text{NH}_3$ data from the VLA . . . . .	186
5.10	HH211 $\text{N}_2\text{H}^+$ data from the IRAM 30m and CARMA . . . . .	187
5.11	IRAS 16253-2429 $\text{N}_2\text{H}^+$ data from the IRAM 30m and CARMA . . . . .	188

5.12	L1152 N <sub>2</sub> H <sup>+</sup> data from the IRAM 30m and CARMA . . . . .	189
5.13	L1527 N <sub>2</sub> H <sup>+</sup> data from the IRAM 30m, CARMA, and NH <sub>3</sub> data from the VLA . . . . .	190
5.14	RNO43 N <sub>2</sub> H <sup>+</sup> data from the IRAM 30m and CARMA . . . . .	191
5.15	RNO43 HCO <sup>+</sup> data showing high velocity inner envelope kinematics . .	192
5.16	IRAS 04302+2402 N <sub>2</sub> H <sup>+</sup> data from the IRAM 30m . . . . .	193
5.17	L483 N <sub>2</sub> H <sup>+</sup> data from the IRAM 30m and NH <sub>3</sub> data from the VLA . .	194
5.18	L673 N <sub>2</sub> H <sup>+</sup> data from the IRAM 30m and NH <sub>3</sub> data from the VLA . .	195
5.19	L1521F N <sub>2</sub> H <sup>+</sup> data from the IRAM 30m and NH <sub>3</sub> data from the VLA	196
5.20	Perseus 5 N <sub>2</sub> H <sup>+</sup> and NH <sub>2</sub> D from CARMA . . . . .	197
5.21	IRAS 03282+3025 N <sub>2</sub> H <sup>+</sup> data from the IRAM 30m and NH <sub>3</sub> data from the VLA . . . . .	198
5.22	IRAS 03282+3035 NH <sub>3</sub> channel maps . . . . .	199
5.23	HH270 VLA1 N <sub>2</sub> H <sup>+</sup> data from the IRAM 30m and CARMA . . . . .	200
5.24	Plots of line-center velocity along cuts in envelopes . . . . .	201
5.25	Histogram plots of measured velocity gradients from single-dish data .	204
5.26	Histogram plots of measured velocity gradients from interferometer data	205
5.27	Velocity gradient direction versus outflow direction . . . . .	206
5.28	Plot of difference between gradient direction at small and large-scales .	207
5.29	Plot of escape velocity versus measured velocity . . . . .	208
5.30	N <sub>2</sub> H <sup>+</sup> spectra of HH211 at three positions . . . . .	209
5.31	3mm continuum maps . . . . .	210
6.1	Schematic representation of expected velocity structures in envelopes .	239
6.2	Axisymmetric infall streamlines and position-velocity plot . . . . .	240
6.3	Filamentary infall streamlines and position-velocity plot . . . . .	241
6.4	L1527 N <sub>2</sub> H <sup>+</sup> channel maps . . . . .	242
6.5	L1157 N <sub>2</sub> H <sup>+</sup> channel maps . . . . .	243
6.6	L1157 N <sub>2</sub> H <sup>+</sup> integrated intensity map and position-velocity diagram . .	244
6.7	L1165 N <sub>2</sub> H <sup>+</sup> channel maps . . . . .	245

6.8	L1165 $\text{N}_2\text{H}^+$ integrated intensity map and position-velocity diagram . .	246
6.9	L1165 $\text{HCO}^+$ map of blue and red-shifted emission and position-velocity diagram . . . . .	247
6.10	CB230 $\text{NH}_3$ channel maps . . . . .	248
6.11	CB230 $\text{NH}_3$ integrated intensity map and position-velocity diagram . .	249
6.12	Plots of $R_C$ versus radius . . . . .	250

# LIST OF TABLES

## Table

2.1	Photometry . . . . .	71
2.2	Model parameters . . . . .	73
3.1	Model parameters . . . . .	82
4.1	Spitzer IRAC Observations . . . . .	125
4.2	Source Properties . . . . .	126
4.3	Moment of Inertia Ratios . . . . .	127
5.1	Source Properties . . . . .	211
5.2	IRAM 30m Observations . . . . .	212
5.3	CARMA Observations . . . . .	213
5.4	Very Large Array Observations . . . . .	214
5.5	Plateau de Bure Interferometer Observations . . . . .	215
5.6	Single-Dish $N_2H^+$ Properties . . . . .	216
5.7	Interferometric $N_2H^+$ Properties . . . . .	217
5.8	Interferometric $NH_3$ Properties . . . . .	218
5.9	Single-Dish Velocity Gradients . . . . .	219
5.10	Interferometric Velocity Gradients . . . . .	220
5.11	3mm Continuum Fluxes . . . . .	221
6.1	Source Properties . . . . .	251
6.2	Model Parameters . . . . .	252

# ABSTRACT

I present an in-depth study of protostars and their surrounding envelopes of dense gas and dust, using a multitude of observational methods to reveal new details of the star formation process. I use mid-infrared imaging from the *Spitzer Space Telescope*, combined with photometry spanning the near-infrared to millimeter wavelengths, to construct a model of the L1527 protostellar system. I modeled both the spectral energy distribution and resolved scattered light images to determine physical properties of the protostellar system. The nature of the apparent central point source in the *Spitzer* images was uncertain until high-resolution L-band imaging from the Gemini observatory resolved the point source into a disk in scattered light, having a radius of 200 AU. Protostellar envelopes are also often found to cast shadows against the 8 micron Galactic background in *Spitzer* imaging, enabling direct probes of envelope structure. The shadow images show that the dense envelopes around twenty-two Class 0 protostars are generally morphologically complex from 0.1 pc scales down to  $\sim 1000$  AU; they are often filamentary, and frequently non-axisymmetric. The observed envelope structure indicates a likely origin in turbulent cloud structure rather than a quasi-static/equilibrium formation. The complex envelope structure also may indicate an increased likelihood of fragmentation during collapse, forming close binaries. To further characterize these envelopes, I have observed them in the dense molecular gas tracers  $\text{N}_2\text{H}^+$  and  $\text{NH}_3$ , both of which closely follow the 8 micron extinction morphology. The magnitude of the velocity gradients and envelope complexity on  $\sim 10000$  AU scales indicates that the velocity structure may reflect large-scale infall in addition to the often assumed rotation. Comparisons with three-dimensional filamentary and symmetric rotating collapse models reinforce the interpretation of velocities reflecting large-scale infall, showing that the structure of the envelope must

be considered when interpreting the velocity field. To more definitively probe rotation, the kinematic structure on sub-1000 AU scales must be studied, where rotation will certainly be a more prominent component of the velocity field.

# CHAPTER 1

## Introduction

Most stars form within giant molecular clouds (GMCs) in the interstellar medium. GMCs are typically tens of parsecs in size, have total masses of  $\sim 10^4 - 10^6 M_{\odot}$ , and have average densities of  $n \sim 10^3 - 10^4 \text{ cm}^{-3}$ . Large-scale molecular clouds must fragment into smaller, higher density regions called cores<sup>1</sup> with densities  $\sim 10^5 - 10^6 \text{ cm}^{-3}$  and sizes of  $\sim 0.1 \text{ pc}$  in order to form individual stars (Goldsmith, 1987). The cores are able to collapse if the gravitational force is greater than supporting forces (e.g. magnetic, thermal and/or turbulent pressure). Shortly after gravitational collapse begins, a protostar forms and illuminates its surrounding envelope of dense gas and dust. Simultaneously, a disk develops around the young star due to conservation of angular momentum of the initial core rotation (e.g. Shu et al., 1987; McKee & Ostriker, 2007). Over time, the infalling envelope dissipates, revealing a pre-main sequence star and disk. This disk then further evolves to form a planetary system around the star. The primary goal of this thesis is to better characterize the process of star formation during the protostellar phase, while it is still embedded in the collapsing envelope of gas and dust.

### 1.1 Observationally Constraining Star Formation

The high density of the collapsing cores surrounding the protostars renders them opaque at optical and ultraviolet wavelengths, but bright in the far-infrared via re-

---

<sup>1</sup>Note that there is confusing nomenclature regarding clouds, cores, and envelopes. In this thesis I will use the following convention: clouds are larger-scale, more diffuse  $> 0.1 \text{ pc}$  structures, cores are high density  $< 0.1 \text{ pc}$  structures that may or may not have formed stars, and envelopes are  $< 0.1 \text{ pc}$  structures in which protostars have certainly formed. The  $0.1 \text{ pc}$  scale is the approximate length scale where the gravitational field of the protostar and core dominate over that of the larger-scale cloud.

processed radiation. Furthermore, dense cores in molecular clouds typically exhibit strong rotational line emission from abundant molecules, enabling probes of physical conditions and kinematics (e.g. Evans, 1999). Because of the high densities and cold temperatures in protostellar and star-less cores, infrared and millimeter-wave photometry, combined with molecular spectroscopy are the main tools in the observational study of star formation in its earliest phases.

### 1.1.1 Infrared and Sub/Millimeter

The launch of IRAS (InfRared Astronomy Satellite) in 1983 (Neugebauer et al., 1984) started a revolution in star formation research. The IRAS mission mapped the entire sky at 12, 25, 60, and 100  $\mu\text{m}$  with unprecedented sensitivity, essentially opening up the far-infrared spectrum for astronomy. Previous studies of young stars had been largely limited to optical and near-infrared wavelengths (e.g. Low & Smith, 1966; Mendoza V., 1966; Becklin & Neugebauer, 1967; Strom et al., 1972; Wilking & Lada, 1983), with a few studies pushing into the mid-infrared (e.g. Cohen, 1973a,b). Far-infrared emission from dense, cold dust was indeed found to be frequently associated with optically opaque cores and dark clouds, leading to the conclusion that they contained embedded protostars (Beichman et al., 1986). Furthermore, most of the luminosity from these objects is emitted in the far-infrared and submillimeter, making these critical wavelength regimes for the study of protostars.

An empirical classification system for young stellar objects (YSOs) was developed as a way of grouping sources based on the slope of the spectral energy distribution (SED) in the infrared, between 2 and 25  $\mu\text{m}$  (Lada, 1987). The SED slope or spectral index of is defined as

$$\alpha = \frac{d\log(\lambda F_\lambda)}{d\log(\lambda)} \quad (1.1)$$

with Class I sources having  $0 < \alpha \leq 3$ , Class II sources having  $-2 \leq \alpha \leq 0$ , and Class III sources having  $-3 < \alpha \leq -2$ . Examples of these SED classes are shown in Figure 1.1. Physically, these spectral slopes relate to the evolutionary state of a YSO. Class I sources are comprised of embedded protostars with dense surrounding envelopes of gas and dust that mostly re-emit radiation from the protostar in the far-infrared.

The Class II sources are pre-main sequence stars surrounded by a dusty disk; they still have far-infrared emission, but most of the luminosity is emitted shortward of  $10\mu\text{m}$  from the star and inner disk. The Class III sources have little or no infrared excess emission, meaning that there is not a surrounding disk or that it is tenuous.

While extremely sensitive, the IRAS observations had poor angular resolution. However, ground-based submillimeter imaging of the thermal dust emission using larger telescopes could spatially resolve the envelopes around protostars (e.g. Ladd et al., 1991). The submillimeter studies indicated that the YSO classification scheme needed to be extended to include an assumed earlier evolutionary state known as Class 0 sources (Andre et al., 1993). This classification accounts for protostars totally obscured in the near to mid-infrared. The criteria for Class 0 put forth by Andre et al. (1993) was that the ratio of submillimeter luminosity ( $L_{submm}$ ; longward of  $350\mu\text{m}$ ) to bolometric luminosity ( $L_{submm}/L_{bol}$ )  $> 0.5\%$  for these sources. This ratio of luminosities indicates that there is a substantial amount of cold dust surrounding the protostar, more than for typical Class I sources, leading to the suggestion that they are in an earlier phase of evolution. While I will concentrate on the study of Class 0 and I objects in this thesis, the properties of the protostars and their envelopes in these phases will have implications for the the further evolution of young stellar systems.

### 1.1.2 Molecular Line Studies of Protostars and Dense Cores

The dark clouds and dense cores (Lynds, 1962; Bok et al., 1971) had become well known sources of molecular line emission (e.g Ho et al., 1978; Dickman, 1978), prior to their classification as star-less or protostellar cores. Martin & Barrett (1978) lists the early discovery papers of the many simple and still most frequently observed ( $N_{atom} \leq 4$ ) molecular species commonly found dense cores. Molecular lines offer a unique probe of the physical conditions inside molecular clouds and dense cores, yielding temperature and density estimates as well as forming the foundation of astrochemistry. The physical conditions in which many molecules such as  $\text{NH}_3$  are known to form and be excited, pointed to high densities and cold temperatures, conditions ideal

for star formation.

Dense cores have been primarily studied using the high density tracers of  $\text{NH}_3$  and  $\text{N}_2\text{H}^+$ . This is because  $\text{H}_2$ , the most abundant molecule, does not emit in cold gas due to large excitation energies resulting from its low moment of inertia, and CO (the next most abundant molecule) becomes optically thick at low rotational levels and depletes onto dust grains at  $A_V \sim 6$  (Frerking et al., 1982; Caselli et al., 1999; Bergin & Tafalla, 2007). However,  $\text{NH}_3$  and  $\text{N}_2\text{H}^+$  can only form at high densities ( $\sim 10^4 - 10^5 \text{ cm}^{-3}$  and their emission tends to remain optically thin, even at high column densities of  $\text{H}_2$ . These properties make  $\text{NH}_3$  and  $\text{N}_2\text{H}^+$  ideal molecules to study the environments immediately surrounding protostars (Ho & Townes, 1983; Myers & Benson, 1983; Womack et al., 1992; Benson et al., 1998), especially since the emission from these molecules was found to strongly correlated with the dust emission of star-less cores (Ward-Thompson et al., 1994).

Large mapping surveys of dense cores were undertaken as instrumentation improved. Benson & Myers (1989) presented a  $\text{NH}_3$  survey of 147 dense cores in dark clouds, finding IRAS sources associated with the majority of cores, demonstrating that dense cores are active sites of star formation. Aside from probing the physical conditions of dense cores, the molecular line maps provide valuable kinematic data, probing the velocity structure of the cold gas in protostellar envelopes on  $\sim 0.1$  pc scales (e.g. Goodman et al., 1993; Caselli et al., 2002) and infall can potentially be traced using optically thick lines (Zhou, 1992; Zhou et al., 1993).

Our current understanding of the star formation process has largely been shaped by these early observational studies. These studies often employed many simplifying assumptions to interpret their data, such as sphericity/axisymmetry, single protostars, inside-out collapse (Section 1.3), and uniform rotation of cores. Some of these assumptions were motivated by the ability to compare with theoretical models, others because the quality of the data did not motivate nor require a more complex analysis. Despite the growing sophistication of observations and models, vestiges of these simplifying assumptions frequently appear in current studies, even when the data do not motivate them.

This thesis examines the morphological structure and kinematics of protostellar envelopes; these properties have implications for the relative importance of turbulence and magnetic fields in the star formation process and the formation of protostellar disks. Furthermore, these features may also have implications for the fragmentation of protostellar systems and hold clues for how infall is terminated. While all these questions cannot be fully addressed in this thesis, the results I present are progress toward solving these problems in star formation. I will give an overview of our current theoretical and conceptual understanding of these questions and how the various observational techniques have been used to test our understanding of the star formation process. Then, I will give an overview of the thesis as it applies to these principal, unresolved questions of the star formation process.

## **1.2 Core Shapes and Initial Conditions of Core formation**

In studies of protostars and dense cores, one of the most frequently used assumptions is spherical symmetry, which simplifies calculation of density, temperature, and abundance profiles. Furthermore, spherical symmetry is often used in theory as an initial condition to reduce computational complexity. This leads to one of the major issues in star formation: whether it is a slow/quasi-static process with cores evolving in approximate or quasi-equilibrium, that may enable the formation of spherical or axisymmetric cores; or is it a rapid/dynamic process in which cores are formed quickly and collapse follows shortly thereafter (Hartmann et al., 2001) and the structure of dense cores would then likely be more complex. The morphological structure of dense cores may enable us to answer this question.

### **1.2.1 Formation Conditions of Pre- and Protostellar Cores**

Since dense cores result from the fragmentation of large-scale molecular clouds, the morphological structure of dense cores may relate back to the initial conditions of core formation. The fragmentation process itself may be related to supersonic turbulent motions within the clouds (Larson, 1981). The formation of cores in a turbulent medium is can be envisioned as follows; turbulent motions within the clouds can

cause shocks and create over dense regions that can be gravitationally bound and collapse (e.g. Klessen et al., 2000; Klessen & Burkert, 2001; Ostriker et al., 2001; Bate et al., 2003). The common thread to most flavors of turbulent star formation is that cores form quickly and collapse rapidly (c.f. Tan et al., 2006; Krumholz et al., 2006), roughly within a free-fall time (e.g. Hartmann et al., 2001; Vázquez-Semadeni et al., 2005; Ballesteros-Paredes et al., 2007). Simulations show that cores formed in turbulent clouds can be highly asymmetric and filamentary in appearance (Offner & Krumholz, 2009; Smith et al., 2011). Thus, the formation of spherical cores in a turbulent medium seems difficult to envision.

Magnetically regulated collapse presents a possible scenario for the formation and collapse of cores in approximate equilibrium. Magnetic fields could be a source of support in individual cores (possibly the entire molecular cloud) if the ions are closely coupled with the neutrals. If magnetic fields are strong and supporting the cloud, the magnetic flux must be dissipated through the process of ambipolar diffusion (AD) before collapse begins, which can take  $\sim 10^7$  yr in the older models (e.g. Mestel & Spitzer, 1956; Mouschovias, 1979, 1991; Fiedler & Mouschovias, 1992; Tassis & Mouschovias, 2007). The cores formed in the magnetically dominated models are axisymmetric and oblate due to the ability of material to collapse vertically along the magnetic field lines.

More recent models show that AD can proceed more rapidly with lower initial mass to flux ratios and in a turbulent medium (Fatuzzo & Adams, 2002; Li & Nakamura, 2004; Basu et al., 2009); however, the cores are still quite symmetric in the numerical models. On the contrary, recent direct measurements of the magnetic field strength (Zeeman effect) toward dense cores indicate that it is insufficient to support the cores against collapse (Crutcher et al., 2009, 2010). Furthermore, it is argued that star formation occurs more rapidly than the AD timescale and molecular clouds may form with gravitational force stronger than magnetic pressure (Hartmann et al., 2001).

### 1.2.2 Observed Core Shapes

Molecular line maps are an ideal way to measure the shapes of dark clouds and cores. The optical images of dark clouds become completely opaque at relatively low column densities, only tracing the outermost regions (Cambr esy, 1999). Benson & Myers (1989) showed that dense cores within dark clouds are generally non-spherical, with major to minor axis ratios averaging 1.6. In addition, many dense cores in Benson & Myers (1989) had associated IRAS sources that were off-center from the emission peaks, further indicating asymmetry. Myers et al. (1991) presented larger-scale maps of dense cores (some protostellar, some pre-stellar) observed in C<sup>18</sup>O, CS, and NH<sub>3</sub>, some of which are shown in Figure 1.2. These maps clearly show that many dense cores are highly asymmetric on 0.1 - 0.2 pc scales. The asymmetries are far greater in magnitude than the asymmetry in axial ratios found in Benson & Myers (1989), an indication that the equilibrium/axisymmetric initial conditions are incorrect and favor a more rapid, turbulent scenario. However, these large-scale maps do not trace near enough to the protostar to rule out axisymmetric structures on small-scales and chemistry likely affects the observed large-scale structure.

Maps of submillimeter dust emission (Huard et al., 1999; Shirley et al., 2000; Chandler & Richer, 2000; Hogerheijde & Sandell, 2000) are a complementary way to probe core structure on smaller scales. Unlike the molecular emission maps, submillimeter images of protostars are often round and centrally peaked, sometimes showing asymmetries on 0.05 pc scales. The centrally peaked nature of the dust emission maps results from the emission being dependent on both density and temperature. Emission from the warmer inner envelope dominates over whatever cold, asymmetric component might be present. Interferometric images of dust continuum have similar difficulties since they are temperature weighted as well, but also often lack sensitivity to recover structures much more extended than a few beamwidths. Thus, even with the increased resolution offered by new instrumentation, there is still not a clear picture of envelope structure on scales < 0.05 pc and the morphology of submillimeter dust emission has perhaps unintentionally reinforced the assumption that protostellar envelopes are spherical.

Therefore, the shapes of dense cores and protostellar envelopes are a key constraint on the dominant star formation paradigm; turbulent/rapid or magnetically controlled and slow. The dense core structures from molecular lines on large-scales and dust emission at small-scales are seemingly at odds with each other. Thus, the structure of protostellar envelopes on small-scales is uncertain. I will use higher resolution dust extinction mapping to determine the morphological structure of protostellar envelopes on 0.1 pc to  $\sim 1000$  AU scales in this thesis.

### 1.3 Protostellar Collapse

The previous sections dealt with the formation and morphological structure of cores; I will now discuss our understanding of how these dense cores collapse to form protostars. An idea of the typical masses and size scales of the collapsing cores in a molecular cloud is gained by applying the Jeans criteria (Jeans, 1902) of mass and length, which assume uniform density and only thermal pressure support. These values are  $\sim 0.5 M_{\odot}$  and  $\sim 0.1$  pc for  $T = 10$ K and  $n = 10^4$   $\text{cm}^{-3}$  gas. The free-fall timescale ( $t_{ff} \propto \rho^{-1/2}$ ) of such a uniform density sphere is  $\sim 3.4 \times 10^5$  yr, indicating that collapse of a cloud to form a protostar can be quite rapid.

Analytic models describing the collapse process were subsequently developed, two of the most successful being Larson (1969); Penston (1969) (Larson-Penston solution) and Shu (1977). The Larson-Penston solution describes an outside-in collapse, while the Shu (1977) collapse is inside-out. However, both models start from highly unrealistic initial conditions. The Larson-Penston solution begins with a constant density sphere, which is not an equilibrium state and the Shu (1977) solution begins with the singular isothermal sphere, an equilibrium state that is highly unstable. Furthermore, the inside-out collapse of the Shu (1977) model requires strict spherical symmetry. These analytic models are instructive in describing the process of protostellar collapse, but actual collapsing envelopes will differ in their properties. Thus, numerical simulations enable the collapse process to be studied beyond the confines of similarity solutions. One such study was carried out by Foster & Chevalier (1993), simulating the collapse of Bonnor-Ebert spheres, a perhaps more realistic, but still

idealized, initial condition. They found that the collapse is qualitatively similar to the Larson-Penston solution. Furthermore, the infall rate in Foster & Chevalier (1993) is initially much larger than the Shu (1977) model, due to the inner constant density region collapsing in approximate free-fall (Henriksen et al., 1997). After the inner region has collapsed, the material initially at larger scales with  $\rho \propto r^{-2}$  has a roughly constant accretion accretion rate (Foster & Chevalier, 1993; Henriksen et al., 1997).

### 1.3.1 Observations of Infall

While these early models have their limitations, the Shu (1977) model and Larson-Penston solution have specific predictions for the velocities of infalling material during collapse. In the Shu (1977) model, the region inside the expansion wave is falling in at the free-fall velocity. However, in the Larson-Penston solution, the outer envelope is collapsing at  $-3.3 \times c_s$  (the isothermal sound speed). Zhou (1992) calculated line profiles for both of these models and found that a Larson-Penston type collapse would be observed to have average velocities about twice that of the Shu (1977) model.

Zhou et al. (1993) used observations of CS and H<sub>2</sub>CO to infer the detection of infall in the envelope of the Class 0 protostar B335 and Walker et al. (1986) interpreted their CS observations of IRAS 16253-2422 as infall. These are optically thick molecular lines and self absorbed at the line-center, primarily emitting in the blue and red-shifted line wings. The key signature of infall is the blue-shifted side of the line being brighter than the red-shifted side. This interpretation also depends on the spherical symmetry of the infalling envelope. Zhou et al. (1993) and Myers et al. (1995) modeled this emission, finding it to be consistent with inside-out collapse, see Figure 1.3. However, Foster & Chevalier (1993) showed that the observed line profiles are not necessarily unique to inside-out collapse, and the molecules used to measure infall observationally are often found in molecular outflows, driven by the protostar, which can also produce a double-peaked line profile. Furthermore, Menten et al. (1987) argues that, at least in the case of IRAS 16293-2422, infall is not required to explain the observations.

Given the possible confusion with outflow emission, observing infall before forma-

tion of the protostar and outflows would be a more ideal test of infall predictions. Observations by Tafalla et al. (1998) toward the star-less core L1544 appear to indicate infall motions. Modeling of the multiple lines observed across the core cannot be easily explained with magnetic, inside-out, or free-fall collapse. On the other hand, the authors do assert that line kinematics appear to reflect infall, but not in a manner consistent with current theories. However, L1544 is clearly not spherical and if envelopes are not axisymmetric then the molecular emission across a core should be more complex. Thus, the blue-asymmetry of optically thick line profiles may not uniquely constrain a particular infall model.

### 1.3.2 Constraining Envelope Parameters with SEDs

One of the principal benefits of the analytic collapse models is that they enable some relevant properties of protostellar envelopes to be fit. The theoretical density profiles calculated from the model parameters can be run through a radiative transfer code to calculate a predicted spectral energy distribution (SED), which can then be fit to observations. The first realistic SED models of protostars within an infalling envelope were computed by Adams & Shu (1986) and Adams et al. (1987), using the rotating collapse model (Ulrich, 1976; Cassen & Moosman, 1981; Terebey et al., 1984, hereafter CMU model) with a protostellar disk included. This model is a perturbation of the Shu (1977) model, but takes into account the initial rotation of the core/envelope and that a rotationally supported region will be formed in the inner envelope at the radius  $R_C$ . The value of  $R_C$  can be approximately calculated using the relation

$$R_C = R_{outer}^4 \frac{\Omega^2}{GM} \quad (1.2)$$

where  $R_{outer}$  is the radius of the infalling material and  $\Omega$  is the angular velocity of the core/envelope at this radius. This equation is derived by assuming conservation of angular momentum and expressing the Keplerian velocity in terms of  $R_C$ . This rotationally supported region makes the average density profile of the envelope drop from  $\rho \propto r^{-3/2}$  to  $r^{-1/2}$ , making the envelope more optically thin toward the center.

The SED of a protostar depends on multiple parameters that can be fit by SED modeling, using the CMU rotating collapse model. The most important model parameters fit are the bolometric luminosity ( $L_{bol}$ ), the mass infall rate of the envelope onto the disk ( $\dot{M}_{env}$ ), and  $R_C$ .  $\dot{M}_{env}$  defines the density of the envelope, increasing this parameter raises the optical depth and shifts the SED peak to longer wavelengths, and  $L_{bol}$  sets the overall scaling of the SED. The outer envelope radius can also be fit, but is generally not well constrained since it is degenerate with  $R_C$  and  $\dot{M}_{env}$ . While it was previously discussed that the analytic models are not able to fully describe the collapse process, the free-falling region of the models in the inner envelope may apply more generically.

Kenyon et al. (1993a) fitted the SEDs of all the then known protostars in Taurus using radiative transfer models of CMU envelopes. They found that the typical infall rate for envelopes in Taurus was  $\sim 4 \times 10^{-6} M_{\odot} yr^{-1}$  and  $R_C \sim 100$  AU. The models could fit the data well where emission is optically thin in the far-infrared and millimeter, but where the envelope is optically thick in the near to mid-infrared, the data are less optimally fit. A following paper (Kenyon et al., 1993b) was able to explain the near-infrared discrepancies with the addition of scattered light cavities carved out by bipolar outflows (e.g. Snell et al., 1980; Bachiller, 1996). The bipolar outflow cavities can provide a low-extinction pathway for light to escape from the central protostar and disk, depending on inclination to the line of sight and outflow cavity width. This feature can potentially be more effective at allowing shorter wavelength light to escape than a large  $R_C$ . Due to its success in SED modeling, the rotating collapse model is still widely employed to model the SEDs of protostars because it is entirely analytic and critical physical parameters of individual systems can be constrained.

### 1.3.3 Modeling Beyond the SED

Despite the ability to fit the SEDs reasonably well with the rotating collapse model in Kenyon et al. (1993a), as described previously, the importance of the outflow cavities, inclination, and source morphology were highlighted by a follow-up paper (Kenyon et al., 1993b). Without accounting for these geometric and morphological

factors, SED fits can be highly degenerate. A wealth of data are now available from 2MASS, IRAS, *Spitzer*, WISE, and *Herschel*. From these data, more accurate models of protostellar systems can be calculated by simultaneously fitting of all observables: the near to far-infrared images, SED, and mid-infrared spectrum (Furlan et al., 2008). The modeling of the images and SEDs is necessary because it is possible to fit the SED while the image of the source may be obviously incorrect and vice-versa.

The scattered light morphology observed around protostars enables certain geometric parameters (i.e. inclination, outflow opening angle) to be fixed as well as constraining the scattered light brightness. This is critical because the outflow opening angle, inclination, centrifugal radius, and infall rate are degenerate to a certain degree. The effect of inclination on the observed SED of a protostar with an outflow cavity is shown in Figure 1.4. With at least some parameters constrained to a reasonable range from imaging, the SED can be fit with more attention given to the physical parameters of the system. Resolved images of the Class 0 protostars were often lacking until *Spitzer* observed them in the mid-infrared (Tobin et al., 2007; Jørgensen et al., 2006) and they have only been factored into modeling recently. However, it remains unclear if the CMU model can reproduce the full range of observables in a particular protostellar envelope, even in an ideal case; this is an avenue of research to be explored in this thesis.

## 1.4 Formation of Multiple Systems and Disks

At least  $\frac{1}{3}$  of stars are found in binary or multiple systems (Lada, 2006; Raghavan et al., 2010; Connelley et al., 2008) with companion separations ranging from sub-AU scales to thousands of AU. This wide range of separations and the prevalence of proto-binary systems (Looney et al., 2000; Connelley et al., 2008) suggests that the core/envelope rotation must play a principal role in the fragmentation into binary/multiple systems (e.g. Tohline, 2002). Note that in this section fragmentation only refers to the formation of binary/multiple systems, different from the molecular cloud fragmentation discussed in Section 1.2.

Fragmentation during collapse is difficult to study analytically, but the ability of

a system to fragment and likely scales can be calculated (e.g. Tohline, 1981; Sterzik et al., 2003). However, more detailed studies require numerical simulations of rotating collapse. Burkert & Bodenheimer (1993) showed that wide binary systems could be formed if there was azimuthal density modulation of the envelope and strong rotation. Bate (2000) and Boss (2002) further showed that axisymmetric cores with a variety of density and rotation profiles can form both close and wide binary systems. Furthermore, observational and theoretical studies indicate that there should be rapid dynamical evolution of the proto-binaries throughout the Class 0 and I phases which yield both wide and tight binary systems (Bate, 2000; Connelley et al., 2008). Thus, rotation alone can cause fragmentation, but non-axisymmetry further encourages it (Bonnell & Bastien, 1993; Machida et al., 2008). Lastly, models with strong magnetic fields also appear to inhibit fragmentation, in addition to slowing or inhibiting collapse. However, as discussed earlier, it appears unlikely that magnetic fields play a significant role in the collapse process.

Disks appear to form ubiquitously during protostellar collapse (Haisch et al., 2001; Hernández et al., 2007) due to conservation of angular momentum from the initial core rotation on large-scales (Cassen & Moosman, 1981). The early collapse models all neglected core rotation, but it was later added to the Shu (1977) model by Terebey et al. (1984). However, rotation had been previously applied to the infalling region in the CMU model. The slow initial rotation on  $\sim 0.1$  pc scales causes disks to form with radii of  $\sim 100$  AU (Cassen & Moosman, 1981; Bodenheimer, 1995; Andrews et al., 2009). Disks themselves also may fragment into binary/multiple systems, possibly providing a route for the formation of very close binary systems (Kratte et al., 2010).

Conservation of angular momentum broadly describes why disks form; however, the disk formation process is intimately coupled to the structure of the surrounding, collapsing protostellar envelope of gas and dust. The disk radii are determined by the initial rotation rate of the collapsing regions of the envelope and the density structure of the infalling material determines the density structure of the disk. Furthermore, mass from the envelope must be processed through the disk before being accreted onto the protostar. To summarize, in order to understand the formation of disks and

binary/multiple systems the structural and kinematic properties of the protostellar envelopes must be closely examined.

#### 1.4.1 Observing Core/Envelope Rotation

The importance of rotation to the sizes of forming disks and fragmentation motivates the need to characterize rotation in the early phases of star formation, before and during collapse. Arquilla & Goldsmith (1986, and references therein) was the first study to examine the the kinematic structure of a large sample of dark clouds using CO on  $\sim 10'$  ( $\sim 1$  pc) scales, finding that some exhibit possible rotation signatures. However, they noted that the clouds are quite asymmetric and that uniform rotation is unlikely; furthermore, a virial equilibrium analysis indicated that the clouds are not rotationally supported.

Goodman et al. (1993) used the  $\text{NH}_3$  mapping data from Benson & Myers (1989) to conduct the first systematic study of velocity structure in a large sample of smaller-scale ( $\sim 0.1$  pc) dense cores. They used the line-center velocity from the  $\text{NH}_3$  emission to fit velocity gradients across the cores, interpreting the gradients as solid-body rotation. The sample had an average velocity gradient of  $1 \text{ km s}^{-1} \text{ pc}^{-1}$ , with a range between  $0.3$  to  $3.3 \text{ km s}^{-1} \text{ pc}^{-1}$ . The cores were found to not be rotationally supported with upper limits on the ratio of rotational energy to total energy ( $\beta$ ) being  $\sim 0.1$ . Caselli et al. (2002) conducted a similar study using  $\text{N}_2\text{H}^+$  ( $J = 1 \rightarrow 0$ ) observations, finding an average velocity gradient of  $\sim 2 \text{ km s}^{-1} \text{ pc}^{-1}$  and a similar range in gradient values; however, they note clear deviations from linearity in many of the velocity fields.

Observations of rotation at high resolution were attempted by Chen et al. (2007) on a sample of nine Class 0 and I protostars using  $\text{N}_2\text{H}^+$  ( $J = 1 \rightarrow 0$ ) observations from the OVRO millimeter array. They found substantially larger velocity gradients in the inner envelopes ( $5.8$  to  $24 \text{ km s}^{-1} \text{ pc}^{-1}$ ). The velocity fields are complex in most cases and probable rotation signatures are only found for a few. Their targets were not in the Goodman et al. (1993) or Caselli et al. (2002) surveys. Thus, it is unclear if the large-scale velocity gradients would be consistent with what was

observed on small-scales. The lack of clear rotation signatures in most envelopes were attributed to outflow-envelope interactions (Arce & Sargent, 2006).

The combined results of these surveys indicate that cores and envelopes could indeed be rotating at large-scales, with the possibility of spin-up at small-scales. However, the angular momenta implied from the core rotation would indicate that disks ranging in radius from 25 to 2500 AU could form from the observed range of velocity gradients. These disk radii are calculated using Equation 1.2, assuming conservation of angular momentum during collapse, a core radius of 10000 AU, and a  $1 M_{\odot}$  core. The smaller disk radii are realistic and consistent with observations (e.g. Andrews & Williams, 2007; Andrews et al., 2009); however, disk radii of thousands of AU are unrealistic and will likely fragment (Rafikov, 2005, 2007).

#### 1.4.2 Velocity Gradients from Infall?

Given that Myers et al. (1991) showed that dense cores are often highly asymmetric, is it reasonable to assume that infall will not present itself in observed velocity gradients? In an axisymmetric system, radial infall at large-scales would only yield a broad linewidth in an optically thin tracer such as  $N_2H^+$  or  $NH_3$ . However, in a non-axisymmetric core, infall from large-scales could give the appearance of a velocity gradient in the absence of rotation. Large-scale infall has been previously suggested for L1544 (Tafalla et al., 1998) and by the dynamical models of Foster & Chevalier (1993). A simple calculation of free-fall velocity at 10000 AU in a  $1 M_{\odot}$  envelope yields  $v_{in}=0.42 \text{ km s}^{-1}$ ; if an envelope is elongated normal to the outflow direction and rotated within the plane of the sky by  $30^{\circ}$  then the observed velocity projected along the line of sight would be  $0.21 \text{ km s}^{-1}$ . Thus, it seems plausible that projected infall could be observed in the velocity field of optically thin lines across cores, contributing to the overall velocity gradient.

This has important implications for the determination of angular momentum in protostellar envelopes. If there is rotation combined with projected infall velocities, then the true rotation rate of the envelope could be smaller than the velocity gradients would imply. I will explore this issue of projected infall and rotation in detail in

this thesis, because this has significant implications for the formation of protostellar disks and fragmentation. Moreover, further investigation is necessary to explore the velocity field complexities on small-scales, relating back to the larger-scale kinematics. This may enable the determination of whether large velocity gradients reflect rotation or projected infall.

## 1.5 Termination of Infall

Despite the large body of work that has gone into understanding the formation of molecular clouds, cores, and their subsequent collapse; how the infall phase ends remains unclear. The theoretical models of protostellar collapse would imply that envelopes should continue to fall in to the central protostar and disk until the mass reservoir is depleted. However, the protostellar envelopes are often not isolated, but are embedded within molecular clouds with a large mass reservoir surrounding it. Outflows have been hypothesized to play a principle role in shutting off the mass infall of the envelope (Shu et al., 1987, 1994; Velusamy & Langer, 1998; Arce & Sargent, 2006). Arce & Sargent (2006) clearly showed that there is a progression of outflow widening from the early to later evolutionary stages, but the reason for the widening is uncertain. Precessing jets often have too narrow of a precession cone to account for excavation of such wide cavities and the outflows in the Class 0 phase are well-collimated (e.g. Reipurth et al., 2000).

One suggestion is made by Wilkin & Stahler (2003): a wide angle wind from the protostar is initially trapped by the infalling gas and as infall decreases with time the wind can break out of the envelope. A limitation of this framework is that it assumes mass is infalling from a spherical envelope, whereas protostars are often forming within filaments as shown by observations (Men'shchikov et al., 2010) and theory (e.g. Ostriker et al., 2001; Heitsch et al., 2006; Hsu et al., 2010). With a filamentary envelope, it is unclear how outflows can shut off infall if most material is falling-in normal to its direction. Understanding how infall is terminated could be critical for understanding how final protostellar masses are determined.

## 1.6 Thesis Overview

In this thesis, I will study protostellar core/envelope structure and kinematics using multiple techniques. I utilize observations in the near and mid-infrared from both ground and space-based observatories, as well as single-dish and interferometric mapping of dense molecular gas tracers. The observational constraints will then be compared with the analytic models of protostellar collapse in an attempt to verify consistency or rule-out theory.

A new approach for testing the CMU rotating collapse model with detailed observational constraints is presented in Chapter 2. I conducted an analysis of *Spitzer Space Telescope*, near-infrared, and submillimeter imaging of the Class 0 protostar L1527. The proximity of the Taurus star forming region ( $d \sim 140$  pc) enables *Spitzer* to provide an incredibly detailed view of its envelope and outflow cavity structure in multiple bands between  $3.6$  to  $8\mu\text{m}$ . The near and mid-infrared scattered light images are used to construct a model of the protostellar envelope and outflow cavity structure, while simultaneously fitting the SED of the protostar from the near-IR to the millimeter.

L1527 is revisited in Chapter 3 using high-resolution ground-based mid-infrared imaging. The high-resolution images resolved the point-like source in the *Spitzer* data into a compact bipolar structure, bearing strong resemblance to our initial model. The original model was first revised to better fit the new data, and I found that a large, highly-flared disk could also explain the observed structure equally well.

A new approach to examining the structure of protostellar envelopes is undertaken in Chapter 4. Using  $8\mu\text{m}$  images from *Spitzer*, I found that protostellar envelopes cast shadows against the Galactic background radiation at this wavelength. These images reveal the morphological structure of the densest parts of the envelopes in great detail from  $0.1$  pc scales down to  $\sim 1000$  AU. Most envelopes found in this study of *Spitzer* archival data are far from round, many are highly filamentary or even one-sided! This Chapter explicitly shows that one must think outside the sphere to understand the process of protostellar collapse.

While the  $8\mu\text{m}$  shadow images reveal the morphology of the protostellar envelopes, they contain no information about the kinematics of the presumably collapsing envelope. I describe a survey of the morphologically complex protostellar envelopes observed in the dense molecular gas tracers  $\text{N}_2\text{H}^+$  ( $J = 1 \rightarrow 0$ ) and  $\text{NH}_3$  (1,1) in Chapter 5. Sixteen envelopes from Chapter 4 were mapped in  $\text{N}_2\text{H}^+$  using the IRAM 30m telescope, collecting single-dish data superior in sensitivity and resolution to previous surveys. Interferometric  $\text{N}_2\text{H}^+$  and  $\text{NH}_3$  observations were then taken for fourteen envelopes and three archival  $\text{NH}_3$  datasets are also presented. These single-dish and interferometric data are used to determine the velocity field and gradients on both large and small scales in protostellar envelopes.

In Chapter 6, the interferometric velocity data from Chapter 5 are more closely interpreted. Models of predicted kinematic structure from axisymmetric collapse as well as non-axisymmetric filamentary collapse are presented. These models are compared to position-velocity diagrams derived from the interferometric molecular line data. I compare the predictions of an inside-out collapse with large-scale rotation, wholly infalling envelopes, and non-axisymmetric rotating and infalling envelopes.

Finally, Chapter 7 summarizes the general conclusions from the thesis and outlines future research directions that have grown out of this research, enabled by new instrumentation coming online in the near future.

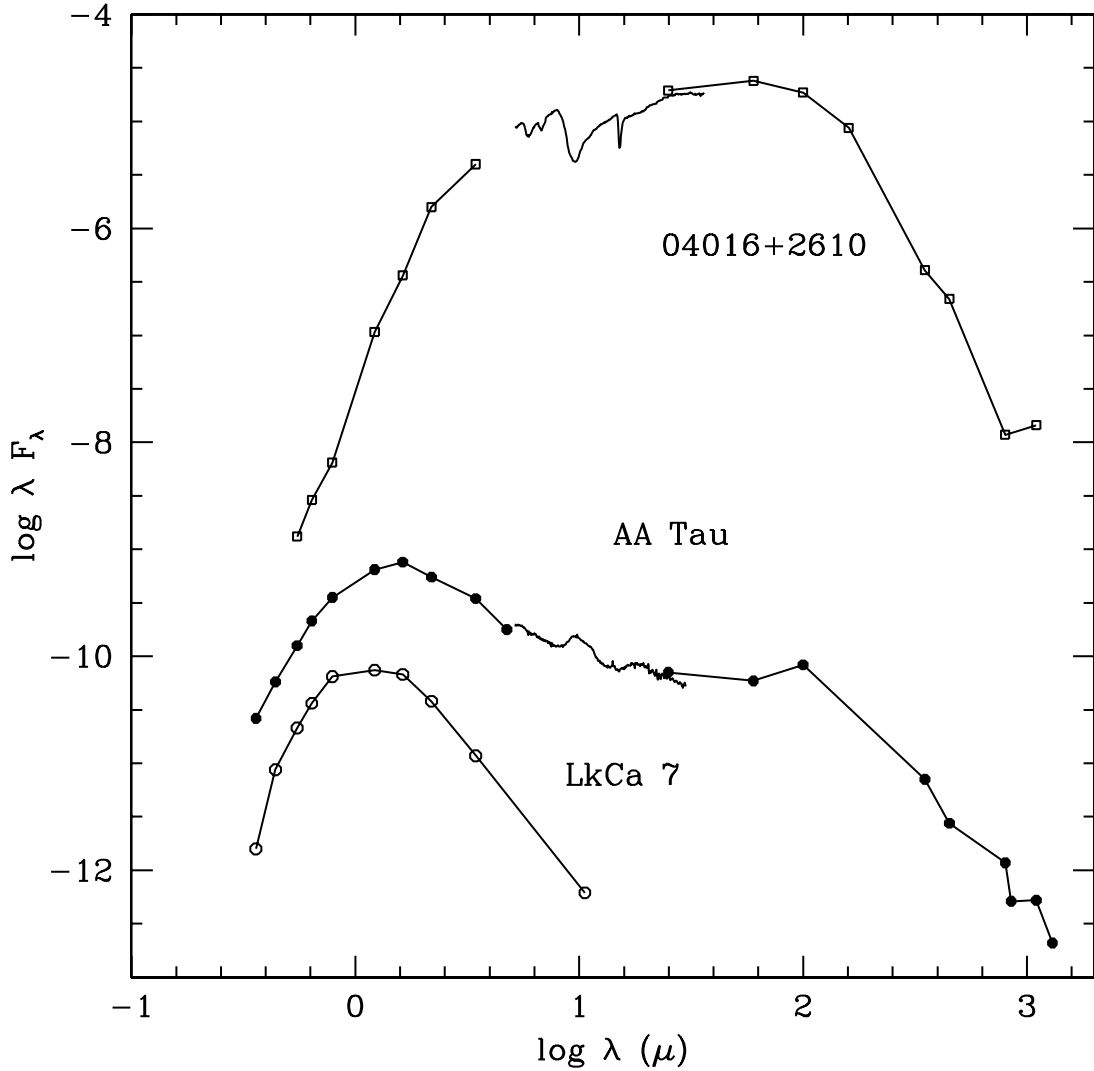


Figure 1.1 Sample spectral energy distributions (SEDs) with *Spitzer* IRS spectra overlaid for Class I (top), Class II (middle), and Class III (bottom) young stellar objects (taken from Hartmann (2009)). In the case of the Class I objects, most of the optical and near-infrared emission is scattered light, not direct stellar emission. For the Class II and Class III objects the optical emission is photospheric. Reproduced by permission of author.

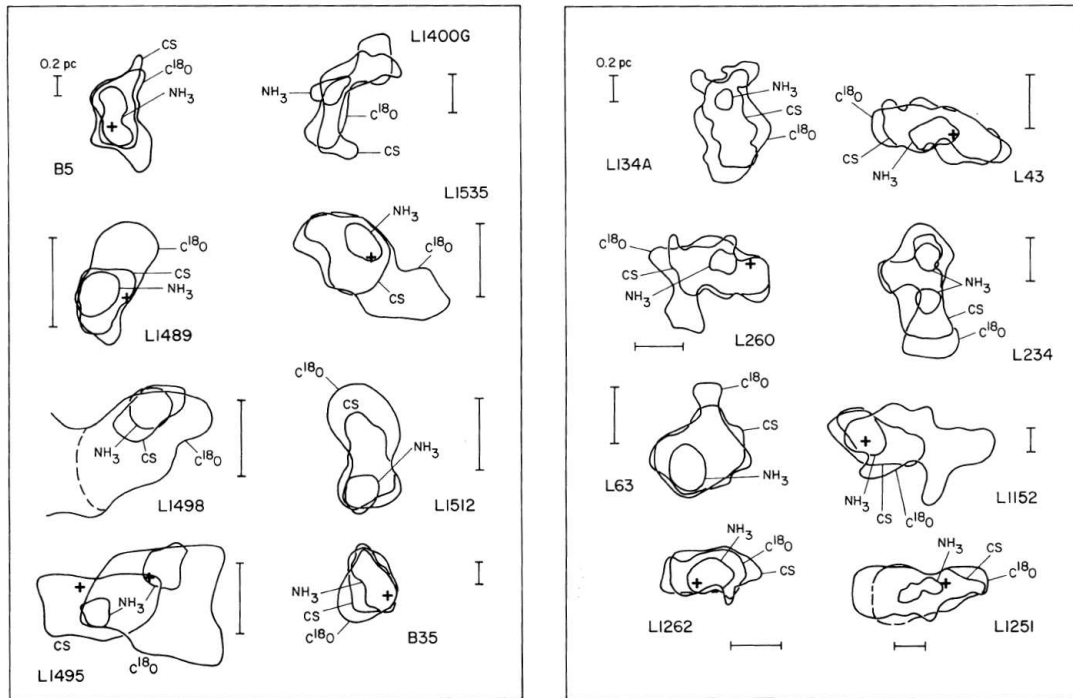


Figure 1.2 Maps of half maximum intensity contours for maps of  $\text{NH}_3$  (1,1),  $\text{C}^{18}\text{O}$   $J = 1 \rightarrow 0$ , and  $\text{CS}$   $J = 2 \rightarrow 1$  taken toward dense cores in dark clouds from Myers et al. (1991). The molecular line emission, tracing dense gas, shows that cores often have complex, asymmetric structure on  $\sim 0.1$  pc scales. Reproduced by permission of the AAS.

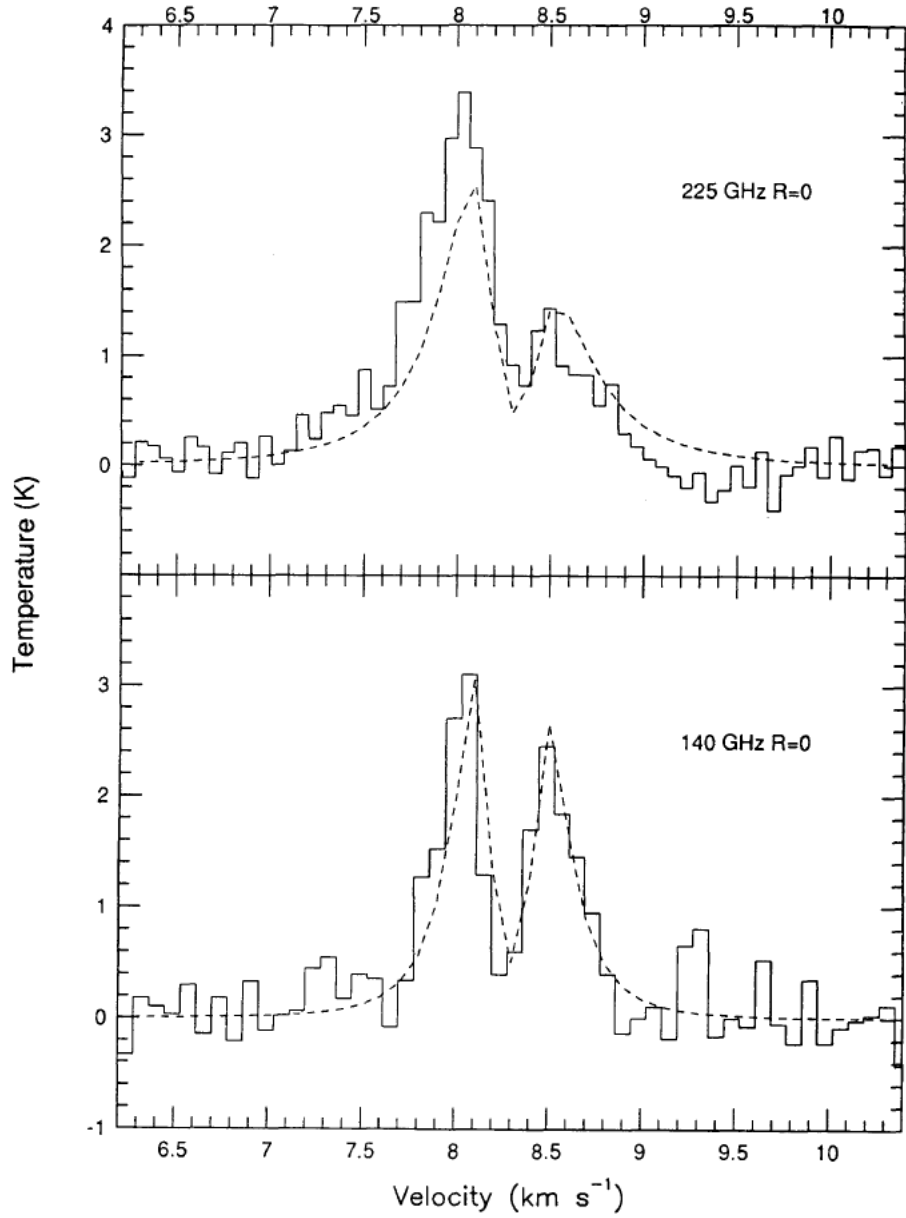


Figure 1.3 Plots of observed H<sub>2</sub>CO line profiles from Zhou et al. (1993) showing the blue-asymmetry with models of inside-out collapse fit (dashed lines). Reproduced by permission of the AAS.

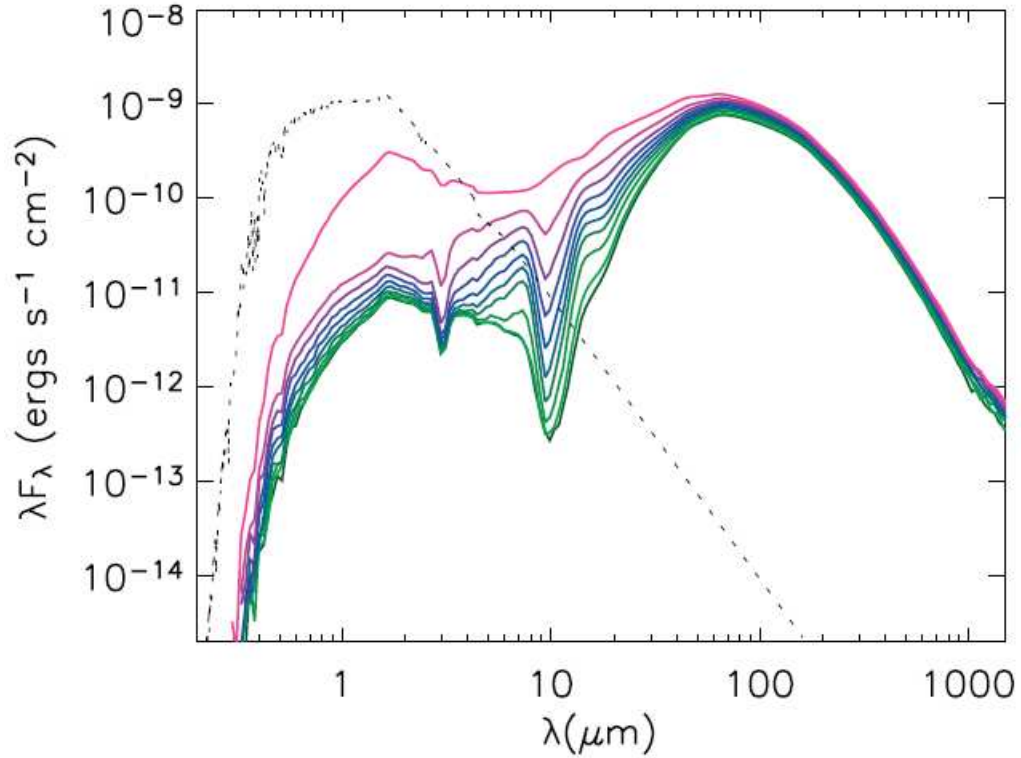


Figure 1.4 Model SEDs (solid lines) for a Class 0 protostar calculated by Whitney et al. (2003a). The different lines correspond to different inclinations where  $\cos(i) = 0.05, 0.15, \dots, 0.95$ . The uppermost line corresponds to  $\cos(i) = 0.95$ , and can be thought of as “face-on” while the bottommost line is  $\cos(i) = 0.05$  can be thought of as “edge-on.” The dashed line is the spectrum of the central protostar assumed to be a 4000 K stellar atmosphere. Reproduced by permission of the AAS.

## CHAPTER 2

# Constraining the Envelope Structure of L1527 IRS: Infrared Scattered Light Modeling

### 2.1 Introduction

The *Spitzer Space Telescope* has given unprecedented views of star forming regions. With *Spitzer*, the earliest stages of star formation are able to be studied with far greater resolution, sensitivity, and through higher extinctions than was previously possible with ground-based near-infrared (NIR) imaging. These capabilities of *Spitzer* enable tests of star formation theories (e.g. Terebey et al., 1984; Shu et al., 1987) in detail using radiative transfer models (e.g. Whitney et al., 2003b). The Terebey et al. (1984, TSC) model, describes the collapse of an initially spherical envelope which becomes rotationally flattened as it collapses. This model has been the standard, most widely used, model describing infalling protostellar envelopes for the past two decades (e.g. Adams et al., 1987; Kenyon et al., 1993a; Osorio et al., 2003; Whitney et al., 2003b; Robitaille et al., 2006; Furlan et al., 2008; Tobin et al., 2007).

Protostars drive powerful, bipolar molecular outflows which carve out cavities in the circumstellar envelope. These cavities can be observed as scattered light nebulae. The TSC envelopes alone predicted too little flux short ward of  $10\mu\text{m}$ , necessitating the inclusion of bipolar outflow cavities into the standard model (Calvet et al., 1994). Thus far, a simple bipolar cavity structure carved out of a TSC envelope has sufficed for modeling images and spectral energy distributions (SEDs) of evolved, Class I,

---

Based on the paper by John J. Tobin, Lee Hartmann, Nuria Calvet, Paola D'Alessio, ApJ, 2008, 679, 1364

protostars. However, recent observations by *Spitzer* are enabling detailed modeling studies of outflow cavities and envelopes of the youngest protostars, the Class 0 objects (Andre et al., 1993). In particular, *Spitzer* observations of outflow cavities in scattered light permit more detailed analysis of the inner structure of protostellar envelopes.

Observations of protostars with the Infrared Array Camera (IRAC) (Fazio et al., 2004) have revealed numerous, prominent scattered light nebulae associated with Class 0 objects (e.g. Noriega-Crespo et al., 2004; Tobin et al., 2007; Seale & Looney, 2008). Scattered light nebulae are also observed in J, H, and Ks (JHK) bands. However, the scattered light in JHK bands is highly attenuated by the dense circumstellar envelope; therefore, scattered light nebulae are often observed to appear brightest in the IRAC channels numbered 1 to 4 (3.6, 4.5, 5.8, and  $8.0\mu\text{m}$ ) (Tobin et al., 2007).

Scattered light images are an important, alternative method of probing the envelope structure of protostars, complementary to submillimeter and millimeter studies of optically-thin dust emission. IRAC images are important to scattered light studies because the envelope structure can be more clearly observed since the dust is less optically thick than at JHK bands. Scattered light images enable clear observation of the outflow cavities and may directly show the effects of the outflow on the envelope. In addition, submillimeter images tend to be elongated along the outflow cavities due to heating from the central protostar and disk. This additional emission complicates analysis of the envelope structure at long wavelengths without knowledge of the outflow cavity structure from scattered light images.

Most physical parameters cannot be derived from scattered light images alone. Radiative transfer modeling, in conjunction with a detailed observational analysis, must be performed to derive the likely physical parameters of an object. The results from radiative transfer modeling can yield insights into the structure of protostars that scattered light images or dust continuum observations alone would not reveal. Observations of L1527 IRS (IRAS 04368+2557) with the *Spitzer Space Telescope* are an ideal starting point for testing models of low-mass star formation.

The L1527 dark cloud is located within the Taurus molecular cloud at a distance

of  $\sim 140$ pc. This object has been observed extensively from the NIR to centimeter wavelengths (Ohashi et al., 1997; Chandler & Richer, 2000; Loinard et al., 2002; Hartmann et al., 2005). L1527 IRS, hereafter L1527, is classified as a borderline Class 0/I object with a large, dense circumstellar envelope (Chen et al., 1995; Motte & André, 2001), I will refer to L1527 as a Class 0 object. A unique property of L1527 is that it is observed at a nearly edge-on ( $\sim 90^\circ$ ) inclination (Ohashi et al., 1997). The tightly constrained inclination makes L1527 ideal for modeling since the inclination-dependent degeneracies on other modeled parameters (e.g luminosity, opening angle, infall rate) (Whitney et al., 2003a) are limited. Also, since L1527 is relatively nearby, the spatial resolution of the observations is about 2 times better than observations of protostars in Perseus and 3 times better than Orion.

The envelope properties of L1527 have been modeled previously. Kenyon et al. (1993a) (KCH93) used TSC envelopes to model the SED from IRAS; Furlan et al. (2008) (F07) used a similar, improved model to fit the SED and MIR spectrum of L1527. Finally, Robitaille et al. (2007) (R07) modeled L1527 using a large grid of TSC models calculated by the Whitney et al. (2003b) code (Robitaille et al., 2006). Here I revisit L1527, performing a more comprehensive observational analysis using scattered light images, MIR spectra and photometry from the NIR to millimeter wavelengths. I use these data combined to construct a new, detailed model describing the envelope structure of L1527 in order to test star formation theories and gain a more clear picture of protostellar structure.

## 2.2 Observations and data reduction

### 2.2.1 Spitzer Space Telescope Data

The data are taken from previous observations of Taurus in the *Spitzer* archive, processed with pipeline version S14.0.0. L1527 has been observed twice; first on 07 March 2004 as part of the guaranteed time observer (GTO) survey of known young stars in Taurus (Hartmann et al., 2005) and again on 23 February 2005 as part of the Taurus Legacy survey (Padgett et al., 2006). The GTO observations were performed

in a 3 position, cycled dither pattern, with a frame time of 12 seconds. The Legacy data mapped the entire Taurus region twice with single frames of 12 seconds each and spatial limited overlap. The legacy data of L1527 are comprised of two frames taken a few hours apart, which require manual processing. I re-mosaicked the data using MOPEX version 061507 to make combined images from both observations and to create a more clean mosaic of the Taurus Legacy data.

The Taurus legacy survey also observed L1527 with the Multiband Imaging Photometer (MIPS) (Rieke et al., 2004). The observations were carried out in mapping mode on 05 March 2005 in two separate observations of all three bands: 24, 70, and  $160\mu\text{m}$ . I used the post-BCD data for the  $24\mu\text{m}$  observations; it was necessary to re-mosaic the  $70\mu\text{m}$  data using filtered BCD images because the post-BCD data have gaps due to only half of the detector functioning. The  $160\mu\text{m}$  data did not fully map L1527 and I could not use the data for photometry.

L1527 has also been observed by the Infrared Spectrometer (IRS) (Houck et al., 2004) onboard the *Spitzer Space Telescope*. The spectrum was taken in both orders of the short-low (5 -  $14\mu\text{m}$ ) and long-low (14 -  $40\mu\text{m}$ ) modules on 27 February 2004. In the analysis, I use the same spectrum as presented in F07. The spectral resolution is  $R \sim 120\text{-}60$  for both modules.

### 2.2.2 Near-Infrared Observations

I observed L1527 at the MDM Observatory at Kitt Peak on 27 and 29 December 2007 using the 2.4m Hiltner telescope with the NIR imager TIFKAM (Pogge et al., 1998). I observed L1527 in the J, H, Ks, and  $\text{H}_2$  ( $2.12\mu\text{m}$ ) filters on 27 December and the  $\text{H}_2$  continuum ( $2.09\mu\text{m}$ ) filter on 29 December; with total integration times in J and H-band of 10 minutes and a total integration time of 35 minutes in Ks,  $\text{H}_2$ , and  $\text{H}_2$  continuum bands. The  $\text{H}_2$  continuum filter is a line-free, narrowband filter with a bandwidth matching the  $\text{H}_2$  filter.

The observations were conducted in a 5 point dither pattern with 1 minute of integration per dither position. After each complete dither pattern, I chopped off source and observed the sky in the same 5 point dither pattern to construct a median

sky. The off-source imaging was necessary because TIFKAM has a 3' field of view and L1527 nearly fills the field. The data were reduced using standard routines from the upsqiid package for flat fielding, sky subtraction, and combining. The J-band image does not detect L1527 and the H-band image only marginally detects L1527. However, L1527 is clearly observed in the Ks-band image. The H<sub>2</sub> image marginally detects L1527 with comparable signal-to-noise (S/N) to H-band, while the H<sub>2</sub> continuum band image does not detect L1527.

### 2.2.3 Additional Infrared Data

I also include mid-infrared data from the Infrared Space Observatory (ISO) in the study. I used ISOCAM data from the 6.7, 9.6, 11.3 and 14.3 $\mu$ m bands observed on 02 October 1997. These bands are overlapped by the IRS instrument, however, I used these images to constrain any extended emission at these wavelengths. I used pipeline processed data from the ISO science archive, performing no further reduction of these data.

Finally, I used data from the Two Micron All Sky Survey (2MASS) (Skrutskie et al., 2006) in the study of L1527. I use the calibrated data frames for the L1527 region from the 2MASS archive.

### 2.2.4 Photometry

I performed aperture photometry on L1527 using the Image Reduction and Analysis Facility (IRAF)<sup>1</sup>. Photometry was not straightforward since a background annulus cannot be used because it includes extended emission surrounding the source. Instead, using the 'imstat' procedure in IRAF, I measured a large area of sky adjacent the source that was devoid of emission to obtain an average background value per pixel. This value was then multiplied by the aperture area measured by IRAF and subtracted from the photometric value of the source. Also, local extinction of the background will result in over-subtraction of the background on the source. This

---

<sup>1</sup>IRAF is distributed by the National Optical Astronomy Observatories, which are operated by the Association of Universities for Research in Astronomy, Inc., under cooperative agreement with the National Science Foundation.

over subtraction is greatest in IRAC channels 3 and 4 where the background interstellar medium (ISM) and zodiacal light emission are highest.

I measured the flux within 1000 and 10000 AU aperture radii centered on the position of L1527;  $\alpha = 04:39:53.9$   $\delta = +26:03.09.6$  (J2000). These apertures correspond to 6 and 60 pixel radii at a distance of 140 pc and the IRAC pixel scale of  $1''.2/\text{pixel}$ . I use two apertures in my analysis because the 1000 AU aperture probes emission on small scales, dominated by the central envelope structure and the 10000 AU aperture probes emission dominated by extended scattered light in the outflow cavity. Lastly, I applied aperture corrections to the photometry using the methods of extended source calibration described on the *Spitzer Science Center* website. Photometry and aperture corrections are listed in Table 2.1.

For the ISO data, I used the same procedure as above, however I was only able to use apertures of 1000 ( $7''.2$ ) and 5000 AU ( $36''$ ) due to the limited field of view. The ISO photometry may have up to 30% errors as aperture corrections were unknown and background subtractions are uncertain.

The 2MASS photometry was performed using the same procedure as the IRAC data. The pixel size of the 2MASS detectors was  $2''.0/\text{pixel}$  so the apertures were 3.57 pixels for 1000 AU and 35.7 pixels for 10000 AU.

Finally, photometry from the TIFKAM data were also taken using the method for IRAC data. The pixel size on the TIFKAM detector corresponds to  $0''.2/\text{pixel}$ , translating to a 35.7 pixel aperture for 1000 AU and a 357 pixel aperture for 10000 AU. The data were calibrated using the faint NIR standards listed in (Hunt et al., 1998).

## 2.3 Observed Morphology

As shown in Figures 2.1 and 2.2, L1527 exhibits bright bipolar scattered light nebulae which extend roughly 1.5 arcminutes (12600 AU) on each side of the central source. In addition to the large, bright cavities, the most striking features are the ‘neck’ and absorption lane between the reflection nebulae. The absorption lane is clearly shown in the Ks-band image (Figure 2.2), having a width of  $\sim 10''$  (1500 AU). The ‘neck’

becomes apparent in the IRAC images as a thin strip of emission bridging the gap between the cavities. The ‘neck’ is shown in more detail in Figure 2.3.

In addition, I observe a bright source between the cavities on the ‘neck’ in the IRAC images, see Figure 2.3. This feature was not detected in the TIFKAM or 2MASS observations. This source appears to be slightly extended as compared to a point source in all IRAC channels, though the surrounding nebulosity makes it difficult to be certain. I will discuss the possible nature of this object in Section 2.5.

In the MIPS  $24\mu\text{m}$  images, L1527 is a point source, but at  $70\mu\text{m}$  there is marginally resolved structure; L1527 appears elongated along the outflow axis, see Figure 2.2. The radius of the envelope at  $70\mu\text{m}$  is about  $70''$  or about  $10000\text{AU}$ . L1527 was not completely mapped at  $160\mu\text{m}$ , but extension along the outflow axis is again observed. Also, I estimate that the L1527 envelope has a radius of approximately  $100''$  or  $14000\text{AU}$  from the  $160\mu\text{m}$  image.

While the bipolar nebulae of L1527 may in general seem prototypical and simple to model, in reality L1527 is very complex. I noticed that in IRAC Channels 1 and 2 there is an inherent lumpiness to the scattered light cavities presumably from substructure in the cavity walls; the substructure becomes unresolved in IRAC channels 3 and 4. In addition to the lumpiness of the scattered light, L1527 shows several asymmetries in brightness and geometry.

### 2.3.1 Asymmetry

The position angle (PA) of the outflow from L1527 is  $\sim 90^\circ$  east of north (Zhou et al., 1996; Hogerheijde et al., 1998). Also, I observe faint Herbig-Haro objects at  $\sim 230''$  west and  $\sim 160''$  east of L1527 in the IRAC images (Figure 2.4); they are consistent with a PA of  $\sim 90^\circ$ . Using this PA as the symmetry axis for the outflow cavities, there is clear asymmetry which is quite plain in Figures 2.1 and 2.2. The southeast side of the cavity opens wider than the northeast and vice versa. Also, the cavity has an azimuthal brightness asymmetry. In the east side cavity, the south side is brighter than the north side and in the west side cavity the north side is brighter than the south side. The asymmetry seems to be a global effect on the entire envelope since the

departures from spherical symmetry are observed to be qualitatively point symmetric. Also, the asymmetry appears to be present at many different wavelengths, even in the submillimeter images, see Figure 2.5. The submillimeter contours are overall boxy in shape. In the southeast and northwest of Figure 2.5, the contours are more extended than the northeast and southeast contours, looking like a parallelogram.

### 2.3.2 Variability

The cavities of L1527 are observed to have substantial brightness variations over time. Comparing the two epochs of observations in Figure 2.6, it can be seen that both sides of the cavity exhibit independent variability over the entire cavity. In 2004 the western cavity was much brighter than in 2005; and in 2004 the eastern cavity is fainter than in 2005.

Figure 2.7 shows the flux averaged over sectors of annuli spaced radially for each epoch. The variation between the two epochs is not large enough to affect modeling and the brightness of the cavities is fairly flat close to the center. The flatness is the result of the curved cavity shape; the distance of the cavity wall to the illuminating source changes slowly in this region. Also, at a radial distance of greater than  $10''$  the cavity brightness falls off roughly  $\propto R^{-2}$  in both epochs, consistent with scattered light from a central point source incident on an optically thick wall (Whitney & Hartmann, 1993). The bump at about  $30''$  is due to a brightened cavity feature present in both cavities at this distance. IRAC Channels 1 and 2 are very similar in their ratios over the entire measured region, see Figure 2.6. IRAC Channels 3 and 4 are similar out to about 50 arcseconds; where the scattered light falls off in these channels. IRAC channels 3 and 4 are not shown in Figure 2.6 as the divided images are very noisy.

### 2.3.3 Local Extinction

#### 2.3.3.1 $8\mu\text{m}$ Absorption

With the data from *Spitzer*, the envelope structure is not only observed through scattered light, but also directly probed in absorption at  $8\mu\text{m}$ . IRAC Channel 4 is

the widest IRAC band with a bandwidth of  $2.93\mu\text{m}$ , extending from  $6.44$  to  $9.38\mu\text{m}$ , overlapping with the  $6.85\mu\text{m}$  organic ice,  $9.0\mu\text{m}$  ammonia ice, and most importantly the  $9.7\mu\text{m}$  silicate feature. The presence of these absorption features in IRAC Channel 4 and a significant interstellar background make it an ideal band to observe MIR extinction. Observing absorption in the MIR is not new, this type of analysis has been performed extensively on infrared dark clouds located in the galactic midplane (e.g. Simon et al., 2006; Ragan et al., 2006). Also, Looney et al. (2007) observed L1157 to have a flattened envelope in  $8\mu\text{m}$  absorption.

To turn the IRAC  $8.0\mu\text{m}$  image into an optical depth image, I first subtracted the estimated zodiacal light; a model calculated value is found in the image header. Then I measure the residual background emission, using the same method I used for the photometry background measurement. The  $8.0\mu\text{m}$  image is then divided by the background measurement and the natural log of each pixel is calculated, yielding an optical depth image. This method assumes a constant background which may not be a realistic assumption. However, given the low S/N of the background and small angular size of L1527, modeling of the background as described in Simon et al. (2006), would not improve the analysis.

Figure 2.4 shows the  $8\mu\text{m}$  optical depth contours overlaid on the IRAC  $8.0\mu\text{m}$  image. In addition to the asymmetries observed in scattered light, the  $8.0\mu\text{m}$  absorption is asymmetric. The north side of the envelope has significantly more optical depth and covers a larger area than the south. This observation infers that there is more material to the north in the line of sight, in agreement with submillimeter observations shown in Figure 2.5. The submillimeter contours are more extended on the north side of L1527 by about  $20$  to  $30''$  than on the south side.

Using these optical depth data, a rough idea of the amount of material in the envelope can be derived. Assuming the  $8.0\mu\text{m}$  opacity from Li & Draine (2001) I derive a mass of  $0.22 M_{\odot}$ . The measured mass is low compared to previous estimates of  $2.4 M_{\odot}$  to  $0.8 M_{\odot}$  from ammonia and dust emission (Benson & Myers, 1989; Shirley et al., 2000; Motte & André, 2001). However, there are large uncertainties in the opacity (emissivity) in the MIR and at long wavelengths. Also, the level of

residual zodiacal light contamination of the IRAC images is uncertain and in general the measurement is uncertain due to low S/N of the background. The measurement is also at best a lower limit as scattered light emission is present over roughly half the envelope masking some of the extinction.

### **2.3.3.2 Inclination Dependent Extinction**

Radiative transfer models (Whitney et al., 2003a) and simple geometry show that the local extinction of the outflow cavity lobes will depend on line of sight inclination. Local extinction refers to self-extinction by the envelope, not the ambient molecular cloud. With constant illumination of a spherically symmetric envelope, the blue-shifted outflow cavity (tilted toward the observer) should appear brighter than the red-shifted cavity (tilted away). The blue and red-shifted cavities are determined from observations of rotational transitions of molecules at submillimeter and millimeter wavelengths, e.g. CO, SiO, HCN, etc. For L1527, the eastern cavity is blue-shifted and the western cavity is red-shifted (Zhou et al., 1996; Bontemps et al., 1996; Ohashi et al., 1997; Hogerheijde et al., 1998). There is some overlap in the velocity channels indicating that L1527 is observed close to edge-on.

In the Ks-band image from TIFKAM, both the blue and red-shifted cavities are visible. However, the blue-shifted cavity is brighter by about a factor of 2 in some regions. 2MASS observations only show the blue-shifted cavity. In the two epochs of IRAC observation, the cavities have appeared roughly equal in brightness in the 2005 epoch, and the blue-shifted cavity being brighter in the 2004 epoch. These observations are consistent with dependence of cavity brightness on inclination highlighted in (Whitney et al., 2003a), indicating that L1527 is close to edge-on but slightly inclined.

This investigation of the observed morphology yields many observational constraints which were necessary to take into account while constructing the model. Some constraints such as observing L1527 nearly edge-on greatly helps modeling by reducing several degrees of freedom for opening angle and inclination. The variability does not greatly hinder the modeling effort since the overall morphology of the object remains constant and the overall increase or decrease in intensity is at most a factor

of 2. Finally, reproducing the observed central source and dark lane requires specific attention in constructing a model of L1527.

## 2.4 Modeling

### 2.4.1 Envelope and Disk Structure

To interpret the observations, I used the radiative transfer code of Whitney et al. (2003b) to construct a model of the L1527 data. This code uses the Monte Carlo method to calculate radiative equilibrium and include multiple scattering. The model has many parameters to tune, some more important than others; I will review the parameters important to the study.

I model the central protostar with a stellar atmosphere for a given effective temperature and radius. In addition to the protostellar luminosity, I found that the model needs strong disk emission. The strong disk emission can come from high accretion luminosity, a bright star illuminating the disk, or a combination of both.

I assume the typical model for T Tauri accretion in which material from the inner disk falls along magnetic field lines onto the protostar creating an accretion shock which is assumed to radiate as a blackbody over an area of 0.01 of the stellar surface (Calvet & Gullbring, 1998). In addition to heating the envelope, emission from this accretion shock heats the disk along with the radiation from the stellar photosphere. Local viscous dissipation also heats the disk, but the dominant disk heating is the protostar plus accretion shock irradiation. These disk heating mechanisms combined result in the disk emitting substantial NIR to MIR radiation.

The total system luminosity is

$$L_{total} = L_* + L_{shock} + L_{disk}, \quad (2.1)$$

where  $L_{shock}$  is the luminosity of the accretion shock on the star,

$$L_{shock} = \frac{GM_*\dot{M}_{disk}}{R_*} \left(1 - \frac{R_*}{R_m}\right) \quad (2.2)$$

and  $L_{disk}$  is the luminosity from viscous energy release,

$$L_{disk} = \frac{GM_*\dot{M}_{disk}}{R_{in}}. \quad (2.3)$$

In these equations,  $M_*$  is the central source mass,  $\dot{M}_{disk}$  is the disk accretion rate of the disk onto the star,  $R_{in}$  is the inner radius of the disk, generally the dust destruction radius where the dusty disk is truncated, and  $R_m$  is the magnetospheric truncation radius. In reality, the disk extends to  $R_m$ ; the disk inside the dust destruction radius  $R_{dd}$  is composed of dust-free gas which may be optically thin or thick. Currently, there are few observational constraints on the properties of the inner disk; thus, it is not included in as an energy source in the model. The gaseous inner disk may be an important detail that the model lacks.

The disk structure is assumed to be a standard flared accretion disk structure (e.g. Hartmann, 1998) with a density profile given by

$$\rho(r, z) = \rho_0 \left(1 - \left(\frac{R_*}{r}\right)^{1/2}\right) \left(\frac{R_*}{r}\right)^\alpha \exp \left[-\frac{1}{2} \left(\frac{z}{h(r)}\right)^2\right] \quad (2.4)$$

where  $r$  is the radial coordinate of the disk, and  $h(r) = h_0(r/R_*)^\beta$ . The model does not assume any temperature structure for the disk *a priori* thus the  $h(r)$  is not calculated self-consistently throughout the disk. The model solves the hydrostatic equilibrium equation to obtain the scale height  $h(r)$  at the dust destruction radius, modified by the flaring power-law  $\beta$ , for the entire disk structure. However, to ensure physically consistent parameters are modeled, I manually specify a scale height for the model determined from the scale height at the dust destruction radius

$$h_{dd} = \left(\frac{kT_{dd}R_{dd}^3}{GM_*\mu m_p}\right)^{1/2} \quad (2.5)$$

where  $T_{dd}$  is the dust destruction temperature, 1400K,  $\mu$  is the atomic mass unit assumed to be 2,  $m_p$  is the mass of a proton,  $k$  is the Boltzmann constant, and  $R_{dd}$

is the dust destruction radius given by

$$R_{dd} = \left( \frac{T_{eff}}{T_{dd}} \right)^{2.1}. \quad (2.6)$$

$T_{eff}$  refers to the effective temperature of the star, including the accretion luminosity. The code states that the power 2.1 comes from an empirical fit, if the wall and star were in equilibrium and assuming perfect blackbody radiation, the power should be 2.

For the circumstellar envelope, I assume a TSC envelope with the density structure given by

$$\rho(r) = \frac{\dot{M}_{env}}{4\pi(GM_*r^3)^{1/2}} \left( 1 + \frac{\mu}{\mu_0} \right)^{-1/2} \left( \frac{\mu}{\mu_0} + \frac{2\mu_0^2 R_c}{r} \right)^{-1}. \quad (2.7)$$

$\dot{M}_{env}$  is the mass infall rate of the envelope onto the disk,  $R_c$  is the centrifugal radius where rotation becomes important,  $\mu = \cos \theta$ , and  $\mu_0$  is the cosine polar angle of a streamline out to  $r \rightarrow \infty$ . Inside of  $R_c$ ;  $\rho_{env} \propto r^{-1/2}$  and outside  $R_c$ ;  $\rho_{env} \propto r^{-3/2}$ . The centrifugal radius controls the optical depth to the center of the envelope, increasing  $R_c$  decreases the overall envelope density. The overall mass of the envelope does not strongly depend on  $R_c$  as the centrifugal radius is generally small compared to the outer envelope radius.

Bipolar cavities in the envelope are obviously required to fit the observations of extended scattered light and thermal emission. These bipolar cavities extend from the central protostar to the outer radius of the envelope. Curved or streamline cavities were options in modeling, I adopted curved cavities as they allowed for greater flexibility in modifying the cavity shape. The curved cavity structure is defined by  $z = C(x^2 + y^2)^{b/2}$ , where  $C$  is a constant determined by a relation between the cavity opening angle and envelope radius, and  $b$  is the shape parameter, the power of the polynomial defining the cavity shape. In the model, it was necessary to use two cavities of different sizes in the inner and outer envelopes. The cavity structure will be discussed further in Section 2.5.

Table 2.2 lists the parameters of the model I found to best fit L1527. The stel-

lar parameters are uncertain and were simply taken to be those of typical Taurus T Tauri stars and were not varied. The total system luminosity (star plus disk accretion) is very important, depending on both the fixed stellar and the accretion disk parameters. There are several parameters for the accretion disk, but in terms of the modeling, the most important ones are the disk accretion rate, which sets the disk and accretion shock luminosity, and scale height specifying the inner disk “wall” at the dust destruction radius, which dominates the emission in the IRAC bands (see Section 2.5). The other disk parameters are relatively unimportant. The envelope infall rate in conjunction with the assumed stellar mass set overall optical depth of the envelope and the amount of long-wavelength thermal emission. The cavity properties are somewhat arbitrary but are simply tuned to match the observed morphology. The inclination angle is essentially edge-on, and the cavity and ambient densities, sometimes used in other modeling, are set to zero in the investigation.

#### 2.4.2 Dust Properties

The default envelope dust properties assumed in the model are  $R_V = 4$  dust grains with 5%  $\text{H}_2\text{O}$  ice coatings. This is one of the standard dust opacity tables included with the Whitney et al. (2003b) model which is derived from Kim et al. (1994). These dust properties are intended to be similar to the ISM dust in Taurus. These dust grains do not include the  $6.0\mu\text{m}$   $\text{H}_2\text{O}$ ,  $6.85\mu\text{m}$   $\text{CH}_3\text{OH}$ , and  $15.2\mu\text{m}$   $\text{CO}_2$  ice features; all these ice features are typically observed in Class 0 and Class I protostars (F07).

The dust properties are a source of uncertainty in the model. Dust grain models appropriate for the ISM may not be appropriate for Class 0 envelopes. If dust grains in the diffuse ISM of Taurus are able to develop ice coatings (Whittet et al., 2001) and grow in dense regions (Flaherty et al., 2007; Román-Zúñiga et al., 2007), this leads to the possibility that considerable grain growth could occur in dense protostellar envelopes. Larger grains would have higher albedo out to longer wavelengths and could help to explain the intensity of the observed scattered light in the MIR.

Driven by the observations, I have constructed a dust model which uses larger dust grains than a standard ISM dust model. The dust model is calculated using

the method described in D'Alessio et al. (2001), with additional optical constants for graphite from Draine & Lee (1984). The grain size distribution is defined by a power law grain size distribution  $n(a) \propto a^{-3.5}$ , with  $a_{min} = 0.005\mu\text{m}$  and  $a_{max} = 1.0\mu\text{m}$ . I used dust grains composed of graphite  $\zeta_{graph} = 0.0025$ , silicates  $\zeta_{sil} = 0.004$ , and water ice  $\zeta_{ice} = 0.0005$ ; abundances are mass fractions relative to gas. The given abundances infer a gas to dust ratio of 133. The dust model does not include organic molecules, all carbon is in the form of graphite, nor does it include the additional ice features detailed at the start of this section. Dust grains larger than  $a_{max} = 1.0\mu\text{m}$  would have too much albedo long-ward of  $8.0\mu\text{m}$  yielding significant extended emission between  $8.0\mu\text{m}$  and  $15\mu\text{m}$ . Observations by ISO do not show significant extended emission above the background at  $9.6$  or  $11.3\mu\text{m}$ . These observations constrain the maximum possible size of dust grains in the outer envelope of L1527 to be  $\sim 1\mu\text{m}$  in radius. The opacity and albedo curves of the assumed dust model is plotted against an ISM dust model (Kim et al., 1994) in Figure 2.8.

### 2.4.3 Model Fitting

Due to the inherent uncertainties in modeling L1527 and observed asymmetries, I did not quantitatively fit the images or SEDs using a  $\chi^2$  or equivalent minimization routine. To fit the observed morphology of the image, I convolved the model image with the appropriate, instrument specific, PSF and compared it to the observed data. If an image looked similar I noted the particular parameter set and ran the model again with more photons to obtain a higher S/N image. The asymmetric cavities of L1527 cannot be duplicated, due to the axisymmetry of the model, but the general morphology modeled is quite similar.

With the high S/N images, I compared the intensity averaged over sectors radially spaced (Figure 2.9) to compare the data and the models. In Figure 2.9 it is seen that the  $3.6\mu\text{m}$  channel agrees the best while the overall strength of the scattered light in the  $4.5$ ,  $5.8$  and  $8.0\mu\text{m}$  channels falls short at all radii, though the shape of the curves is quite similar. At Ks-band, the model also roughly agrees with the observations. Similar to the IRAC data, the Ks-band plot also has the bump at  $30''$ , probably due

to a bright spot in the cavity or an outflow knot. In addition, the intensity of the modeled central object in the IRAC bands does roughly agree with the observations.

The SED fitting was done by eye, adjusting the luminosity controlling parameters until the model was as close to the observed SED as possible. I was able to nearly bring the overall SED of the model and observations into agreement. Also, the asymmetry of the cavities does account for some of the discrepancy between the model and observed SED in the 10000 AU aperture. Also, I apply a foreground extinction of  $A_V = 3$  to the SED and images for fitting. The addition of extinction extinguishes the extended scattered light the model predicts in the visible while hardly affecting the portion of the SED I am fitting. The extinction toward L1527 is uncertain since it is a protostar embedded within a dark cloud. However, the assumed extinction is not atypical for Taurus.

## 2.5 Results

In order to match the observed morphology of L1527, changes to the standard Whitney et al. (2003b) model were necessary. The largest necessary change was to the bipolar cavity configuration. Here I describe the changes to the standard parameter set of the model and review the resulting physical parameters and their significance.

### 2.5.1 Reproducing the Scattered Light Morphology

At the start of the modeling effort I adopted the parameters fit by F07; see Table 2.2. I soon found that I could not replicate the dark lane, ‘neck’, or central object with the standard bipolar cavity geometry of the model and a relatively flat disk. In Figure 2.12 I show how the model looks using the default, single cavity structure. These images do show a dark lane, however it is very thin, and there is no central source in the IRAC images. The appearance of this dark lane is similar to those observed by Padgett et al. (1999), which are the relatively thin shadows of dusty circumstellar disks. The thickness of the dark lane in L1527 requires a structure that is as wide as it is thick, unlike a disk. I concluded that the observed dark lane and ‘neck’ must be due to the envelope structure and the standard bipolar cavities of the model would

not suffice.

To reproduce the observed ‘neck’ morphology I used an inner, narrow outflow cavity with an offset outer outflow cavity; this ‘dual-cavity’ geometry is shown schematically in Figure 2.10. In Figure 2.3, I compare the results of this model convolved with the IRAC PSF to the 3.6  $\mu\text{m}$  IRAC image. Then in the bottom panel of Figure 2.3, I show how the modeled central source actually appears at high resolution. The bright emission ridges in the IRAC images are produced at the base of the outer cavity; the inner cavity offsets the outer cavity, producing neck absorption while still transmitting enough scattered light to form the central source. The dual-cavity model has some direct support in the image; as shown in the upper left panel of Figure 2.3, the scattered light cavity appears much narrower near the source, especially on the western side. Possible physical motivations for the envelope structure I have created are discussed in Section 2.6.

In order to match the morphology of L1527 using the dual-cavity structure, the opening angle and cavity shape parameter are relatively well constrained. As discussed in Section 2.4 the cavities modeled are defined by a polynomial of a variable degree; I refer to the polynomial degree as the shape parameter. The shape parameter determines how quickly the cavity widens in the inner envelope. The cavity offset is associated with the inner/outer cavity opening angles and shape parameters. The best fitting outer cavity offset is 100 AU, a larger offset creates a central source that is too resolved. A smaller offset creates an unresolved central source.

The opening angle of the outflow cavities is defined as the angle measured from the center of the envelope to the outer envelope radius. Thus, near the center of the envelope, the cavity opens wider than the opening angle defined. The opening angle of the outer cavity is modeled to be  $20^\circ$  and the inner cavity opening angle is modeled to be  $15^\circ$ . The inner cavity is modeled to have a shape parameter  $b = 1.5$  and the outer cavity has a shape parameter  $b = 1.9$ . I need to model the outer cavity to have a shape parameter such that it opens wide a short distance from the envelope center. The inner cavity then casts a shadow on the widely opening outer cavity, and creates the apparent central point source in scattered light. The

shape parameters for the cavities are empirical. I adjusted the inner and outer shape parameters and opening angles until the models appeared similar to the observations. In the end, the morphology of the scattered light in the modeled cavities is similar to the observations.

The scattered light in the model and observations require a large envelope. To match the scattered light profile in Figure 2.9 and extent of scattered light in the images, it was necessary to use an envelope with a 15000 AU outer radius. Larger radii give too much optical depth to the center of the envelope. With smaller radii, the scattered light ends prematurely. In addition to the outer radius, the overall optical depth greatly depends on  $R_c$ ,  $\dot{M}_{env}$ , and  $M_*$ . I assume that the central protostar has a mass of  $0.5M_\odot$ , however this is an unknown. The best  $\dot{M}_{env}$  that I was able to fit is  $1.0 \times 10^{-5} M_\odot yr^{-1}$ . KCH93 alternatively express the infall rate as

$$\rho_1 = 5.13 \times 10^{-14} \left( \frac{\dot{M}_{env}}{10^{-5} M_\odot yr^{-1}} \right) \left( \frac{M_*}{1M_\odot} \right)^{-1/2}. \quad (2.8)$$

For the  $\dot{M}_{env}$  and  $M_*$ , I find  $\rho_1 = 3.75 \times 10^{-14} \text{ g cm}^{-3}$ ; corresponding to a dense circumstellar envelope appropriate for modeling a Class 0 or I object. A Class 0 object is expected to have a small  $R_c$  and high  $\dot{M}_{env}$ .

For the outer disk radius, I also used the same value as  $R_c$ , it is generally accepted that the disk will form inside the centrifugal radius. Outside  $R_c$ , the angular momentum is not great enough to prevent infall. The value of  $R_c$  modeled must be smaller than the outer cavity offset in order to create the shadowing effect due to the control  $R_c$  has on the optical depth. The best fitting  $R_c$  is 75 AU.

Modeling the inclination of L1527 was trivial as it is observed to be nearly edge-on. An inclination of  $85^\circ$  agrees well with the observations; an inclination much lower than  $80^\circ$  blends the inner cavity scattered light with that of the outer cavity.

### 2.5.2 SED Fitting: Disk Emission

The fundamental constraint that I need to model is the total system luminosity. Integrating over all available photometric data points, I measure a bolometric luminosity

( $L_{bol}$ ) of  $1.97 L_{\odot}$ . The  $L_{bol}$  gives an observational constraint on the total system luminosity being modeled. The measured  $L_{bol}$  is consistent with the recent estimate of  $1.9 L_{\odot}$  by F07.  $L_{bol}$  is probably a lower limit on the total luminosity because the object is observed edge-on and some radiation from the central protostar may escape through the outflow cavity without scattering or reprocessing. However, it is unlikely that the true luminosity is vastly larger because the outflow cavities do not span a large solid angle as seen from the source; thus most of the central source emission should be absorbed and reemitted by the envelope.

The central protostar is chosen to be a  $1 L_{\odot}$  star with an effective temperature of  $4000\text{K}$ , a radius of  $2.09 R_{\odot}$ , and a mass of  $0.5M_{\odot}$ . These stellar parameters are chosen from the stellar birthline of a typical T Tauri star (Hartmann, 1998) as an estimate for the properties of the central protostar. These parameters are an assumption, observations do not constrain the central source. Though L1527 is probably a binary (Loinard et al., 2002), I do not attempt to model multiple stars and/or disks. Doing so would have increased complexity and essentially just given a free parameter, as there are no constraints on the binary pair, other than projected separation.

The brightness of the scattered light combined with an approximate limit on the bolometric luminosity makes it impossible to explain the observations without a dominant contribution from the circumstellar disk at IRAC wavelengths. For plausible parameters, the infrared emission of the central protostar is much too faint for a given total luminosity. A much redder central source SED is required, with a high proportion of the luminosity being emitted in the NIR to MIR, in order to explain the observations.

For the fixed protostellar parameters, the best results required an accretion luminosity of  $\sim 1.6 L_{\odot}$  corresponding to a disk accretion rate of  $3.0 \times 10^{-7} M_{\odot} \text{ yr}^{-1}$ , so that the true bolometric luminosity in the model is  $\sim 2.6 L_{\odot}$ . Most of this accretion luminosity is radiated in the optical to ultraviolet by the accretion shock. Both the star and the accretion shock heat the disk, producing the NIR to MIR emission. This irradiation heating of the disk dominates the local viscous dissipation and so the total luminosity, star plus accretion shock, is the important parameter. Thus in principle I

could either make the star fainter and allow the accretion shock to emit essentially all the radiation; conversely, I could reduce the disk accretion rate by making the central star brighter, such that the total luminosity remains constant. Thus, the model results in an upper limit to the accretion luminosity and hence an approximate limit to the disk accretion rate of order  $5 \times 10^{-7} M_{\odot} \text{ yr}^{-1}$ . This disk accretion rate is fairly high compared to most Class II objects which accrete about  $10^{-8} M_{\odot} \text{ yr}^{-1}$ . However, stellar and accretion luminosity cannot be distinguished with the model. Though, significant accretion makes sense in the case of a young protostar.

With the limitations on the bolometric luminosity it was difficult to produce enough scattered light in the IRAC bands. Most of the radiation at these wavelengths comes from the inner disk “wall”, i.e. the inner edge of the disk where dust is evaporated (e.g. Dullemond et al., 2001; Tuthill et al., 2001; Muzerolle et al., 2003). In the model, this inner disk region emits at about 1400 K, the dust destruction temperature. The total luminosity thus depends upon the wall height, and, in this case, strongly upon the disk wall geometry. With the assumed stellar and accretion luminosity, the dust destruction radius is  $(14.25R_{*}, 0.139 \text{ AU})$ . The disk is modeled with a scale height  $h(100\text{AU}) = 10.52\text{AU}$  with a flaring power of  $\beta = 1.125$  and a radial density exponent  $\alpha = -2.125$ . The scale height is calculated using Equation 2.5. The total disk thickness at  $R_{dd}$  is about 0.12 AU.

Even with this bright inner disk wall, more NIR to MIR photons needed to be produced in the disk. In particular, the initial assumption that the disk wall is vertical meant that many wall photons were not emitted toward the poles, where needed. I have modified the inner disk wall to resemble the inner disk structure calculated by Tannirkulam et al. (2007), which creates a wedge-shaped wall resulting from dust settling (D’Alessio et al., 2006). The wedge-shaped inner disk wall will emit optically thick radiation with a temperature distribution as determined by the radiation transfer. This wedge structure will emit more NIR and MIR radiation toward the poles, into the outflow cavity, than the vertical wall. The central star plus disk spectrum as observed pole-on is shown in Figure 2.11 as the dotted line. The central star plus disk spectrum has a very strong NIR to MIR excess making the

spectrum very flat from visible to mid infrared wavelengths.

Despite the extraordinary lengths that I have taken to get more NIR to MIR light out of the model, it still falls short by about a factor of two at large spatial scales in IRAC channels 1 - 3. It may be that complex structure in the cavity walls, seen in the real object as bright spots, accounts for the difference. An alternate way to increase the scattered light flux is to include dust in the outflow cavity. This would scatter some of the light from the central protostar and disk that would otherwise escape. However, it is not clear whether dust grains would condense in the evacuated outflow cavity. I experimented with including dust in the outflow cavity and found that the shadow cast by the inner cavity is washed out if there is dust in the cavity near the central object, where dust grains would be expected to possibly condense.

Even with the difficulties in constructing a model of L1527, the end result well approximates the observed morphology in the infrared images (Figure 2.13a,b), IRS spectrum, and SED (Figure 2.11). Though I did not directly fit the submillimeter observations of L1527, the model image at  $850\mu\text{m}$  does approximate the observed morphology (Figure 2.5). Fitting the observed details in the image are as important as fitting the spectrum itself.

Figure 2.12 shows how the L1527 model looks using only a single cavity. Comparison to Figure 2.13a,b illustrates the benefits of the dual-cavity model in the case of L1527. The single-cavity images in Figure 2.12 fail to produce the thick dark lane and central source between the outflow cavities with the same parameters as the dual-cavity model. Thus I have concluded that L1527 is probably not represented by simple bipolar cavities carved from a TSC envelope.

## 2.6 Discussion

### 2.6.1 Comparison to Previous Models

The first attempt at modeling L1527 was done by KCH93. That study used simple TSC envelopes without cavities to model the spectrum of many Class 0 and Class I sources in Taurus. KCH93 modeled fixed outer radii of 3000 AU while varying

luminosity, envelope density, centrifugal radius, and inclination. For L1527, KCH93 modeled greatly larger values of envelope density  $\rho_1 = 3.16 \times 10^{-13} \text{ g cm}^{-3}$  compared to my of  $\rho_1 = 3.75 \times 10^{-14} \text{ g cm}^{-3}$  and  $R_c = 300 \text{ AU}$  versus my value of  $R_c = 75 \text{ AU}$ . The high envelope density modeled by KCH93 is partially explained by the larger  $R_c$ ; a large  $R_c$  decreases the optical depth to the envelope center. The luminosity of  $1.3 L_\odot$  modeled by KCH93 is somewhat lower than my value of  $2.6 L_\odot$ . The differences are likely due to the different modeling techniques and less long wavelength photometry in KCH93. Also, my modeled inclination of  $\sim 85^\circ$  is within their estimated range of  $60\text{-}90^\circ$ ; see Table 2.2 for a comparison between KCH93 and the modeled parameters. The differences in my modeled envelope parameters and those of KCH93 may be due to the absence of outflow cavities in the KCH93 models as well as differences in abundances assumed for the dust models. The large  $R_c$  modeled by KCH93 is necessary to fit the NIR photometry without including cavities.

F07 also modeled L1527 by SED fitting of multi-wavelength photometry and the IRS spectrum. This study uses a recent revision of the model used in KCH93, with outflow cavities. Many of the physical parameters modeled are similar to my results, while some differ. The envelope density,  $\rho_1 = 1.00 \times 10^{-14} \text{ g cm}^{-3}$  differs from my value of  $\rho_1 = 3.75 \times 10^{-14} \text{ g cm}^{-3}$ . Also, the modeled envelope radius is similar, 10000 AU compared to my value of 15000 AU. Additionally, the luminosity modeled by F07 was  $1.8 L_\odot$ , slightly less than my value of  $2.6 L_\odot$ . A limitation of the F07 model is that there is no way to define an aperture to compare the small and large scale emission. The model works fine for the  $10\text{-}50 \mu\text{m}$  range in wavelength if all the flux comes from small scales, see Figure 2.11. However, for  $\lambda < 10 \mu\text{m}$  and  $\lambda > 100 \mu\text{m}$  the amount of flux measured can vary greatly depending on the aperture. Despite the aperture limitations, the model results are meaningful as the wavelength range of the IRS spectrum is not sensitive to aperture and the spectrum is fit quite well. See Table 2.2 for a comparison of all modeled parameters.

In a recent study employing the Whitney et al. (2003b) model, R07 fit L1527 photometry from IRAC, MIPS, and IRAS against a grid of 200,000 model SEDs. These envelope models are based on the standard bipolar cavity structure of the Whitney

et al. (2003b) model as described in Section 2.4. The fits of this model grid seem to vary depending on the method of fitting. The models which fit SEDs using the total integrated flux an entire object are consistent with my results. However, the parameters derived from their resolved source analysis of L1527 are mostly inconsistent with my results. This analysis used multiple apertures to examine the integrated flux on small to large scales. I can account for this inconsistency by observing that their best fitting models greatly overestimate the long wavelength SED. This is because the luminosities modeled by R07 are 155 and 20  $L_{\odot}$ , much larger than my modeled luminosity of 2.6  $L_{\odot}$  and the measured  $L_{bol}$  of  $\sim 2 L_{\odot}$ . The very high luminosities modeled probably result from the lack of a strong NIR to MIR excess from the disk and improper weighting of the far-infrared photometry. The central protostar is modeled to be the primary source of scattered light photons. In my models, the NIR to MIR scattered light comes from a combination of accretion and the inner disk wall. Also, the R07 analysis did not apply aperture corrections to IRAC channels 3 and 4. Those channels have correction factors less than 1 for apertures larger than  $10''$ . In addition to high luminosities, R07 modeled high envelope densities,  $\rho_1 = 2.81 \times 10^{-12}$  and  $8.77 \times 10^{-13} \text{ g cm}^{-3}$  compared to my density of  $\rho_1 = 3.75 \times 10^{-14} \text{ g cm}^{-3}$ . The high envelope densities are necessary to extinct the high stellar luminosity. Also, the lack of an envelope structure to create the central object in the R07 models makes it difficult to fit the small and large scale IRAC fluxes simultaneously with reasonable parameters.

### 2.6.2 Envelope Neck

To fit the SED and image of L1527 in multiple apertures at all wavelengths, I found it necessary to introduce a new type of outflow cavity structure. I am limited by axisymmetry in the Whitney et al. (2003b) model in ways to create the observed central object and separated cavities. The model may be an axisymmetric approximation to a more complex structure. Having discussed the morphological reasons for adopting the ‘dual-cavity’ structure in Section 2.5, I now review the physical motivations for such a structure.

Delamarter et al. (2000) created MHD simulations of protostellar outflows originating from a spherical wind driven by the central protostar. The density structure assumed for the envelope was the parametrization of the TSC model for the collapse of a flattened sheet (Hartmann et al., 1996) interacting with a spherically-symmetric outflow. The enhanced density at the equator of the infalling material resulted in higher ram pressure working against the ram pressure of the wind, creating a kind of ‘neck’ structure. The TSC model does not have an enhanced equatorial density as in the Delamarter et al. (2000) model. However, Ohashi et al. (1997) observed a dense, possibly rotating, inner envelope toroid in L1527 with interferometric C<sup>18</sup>O observations. Alternatively, one might suppose that the ram pressure of the wind varies from the axis in such a way to produce a ‘neck’, with weaker flow near the equator than the poles; the effect would be similar because the relevant quantity is the ratio of wind to inflow ram pressures, not the absolute values. As outflows are clearly collimated, with high-density jets along the axis, this supposition is physically plausible.

It is also worth noting that the ‘neck’ region of L1527 is not axisymmetric. A precessing jet (Gueth et al., 1996; Ybarra et al., 2006) could partially evacuate the polar regions allowing the spherical outflow to expand, creating a wider outflow cavity with a standard TSC envelope.

Another possibility is that binary accretion patterns are responsible for the observed morphology. Figures 2.1 and 2.2 of Bate & Bonnell (1997) show that protobinary stars create an evacuated inner region of the protostellar envelope, with streams of material falling in at particular longitudes. Thus, the ‘neck’ might be related to these streams and evacuated region, while the outer cavity is dominated by the outflow interacting with a more axisymmetric envelope. It is worth considering this further as L1527 appears to be a binary system (Loinard et al., 2002).

### **2.6.3 Variability and Asymmetry**

In addition to possibly causing asymmetry in the overall structure, binary interactions could contribute to the variability observed in L1527. As described in Section 2.3

the variability seems to affect each cavity lobe independently. Both cavities vary in brightness but one becomes fainter as the other becomes brighter. The variability is consistent with the scattered light from a central source; the light travel time out to the edges of the observed scattered light image is  $\sim 0.25$  years and observations were almost a year apart.

Resolved observations of the HH30 disk have shown substantial variability over the past 15 years (Watson & Stapelfeldt, 2007). The mechanism behind these variations is uncertain but it is conjectured that inner disk warps caused by a companion, accretion shocks unevenly heating the disk, and/or binary interactions could be causing uneven patterns of illumination. These proposed mechanisms may cause selective illumination of different parts of the cavity from the disk since most NIR to MIR photons come from the disk. A process similar to the variability in the disk of HH30 may be being observed in the envelope of L1527.

Variability of the scattered light intensity is not unexpected since Class 0 objects are known to still be accreting material and the models require high accretion and infall rates. The variability is easier to understand if the disk accretion luminosity is large, as I have modeled it to be. T Tauri stars which show the most variation are most commonly accreting systems.

In Section 2.3 I described the azimuthal asymmetry of L1527; the brightness difference of the north and south sides of the cavities. The radiative transfer study by Wood et al. (2001) showed that misaligned circumstellar disks could cause asymmetric illumination of the outflow cavities in the radial and azimuthal directions. In the case of T Tau, Figure 2.2 of Wood et al. (2001) shows that one side of the cavity could be significantly more illuminated than the other, similar to what I observe in L1527. The contoured IRAC and Ks-band images of L1527 in Figure 2.13a clearly show the azimuthal asymmetry of L1527. Individual circumstellar disks around the central binary (Loinard et al., 2002) could be producing the observed brightness asymmetries.

I noted in Section 2.3 that even the submillimeter image shows asymmetry, see Figure 2.5. The boxy contours are extended along the outflow axis, probably due to the heating along the outflow cavity walls and possibly dust in the cavity; the

contours should be round without a cavity present. The contours are more extended in the southeast and northwest, indicating asymmetric heating in the same locations as asymmetric scattered light suggesting that they are related.

#### 2.6.4 Interpretation of Physical Parameters

In Section 2.5 I described the physical parameters of the model I have constructed. Two of the most important parameters derived in the modeling are the mass infall rate  $\dot{M}_{env}$  and the mass accretion rate  $\dot{M}_{acc}$ . Assuming a central stellar mass of  $0.5 M_{\odot}$ , I model a  $\dot{M}_{acc}$  of  $3 \times 10^{-7} M_{\odot} \text{ yr}^{-1}$ , an order of magnitude larger than a typical T Tauri star for which  $\dot{M}_{acc} \sim 10^{-8} M_{\odot} \text{ yr}^{-1}$ . My high  $\dot{M}_{acc}$  modeled is further supported by the strong forbidden optical emission lines (i.e. [OI], [NII], [SII]) and Hydrogen alpha observed by Eiroa et al. (1994) and Kenyon et al. (1998); these observations infer high disk accretion rates as well as jet emission.

In the model,  $\dot{M}_{env}$  is about two orders of magnitude larger than  $\dot{M}_{acc}$ , which means that the disk is rapidly building up mass since it cannot pump material onto the star quickly enough. Thus the disk will either get very massive in a short period of time or the excess mass is expelled by the outflow. Also, the widening of the outflow cavities may be working to quench the mass infall, not enabling the disk to gain a very large final mass (Arce & Sargent, 2006).

With the best fitting  $\dot{M}_{env}$ , similarly  $\rho_1$  which I get from the assumed stellar mass, I get an envelope with a density similar to that of many Class I objects as modeled by F07. While the envelope of L1527 is not substantially more dense than a typical Class I protostar, the envelope is substantially larger in spatial extent. I observe the very extended scattered light with IRAC, but no other Class I object in Taurus has such extended scattered light except for L1551 IRS 5 (e.g. Osorio et al., 2003) and L1551NE (Swift & Welch, 2008). However, SED models by F07 fit large envelopes for most Class I sources for which extended scattered light is not observed. This contradiction suggests that the size of the envelope may not be well constrained by SED modeling and spatially resolved observations are required to constrain this parameter.

Related to  $\dot{M}_{env}$  is the overall mass in the envelope. The mass of the best fitting model was  $1.72 M_{\odot}$ . This mass is comparable to the  $2.4 M_{\odot}$  measured by Benson & Myers (1989) from ammonia observations. Observations of dust emission yield masses of  $0.8 M_{\odot}$  from Shirley et al. (2000), and  $0.9 M_{\odot}$  from Motte & André (2001). While these measurements are low, the dust emissivity may be uncertain by a factor of 3 (Shirley et al., 2000) which could account for the difference.

My best fitting model was not strongly dependent on the value of  $R_c$ , but it had to be less than the outer cavity offset to create the shadow effect. The disk radius was chosen to match  $R_c$  at 75 AU, given the upper limit on  $R_c$  by the cavity offset, my disk will be small compared to the typical 200 AU size of disks as observed by Andrews & Williams (2007). This implies that disk of L1527 is still being built up and there are likely complex dynamical interactions on small scales in the inner envelope as hinted to previously.

### 2.6.5 Class 0 versus I

The Class 0 definition from Andre et al. (1993) requires that the ratio of submillimeter luminosity to the bolometric luminosity is  $5 \times 10^{-3}$ . This definition is not exclusive of the I through III classification of Lada (1987). A Class 0 object can also be a Class I object if there is detected emission in the NIR to MIR. *Spitzer* has revealed previously undetected MIR scattered light emission from many Class 0 protostars (Tobin et al., 2007; Seale & Looney, 2008).

With the inclusion of outflow cavities in the standard envelope models, this Class 0 definition immediately becomes muddled. Using L1527 as an example, with the observed inclination, it is clearly a Class 0 object, all the power is in the long wavelength portion of the SED, see Figure 2.11. However, I can predict what my L1527 model would look like at different inclinations. As L1527 is tilted within the line of sight, one sees further down the cavity through increasingly less extinction. The peak of the long wavelength SED does not change, but more power goes into shorter wavelengths. There is a point when the object no longer meets the criterion for a Class 0 object and is a typical Class I, see Figure 2.14. For example, my model spectra at varying

inclinations are similar in shape to the spectra of Class I protostars in Taurus from F07. Specifically, at an inclination of  $63^\circ$ , my model is similar to DG Tau B, at  $49^\circ$  it is similar to IRAS 04239+2436, and the same applies for a few others.

From the SEDs shown at various inclinations in Figure 2.14, I show that L1527 may not necessarily be a Class 0 object and could be a Class I if it were oriented differently. Because Class definitions are dependent on the SED, spatially resolved observations are crucial to the understanding of protostellar structure and evolution. There are spatially resolved observations of several Class I protostars in Taurus from Padgett et al. (1999); these Class I objects are quite different from L1527. The scattered light morphologies observed by Padgett et al. (1999) are all very small in spatial extent ( $\sim 2000$  AU) compared to L1527, which is extended over nearly 30000 AU. Without resolved observations, one would be ignorant of their inherent differences.

### 2.6.6 General Applicability of the Model

An important question must be asked of my results; is L1527 a special case in requiring a modified cavity structure to fit its morphology or are my results more generally applicable? Some protostars associated with scattered light nebulae seem to show a similar morphology to L1527; a point source located between two outflow cavities. However, not all sources have cavity structures as bright as L1527 and not all objects appear to have a cavity separation like L1527, although this may be an issue of angular resolution and inclination.

The observations by Padgett et al. (1999) appear to be consistent with a single outflow cavity model; Stark et al. (2006) modeled these objects as such. However, in contrast to L1527, these objects seem to be more evolved, Class I objects. Protostars may evolve such that a more simplified model will suffice as the infall phase is ending. The dual-cavity model may only be applicable to the very young, high mass infall phase.

Seale & Looney (2008) cataloged many remarkably bright outflow cavity structures in archived observations from the *Spitzer Space Telescope*. Several objects

(IRAS 05491+0247, IRAS 18148-0440, L1251B, and others) show bright cavity structures with an apparent point source in the middle. From this catalog of scattered light nebulae observed with IRAC, it appears that the model I have developed for L1527 may be more than just a special case.

I stress that this morphology of an observed central object and separated outflow cavities for Class 0 sources is only observed between  $3\mu\text{m}$  and  $8\mu\text{m}$  thus far. Shorter wavelengths are too extinguished to detect the central object and longer wavelengths wash out the separation because the dust is less opaque to the incident radiation. Objects with a less dense circumstellar envelope may show a central object at K-band as seen in NICMOS observations by Meakin et al. (2003) and Hartmann et al. (1999). Also, an object must be viewed nearly edge-on for this morphology to be apparent. Sources inclined much less than  $80^\circ$  will blend the central object with the blue-shifted outflow cavity. Though, a gap caused by the inner envelope shadowing should still be visible between the red and blue-shifted cavities.

In addition to the necessity of edge-on observation, objects also must be nearby. The central object of L1527 is only separated from the bright outflow cavity by  $\sim 3''.6$ . If the distance to L1527 were twice what it is, the separation may be smeared out by the PSF. These criteria for observation of this morphology will create a selection effect; however, increased spatial resolution in the NIR to MIR is not far away and detailed modeling may be able to disentangle the inclination effects.

### 2.6.7 Dust Properties and Emission Processes

As discussed in Section 2.5, I was not able to completely model the SED with the assumed dust model. My dust model is not unique, there could be different dust grain size distributions in different parts of the envelope; large grains in the dense inner regions and small grains in the outer regions. *Spitzer* has provided a wealth of data with which more precise dust models may be developed; most importantly, the infrared extinction law in the IRAC wavelengths has been found to be flatter than expected (Indebetouw et al., 2005a; Flaherty et al., 2007; Román-Zúñiga et al., 2007). This flat extinction law implies that grain growth has occurred in dense regions

(Román-Zúñiga et al., 2007). Thus protostars start out with dust that is larger than general ISM dust. These extinction law measurements support the adoption of a larger dust grain model for the modeled envelope. The larger dust grains have significantly more albedo in the NIR to MIR.

Also, as shown in Figure 2.11, the model spectrum tends to fall below most of the submillimeter data points. This trend again indicates that there are details missing from the assumed dust model. Other, more complex organics may more accurately represent an envelope dust model (e.g. Pollack et al., 1994). Also, heating of the outer envelope from the interstellar radiation field could be responsible for the observed submillimeter fluxes slightly disagreeing with the model. The upcoming *Herschel Space Telescope* will give new insights into the submillimeter properties of dust.

In addition to the scattered light emission, there is a possibility of some shock-excited molecular line emission resulting from the jets and outflows in the cavities. The strong Herbig-Haro spectrum detected in the cavity of L1527 (Eiroa et al., 1994; Kenyon et al., 1998) suggests that the outflow cavities could have some NIR to MIR emission from H<sub>2</sub> ro-vibrational lines. Many H<sub>2</sub> lines are present throughout all the IRAC bands. However, IRS observations of protostars in F07 showed no evidence for strong emission lines at IRAC wavelengths. My narrowband H<sub>2</sub> (2.12 $\mu$ m) observations of L1527 did detect some weak emission in excess of observations with the H<sub>2</sub> (2.09 $\mu$ m) continuum filter. However, the H<sub>2</sub> emission is at most 8% of the total Ks-band flux which is within the errors for the flux at Ks-band and would not greatly affect modeling.

In studies of other protostars, Fuller et al. (1995) detected H<sub>2</sub> emission in the cavity of L483. However, the emission was localized to a small section of the cavity, appearing to be an outflow knot within the cavity. Also, Hartmann et al. (1999) did not detect any excess H<sub>2</sub> emission from the IRAS 04325+2402 scattered light nebula. Therefore, the dominant emission mechanism in the NIR to MIR for protostars is scattered continuum emission from the central star and disk and line emission should not significantly contribute to the total flux.

### 2.6.8 Predictions

The dual-cavity model can probably be tested easily by high resolution imaging of the L1527 central object in the MIR. A model image with  $0''.11$  pixels convolved with  $0''.5$  seeing is shown in Figure 2.15. These model images simulate what could be observed from a ground-based MIR telescope at L', M, or even  $7.7\mu\text{m}$ . Imaging of this structure is within the capabilities of even modest aperture, infrared optimized telescopes, so long as the PSF is well sampled. As discussed in Section 2.3, the central object appears marginally resolved in the IRAC data, but the resolution is too low to observe the small scale structures being modeled. I would probably see some of the inner envelope structure in the IRAC images if the PSF was more finely sampled at  $3.6\mu\text{m}$ .

Excellent seeing or adaptive optics (AO) are required to observe the inner envelope structure. But AO observations are difficult for protostars due to the high extinctions obscuring guide stars near the central object. However, at  $7.7\mu\text{m}$  the seeing typically can be better than  $0''.5$  naturally, thus imaging farther into the MIR may be ideal for observing the inner envelope.

The model may be an axisymmetric approximation to some complicated feature, thus high resolution observations may not completely reflect the image shown in Figure 2.15. I expect high resolution imaging to show some resolved structure that is probably responsible for the complicated morphology observed.

## 2.7 Conclusions

I have presented a detailed analysis of infrared scattered light observations of the Class 0 object L1527 (IRAS 04368+2557). L1527 presents itself as a very intriguing object, having bright scattered light emission at NIR to MIR wavelengths, and outflow cavities which are asymmetric in brightness and shape. The extended emission of L1527 is also variable; observations taken a year apart show significant variability. This variability is not constant for the entire object, the two cavities seem to brighten and fade independently.

I have constructed a model of L1527 which approximates the observed morphology of L1527 in the IRAC and Ks-band images as well as the overall SED. The model uses a modified cavity structure with a narrow cavity near the central protostar and a wider cavity offset from the central protostar. This modified cavity structure creates an apparent central point source in the IRAC images from light scattering on the inner cavity. The inner cavity also casts a shadow on the outer cavity creating the observed separation and dark lane between the outflow cavities. While modeling is inherently not unique at defining the structure of objects, modeling can tell what the structure is not. This chapter shows that L1527 is probably not represented by simple bipolar cavities carved from a TSC envelope, but possibly represented by the structure I have created.

I have demonstrated the importance of simultaneously fitting the morphology of the spatially resolved images as well as the SED. Only fitting the SED could lead to modeling unphysical parameters if the parameter space is not adequately restricted. It can be argued that I also have essentially turned knobs until the imaged looked right. Though, there are clearly asymmetries that are not reflected in the model which impact the SED and image fit. Within the limits of axisymmetry, my model fits the observed images and SED quite well. Also, the robustness of the SED fit is probably limited by the uncertain envelope dust model. My modeled cavity structure may be an axisymmetric approximation of a complex structure resulting from outflow-envelope interactions or binary accretion effects.

The dual-cavity model I have developed is specifically for L1527, however, the model may be more generally applicable. Archived observations from the *Spitzer Space Telescope* of other Class 0 protostars show similar features to L1527; a central object observed between the outflow cavities (Seale & Looney, 2008). This central object can probably be resolved using current ground-based MIR instrumentation. This chapter demonstrates that observations of the circumstellar envelope by scattered light in conjunction with radiative transfer modeling provide new insights into envelope structure which were previously beyond reach.

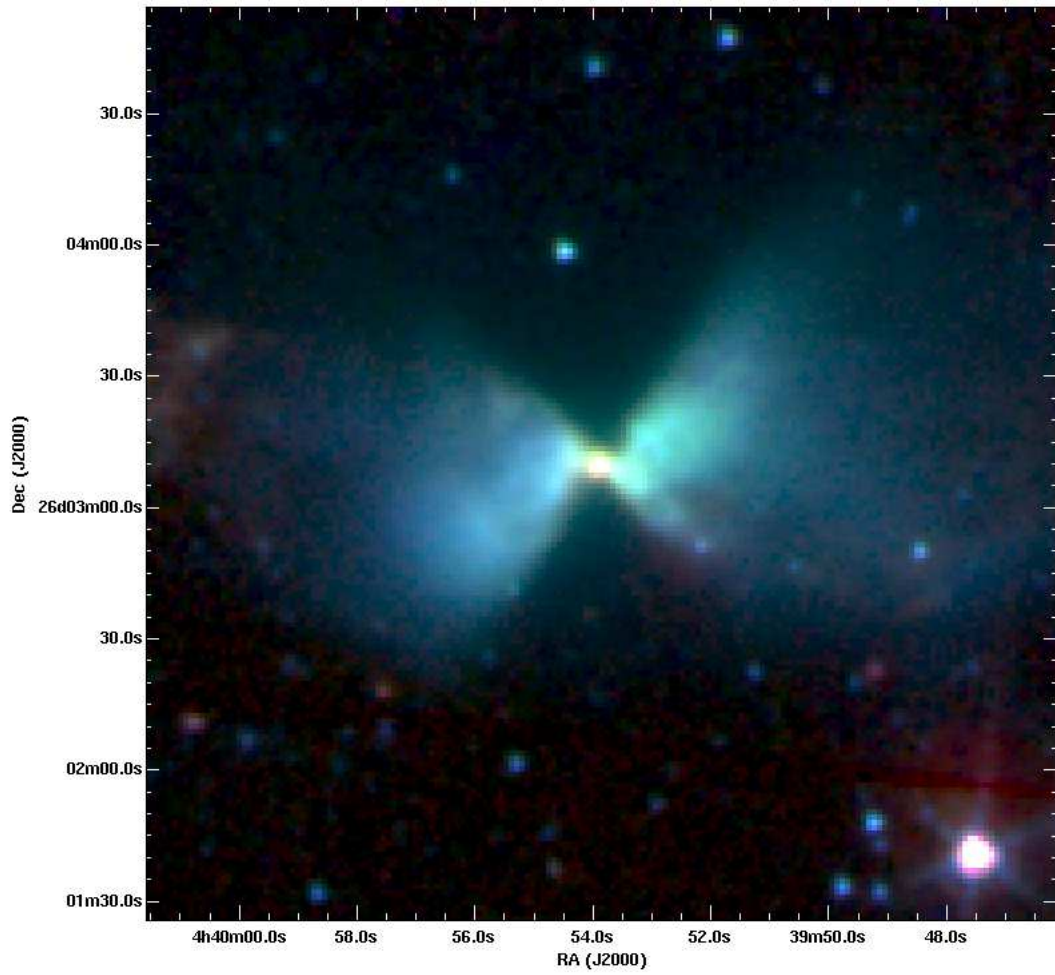


Figure 2.1 False-color IRAC image of L1527 IRS (IRAS 04368+2557), Blue:  $3.6\mu\text{m}$ , Green:  $4.5\mu\text{m}$ , and Red:  $8.0\mu\text{m}$ . Image box is  $200''$  on a side, corresponding to  $\sim 28000$  AU at a distance of 140pc.

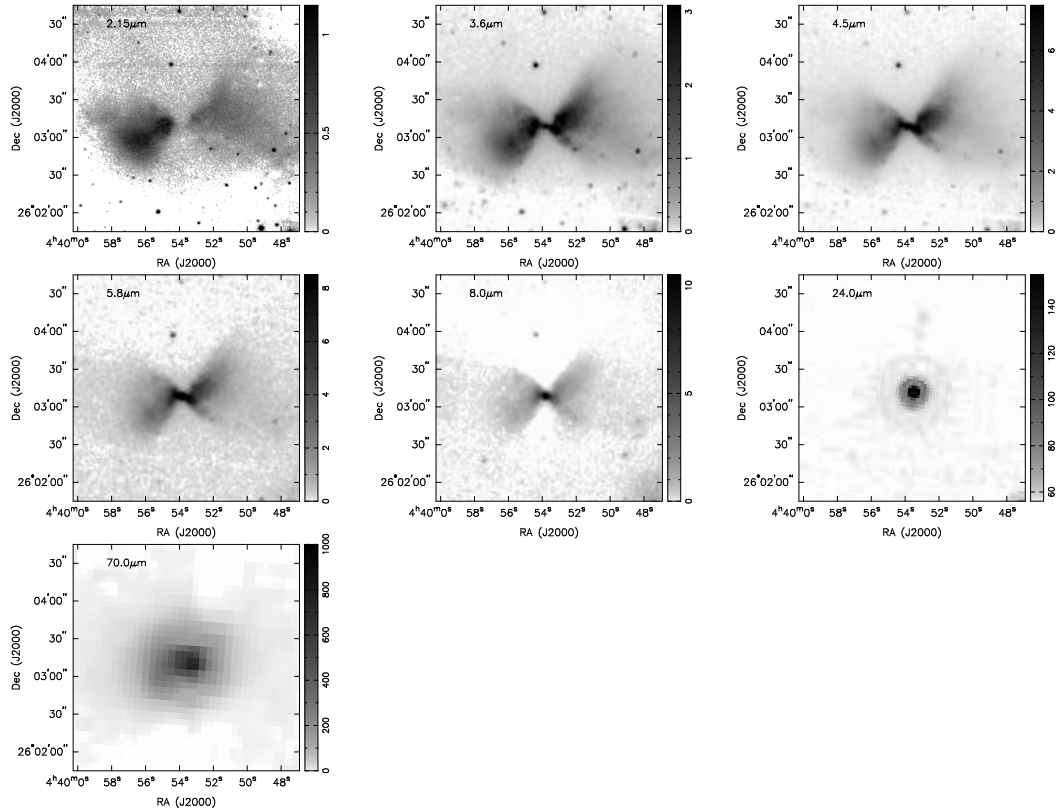


Figure 2.2 Near-infrared and *Spitzer* images of L1527 as observed by TIFKAM, IRAC, and MIPS. Images are  $180''$  on a side, corresponding to  $\sim 25000$  AU at a distance of 140pc. Units of intensity are MJy/sr.

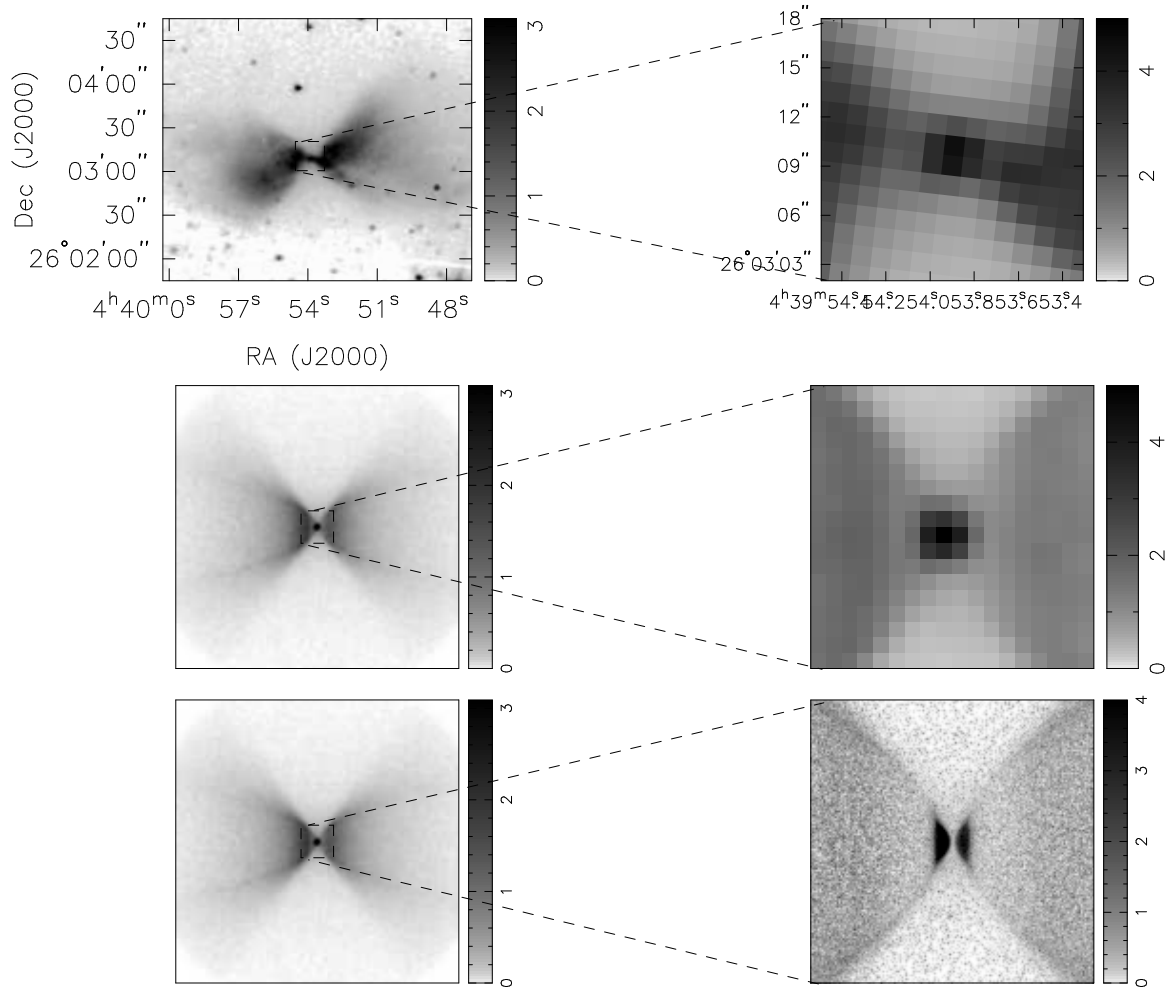


Figure 2.3 Top: IRAC 3.6 $\mu$ m image of L1527 zooming on on the ‘neck’ as described in Section 2.3. Middle: Best fitting model image zooming in on inner envelope structure. Bottom: Best fitting model image with unconvolved view of of the inner envelope. Units are MJy/sr.

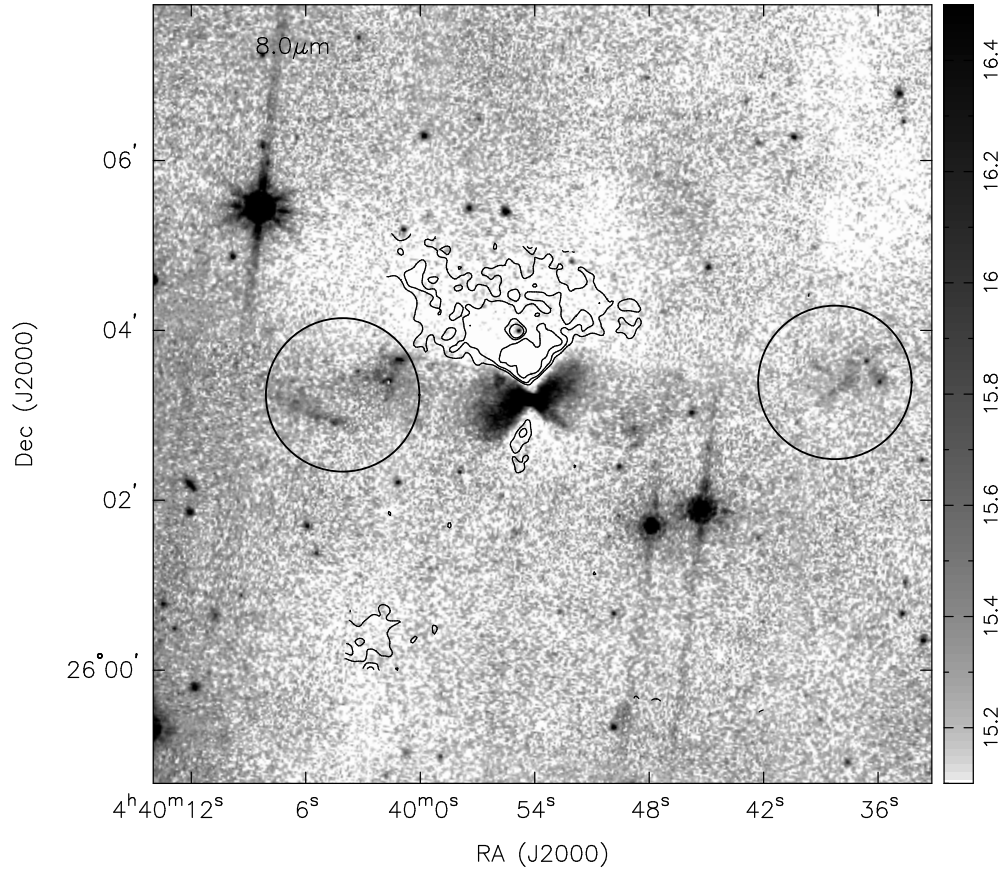


Figure 2.4 Wide-field view of L1527 region at  $8.0\mu\text{m}$ . Herbig-Haro objects in apparent association with L1527 are circled. These objects infer an outflow PA  $\sim 90^\circ$ . Assuming an outflow velocity of  $100\text{km/s}$ , these outflow knots have a dynamical age of only 1100 - 1600 yrs. Contours are  $8.0\mu\text{m}$  optical depth contours corresponding to  $\tau = 0.08, 0.10, 0.126$  and  $0.16$ . The contours match up with the regions where there is a lack of background emission. Units are  $\text{MJy/sr}$ .

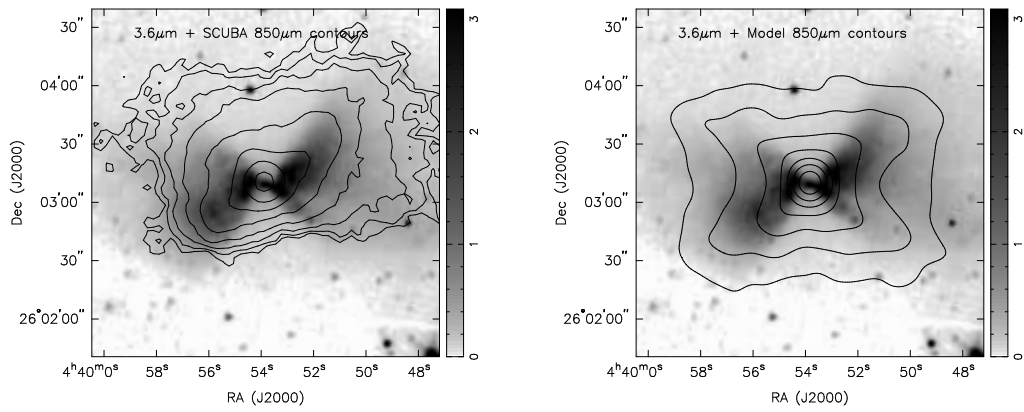


Figure 2.5 Left: IRAC  $3.6\mu\text{m}$  image with  $850\mu\text{m}$  SCUBA contours from Chandler & Richer (2000). Right: IRAC  $3.6\mu\text{m}$  image with model  $850\mu\text{m}$  contours. Notice the boxiness of the contours and how the south side flux falls off rapidly as compared to the north side flux in the SCUBA image. The model image is able to duplicate the boxy features of the SCUBA data on the inner contours. The SCUBA contours clearly show an asymmetry corresponding to the bright patches as observed in the IRAC images. The contours are 2.07, 3.49, 5.58, 9.91, 16.71, 28.16, 47.46, and 80.0 MJy/sr.

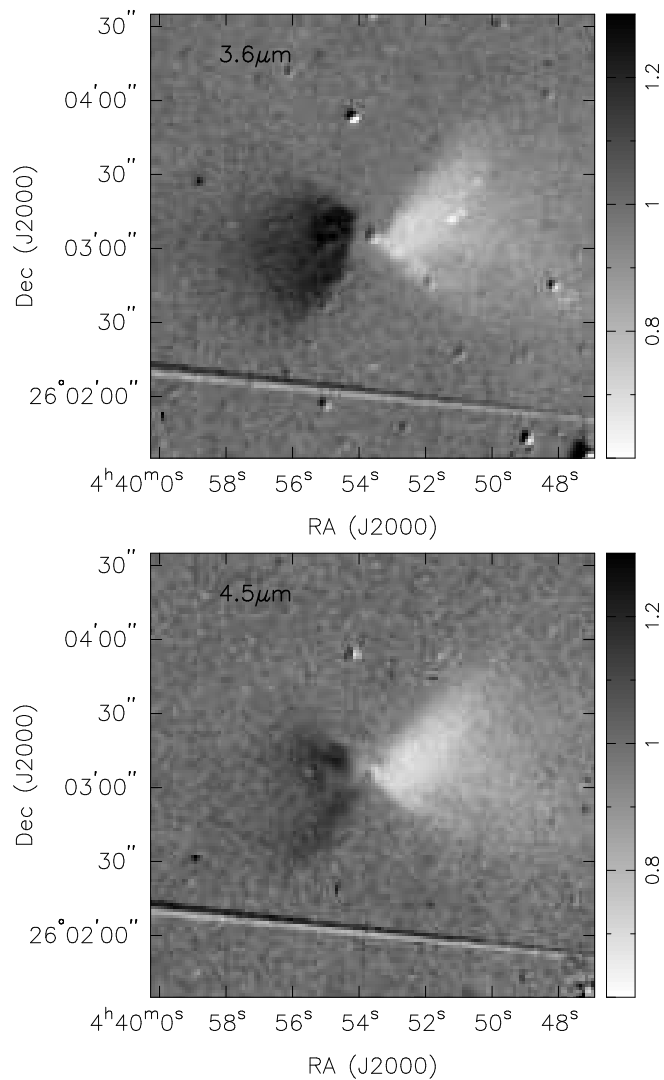


Figure 2.6 IRAC images of L1527 with the 2004 epoch divided by the 2005 epoch. The lighter gray to white signifies less flux in the 2004 epoch, while darker gray means more flux. The variability is present in IRAC Channels 3 and 4, but the noise is much higher.

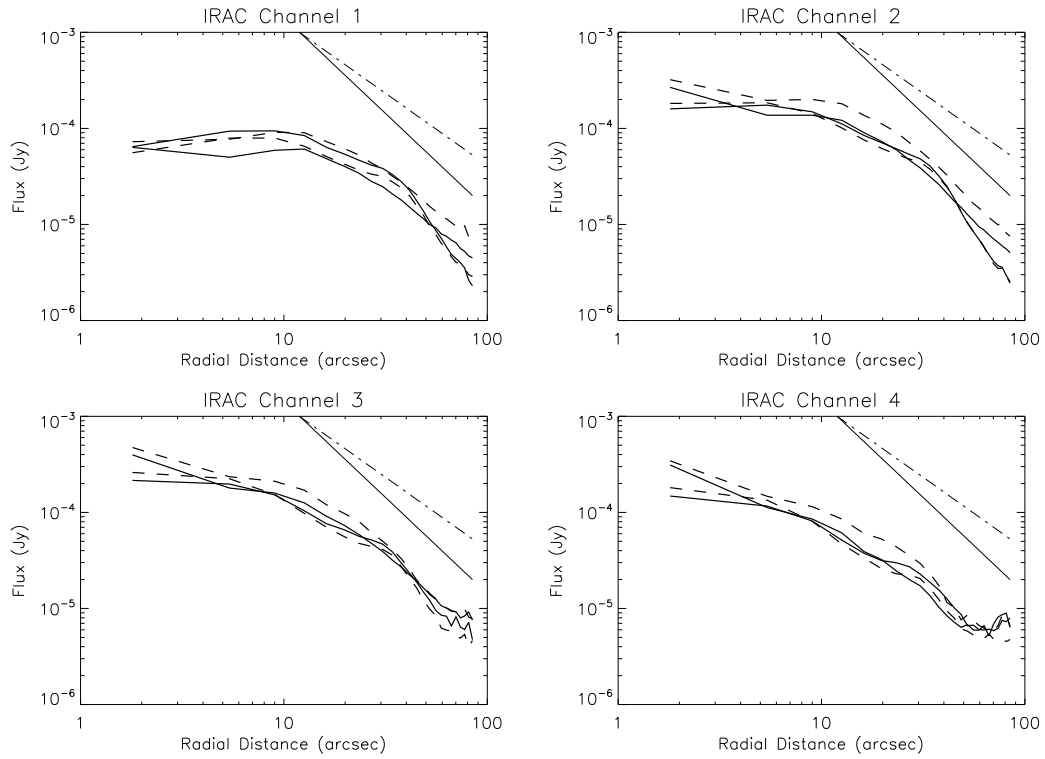


Figure 2.7 Average flux in a  $3''.6$  width annulus measured radially from the center. The 2004 (solid lines) and 2005 (dashed lines) epochs are plotted, there are two lines per epoch corresponding to the east and west cavities. The straight lines drawn in the upper right correspond to power-laws of -2 (solid line) and -1.5 (dot-dashed line).

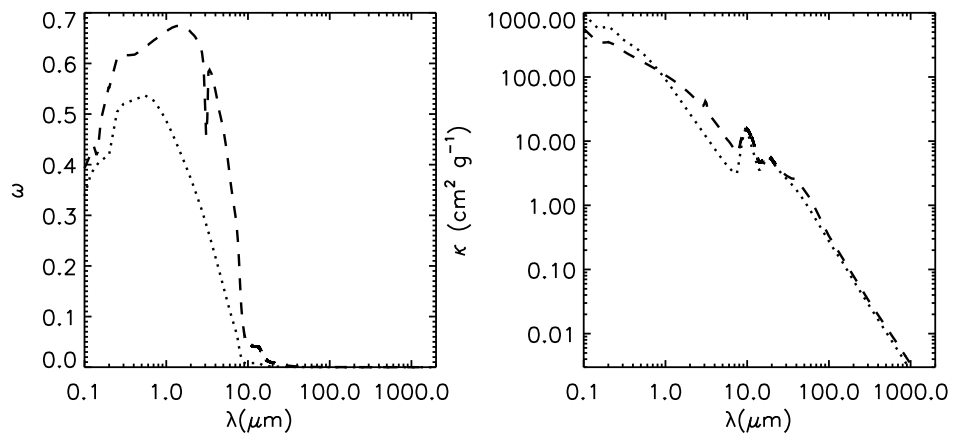


Figure 2.8 Albedo (left) and opacity (right) curves of dust models. The dashed line is the larger grain dust model I used, and the dotted line is an ISM dust model (Kim et al., 1994).

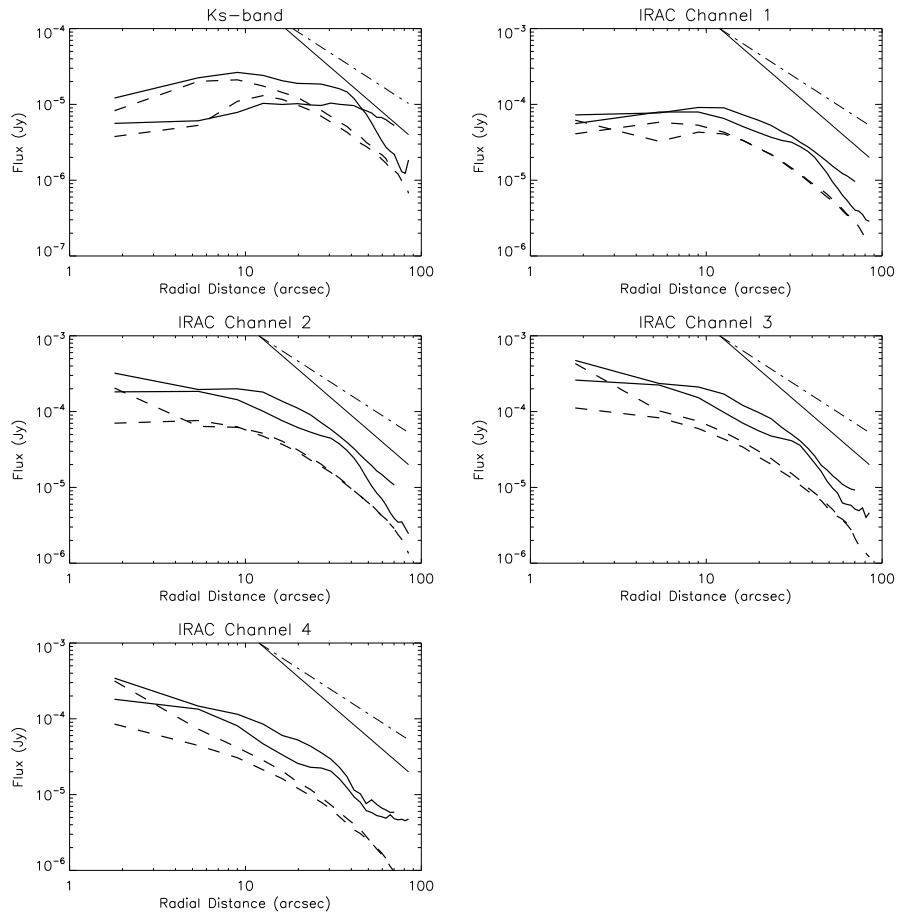


Figure 2.9 Same as Figure 2.7 except the data (solid lines) and model (dashed lines) are plotted. The data the average of the two epochs, except Ks-band.

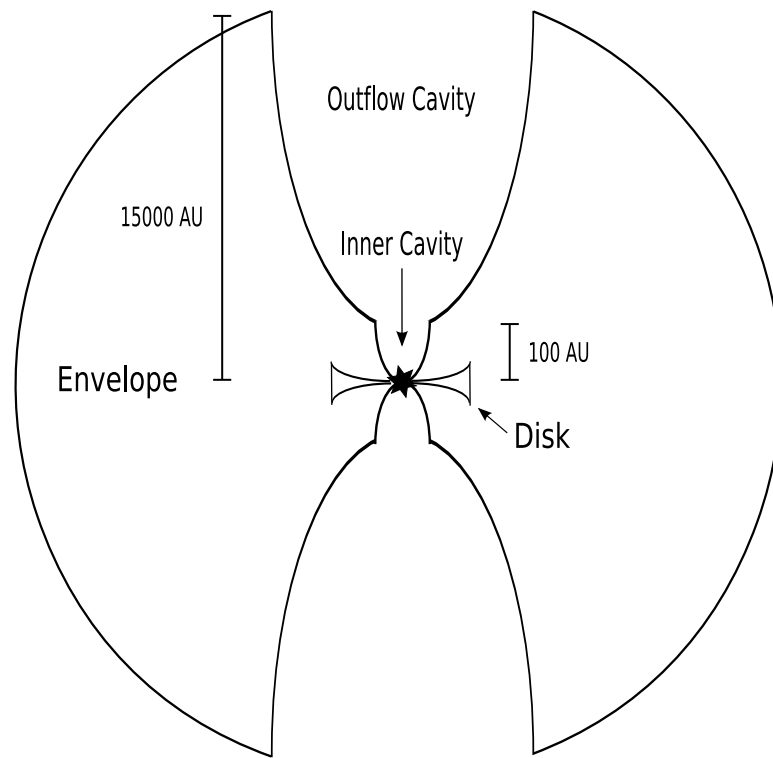


Figure 2.10 Schematic representation of modeled cavity and envelope structure. Inner envelope regions are not drawn to scale.

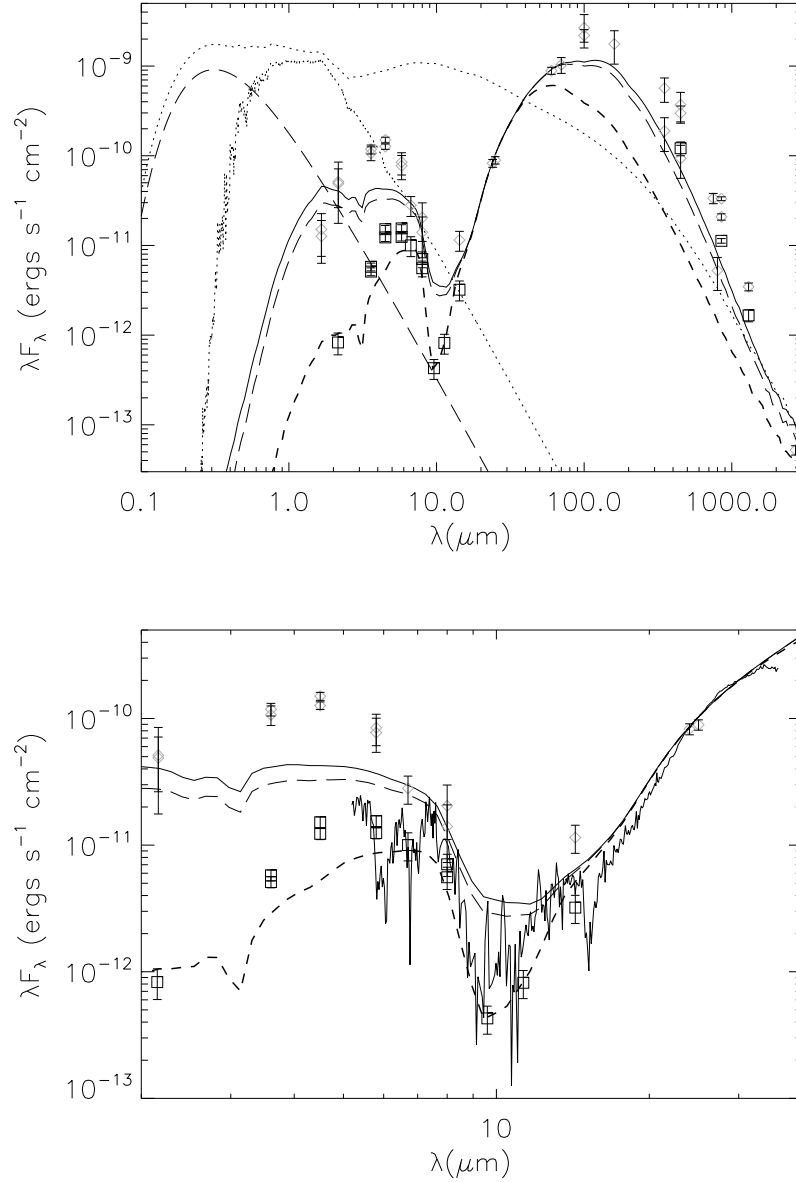


Figure 2.11 The full SED of L1527 (Top) with the model, excluding the IRS spectrum. A zoomed in portion of the SED (Bottom) is plotted with IRS spectrum from 2 - 40 $\mu$ m. The model SED is plotted for apertures of 10000 AU (solid line), 6000 AU (long-dashed line), and 1000 AU (short-dashed line). Photometry taken with apertures of 71''4 (diamonds) and 7''14 (boxes) corresponding to 10000 AU and 1000 AU apertures are plotted. The long wavelength data have varying apertures which are comparable to the 6000 and 10000 AU apertures. I also plot the spectrum of the central protostar and disk (coarse dotted line) illuminating the envelope viewed face-on; the 4000K stellar atmosphere (fine dotted line) and the accretion shock (long dashed line at short  $\lambda$ ) of the infalling material onto the star.

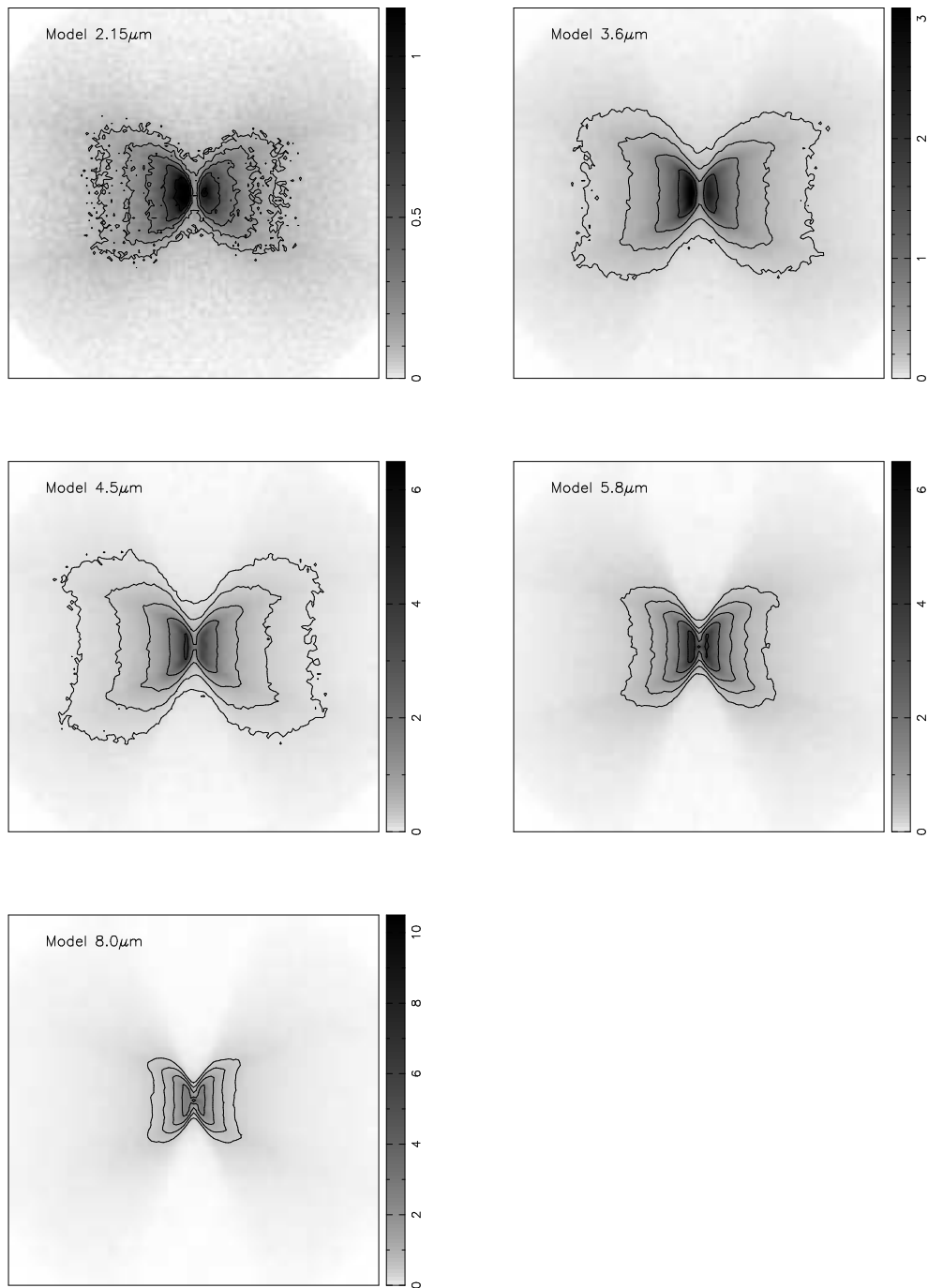


Figure 2.12 Model images generated using a single cavity; all other parameters are identical to the dual-cavity model. In comparison to the observations, these images clearly do a much worse job reproducing the data than the dual-cavity images. Notice the lack of a central source and thick dark lane in contrast to the dual-cavity model. Images are  $180''$  on a side, corresponding to  $\sim 25000$  AU at a distance of 140pc, units are MJy/sr.

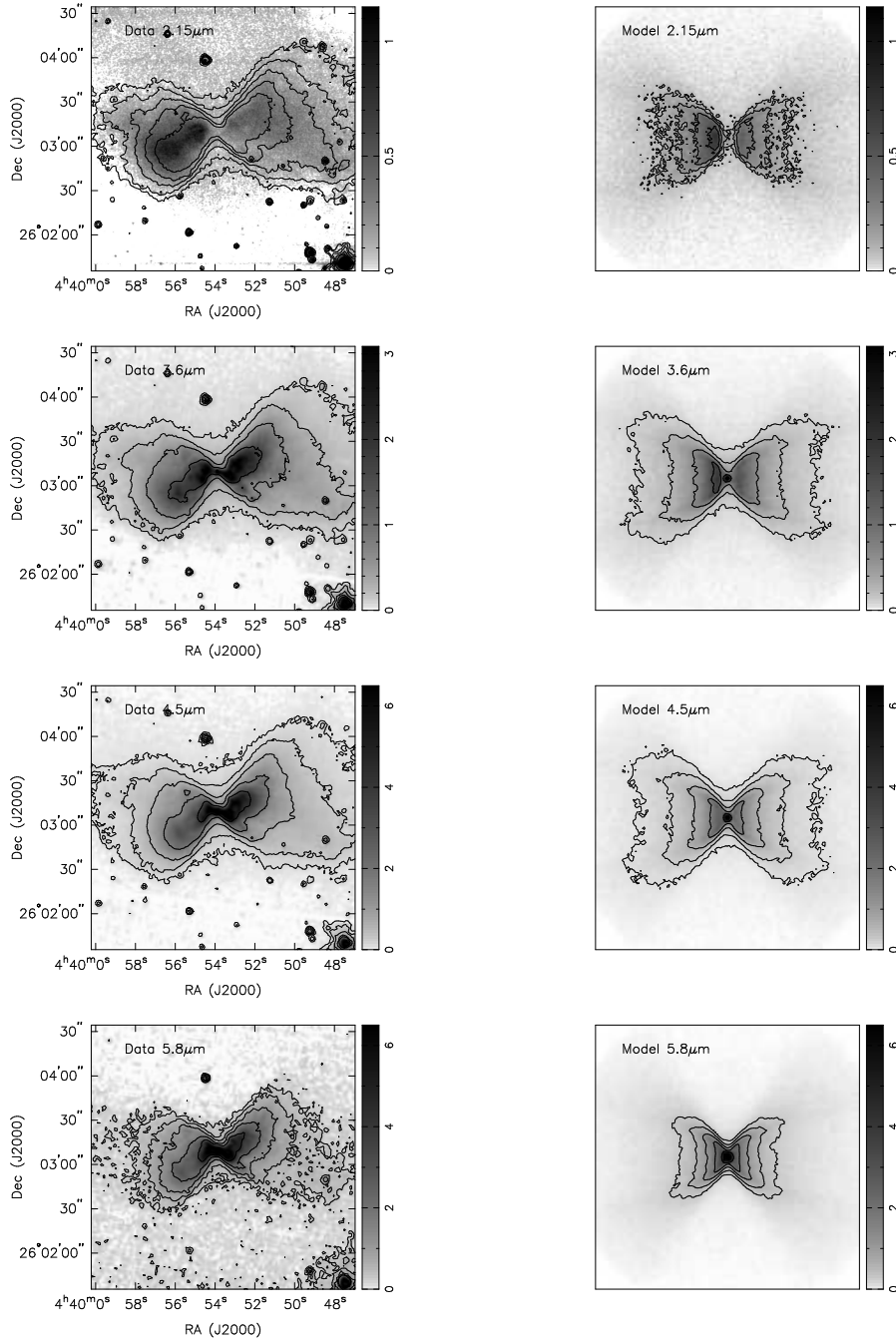


Figure 2.13a Left: L1527 images as in Figure 2, Right: Best fit model. (a) Images for 2.15, 3.6, 4.5, and  $5.8\mu\text{m}$ , (b) Images for 8.0, 24, and  $70\mu\text{m}$ . The contours for the L1527 data on the left clearly show the azimuthal asymmetry. Images are  $180''$  on a side, corresponding to  $\sim 25000$  AU at a distance of 140pc, units are MJy/sr.

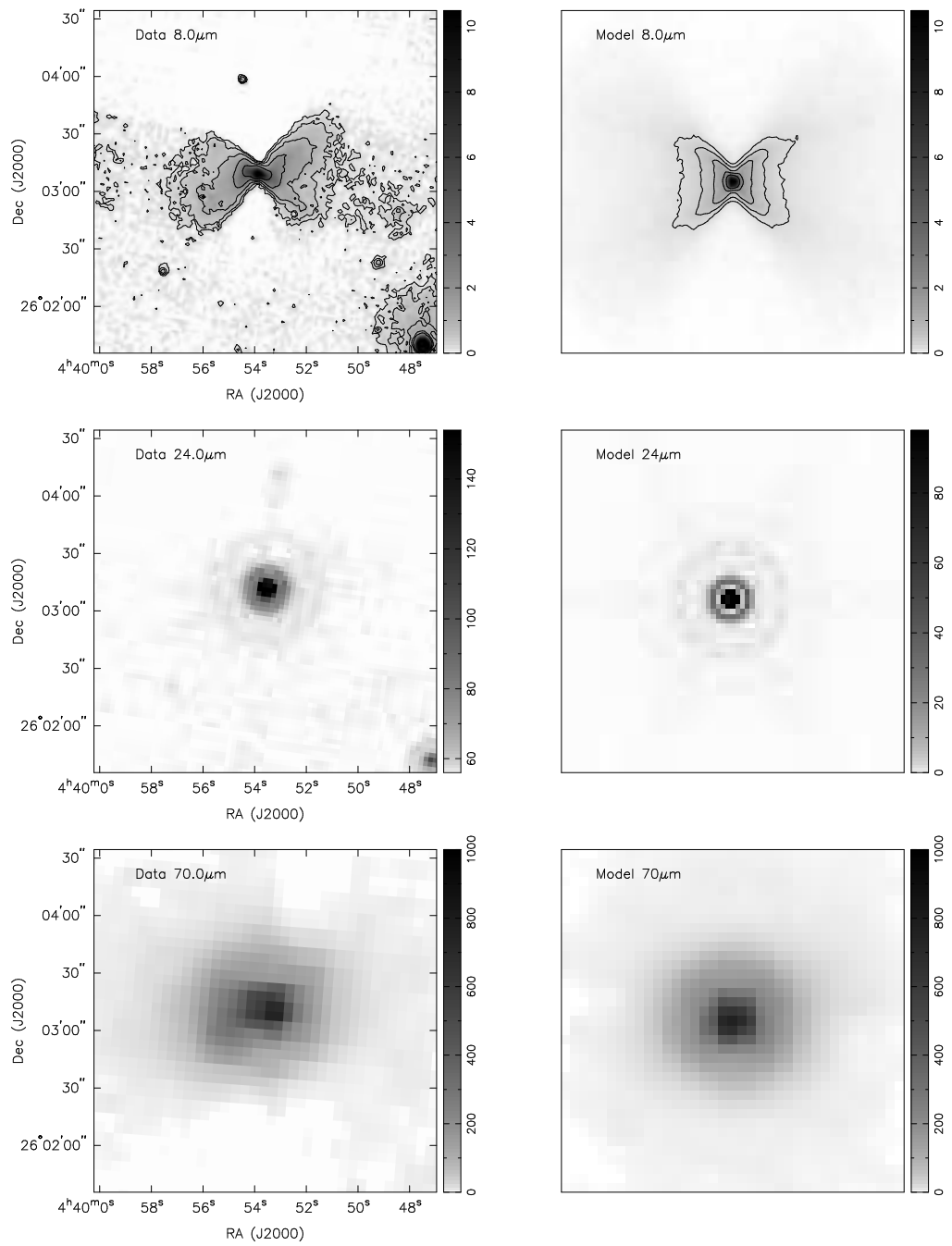


Figure 2.13b

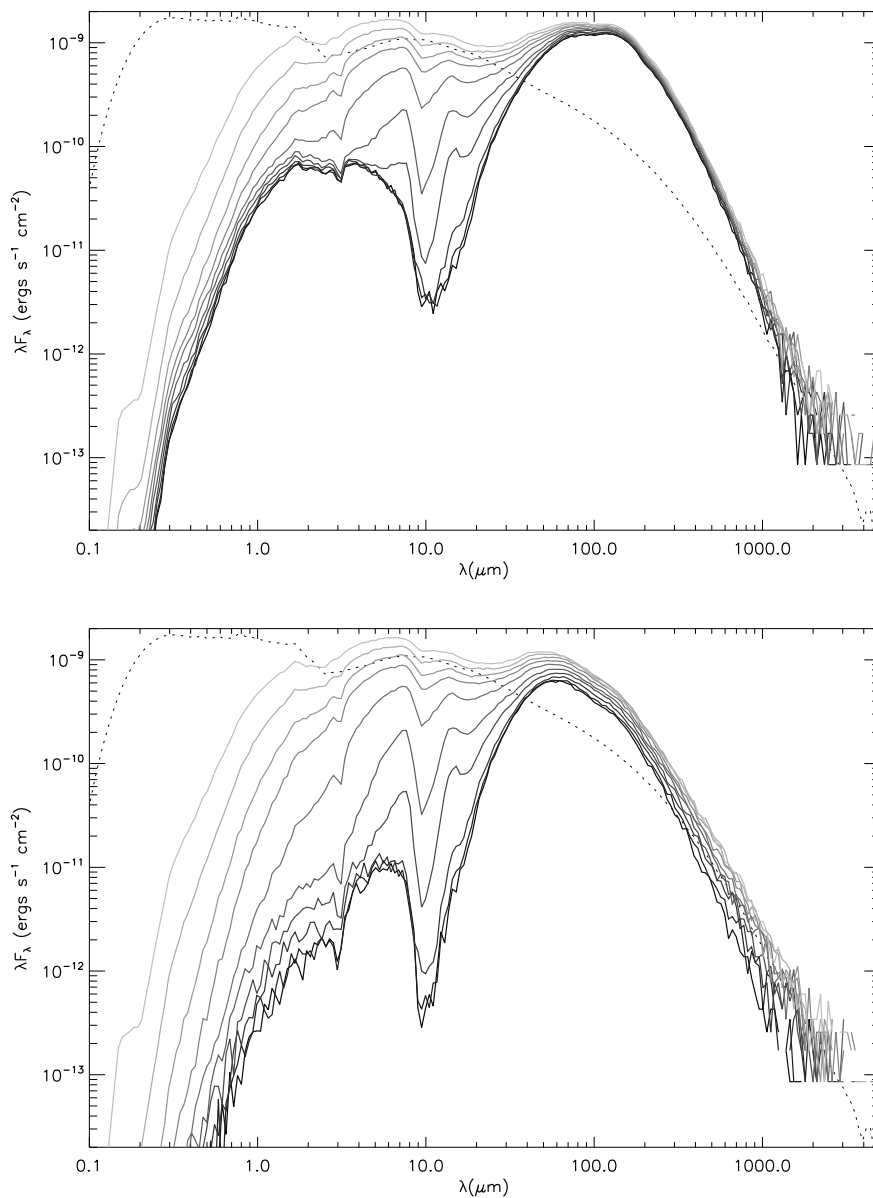


Figure 2.14 SEDs of the best fitting model from L1527 at multiple inclinations. The lines plotted from lightest to darkest correspond to inclinations of 18, 32, 31, 49, 57, 63, 70, 76, 81, and 87° measured in apertures of 5000 AU (top panel) and 1000 AU (bottom panel). The dotted line is the central star and disk as viewed face-on.

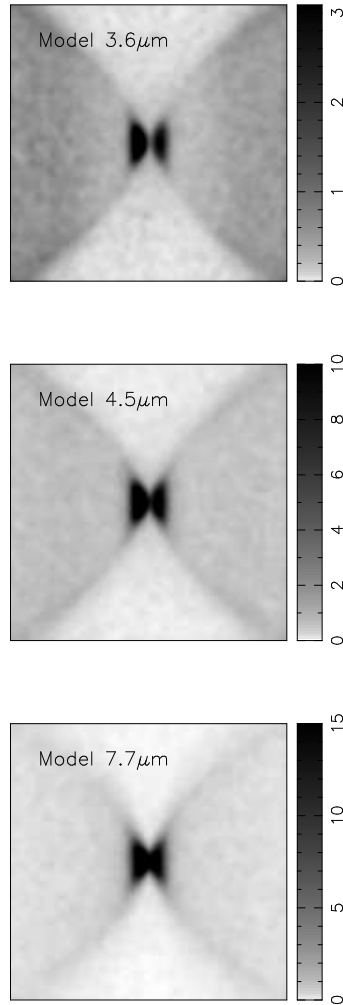


Figure 2.15 Simulated images convolved with  $0''.5$  seeing. These images are comparable to the abilities of current ground-based infrared telescopes. The  $3.6\mu\text{m}$  image is comparable to  $L'$ -band,  $4.5\mu\text{m}$  is comparable to  $M'$ -band, and the  $7.7\mu\text{m}$  is comparable to a narrow-band filter.

Table 2.1: Photometry

Wavelength ( $\mu\text{m}$ )	$F_\lambda$ (mJy)	Aperture (arcsec)	Aperture <sup>a</sup> Correction	Instrument	Observation Date	References
1.66	$7.0 \pm 3.5$	71.43	-	TIFKAM	12-27-2007	1
1.66	$8.35 \pm 4.17$	71.43	-	2MASS	10-14-1998	1
2.16	$0.594 \pm 0.162$	7.143	-	TIFKAM	12-27-2007	1
2.16	$35.2 \pm 16.2$	71.43	-	TIFKAM	12-27-2007	1
2.16	$36.94 \pm 24.3$	71.43	-	2MASS	10-14-1998	1
3.6	$6.936 \pm 0.69$	7.143	1.014	IRAC	03-07-2004	1
" "	$141.8 \pm 16.2$	71.43	0.9164	IRAC	03-07-2004	1
3.6	$6.132 \pm 0.61$	7.143	1.014	IRAC	02-23-2005	1
" "	$128.3 \pm 22.6$	71.43	0.9164	IRAC	02-23-2005	1
4.5	$22.75 \pm 2.28$	7.143	1.061	IRAC	03-07-2004	1
" "	$225.1 \pm 16.3$	71.43	0.9463	IRAC	03-07-2004	1
4.5	$18.43 \pm 1.84$	7.143	1.061	IRAC	02-23-2005	1
" "	$190.0 \pm 13.1$	71.43	0.9463	IRAC	02-23-2005	1
5.8	$29.93 \pm 2.99$	7.143	0.9918	IRAC	03-07-2004	1
" "	$149.5 \pm 45.0$	71.43	0.7926	IRAC	03-07-2004	1
5.8	$24.08 \pm 2.41$	7.143	0.9918	IRAC	02-23-2005	1
" "	$163.4 \pm 45.5$	71.43	0.7926	IRAC	02-23-2005	1
6.7	$22.36 \pm 5.6$	7.2	-	ISOCAM	10-02-1997	1
" "	$62.68 \pm 15.7$	36	-	ISOCAM	10-02-1997	1
8.0	$18.83 \pm 3.8$	7.143	0.9423	IRAC	03-07-2004	1
" "	$54.54 \pm 25.0$	71.43	0.7629	IRAC	03-07-2004	1
8.0	$14.87 \pm 3.0$	7.143	0.9423	IRAC	02-23-2005	1
" "	$37.43 \pm 18.0$	71.43	0.7629	IRAC	02-23-2005	1
9.6	$1.37 \pm 0.34$	7.2	-	ISOCAM	10-02-1997	1
11.3	$3.081 \pm 0.77$	7.2	-	ISOCAM	10-02-1997	1
14.3	$15.3 \pm 3.8$	7.2	-	ISOCAM	10-02-1997	1
" "	$54.76 \pm 13.7$	36	-	ISOCAM	10-02-1997	1
24	$660.6 \pm 66$	13	1.167	MIPS	03-05-2005	1
25	$743.6 \pm 70$	45 x 300	-	IRAS	-	2
60	$17770 \pm 1600$	90 x 300	-	IRAS	-	2
70	$24170 \pm 4834$	75	1.0	MIPS	03-05-2005	1
100	$73260 \pm 11700$	180 x 300	-	IRAS	-	2
100	$89000 \pm 36000$	60	-	Yerkes (KAO) <sup>b</sup>	03-1987	3
160	$94000 \pm 38000$	60	-	Yerkes (KAO)	03-1987	3
350	$22000 \pm 9000$	60	-	Yerkes (IRTF)	10-1987	3
350	$66000 \pm 20000$	45	-	SCUBA	01-1998	4
450	$14000 \pm 5600$	60	-	JCMT/UKT	01-1989	4
450	$44800 \pm 9000$	45	-	SCUBA	01-1998	4
450	$18200 \pm 3200$	40	-	SCUBA	01-1998	5
450	$55500 \pm 20900$	120	-	SCUBA	01-1998	5
750	$8400 \pm 1100$	45	-	SCUBA	01-1998	4
800	$1400 \pm 560$	60	-	JCMT/UKT	01-1989	3
850	$5900 \pm 480$	45	-	SCUBA	01-1998	4
850	$3190 \pm 190$	40	-	SCUBA	01-1998	5
850	$9410 \pm 460$	120	-	SCUBA	01-1998	5
1300	$720 \pm 110$	40	-	SCUBA	01-1998	5
1300	1500	30	-	IRAM	-	6

Continued on Next Page...

Table 2.1 – Continued

Wavelength	$F_\lambda$	Aperture	Aperture <sup>a</sup>	Instrument	Observation	References
2700	$47 \pm 5.6$	60 x 60	-	NMA <sup>c</sup>	01-1995	7

References: (1) This work; (2) Neugebauer et al. (1984); (3) Ladd et al. (1991); (4) Chandler & Richer (2000); (5) Shirley et al. (2000); (6) Motte & André (2001); (7) Ohashi et al. (1997)

<sup>a</sup>Corrections for IRAC data were derived from the prescription for extended source calibration on the *Spitzer Science Center* website. Corrections for MIPS data are taken from the MIPS data handbook.

<sup>b</sup>Kuiper Airborne Observatory

<sup>c</sup>Nobeyama Millimeter Array

Table 2.2: Model parameters

Parameter	Description	This paper	KCH93	R07 Standard Integrated	R07 Full SED Resolved	R07 IRAC SED Resolved	Furlan 2007
$R_*(R_\odot)$	Stellar radius	2.09	-	-	8.21	21.57	2.0
$T_*(K)$	Stellar temperature	4000	-	2932 - 3869	4260	4360	4000
$L_*(L_\odot)$	System luminosity	2.75	1.35	0.64 - 3.84	20	155	1.8
$M_*(M_\odot)$	Stellar mass	0.5	-	0.15 - 0.59	1.46	4.07	-
$M_{disk}(M_\odot)$	Disk mass	0.1	-	$6.3 \times 10^{-5}$ - 0.016	$8.58 \times 10^{-4}$	0.142	-
$h(100)$ (AU)	Disk scale height at 100AU	10.52	-	3.18 - 9.67	8.09	3.891	10
$\alpha$	Disk radial density exponent	2.125	-	-	2.155	2.042	-
$\beta$	Disk scale height exponent	1.125	-	-	1.155	1.042	-
$\dot{M}_{disk}(M_\odot yr^{-1})$	Disk accretion rate	$3.0 \times 10^{-7}$	-	$9.77 \times 10^{-12}$ - $5.01 \times 10^{-8}$	$1.98 \times 10^{-8}$	$7.29 \times 10^{-7}$	-
$R_{trunc}(R_*)$	Magnetosphere co-rotation radius	3.0	-	-	5.0	5.0	-
$F_{spot}$	Fractional area of accretion hotspot	0.01	-	0.01	0.01	0.01	-
$R_{disk,min}(R_*)$	Disk inner radius	14.25	-	$R_{dd}$	7.84	8.33	1.0
$R_{disk,max}$ (AU)	Disk outer radius	75	-	33.8 - 1303.3	58.398	33.703	200
$R_c$ (AU)	Centrifugal radius	75	300	-	58.398	33.703	200
$R_{env,min}(R_*)$	Envelope inner radius	42.75	-	-	7.84	8.33	-
$R_{env,max}$ (AU)	Envelope outer radius	15000	3000	-	16200	9120	10000
$\dot{M}_{env}(M_\odot yr^{-1})$	Envelope mass infall rate	$1.00 \times 10^{-5}$	$4.22 \times 10^{-5a}$	$0.911$ - $5.05 \times 10^{-5}$	$1.37 \times 10^{-4}$	$2.63 \times 10^{-4}$	$5.34 \times 10^{-6a}$
$\rho_1(g cm^{-3})$	Envelope Density at 1 AU	$3.75 \times 10^{-14}$	$3.16 \times 10^{-13}$	$0.341$ - $1.89 \times 10^{-13a}$	$8.77 \times 10^{-13}$	$2.81 \times 10^{-12}$	$1.00 \times 10^{-14}$
$b_{in}$	Inner cavity shape exponent	1.5	-	-	-	-	-
$b_{out}$	Outer cavity shape exponent	1.9	none	1.5	1.5	1.5	streamline
$z_{in}$ (AU)	Inner cavity offset	0	-	-	-	-	-
$z_{out}$ (AU)	Outer cavity offset height	100	-	-	-	-	-
$\theta_{open,in}$ ( $^\circ$ )	Inner cavity opening angle	15	-	-	-	-	-
$\theta_{open,out}$ ( $^\circ$ )	Outer cavity opening angle	20	-	-	43	16	27
$\theta_{inc}$ ( $^\circ$ )	Inclination angle	85	60-90	41-81	81	75	89
$\rho_c(g cm^{-3})$	Cavity density	0	-	-	$1.40 \times 10^{-20}$	$1.42 \times 10^{-20}$	-
$\rho_{amb}(g cm^{-3})$	Ambient density	0	-	-	$3.838 \times 10^{-22}$	$1.42 \times 10^{-20}$	-

<sup>a</sup>Assumes a  $0.5M_\odot$  central stellar mass.

## CHAPTER 3

# The Inner Envelope and Disk of L1527 Revealed: Gemini L'-band Scattered Light Imaging

### 3.1 Introduction

In the earliest stages of star formation, the Class 0/I phases (Andre et al., 1993; Lada, 1987), the newborn protostar is embedded within a dense envelope of gas and dust. In the Class 0 phase, little or no emission is generally detected shortward of  $\sim 10\mu\text{m}$  due to high extinction toward the central object; however, the bipolar outflows from the central protostar and disk carve cavities in the envelopes creating scattered light nebulae visible in the near to mid-infrared (1-8 $\mu\text{m}$ ). The morphology of the outflow cavities then result from a ram pressure balance between the infalling envelope and outflow (Shu et al., 1991).

Early models of infalling envelopes assumed spherical collapse (Shu, 1977) along with slow rotation (Ulrich, 1976; Cassen & Moosman, 1981; Terebey et al., 1984), which were later modified for infall from initially flattened geometries (Hartmann et al., 1996). The rotating collapse model provides a natural route for the formation of circumstellar disks within the protostellar envelope. However, disks in Class 0 objects have been difficult to study primarily because of the surrounding envelope (e.g. Jørgensen et al., 2009) and insufficient resolution at millimeter wavelengths to isolate the protostellar disk. In addition, the small-scale structure of outflow cavities in Class 0 protostars has also been elusive due to the envelope extinguishing near-IR

---

Based on the paper by John J. Tobin, Lee Hartmann, Laurent Loinard, *ApJL*, 2010, 722, 12

scattered light emission, shifting the scattered light emission peak into the mid-IR (Tobin et al., 2007, 2008).

One of the nearest low-mass protostars in Taurus ( $d = 140\text{pc}$ ), L1527 IRS (hereafter L1527), has been a favorite target for studies of outflow and envelope structure (e.g. Ohashi et al., 1997; Chandler & Richer, 2000; Robitaille et al., 2007; Tobin et al., 2008; Gramajo et al., 2010). It has been classified as Class 0 protostar (Chen et al., 1995) but could be a Class I system given its edge-on orientation (Ohashi et al., 1997), which enhances the amount of extinction along the line of sight (Tobin et al., 2008). The moderate resolution IRAC images of L1527 from *Spitzer* reveal bright bipolar cavities extending  $\sim 10000$  AU in radius (Hartmann et al., 2005; Tobin et al., 2008). The outflow cavities are separated by what appears to be a large-scale ( $\sim 1000$  AU) dark lane; however, a central point-source between the cavities was observed within the dark lane from  $3.6$  to  $8\mu\text{m}$ . In Tobin et al. (2008, hereafter Chapter 2), I was able to explain this by constructing a model assuming that the point-source was a compact inner outflow cavity, unresolved by *Spitzer*, connecting with the larger outer cavity. I then proposed high-resolution mid-IR imaging to test this model.

In this chapter, I present high resolution L'-band ( $3.8\mu\text{m}$ ) observations of L1527 from the Gemini North telescope. This is the highest resolution mid-IR image of the inner envelope/outflow cavity around a Class 0 protostar. The observations confirm my prediction of a compact, bipolar scattered light structure; quite similar to the model constructed in Chapter 2 but strongly resembling a disk in scattered light.

## 3.2 Observations and Data Reduction

I observed L1527 with the 8.1 meter Gemini North telescope at Mauna Kea on 2009 October 24 and 2009 December 11 using the Near-Infrared Imager (NIRI) in L'-band ( $3.8\mu\text{m}$ ). The camera was used in f/14 mode which provides a  $0.049'' \text{ pix}^{-1}$  scale; I only used the central  $512 \times 512$  area of the detector for faster read-out which enabled integrations short enough to avoid saturation from sky background. I observed with a standard 5-point “dice-5” dither pattern with  $5''$  steps and a nearby star was used for tip-tilt correction and guiding. At each position 150 coadded images of 0.2 seconds

were taken; a total of 35 images were taken yielding 16 minutes of integration during the first observation and 176 images totaling 88 minutes of integration during the second observation. However, the first 38 images in the second observation were unusable due to variable sky background. Observations of the standard star HD 22686 show that the seeing was  $\sim 0.3''$  on both nights.

The raw data were reduced using the Gemini IRAF<sup>1</sup> package. Flat field images were generated from sky flats constructed by median combining the dithered images. Each on-source frame was sky subtracted using a median sky generated from the on-source frame and the two images taken immediately before and after. This method of sky subtraction compensates for the rapid variations in sky brightness at L'-band. The sky subtracted images were then combined using the imcombine task of IRAF using the offsets given in the header; L1527 was quite faint in the individual frames and could not be used for further refinement of the offsets. The datasets from both epochs of observation were combined yielding a final image with 85 minutes of integration.

I also include data taken with the Infrared Array Camera (IRAC) (Fazio et al., 2004) on the *Spitzer Space Telescope*. These data were taken in 24 February 2004 as part of the GTO Taurus survey and were presented in Tobin et al. (2008) and Hartmann et al. (2005).

### 3.3 Results

The images of L1527 at L'-band and  $3.6\mu\text{m}$  are shown in Figure 6.3.1. The IRAC image clearly shows the point-like structure appearing in the center of the envelope between the large scattered light cavities. The Gemini L' image resolves the point-like structure into a compact, bipolar scattered light nebula at the center of L1527. The two lobes are separated by a narrow dark lane  $\sim 0.45''$  (60 AU) wide, consistent with a circumstellar disk shadow. The L' image reveals structure similar to that of the *Hubble* NICMOS images of Class I protostars in Taurus from Padgett et al. (1999). However, this is the first time such an image has been captured of a Class 0 protostar.

---

<sup>1</sup>IRAF is distributed by the National Optical Astronomy Observatories, which are operated by the Association of Universities for Research in Astronomy, Inc., under cooperative agreement with the National Science Foundation.

The total extent of the bipolar structure in the direction of the outflow (east-west) is  $\sim 2.5''$  (350 AU) and  $\sim 1.8''$  (250 AU) in width. The extent of the scattered light along the outflow and dark lane is much thicker than a prototypical disk (i.e. HH30, Burrows et al., 1996) indicating that the disk in L1527 is more vertically extended or that the scattering is coming from the inner envelope. The eastern lobe is about twice as bright as the western lobe; consistent with eastern side being slightly inclined toward within the line of sight ( $\sim 85^\circ$ ) (Chapter 2). The orientation of the disk dark lane indicates that the rotation axis of the system has a position angle  $\sim 85^\circ$  east of north. Extended, low surface brightness emission from the outflow cavity is also seen extending away from the inner envelope in the Gemini image. The cavity is quite narrow until  $\sim 6''$  (840 AU) from the center; this narrowness was not well resolved in the *Spitzer* image. Past  $6''$ , the cavity expands rapidly to very wide angles. The total flux within a  $7''.14$  (1000 AU) aperture radius is  $6.5 \pm 0.6$  mJy, consistent with the IRAC flux from Chapter 2.

### 3.3.1 Models

I use the Monte Carlo radiative transfer code of Whitney et al. (2003c) to interpret the observations. The model components are described in Chapter 2, but I discuss some important aspects here for completeness. The envelope density structure is the standard rotating collapse solution (Cassen & Moosman, 1981; Terebey et al., 1984) in which envelope density scales with the infall rate  $\dot{M}_{env}$  with  $\rho \propto R^{-3/2}$  outside the centrifugal radius ( $R_C$ ) and  $\rho \propto R^{-1/2}$  inside  $R_C$ . Conical outflow cavities are carved out of the envelope, their shape is defined by a polynomial, the degree of the polynomial is the shape parameter. The dust model presented in Chapter 2 is also used for the envelope, having grains up to  $1\mu\text{m}$  in radius.

The disk is defined by its initial scale height  $H_0$  at the stellar radius  $R_*$  and flaring power law  $H \propto R^\beta$ , radial density profile  $\rho \propto R^{-\alpha}$ , mass, and outer radius. The vertical structure of the disk is assumed to be Gaussian with an initial scale height defined to be in hydrostatic equilibrium at the dust destruction radius ( $T_d=1600\text{K}$ ). Values of  $\beta = 9/8, 5/4$  are commonly used, corresponding to isothermal scale heights with

$T_{disk} \propto R^{-3/4}$  and  $R^{-1/2}$ . The gas and dust of the disk are assumed to be well mixed. The dust opacities for the disk are taken from Wood et al. (2002) which were used to model the SED of HH30. The dust is distributed in a quasi-settled manner with grains up to 1mm in the disk midplane while smaller grains remain extended. The transition between these dust populations is defined to be  $n_{H_2}=10^{10} \text{ cm}^{-3}$  or the first scale height.

In Chapter 2, I inferred that the apparent point source seen at  $3.6\mu\text{m}$  was in fact a bipolar structure seen in reflected light, with the true central source actually hidden by extinction. To create this structure, I constructed a dual-cavity model having a narrow inner cavity with an outer cavity offset by 100 AU (see Figure 2.10 for an illustration). Comparing the top and middle rows of Figure 3.2 shows that the prediction was qualitatively correct. I next take advantage of the high spatial resolution of the Gemini data to gain an improved understanding of the inner structure. I required that models reproduce both the  $L'$  and IRAC images and the broadband SED and IRS spectrum (Furlan et al., 2008, and Chapter 2), as it is important to use as many constraints as possible (Chapter 2, Gramajo et al., 2010).

I first adjusted the parameters of the dual-cavity model to better reproduce the Gemini observations by varying the inner and outer cavity shapes and opening angles. As shown in Figures 3.2 and 3.3, my best-fit dual-cavity model reproduces the observations reasonably well (note that the images for the refined dual-cavity model are not shown as they are nearly identical to the disk model as discussed below). The envelope infall rate for this model was  $10^{-5}M_{\odot} \text{ yr}^{-1}$ ; the outer cavity was offset from the inner cavity by 85 AU. The disk parameters are  $H(10 \text{ AU})= 1.87 \text{ AU}$  with  $\beta = 1.25$ ,  $H_0 = 0.0332 R_*$ ,  $M_{disk}= 0.05 M_{\odot}$  and  $R_{disk}= 25 \text{ AU}$ ; a model with  $\beta = 1.125$  was also able to be fit, but with double the initial scale height; the full parameter set is listed in Table 3.1.

I did not consider a disk model in Chapter 2 because the large-scale dark lane seemed to be too thick to be reproduced with a disk. However, using the detailed Gemini image, I can describe disk parameters which yield scattering surfaces comparable to that of the dual-cavity model. The highly-flared disk in this model had

$H(10 \text{ AU}) = 1.95 \text{ AU}$  ( $H(190 \text{ AU}) = 82 \text{ AU}$ ), with  $\beta = 1.27$ ,  $\alpha = 3.0$ ,  $H_0 = 0.03 R_*$ ,  $M_{disk} = 0.005 M_\odot$  and  $R_{disk} = 190 \text{ AU}$ . The envelope infall rate was lowered to  $0.8 \times 10^{-5} M_\odot \text{ yr}^{-1}$  in order to allow more scattered light from the disk to escape through the envelope. I also used the envelope dust model for the disk upper layers rather than the default dust model; this increased the  $L'$  intensity and reduced emission from 10 to 60  $\mu\text{m}$  (see Table 3.1 for other parameters) bringing the model into closer agreement with the observations. As shown in Figures 3.2 and 3.3, this model also provides reasonable agreement with the observations.

### 3.4 Discussion

The dual-cavity model in Chapter 2 was justified based on simulations with a wide-angle outflow and a highly flattened envelope density distribution (Delamarter et al., 2000). However, it is unclear if such a flattened envelope is present in L1527, as there is no evidence for this in submillimeter observations (Chandler & Richer, 2000). In addition, the outflow cavity on scales larger than 840 AU from the central object does not easily fit within this framework due to the rapid widening of the scattered light nebula beyond 840 AU (Section 3.3; Figure 6.3.1) This is difficult to explain with a simple conical cavity because there is no direct line-of-sight from the protostar/disk to these parts of the outflow cavity. Therefore I suggest that the morphology of the scattered light nebulosity on large scales is not due directly to the outflow but to the morphology of the envelope and/or ambient medium (Tobin et al., 2010b). In any case it appears difficult to explain the complex shape of the scattered light structures with a simple outflow-envelope interaction.

Given these difficulties, the disk scenario seems attractive. Images of disks in silhouette have previously been observed around T-Tauri stars (Class II sources) and Class I protostars (e.g. Padgett et al., 1999; Burrows et al., 1996). The small-scale scattered light morphology of L1527 bears a resemblance to that of IRAS 04302+2247 and HH30. The problem for this model is that the disk must be highly flared, with the aspect ratio of the disk extinction lane relative to the extent of the scattered light surfaces being about a factor of two larger than other objects. To reproduce

the compact scattered light and large-scale dark lane with a disk, it was necessary to adopt a high degree of flaring in the disk ( $\beta=1.27$ ), a steep density profile ( $\alpha=3.0$ ), a large disk radius ( $R_d=190\text{AU}$ ), and a small disk mass ( $M_d=0.005M_\odot$ ). (Note that the mass is simply a formal parameter of the model for scaling the density. Extrapolating disk masses from fitting scattered light in the disk upper layers is problematic since they contain a small fraction of the total mass.) These observations and modeling emphasize not only that disks form early during protostellar collapse (Jørgensen et al., 2009; Vorobyov, 2009) but also that disks with large radii are able to form during the Class 0 phase (see also Enoch et al., 2009) with radii comparable to Class II disks in Taurus (Andrews & Williams, 2007).

In general, dust growth and/or depletion in upper disk layers relative to ISM conditions is needed to reproduce the scattered light images of edge-on disk systems and the SEDs of T Tauri stars (D'Alessio et al., 2006; Duchêne et al., 2010; Furlan et al., 2008). Thus, it may be that the postulated L1527 disk has had much less dust evolution and thus has more small dust in upper layers, making it easier to explain the wide extinction lane observed (e.g. D'Alessio et al., 2006).

Loinard et al. (2002) directly imaged the disk of L1527 and a binary companion separated from the primary by  $0.17''$  (24 AU) with VLA  $\lambda=7\text{mm}$  observations. These observations are overplotted on the  $L'$  image in Figure 6.3.4. The observed disk is quite compact - only  $\sim 0.3''$  (40 AU) in diameter. Though this system is a close binary, I do not expect the companion to affect the modeled parameters significantly, because my results mostly constrain the outer disk. The compactness of the disk measured Loinard et al. (2002) is not inconsistent with the disk model since the  $\lambda=7\text{mm}$  observations will only be sensitive to the densest part of the disk and where the grains are largest. Their measured disk mass of  $0.1M_\odot$  is substantially larger than my disk model (which is uncertain as discussed previously). Note that the disk mass is strongly dependent on the assumed dust mass opacities; Loinard et al. (2002) used a dust opacity model based on Pollack et al. (1994) which had  $\kappa_{7mm}=4.9\times 10^{-4}\text{ cm}^2\text{g}^{-1}$  (P. D'Alessio private communication). Andrews & Williams (2005) used  $\kappa_{850\mu m}=0.035\text{ cm}^2\text{g}^{-1}$  with  $\kappa \propto \lambda^{-1}$  which yields  $\kappa_{7mm}=0.00425\text{ cm}^2\text{g}^{-1}$  when extrap-

olated. The difference between the  $\kappa_{7mm}$  values can be attributed to the Pollack et al. (1994) dust model only considering grains up to  $1\mu\text{m}$  in size while the dust model used by Andrews & Williams (2005) considered grains up to 1mm in size. Scaling the Loinard et al. (2002)  $\lambda=7\text{mm}$  mass to  $\kappa_{7mm}$  from Andrews & Williams (2005) gives  $M_{disk}=0.0095M_{\odot}$ , in agreement with the mean disk mass of Taurus.

From the observations and modeling it is now clear that the small-scale scattered light in L1527 is most likely due to a disk. However, the assumed parameters needed to fit the disk model (e.g. steep density profile) may only have been necessary to enable my simplistic treatment of disk structure to work for L1527. Models which solve for the vertical structure of the disk self-consistently (i.e. D’Alessio et al., 1998), given the irradiation from the central object have a density structure that is not Gaussian (as assumed in my modeling) but falls off less rapidly with  $z$  because the temperature increases with vertical height  $z$ . Indeed, even in the context of an isothermal structure, the Gaussian density distribution becomes a poor approximation as the ratio of the vertical height to radial distance becomes  $z/R \rightarrow 1$ . These issues deserve further investigation with physically self-consistent radiative transfer modeling of L1527.

### 3.4.1 Conclusions

I have presented high-resolution  $L'$  imaging of the inner envelope of L1527 demonstrating that much can be learned of inner envelope structure and newly forming disks with high resolution scattered light observations of Class 0 protostars. The observations strongly resemble the dual-cavity model constructed in Tobin et al. (2008); however, the observations can be equally well reproduced by a large, highly flared disk or a refined dual-cavity structure. However, the global scattered light structure is difficult to interpret as purely an outflow cavity. I therefore suggest that the bright scattered light structure is most likely be a vertically extended disk-in-formation with material falling onto it.

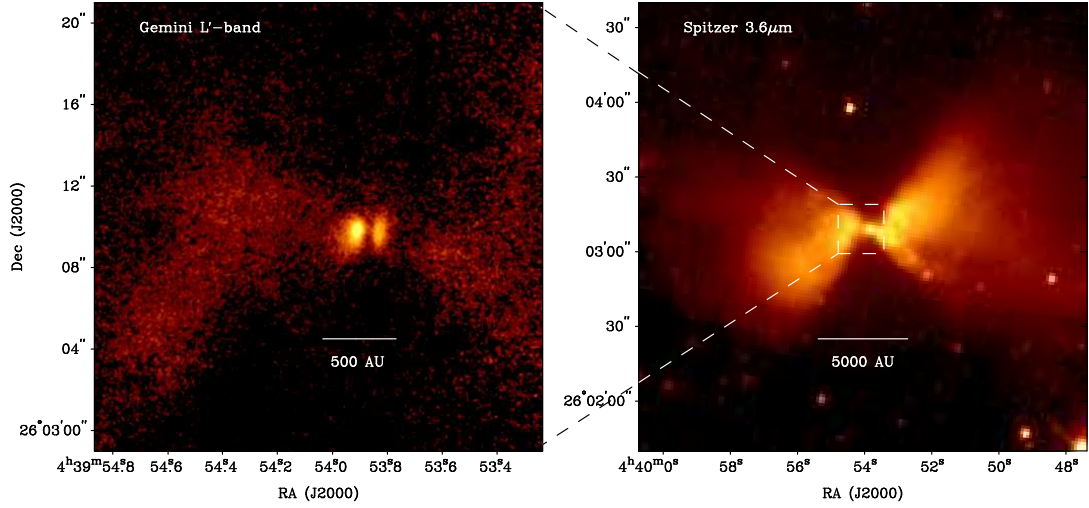


Figure 3.1 Left:  $L'$  image of L1527 showing the full range of the outflow cavity viewed. Notice how the outflow cavity rapidly widens about  $6''$  (840 AU) from the protostar. Right: Full IRAC  $3.6\mu\text{m}$  image of L1527. The region viewed in the  $L'$  observations is outlined.

Table 3.1. Model parameters

Parameter	Description	Dual-Cavity Model	Disk Model
$R_*(R_\odot)$	Stellar radius	2.09	2.09
$T_*(\text{K})$	Stellar temperature	4000	4000
$L_*(L_\odot)$	System luminosity	2.75	2.75
$M_*(M_\odot)$	Stellar mass	0.5	0.5
$M_{disk}(M_\odot)$	Disk mass	0.05	0.005
$h(10\text{AU})$	Disk scale height at 10AU	1.87	1.95
$H_0$	Disk scale height at $R_*$	0.0332	0.03
$\alpha$	Disk radial density exponent	2.25	3.0
$\beta$	Disk scale height exponent	1.25	1.27
$\dot{M}_{disk}(M_\odot \text{ yr}^{-1})$	Disk accretion rate	$3.0 \times 10^{-7}$	$3.0 \times 10^{-7}$
$R_{trunc}(R_*)$	Magnetosphere co-rotation radius	3.0	3.0
$F_{spot}$	Fractional area of accretion hotspot	0.01	0.01
$R_{disk,min}(R_*)$	Disk inner radius	14.25	14.25
$R_{disk,max}(\text{AU})$	Disk outer radius	25	190
$R_c(\text{AU})$	Centrifugal radius	25	190
$R_{env,min}(R_*)$	Envelope inner radius	42.75	42.75
$R_{env,max}(\text{AU})$	Envelope outer radius	15000	15000
$\dot{M}_{env}(M_\odot \text{ yr}^{-1})$	Envelope mass infall rate	$1.00 \times 10^{-5}$	$0.8 \times 10^{-5}$
$b_{in}$	Inner cavity shape exponent	1.3	-
$b_{out}$	Outer cavity shape exponent	1.7	1.5
$z_{out}(\text{AU})$	Outer cavity offset height	85	-)
$\theta_{open,in}(\text{^\circ})$	Inner cavity opening angle	15	-
$\theta_{open,out}(\text{^\circ})$	Outer cavity opening angle	15	20
$\theta_{inc}(\text{^\circ})$	Inclination angle	85	85
$\rho_c(\text{g cm}^{-3})$	Cavity density	0	0
$\rho_{amb}(\text{g cm}^{-3})$	Ambient density	0	0

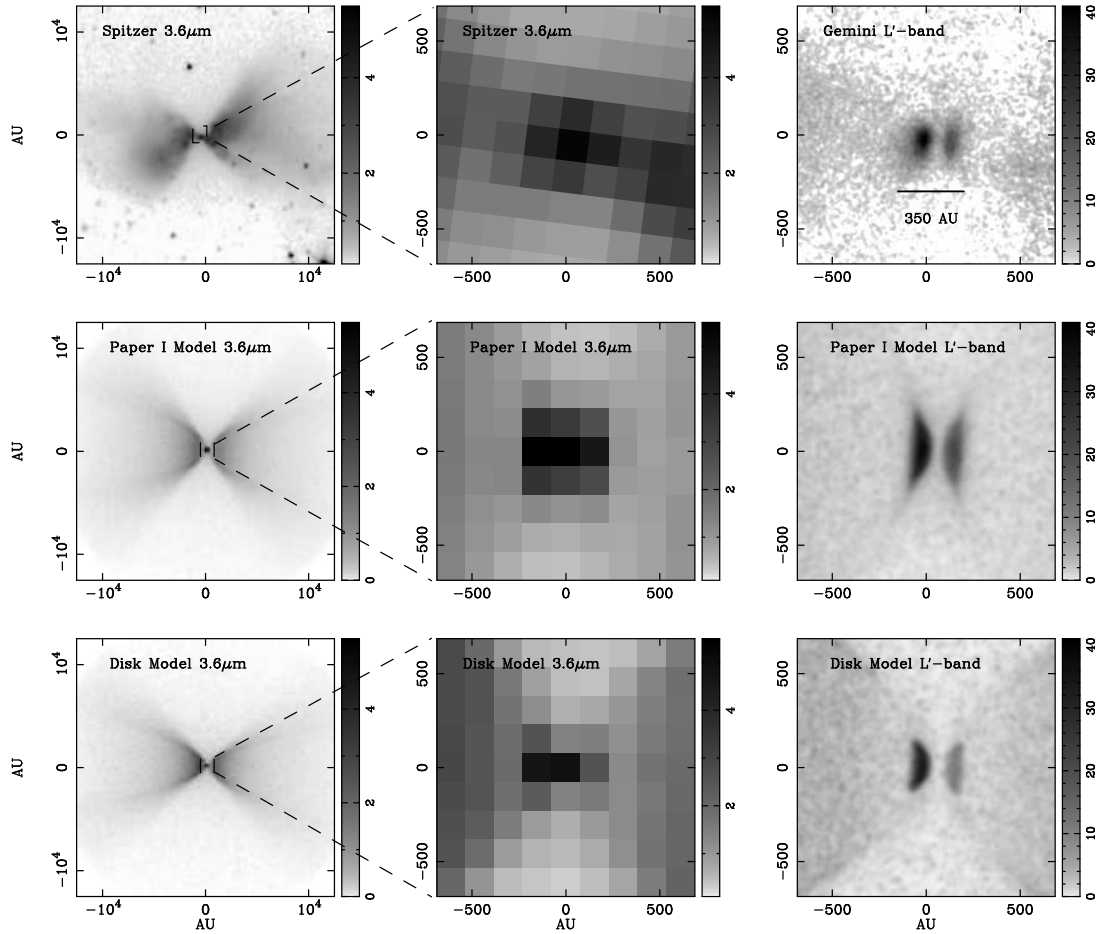


Figure 3.2 Comparison of models to the observations. Top row: Observations of L1527 from Spitzer and Gemini. Middle Row: Initial model of L1527 from Chapter 2 without any knowledge of L1527 at high resolution. Bottom Row: Disk plus single-cavity model. Note that the refined dual-cavity model images are not shown as they are nearly identical to the disk models.

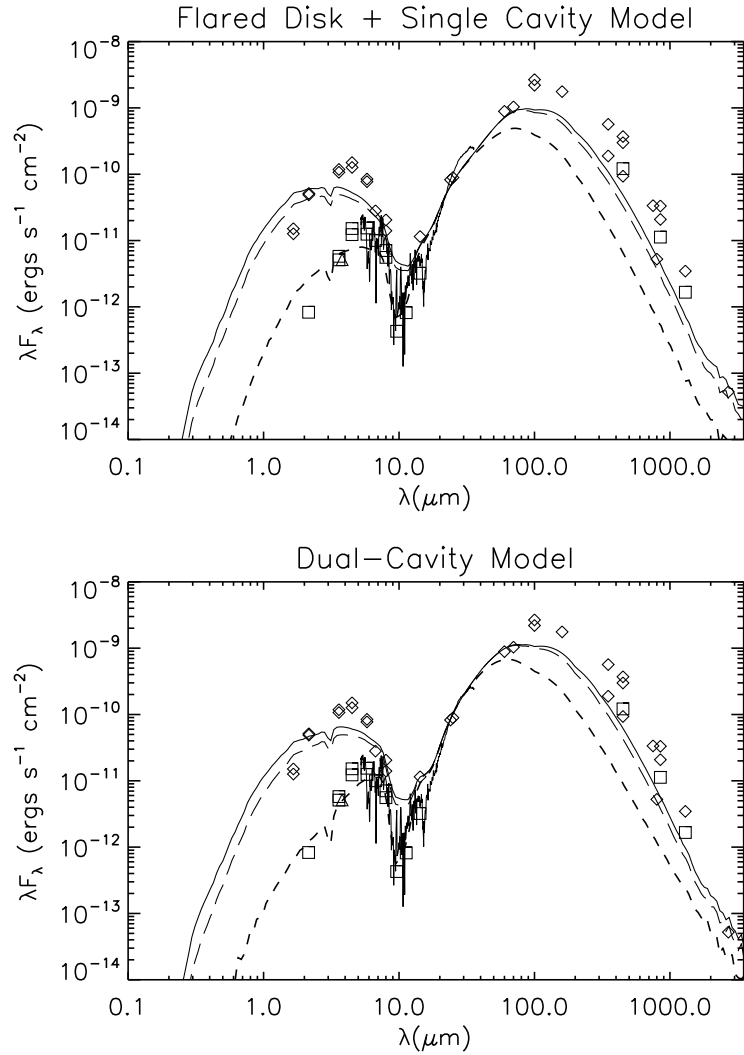


Figure 3.3 Model SEDs for L1527 with photometry and IRS spectrum from Tobin et al. (2008, and references therein.). Photometry taken with apertures of  $71''$  (diamonds) and  $7''$  (boxes) (10000 AU and 1000 AU) are plotted. The triangle at  $3.8\mu\text{m}$  is the Gemini  $L'$  flux within 1000 AU. The model SEDs are plotted for the Disk model (left) and the refined dual-cavity model (right) with multiple model apertures of 10000 AU (solid line), 6000 AU (long-dashed line), and 1000 AU (short-dashed line). The model is clearly deficient in flux at long wavelengths; however, external heating is not taken into account and the dust temperatures fall below 10K in the outer envelope emitting less in the far-IR and submm.

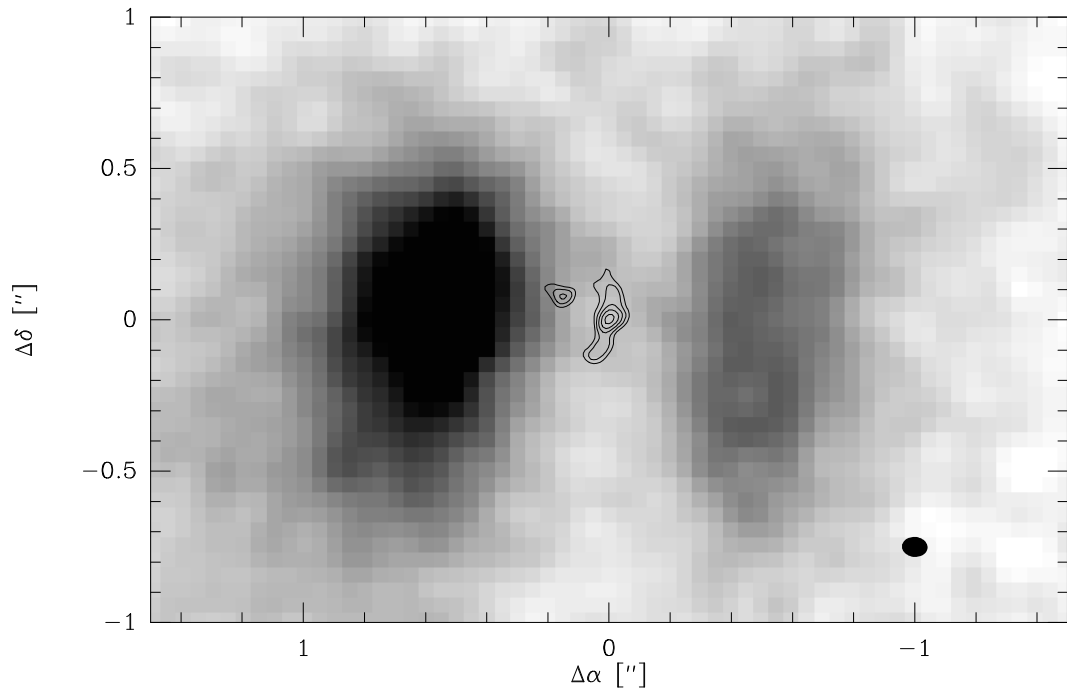


Figure 3.4  $L'$  image of L1527 with 7mm dust continuum observations (contours) from VLA observations by Loinard et al. (2002). Notice that the position angle of the long axis of the disk is in the same direction as the disk extinction lane,  $\sim 5^\circ$  East of North. The second 7mm point source just east of the disk is the binary companion.

## CHAPTER 4

# Complex Structure in Class 0 Protostellar Envelopes

### 4.1 Introduction

Sphericity and axisymmetry have been standard assumptions on which the theoretical understanding of star formation has rested for some time. One of the early models of protostellar collapse by Shu (1977) was based on the singular isothermal sphere developed and extended to include rotation by Terebey et al. (1984, TSC), creating a rotationally flattened envelope. Further modifications have been introduced over time, including models with flattened, sheet-like envelopes (Hartmann et al., 1996) and ‘pseudo-disks’ resulting from magnetic collapse (e.g. Galli & Shu, 1993), while still assuming axisymmetry. Spherical/axisymmetric envelope models have been used extensively to calculate spectral energy distributions (SEDs) of embedded protostars or disks (e.g. Kenyon et al., 1993a; Whitney & Hartmann, 1993; Whitney et al., 2003c). In particular, the TSC envelope model has been highly successful in modeling the SEDs of Class 0 and Class I protostars; by including outflow cavities, such models are also able to reproduce near and mid-infrared scattered light images (e.g. Adams et al., 1987; Furlan et al., 2008; Kenyon et al., 1993a; Stark et al., 2006; Tobin et al., 2007, 2008). However, it is not clear whether or not envelopes around protostars are accurately described by symmetric models.

Recently, observations with the *Spitzer Space Telescope* have given a high-resolution

---

Based on the paper by John J. Tobin, Lee Hartmann, Leslie W. Looney, & Hsin-Fang Chiang, *ApJ*, 2010, 712, 1010

view of envelope structure around two Class 0 protostars in extinction at  $8\mu\text{m}$  against Galactic background emission, L1157 appears flattened and L1527 has an asymmetric distribution of material (Looney et al., 2007; Tobin et al., 2008). This method enables one to observe the structure of collapsing protostellar envelopes on scales from  $\sim 1000\text{AU}$  to  $0.1\text{ pc}$  for the first time with a mass-weighted tracer. In contrast, single-dish studies of envelopes using dust emission in the sub/millimeter regime generally have lower spatial resolution. The continuum emission depends upon temperature as well as mass, while molecular tracers are affected by complex chemistry. Interferometry can provide higher resolution of both continuum and molecular tracers, but large scale structure is resolved out, in contrast to the  $8\mu\text{m}$  extinction maps.

In this chapter, I analyze archival IRAC images of 22 Class 0 protostars whose dusty envelopes can be detected in extinction at  $8\mu\text{m}$ . Most of the envelopes in the sample are found to be irregular and non-axisymmetric. I demonstrate that the extinction observed is indeed due to the circumstellar envelope and not background fluctuations by comparing near-IR extinction measurements with those at  $8\mu\text{m}$ . Near-infrared imaging of lower-extinction regions is used to correct for foreground emission and/or instrumental effects. I also derive quantitative measures of the envelope asymmetries using projected moment of inertia ratios. The results indicate that infalling envelopes are frequently complex and non-axisymmetric, which might be the result of gravitational collapse from complex initial cloud morphologies. I also suggest that protostars exhibit a preference to form near the edges of clouds or bends in filaments, which could be due to the effects of gravitational focusing.

## 4.2 Observations and Data Reduction

The primary dataset used in this study is comprised of archived *Spitzer Space Telescope*  $8\mu\text{m}$  images taken with the IRAC instrument. I have also taken near-IR (H & Ks-band) images of the protostars and surrounding regions with a rich stellar background as an additional constraint on column density using near-IR extinction mapping via the near-infrared color excess (NICE) method (Lada et al., 1994).

### 4.2.1 *Spitzer* IRAC Observations

Motivated by prior detections of envelopes in extinction, I downloaded the pipeline-reduced data for cataloged Class 0 protostars (e.g. Froebrich, 2005; Seale & Looney, 2008) as well as the c2d (Evans et al., 2003) observations of dense cores and molecular clouds to determine if a protostar has an  $8\mu\text{m}$  extinction envelope associated with it. Of the cataloged protostars, I have clearly detected 22 envelopes in extinction within the nearby star forming clouds (Taurus, Perseus, Cepheus, Chameleon, Orion). I was not able to obtain meaningful results for sources in which the background emission is too faint to reliably derive  $8\mu\text{m}$  extinction, or in cases where the protostar is too bright, thus swamping its envelope structure with emission on the wings of the point-spread function (PSF), or in very crowded regions with many protostars, outflows, and extended foreground (PAH) emission. Pre-stellar/starless cores (e.g., Stutz et al. (2009) and Bacmann et al. (2000)) are not considered in this study.

For each source with identified extinction, I downloaded the basic calibrated data (BCDs) and mosaicked the individual frames using MOPEX after running the *Spitzer* IRAC artifact mitigation tool written by S. Carey. Because the IRAC data use sky darks rather than true darks, all dark frames contain some level of zodiacal light emission that is subtracted from the BCDs. For this work, it is necessary to eliminate the zodiacal light from the images. Thus, during the artifact mitigation process I subtracted the difference between the zodiacal background of the target and the sky dark zodiacal background as written in the BCD headers which are determined from a zodiacal light model (Meadows et al., 2004).

I list the selected sources, observations dates, integration times, and AOR keys in Table 4.1. The sources in which the data were originally observed in my own collaborations are also identified with the program number. Also, some objects had multiple epochs of observation. In these cases, the datasets were combined if the data were taken close enough in time such that the difference between estimated zodiacal emission was negligible. If the observations were taken more than a few days apart, I used the set of observations with the longest integration time.

### 4.2.2 Near-IR Observations

To complement the *Spitzer*  $8\mu\text{m}$  data, I observed selected protostars from the sample in H and Ks-bands for the purpose of measuring extinction toward background stars viewed through the envelope. I have identified the protostars for which near-IR data were taken in Table 4.1. Data for L1152, L1157, L1165, L723, and L483 were taken at the MDM Observatory on Kitt Peak using the near-IR instrument TIFKAM on the the 2.4m Hiltner telescope during photometric conditions between 29 May 2009 and 4 June 2009. TIFKAM provides several imaging modes, I used the F/5 camera mode which provides a  $\sim 5'$  field-of-view (FOV) over the  $1024^2$  array. I observed the targets in a 5-point box dither pattern with  $30''$  steps, taking 5x30 second coadded images at each position in H and Ks-bands. Total integration times were generally 50 minutes in Ks-band and 40 minutes in H-band, these were varied depending on seeing and sky-background. I was not concerned with preserving extended emission from the protostars, therefore I median combined the images of a single dither pattern to create a sky image for subtraction. The data were reduced using the UPSQIID package in IRAF<sup>1</sup>.

The observations of BHR71, IRAS 09449-5052, and HH108 were taken with the ISPI camera (van der Bliik et al., 2004) at CTIO using the 4m Blanco Telescope during photometric conditions on 11 June 2009. The ISPI camera features a  $10.5'$  FOV on a  $2048^2$  array. I observed the protostars using a 10-point box dither pattern with  $60''$  steps with 3x20 second coadded images in Ks-bands and generally 2x30 second coadded images in H-band. The total integration time for BHR71 was 30 minutes in each band, and 20 minutes for IRAS 09449-5052. Again, I median-combined the on-source frames to create the sky image; however, due to the larger field and steps in the dither pattern extended emission is preserved in these data. I used standard IRAF tasks for flat-fielding and sky subtraction. I could not simply combine the data using an alignment star due to optical distortion. To correct for this, I fit the world-

---

<sup>1</sup>IRAF is distributed by the National Optical Astronomy Observatories, which are operated by the Association of Universities for Research in Astronomy, Inc., under cooperative agreement with the National Science Foundation.

coordinate system (WCS) to each flat-fielded, sky-subtracted frame using `wcstools` (Mink, 1999) and the 2MASS catalog. Then I used the IRAF task `CCMAP` to fit a 4th order polynomial to the coordinate system. A difficulty encountered was the lack of 2MASS stars in the center of the images since the targets are protostars with highly opaque envelopes. In addition, the 2MASS catalog tends to have some false source identifications associated with diffuse scattered light in the outflow cavity of protostars. Thus, since not all polynomial fits were acceptable, I applied the best fitting solution to all images. I then used the stand-alone program `SWARP` (Bertin et al., 2002) to combine the individual frames while accounting for the distortion.

Lastly, I conducted additional observations of BHR71 with the PANIC camera on the 6.5m Magellan (Baade) telescopes. The data were taken during photometric conditions on 17 and 18 January 2009. The PANIC instrument has only a  $\sim 2'$  FOV, thus I took 3 fields of BHR71, one centered on the protostar, one  $2'$  east and  $45''$  south, and a last field  $2'$  west and  $45''$  north. The data were taken in a 9-point dither pattern with 2x20 second images taken at each position (coadds are not supported with PANIC). The total integration time for each field was 12 minutes in H and Ks-bands. The seeing during these observations was  $\sim 0.4''$ ; thus, these images detect fainter stars despite shorter integration times than to the ISPI observations. Separate offset sky observations were taken for the central field, the east and west fields were median combined to create the sky image. The data were reduced using the `UPSQUID` package in IRAF.

For all the above datasets, photometry of stars in the images was measured using the `DAOPHOT` package in IRAF. I used `DAOPHOT` to identify point-sources, create a model PSF from each combined image, and measure instrumental magnitudes using PSF photometry. The magnitude zeropoints were determined by matching the catalog from `DAOPHOT` to the 2MASS catalog and fitting a Gaussian to a histogram of zeropoint measurements. The H and Ks-band catalogs were then matched using a custom IDL program which iteratively finds corresponding star in each catalog and computes the  $H - Ks$  color. Only sources with detections at H and Ks-bands were included in the final catalog.

### 4.3 Results

In Figures 4.1 - 4.5, I display the 22 systems for which there was an envelope detected in extinction. The  $3.6\mu\text{m}$  image is shown in the left panels, the  $8.0\mu\text{m}$  image with optical depth contours (see Section 4.4) from  $8\mu\text{m}$  data in the middle panel, the  $8.0\mu\text{m}$  image with SCUBA  $850\mu\text{m}$  contours overlaid in the right panel. In the case of HH108, (Figure 4.1) there were no IRAC data, so I plot the Ks-band image, MIPS  $24\mu\text{m}$  image and optical depth contours and the Ks-band image with SCUBA  $850\mu\text{m}$  contours overlaid. The  $3.6\mu\text{m}$ /Ks-band image for each source shows the scattered light cavity and, for some of the data with very deep integrations, the envelopes are outlined by diffuse scattered light. The  $8.0\mu\text{m}$  images and optical depth contours show the envelope structure in extinction, and the overlaid SCUBA data from Di Francesco et al. (2008) show how the thermal envelope emission correlates with the  $8.0\mu\text{m}$  extinction.

The most striking feature of the  $8\mu\text{m}$  extinction maps is the irregularity of envelopes in the sample. Most envelopes show high degrees of non-axisymmetry; in most cases, spheroids would not provide an adequate representation of the structure. Some of the most extreme examples have most extinguishing material mostly on one side of the protostar (e.g. CB230, HH270 VLA1) or the densest structures are curved near the protostar (e.g. BHR71, L723). The structures seen in extinction at  $8\mu\text{m}$  do not seem to be greatly influenced by the outflow. The  $3.6\mu\text{m}$  images show that the outflow cavities of these sources are generally quite narrow, with a relatively small evacuated region; the dense material detected in extinction is often far from the outflow cavities and thus seems unlikely to be produced by outflow effects (see Section 4.6.1 for further discussion).

For convenience, I categorize the systems into 5 groups according to their morphology, though some systems have characteristics of multiple groups. Figure 4.1 shows the envelopes that have a highly filamentary or flattened morphology; Figure 2 shows envelopes that have most material (in projection) on one side of the protostar; Figure 4.3 shows the protostars whose envelopes are more or less spheroidal in pro-

jection; Figure 4.4 shows the protostars which appear to be binary (i.e., one protostar is present and about 0.1 pc away there is an extinction peak probably corresponding to a starless core). Lastly, Figure 4.5 shows envelopes that do not strictly fall within the above categories, and are simply classified as irregular.

This dense complex structure is less apparent in the SCUBA maps primarily because it has a resolution of  $\sim 12''$  at  $850\mu\text{m}$  while IRAC has a diffraction limited resolution of  $\sim 2''$ . SCUBA also has limited sensitivity to extended structure due to the observation method; thus IRAC can better detect non-axisymmetries on smaller and larger scales than seen in SCUBA maps. In addition, the strongest emission from most envelopes appears to be axisymmetric because the protostar is warming the envelope (Chiang et al., 2008, 2010); the extinction maps are not affected by the envelope temperature distribution.

## 4.4 Optical Depth Maps

Though the morphology of extinguishing material is clear from direct inspection of the images, it is desirable to convert the  $8\mu\text{m}$  intensities to optical depth maps to make quantitative measurements. I initially assumed that the observed intensities can be interpreted as pure extinction with no source emission, i.e.

$$\frac{I_{obs}}{I_{bg}} = e^{-\tau} \quad (4.1)$$

where  $I_{obs}$  is the observed intensity per pixel and  $I_{bg}$  is the measured background intensity, both corrected for the estimated zodiacal light intensity as discussed in Section 4.2.1. However, the attempts to model the filamentary structure in L1157 (Section 4.5.2) and the very low column densities measured led me to conclude that the maps contain more foreground emission and/or zero-point correction than I originally thought. This may not be surprising, as measurements of the zodiacal light intensity during the *Spitzer* First Look Survey were 36% higher than predicted by the model (Meadows et al., 2004). Either there is residual zodiacal light not accounted for by the model, or there is foreground dust emission, scattered light within the detector

material (Reach et al., 2005), or some combination of these factors. Unfortunately, because IRAC operates without a shutter, it is impossible to determine the true level of diffuse emission.

Thus, in the initial analysis I was calculating

$$\frac{I_{obs} + I_{fg}}{I_{bg} + I_{fg}} = e^{-\tau} \quad (4.2)$$

which will yield an erroneously low value of  $\tau$ . This is because as  $I_{fg}$  increases, the ratio of  $I_{obs} + I_{fg}/I_{bg} + I_{fg}$  will increase toward 1, causing the measured optical depth to decrease.

I therefore obtained the ground-based near-infrared imaging data to develop an independent estimate of the extinction in lower-column density areas, and thus made a better estimate of the foreground contribution. The Ks-band images of BHR71 and L483 with optical depth contours overlaid in Figure 4.6 show that many background stars can be detected through to dense envelope. The details of the foreground correction are discussed in the Appendix.

With the estimated foreground contribution was subtracted, I was able to calculate a more accurate optical depth map following Equation 4.1. I now must calculate the background emission in the image; fortunately in most images the background is relatively uniform. I estimated the background emission by fitting a Gaussian to a pixel histogram constructed from an area in the image not affected by the extinction of the envelope. For the sources IRAS 05295+1247, HH211, and L1165, the background has clear gradients. To account for this, I constructed a background model by performing a two-pass median filter of the entire image with a convolving beam 90'' (IRAS 05295+1247) and 144'' (L1165, HH211) in size; this method is similar to that of Simon et al. (2006); Ragan et al. (2009); Butler & Tan (2009). I used the first pass to identify stars in the background measurement field, then rejected those pixels in the second pass. The median background computed from the first and second passes are generally within a few percent of each other. The large convolving beam ensures that the envelope is filtered out from the background model.

I then divided each pixel by the background value, or, in the case of IRAS 05295+1247/L1165, divided the intensity map by the background model. Then taking the natural logarithm of each pixel intensity yielded the optical depth map. In the case of HH108, I constructed an optical depth map from the MIPS  $24\mu\text{m}$  image because there are no IRAC data for this object.

I give the values of  $I_{fg}$ ,  $I'_{bg}$  (see Appendix),  $\tau_{max}$ , and  $\sigma\tau$  for each source in Table 4.2. In all cases,  $I_{fg}$  is comparable to measured intensity at the darkest spot in the uncorrected  $8\mu\text{m}$  image. Thus, I can infer that the darkest part of an envelope is completely opaque. To set an upper limit on the optical depth in these areas, I use the pixel value in the uncertainty image as  $I_{obs}$  and compute the optical depth; this is the maximum optical depth ( $\tau_{max}$ ) in an image. To correct the images without near-IR data, I use the result that in the most opaque areas of the images  $I_{fg}$  is the observed intensity and take this value as an estimate of the foreground contribution.

## 4.5 Quantitative Results

### 4.5.1 Non-Axisymmetric Structure

To quantify the evident envelope asymmetry of many sources, I calculate projected moment of inertia ratios using  $\tau$  as a surrogate for mass. I calculate the ratios by computing

$$\frac{I_{\perp}}{I_{\parallel}} = \frac{\sum_i \tau_i (x_i - x_o)^2}{\sum_j \tau_j (y_j - y_o)^2} \quad (4.3)$$

where  $x_o$  and  $y_o$  are the coordinates of the protostar and  $I_{\perp}$  is the moment of inertia of material distributed perpendicular to the outflow along the abscissa and  $I_{\parallel}$  is for material located parallel to the outflow axis along the ordinate axis. The subscripts  $i$  and  $j$  denote the independent points where the optical depth is measured. I rotate the optical depth images such that the outflow is along the ordinate axis of the image to simplify interpretation. I also calculate the moment of inertia ratios for  $I_{\perp}$  left and right of the protostar ( $I_{\perp,l}/I_{\perp,r}$ ) and the same for  $I_{\parallel}$  ( $I_{\parallel,l}/I_{\parallel,r}$ ). I measure the ratios out to a radius of 0.05 pc for most protostars at the adopted distance in Table 4.1 and I set an inner radius of 0.01 pc. The outer radius is restricted so the moments

of inertia are sensitive to the densest structures closest to the protostar and not influenced by extended diffuse material. Also, areas where emission is present are masked by requiring that the optical depths be positive.

Each ratio quantifies a different aspect of the distribution of material around the protostar.  $I_{\perp}/I_{\parallel}$  describes how much material is located along the outflow axis versus perpendicular to it, a ratio greater than 1 would correspond to more material away from the protostar, perpendicular to the outflow. A ratio less than 1 corresponds to having more material close to the outflow axis, extended in the direction of the outflow.  $I_{\perp,l}/I_{\perp,r}$  describes the asymmetry about the outflow axis by comparing the measurements on the right and left sides of the protostar and  $I_{\parallel,l}/I_{\parallel,r}$  describes the asymmetry about the outflow but in the vertical direction. Taken together these ratios describe the distribution of material around the protostar, convenient for comparison to theoretical models.

The projected moment of inertia ratios for the envelopes are given in Table 4.3. There are more envelopes that are extended perpendicular to the outflow than along it (most  $I_{\perp}/I_{\parallel}$  ratios are  $> 1$ ). Many objects exhibit large ratios and they can be described as highly flattened/elongated. HH270 VLA1 and L1152 seem to be the only examples of envelopes strongly extended in the direction of their outflows in the sample. However, both L673-SMM2 and Serp-MMS3 have components of their envelopes oriented parallel and perpendicular to their outflows. This yields a  $I_{\perp}/I_{\parallel}$  ratio  $\sim 1$  but in the other ratios, non-axisymmetry is evident.

The most symmetric envelope is IRAS 16253-2429, as shown by its moment of inertia ratios all being near 1. The two most non-axisymmetric envelopes appear to be HH270 VLA1 and CB230. HH270 VLA1 has most of its material located southwest of the protostar and CB230 has most of its material located to the west and in a moderately-flattened configuration.

#### 4.5.2 Flattened Structure

There are six sources that have remarkably flat structure compared to the rest of the sample, shown in Figure 4.1: L1157, L723, HH108, Serp-MMS3, L673-SMM2, and

BHR71. With respect their molecular outflows, L1157 and BHR71 are viewed nearly edge-on; the primary protostar in HH108 seems to be edge-on as well. Serp-MMS3 and L673-SMM2 are not well studied; however,  $3.6\mu\text{m}$  image of Serp-MMS3 indicates that it is at least inclined by  $60^\circ$  or more and L673-SMM2 harbors several protostars and their inclinations are not known. The orientation of L723 is uncertain as there are two embedded sources driving outflows and due to the complexity of the data I omit this object from the analysis.

For these sources, I ask the question: are these envelopes flattened sheets/pseudo-disks (Hartmann et al., 1994, 1996; Galli & Shu, 1993) or filaments? To attempt to answer this question, I compare the observed vertical structure of the flattened envelopes to analytic prescriptions for isothermal hydrostatic filaments and sheets.

The scale height of an isothermal filament in hydrostatic equilibrium is

$$H_f = \frac{c_s^2}{2G\Sigma_{0,f}} \quad (4.4)$$

where  $c_s$  is the isothermal sound speed, I assumed  $T=10\text{K}$ , and  $\Sigma_{0,f}$  is the peak surface density measured at the center of the filament (Hartmann, 2009). When parametrized in terms of  $8\mu\text{m}$  optical depth and assuming  $\kappa_8 = 10.96 \text{ cm}^2\text{g}^{-1}$ ,

$$H_f = \left(\frac{0.96}{\tau_{0,f}}\right) \left(\frac{T}{10\text{K}}\right)^{-1} \times 0.01\text{pc}. \quad (4.5)$$

Thus, a 10 K filament with a scale height of 0.01 pc will have  $\tau \sim 1$  at  $8\mu\text{m}$ .

Similarly, the scale height of an isothermal infinite sheet is given by

$$H_s = \frac{c_s^2}{\pi G\Sigma_{0,s}}. \quad (4.6)$$

In this case,  $\Sigma_{0,s}$  is *not* the surface density measured at the center of the sheet viewed edge-on but it is the surface density through the  $z$ -direction of the sheet. Thus, I must make an assumption about depth of the sheet into the line of sight. Making the same assumption about temperature as the filament case, I can write the scale

height of a sheet as

$$H_s \sim \frac{1.2}{\tau_{0,f}} \left( \frac{d}{t} \right) (0.01pc) \quad (4.7)$$

where  $d$  is the line-of-sight depth through the sheet and  $t$  is the thickness of the sheet in the plane of the sky. Together,  $d$  and  $t$  specify the aspect ratio of the sheet;  $d$  is assumed to be 0.1 pc (the diameter of most envelopes in the sample) and  $t$  is taken to be the FWHM of the Gaussian fit to the vertical structure described in the next paragraph. For an aspect ratio of 10, the peak optical depth would have to be  $\sim 12$  in order to have a scale height of 0.01 pc.

I analyzed the structure by averaging the extinction map along the extended dimension in three pixel bins, and then fitting a Gaussian to the perpendicular structure in each bin. The peak of the Gaussian fit is taken to be the central optical depth. Then, in Figure 4.7 I compare the observed vertical structure to the expected vertical structure for a filament and sheet as a function of distance from the protostar, converting from the Gaussian  $\sigma$  parameter to  $H$  (for instance, I find that  $\sigma \sim 1.5H$  for a filament).

For the case of L1157, the 10 K hydrostatic filament appears to be in reasonable agreement with the observed extinction, while the sheet scale height is about a factor of 3 more than observed. If the  $8\mu\text{m}$  extinction was not corrected for foreground emission, the predicted filament scale heights were a factor of 5 too large. As it is hard to imagine anything thinner than a pressure supported filament, this result is further verification of the need for correcting the  $8\mu\text{m}$  extinctions for foreground emission.

The envelope around Serp-MMS3 is also fit well by a filament over  $\sim 0.1\text{pc}$ . I only fit the northeast part of the filament for this source because the data of the southwest portion of the envelope is quite complicated. In L673-SMM2, I attempted to fit both the north and south portions of the filament, avoiding the region near the protostars. The filament model does not fit as well as L1157 or Serp-MMS3; the observed scale heights are always less than those predicted for a filament. I suspect that this discrepancy is due to the densest part of the filament being unresolved,

underestimating the peak column density.

Neither sheet nor filament models yielded good fits to BHR71 which has a more complicated envelope structure than L1157 and a larger optically thick region. The predicted scale height for a filament tends to be about 2.5 times smaller than observed; thus a sheet seems to be more consistent with the observed data. Alternatively, the dense structure may not be in hydrostatic equilibrium.

### 4.5.3 Mass Estimates

With the optical depth maps at  $8.0 \mu\text{m}$ , I have the opportunity to estimate envelope masses independently of the temperature and chemical effects. The results do depend on the assumed opacity, but recent extinction law studies using *Spitzer* have yielded better constraints on the opacity at  $8\mu\text{m}$ . However, the column density cannot be traced in regions where the envelope is optically-thick.

To derive a column density from the optical depths, I assume the dust plus gas opacity  $\kappa_{8\mu\text{m}} = 10.96 \text{ cm}^2 \text{ g}^{-1}$  (Butler & Tan, 2009) which corresponds to the Weingartner & Draine (2001)  $R_V = 5.5$  Case B dust model which found to agree reasonably well with the extinction laws derived at IRAC wavelengths (Román-Zúñiga et al., 2007; McClure, 2009). This opacity is calculated by convolving the IRAC filter response with the expected background spectrum shape, and opacity curve.

To calculate the mass of a particular envelope, I simply sum all the pixels with  $\tau$  greater than  $\sigma\tau$  within 0.15, 0.1, and 0.05 pc radii around the envelope and assume the relation

$$M_{env} = d\Omega \times D^2 \times (1.496 \times 10^{13} \frac{cm}{AU})^2 \times \sum_i^N \frac{\tau_i}{\kappa} \quad (4.8)$$

where  $d\Omega$  is the pixel solid angle,  $(1.2'')^2$ , and  $D$  is the distance in parsecs.

The masses determined using this method are probably lower limits at best because most envelopes become completely opaque in the densest areas. Moreover, the uncertainty in optical depth increases as optical depth increases. The maps are also probably not sensitive to some mass on large scales due to signal-to-noise limitations and on small scales emission is present which prevents measurement of optical depth.

The measured envelope masses are given in Table 4.2 along with the measure-

ments from ammonia and submillimeter studies. The 0.05 pc radius is probably most comparable to the mass measurements from the other methods. This is because most ammonia cores are generally about 0.1-0.15 pc in diameter and submillimeter fluxes are generally measured in apertures with diameters of 80-120'' which correspond 0.1 - 0.15 pc in diameter for an assumed distance of 300 pc. The masses measured are comparable with the other methods at smaller radii.

A trend is seen in that some protostars are surrounded by significant mass at large and small radii. All the protostars in the sample are have nearly  $1 M_{\odot}$  of material within 0.05 pc; there is possibly even more mass within 0.05 pc since the regions where the protostar is emitting are not probed and the material could be optically thick. Even the very low-luminosity protostars (e.g. IRAM 04191, L1521F, Perseus 5) are surrounded by many solar masses of material. For reference, the bolometric luminosities are listed for the observed sources in Table 4.2, there is no obvious correlation between luminosity and envelope mass.

## 4.6 Discussion

The observations of dense, non-axisymmetric structures in Class 0 envelopes have significant implications for our understanding of the star formation process. The dense structures that I observe either result from the initial conditions of their formation or they have been induced on an otherwise axisymmetric envelope during the collapse process. I will discuss why these dense structures are not likely induced by outflows, the most obvious perturber, and then discuss how non-axisymmetric infall could affect subsequent evolution of the system. I also discuss how the envelope structures may give clues to the initial conditions of their formation and what relationship the larger scale cloud structure around the protostar may have on its formation.

### 4.6.1 Outflow-induced structure

Outflows carve cavities in protostellar envelopes and necessarily affect the structure of the protostellar environment at some level. However, it is highly unlikely that outflows are responsible for much of the complex envelope morphology I observe.

While a few objects such as L1527 exhibit relatively wide molecular outflows and outflow cavities (e.g., Jørgensen et al. (2007)), most of the outflow cavities (as seen most clearly in scattered light at  $3.6\mu\text{m}$ , but also detectable in the  $8.0\mu\text{m}$  images) are relatively narrow and well-collimated, in agreement with molecular observations (e.g. Arce & Sargent, 2006; Jørgensen et al., 2007); this makes it difficult to imagine that the outflow is strongly affecting most of the envelope. Moreover, if the observed dense, asymmetric envelope structures were the result of outflow sculpting, one would expect close spatial association of these structures with the outflow cavities; in contrast, the cavities in most objects are spatially distinct from the dense structures, sometimes by quite large distances, and with no systematic alignment perpendicular to the cavities.

HH270 and IRAS 16253 are exceptions to this general rule, with strong concentrations of extinction along cavity walls; however, both these systems are strongly asymmetric perpendicular to the outflow cavities, which indicates that the density structures are mostly the result of existing inhomogeneities in the ambient medium. Similarly, it has been suggested that the outflow in L483 is strongly affecting molecular material based on observations of  $\text{N}_2\text{H}^+$  emission (Jørgensen, 2004); however, the strong density enhancement on one pole of the outflow relative to the other is difficult to understand as purely a result of mass loss, given the general bipolar symmetry of most systems.

To summarize, the outflows do not appear to have significantly affected the current envelope morphologies in most cases. The spatial separation of the outflow cavities and the dense, extinguishing structures make it less likely that outflows can significantly limit mass accretion onto the central protostar. The common inference that bipolar flows widen with age, dispersing the envelope (e.g. Arce & Sargent, 2006; Seale & Looney, 2008) may result more directly from collapse of dense structures rather than a changing of the outflow angular distribution.

#### **4.6.2 Dense Non-axisymmetric Structure**

The shapes of dense cores have been studied on large scales ( $>0.1\text{ pc}$ ) using optical extinction (Ryden, 1996) and molecular line tracers of dense gas (Benson & Myers,

1989; Myers et al., 1991; Caselli et al., 2002). However, optical extinction only traces the surface of dense clouds and most envelopes appear round in the dense molecular tracers because they are generally only spanned by 2.5 beams or less. The low-resolution molecular line studies are slightly more advantageous compared to the optical since they only detect dense material and associated IRAS sources are often located off-center from the line emission peaks indicating non-axisymmetry.

The advantage of  $8\mu\text{m}$  extinction in studying envelopes compared to other methods is that it provides high resolution, undiminished sensitivity to dense extended structures, and its a tracer that depends only on density. This enables me to trace non-axisymmetric structure from large scales down to 1000 AU scales. Figure 5.6 exemplifies the details revealed by  $8\mu\text{m}$  extinction maps; the  $8\mu\text{m}$  extinction contours of CB230 are overlaid on the optical Digitized Sky Survey image showing the strong asymmetry of dense material while the optical image shows no hint of what is going on at small scales. The necessity of  $8\mu\text{m}$  extinction to see small scale non-axisymmetric structure holds true for all the sources. The magnitude non-axisymmetry varies significantly between sources; but the important point is that all sources exhibit non-axisymmetry and that sources with “regular” morphology are the exception rather than the rule.

CB230 and the other one-sided envelopes shown in Figure 4.2 are particularly intriguing. While the outflows may have done some sculpting, the dynamics of the star formation process itself has caused the strong asymmetries perpendicular to the outflow. The curvature of dense structures in BHR71 and L723 as well as the outflow being oriented non-orthogonal to many dense filamentary structures (e.g., L673, HH108, SerpMMS3, L1448 IRS2) may indicate that the angular momentum of a collapsing system may not have a strongly preferred direction set by the large scale cloud structure.

It is important to point out that these non-axisymmetric structures exist down to small scales quite near the protostar and only at about  $\sim 1000$  AU they become obscured by emission from the protostar  $8\mu\text{m}$ . As shown in Table 4.2, all the envelopes have a nearly  $1 M_{\odot}$  or more mass within 0.05 pc. Material at  $\sim 1000$  AU potentially

has an infall timescale of  $\sim 5 \times 10^4$  yr and at 10000 AU the infall timescale is  $\sim 5 \times 10^5$  yr assuming a  $0.96 M_{\odot}$  initial core at the start of collapse (Section 4.3 (Shu, 1977)). This is consistent with Class 0 protostars having accumulated less than about half their final mass at the present epoch (Myers et al., 1998; Dunham et al., 2010).

### 4.6.3 Implications of Non-Axisymmetric Collapse

The envelope asymmetries may well result from the initial cloud structure. Stutz et al. (2009) recently surveyed pre-stellar/star-less cores using 8 and  $24\mu\text{m}$  extinction; their results, and those of Bacmann et al. (2000), showed that even pre-collapse cloud cores already exhibit some non-axisymmetry. Given the initial asymmetries the densest, small-scale regions are likely to become even more anisotropic during gravitational collapse (Lin et al., 1965). I note that gravity is not the only force at work in these clouds; turbulence and magnetic fields may also play roles in forming the envelope morphologies (Section 4.6.4).

The smallest scales I observe,  $\sim 1000$  AU, is where angular momentum will begin to be important as the material falls further in onto the disk. The envelope asymmetries down to small scales imply that infall to the disk will be uneven; therefore, non-axisymmetric infall may play a significant role in disk evolution and the formation of binary systems. Several theoretical investigations (e.g. Burkert & Bodenheimer, 1993; Boss, 1995) showed that collapse of a cloud with just a small azimuthal perturbation can form binary or multiple systems; thus, *large* non-axisymmetric perturbations should make fragmentation even easier. Fragmentation can even begin before global collapse in a filamentary structure (Bonnell & Bastien, 1993, and references therein). Numerical simulations of disks with infalling envelopes (e.g. Kratter et al., 2010; Walch et al., 2010) informed by the results of this study could reveal a more complete understanding of how non-axisymmetric infall affects the disk and infall process.

Several sources in the sample are known wide binaries (BHR71, CB230) (Bourke, 2001; Launhardt et al., 2001) and close binaries (L1527, L723, IRAS 03282+3035) (Loinard et al., 2002; Girart et al., 1997; Chen et al., 2007). The *Spitzer* observations indicate that SerpMMS3 may be a binary and that L673-SMM2 is likely a multiple.

Other sources in the sample may be close binaries but this property can only be revealed by sub-arcsecond imaging. Looney et al. (2000) showed that many protostars are indeed binary when viewed at high enough resolution at millimeter wavelengths. A recent study of Class 0 protostars at high resolution by Maury et al. (2010) noted that their results taken with Looney et al. (2000) show a lack of close binary systems with 150-550AU separations. This may signify that non-axisymmetric infall throughout the Class 0 phase is important for binary formation later when centrifugal radii extend out to 150-550AU.

#### **4.6.4 Turbulent formation**

The dense, non-axisymmetric structures around Class 0 protostars are not obviously consistent with quasi-static, slow evolution, which might be expected to produce simpler structures as irregularities have time to become damped. With rotation, one might get a flattened system during collapse, as is well known (Terebey et al., 1984), but one needs non-axisymmetric initial structure to get strong non-axisymmetric structure later on. This raises the question of the role of magnetic fields in controlling cloud dynamics. In some models (e.g. Fiedler & Mouschovias, 1992; Galli & Shu, 1993; Tassis & Mouschovias, 2007; Kunz & Mouschovias, 2009, and references therein), protostellar cores would probably live long enough to adjust to more regular configurations; in addition, collapse would be preferentially along the magnetic field, which would also provide the preferential direction of the rotation axis and therefore for the (presumably magnetocentrifugally accelerated) jets (Basu & Mouschovias, 1994; Shu et al., 1994). The complex structure and frequent misalignment between collapsed structures and outflows pose challenges for such a picture.

In contrast, more recent numerical simulations (e.g. Padoan et al., 2001; Klessen et al., 2000; Ballesteros-Paredes et al., 1999) suggest that cores are the result of turbulent fluctuations which naturally produce more complex structure with less control by magnetic fields amplified by subsequent gravitational contraction and collapse (e.g. Elmegreen, 2000; Klessen et al., 2000; Klessen & Burkert, 2000; Heitsch et al., 2001; Padoan & Nordlund, 2002; Hartmann, 2002; Bate et al., 2003; Mac Low & Klessen,

2004; Heitsch & Hartmann, 2008; Heitsch et al., 2008a,b, see review by Ballesteros-Paredes et al. 2007 (PPV)). Thus, the structure of protostellar envelopes provides an indication of which of the two contrasting pictures of core formation, with differing assumed timescales of formation and differing importance of magnetic fields, is more nearly correct.

The timescale argument against ambipolar diffusion can be mitigated since turbulence is known to accelerate ambipolar diffusion Fatuzzo & Adams (2002); Basu et al. (2009). The filamentary envelopes may also enhance ambipolar diffusion as necessary. For example, a cylinder with an aspect ratio of 4:1 (similar to L1157) will have a factor of  $\sim 10$  less volume than a sphere with a diameter equal to the cylinder length. If both have the same infall rate, the filament has a factor of  $\sim 10$  higher density than the sphere. Thus, using

$$\tau_{AD} \sim 5 \times 10^6 \left( \frac{10^4 \text{cm}^{-3}}{n(H_2)} \right)^{\frac{1}{2}} \text{yr} \quad (4.9)$$

given in Spitzer (1968), the ambipolar diffusion timescale,  $\tau_{AD}$ , is reduced by an order of magnitude! With a shorter ambipolar diffusion timescale, the magnetic support of the initial disk could be lower than the levels suggested in Galli et al. (2006), allowing for Keplerian rotation of the resulting circumstellar disk.

The timescale issue aside, it is still difficult to get non-axisymmetric structures from magnetic collapse. Simulations by Basu & Ciolek (2004); Ciolek & Basu (2006) indicated that magnetically sub-critical or critical cores will tend to be round or axisymmetric while the super-critical cores would show higher degrees of non-axisymmetry. The results are more consistent with fast, super-critical collapse. Further high resolution simulations, such as those by Offner & Krumholz (2009), would help make a better connection between theory and observation.

Alternatively, if a spherical core forms within a turbulent medium, as in Walch et al. (2010), the turbulence within the core itself could give rise to a non-axisymmetric structure. However, two difficulties of this scenario are immediately obvious; first, producing a spherical or even symmetric core in a turbulent environment seems diffi-

cult; and second, dense, star forming cores are found to be very quiescent compared to their external medium (Goodman et al., 1998; Pineda et al., 2010). Rather than the core itself being turbulent, anisotropies in the turbulent pressure surrounding a dense core could also give rise to non-axisymmetric structure from an initially symmetric core. One could also envision a scenario where an envelope is impacted by colliding flows causing non-axisymmetries.

#### 4.6.5 Relationship with Larger Structures

While some systems in the sample seem to be in relative isolation, most are part of large-scale filamentary structure. With the dataset presented, I can examine the spatial relationship of the protostars within their natal material to see if there are trends which influenced by the non-axisymmetries. Here I examine several of the protostars where one can clearly discern the morphology of larger scale material.

The L1165 dark cloud is comprised of a long filament running from southeast to northwest for  $\sim 8'$  (0.6pc) that turns northeast forming a roughly  $90^\circ$  angle and extends  $\sim 10'$  (0.75pc). An image of the L1165 region at  $8\mu\text{m}$  and a near-IR extinction map are shown in Figure 4.9. Both the protostar (IRS1) and another very bright source about  $1.5'$  north (IRS2) have formed near the ‘elbow’ of the filament. IRS2 is likely a young star because the spectral index from  $6\text{--}13\mu\text{m}$  is  $\sim -1$  indicating that it is a Class II object. IRS2 is detected at  $24\mu\text{m}$  (fainter than IRS1) but not at  $70\mu\text{m}$ . It is intriguing that these two young stars have formed at the ‘kink’ in the filament while there are no apparent protostars elsewhere in the filament. Two other examples of multiple stars forming at filament kinks are L673-SMM2 and Serp-MMS3.

The protostars HH108 IRS1 and HH108 IRS2, (IRAS and MMS respectively in Chini et al. (2001)) have also formed with a filament. HH108 IRS1 is more luminous and IRS2 only appears in emission longward of  $24\mu\text{m}$ . IRS2 appears as an opaque spot in the  $24\mu\text{m}$  extinction image in Figure 4.1. The envelope of IRS1 appears to be a collapsed portion of the larger filament and is located at a bend. On the other hand, the envelope of IRS2 appears round, but slightly extended along the filament.

The protostars CB230 and IRAS 03282+3035 are both located at the edges of dark

clouds. One can clearly see the edge of the envelope around IRAS 03282+3035 in diffuse scattered light at  $3.6\mu\text{m}$  corresponding to the edge of  $8\mu\text{m}$  extinction (Figure 4.3). CB230 is an isolated Bok globule, shown in Figure 4.8. The dark cloud in the optical extends to the west from the protostar  $\sim 11'$  (0.95 pc) with highest densities near the protostar at the extreme eastern edge of the cloud. The optical depth map shows the extreme asymmetric distribution of material. In addition, there is an optical star associated with a reflection nebula  $\sim 7.25'$  west of the protostar, but it is not detected by IRAS and not observed by *Spitzer*.

The L1448 dark cloud contains several embedded protostars visible at  $8\mu\text{m}$  (Tobin et al., 2007). The most isolated protostar is L1448 IRS2, the rest are surrounded by bright emission from outflow knots. IRS1 and IRS2 are located toward the western edge of the cloud IRS3A/B are located on the northeastern corner of the cloud and L1448-mm is located in the southeast corner. There is a filament of material running between IRS2 and IRS3 seen in diffuse scattered light (Figure 4.1 in Tobin et al. (2007)),  $8\mu\text{m}$  extinction, and ammonia emission (Anglada et al., 1989). Also, the filament abruptly cuts off  $\sim 40''$  north of IRS2.

Protostars highlighted seem to have a tendency to form at the edges of clouds or where there are turns or 'kinks' in a filamentary structure. This behavior is qualitatively what would be expected if gravitational focusing is important. Put simply, gravitational focusing causes the edges of clouds and where there are discontinuities (bends and kinks) to form stars first by creating gravity focal points. In a filament undergoing global collapse, the ends of that filament will be moving inward the fastest and will encounter slower moving material. This 'gravitational traffic jam' creates the gravity focal point. In addition, the filament will also be collapsing in the vertical direction which causes material to flow toward the focal point in from orthogonal directions rather than just the transverse direction. A scenario such as this would cause the ends of the filament to form stars rather than at the center of the filament. Quantitatively, this scenario appears when you modify the spherical (3D) free-fall timescale for a (1D) filamentary geometry. Gravitational focusing is seen in theoretical work by (Burkert & Hartmann, 2004) which simulated a complex

object with many thermal Jeans masses. The gravitational focusing causes non-linear collapse near cloud boundaries and other discontinuities (see also Bonnell & Bastien 1993). The results are consistent with a picture in which turbulent fragmentation provides “seeds” which then are amplified by gravity (Heitsch et al., 2008b; Heitsch & Hartmann, 2008).

I note, however, that BHR71 and L483 seem to have formed at the centers of centrally condensed Bok globules, so complete universality for this mechanism cannot be claimed. However, the filamentary regions highlighted in the above paragraphs may be representative of star forming environments because the theoretical work shows that turbulent star formation generally gives rise to filaments (e.g. Heitsch et al., 2008b; Heitsch & Hartmann, 2008). Also, the preference of forming stars in clumps at the ends of filaments also appears to apply to young star clusters and loose star-forming associations (e.g. Orion Nebula Cluster, NGC2264, Chameleon, Taurus) (Fűrész et al., 2006, 2008; Tobin et al., 2009; Luhman, 2008; Hartmann, 2002). Thus, gravitational focusing may be at work from the formation of clusters to the formation of individual protostars. Further theoretical work building on that of Burkert & Hartmann (2004) including effects of turbulence and/or magnetic fields would enable a better understanding of this idea and determine how much gravity must dominate over other forces present in the cloud.

## 4.7 Conclusions

In this chapter, I have shown the complex structure of envelopes surrounding Class 0 protostars as viewed in extinction at  $8\mu\text{m}$  using *Spitzer* IRAC images. The non-axisymmetries revealed by the IRAC extinction maps were not obvious in submillimeter maps by SCUBA. The  $8\mu\text{m}$  images were found to be significantly contaminated by foreground emission and I corrected for this using near-IR extinction measurements toward background stars. This method demonstrated that the densest parts of the envelopes observe are completely opaque at the observed signal-to-noise levels. I have characterized the non-axisymmetry of the envelopes in terms of projected moments of inertia ratios. Most envelopes are more extended perpendicular to the outflow, but

there are exceptions. The measurements also yield estimates of the mass surrounding the protostars at small and large scales.

Most envelopes show highly non-axisymmetric structure from  $\sim 1000$  AU to 0.1 pc scales. These asymmetric structures are *not* caused by outflow-envelope interactions as the outflows are still highly collimated and spatially located away from asymmetric structures and envelopes tend to be more extended perpendicular to the outflow. I suggest that the widening of outflows with age may result more directly from collapse of dense structures rather than a changing of the outflow angular distribution. In the entire sample, I find significant mass present in the envelopes on scales less than 0.05 pc. This supports the idea that Class 0 protostars are in the main phase of mass accretion and the asymmetries of the material down to small scales indicates that material will likely fall onto the disk unevenly possibly enhancing gravitational fragmentation. This could help explain the formation of close binary or multiple systems.

The highly non-axisymmetric envelopes may result directly from the collapse of mildly asymmetric cores found by Bacmann et al. (2000); Stutz et al. (2009) because fast collapse will enhance anisotropies (Lin et al., 1965); turbulence and colliding flows could also play a role in creating asymmetries. The observed structure points to non-axisymmetric and probably non-equilibrium initial conditions. If the magnetic field plays a major role in the collapse process of these envelopes, it is clearly not working to make the infall process more symmetric. Comparison to simulations indicates that super-critical collapse is more consistent with the observations.

Finally, there seems to be a preference of where stars form within larger scale structures. Several systems form protostars at the ends of filaments and at bends or kinks in the more-extended molecular gas, which suggests that the initial shape of a cloud has much to do with where stars form. This is reminiscent of the preference for stars to form in clusters double clusters as seen in local star forming regions such as Orion, NGC2264, and Chameleon.

## 4.8 Appendix

As discussed in Section 4.4, it was necessary to correct the data for foreground emission. Some analyses have used submillimeter emission maps to correct for foreground emission (Johnstone et al., 2003) and Ragan et al. (2009). These analyses assume that the absorbing material has become optically thick at the points where submillimeter emission is increasing but the IRAC  $8\mu\text{m}$  intensity reaches its minimum and the  $8\mu\text{m}$  intensity at that position is taken to be the foreground emission. However, I cannot apply this method to the envelopes in the study because the protostar warms its envelope making the submillimeter emission dependent on both temperature and density.

Instead, I compared the near-IR extinction of background stars (viewed through the envelopes) to the  $8\mu\text{m}$  extinction enabling the determination of the foreground emission. The main difficulty in applying this method is that the envelope must be viewed against a rich stellar background to enable an accurate determination of  $I_{fg}$ . In addition, the near-IR image must be deep enough to measure accurate photometry in at least H and Ks bands; data from the 2MASS survey are too shallow. To the best of my knowledge, this is the first time this method has been employed to constrain the amount of diffuse foreground emission in the construction of extinction maps from extended emission.

I start by assuming that the foreground emission can be taken as a constant offset to the true background by

$$I'_{obs,bg} = I_{obs,bg} + I_{fg} \quad (4.10)$$

where  $I'_{obs,bg}$  is the background intensity or observed intensity in an extinguished region which has some constant  $I_{fg}$  present due to the possible effects listed in the previous paragraph. The presence of foreground emission changes the the optical depth relationship of Equation (4.1) to be

$$\frac{I'_{obs}}{I'_{bg}} = \frac{I_{obs} + I_{fg}}{I_{bg} + I_{fg}} = e^{-\tau'_s} \quad (4.11)$$

where  $\tau'_8$  is the measured optical depth from the IRAC images that are not corrected for foreground emission. As  $I_{fg}$  increases, the ratio of  $I'_{obs}/I'_{bg}$  increases, causing the measured optical depth to decrease.

The NICE method (Lada et al., 1994) enabled me to measure the extinction toward stars by assuming the background stars can be described by a single, average color. The extinction is determined from

$$A_H - A_{Ks} = [(H - Ks)_{obs} - \langle H - Ks \rangle_{off}] = A_{Ks} \left( \frac{A_H}{A_{Ks}} - 1 \right) \quad (4.12)$$

where  $(H - Ks)_{obs}$  is the color of an individual star, while  $\langle H - Ks \rangle_{off}$  is the mean color of the background stellar population.  $A_H/A_{Ks}$  is known from near-IR extinction law measurements to be  $\sim 1.56$  (e.g. Indebetouw et al., 2005b; Rieke & Lebofsky, 1985). This value can vary between 1.5-1.6 for the different possible power-law dependencies of the near-IR extinction law which assumes  $A_\lambda \propto \lambda^{-\beta}$  and  $\beta$  is known from observation and dust models to be between 1.6 and 1.8 (e.g. Weingartner & Draine, 2001). The value I assume from Rieke & Lebofsky (1985) has  $\beta = 1.71$ . The result is

$$A_{Ks} = 1.77 \times [(H - Ks)_{obs} - \langle H - Ks \rangle_{off}]. \quad (4.13)$$

I determined  $\langle H - Ks \rangle_{off}$  by using the 2MASS catalog to calculate the  $(H - Ks)$  color of stars near the protostar but estimated to be relatively free of extinction, as judged from visual inspection of the the optical DSS images. Then I create a histogram of  $(H - Ks)$  colors and fit a Gaussian to the distribution. The mean is then taken to be the value for  $\langle H - Ks \rangle_{off}$ ; this value is generally  $\sim 0.2$ . Then for each star I have a measure of extinction at Ks-band,  $A_{Ks}$ . The value of  $A_{Ks}$  is uncertain for an individual star; therefore I compare  $A_{Ks}$  to  $A_{8\mu m}$  at many points throughout the envelope. The appropriate extinction laws (Flaherty et al., 2007; Román-Zúñiga et al., 2007; McClure, 2009) indicate that  $A_{8\mu m} = 0.5 \times A_{Ks}$  for most star forming regions. I can then extrapolate the optical depth at  $8\mu m$  from near-IR extinction ( $\tau_{8,Ks}$ ) to be

$$\tau_{8,Ks} = (1.068)(0.5) \times A_{Ks} \quad (4.14)$$

where  $A_{K_s}$  is determined from the near-IR extinction measurement. Figure 4.10 shows the uncorrected relationship between  $A_{K_s}$  to  $A_{8\mu m}$  for BHR71 and L483. The deviation of the predicted relationship from the observations clearly illustrates the necessity of applying this method to the sample to determine the level of foreground contamination.

Figure 4.10 clearly indicates that the initial optical depth measurements from Equation (4.11) needed to be corrected for extra emission. The near-IR extinction analysis yields the true optical depth from

$$\frac{I_{obs}}{I_{bg}} = e^{-\tau_{8,K_s}} \quad (4.15)$$

which is equivalent to

$$\frac{I'_{obs} - I_{fg}}{I'_{bg} - I_{fg}} = e^{-\tau_{8,K_s}}. \quad (4.16)$$

Solving for  $I_{fg}$  and some algebraic manipulation give

$$I_{fg} = \frac{I'_{bg}(e^{-\tau'_8} - e^{-\tau_{8,K_s}})}{1 - e^{-\tau_{8,K_s}}}. \quad (4.17)$$

This relationship assumes that  $I_{fg}$  is nearly constant across the envelope, which is a reasonable assumption for the possible sources of foreground given the relatively small angular size of the envelopes.

I have already described how  $I'_{bg}$  is measured in the previous section. However,  $\tau'_8$  from Equations 4.11 and 4.17 requires some special consideration.

Since the near-IR extinction toward these points is determined using stars, there may be point sources detected at the same position in the  $8\mu m$  image which will have a negative value in the optical depth map. This is particularly clear in Figure 4.6 where some background stars are surrounded by a “hole” in the optical depth map. To ensure that the measurements of  $\tau'_8$  from the  $8\mu m$  extinction map are mostly unaffected by stars, I measure the average optical depth in an annulus from 4 to 7 pixels around the star at each position. This does introduce some error if a star is very bright at  $8\mu m$ , seen in Figure 4.11 as points with high  $A_{K_s}$  but low  $A_{8\mu m}$ , but

for most points in the envelope this method works well. Additional points with high  $A_{Ks}$  and low  $A_{8\mu m}$  are likely due to the presence of diffuse emission at  $8\mu m$  from scattered light in the outflow cavity, outflow knots, and/or a star(s) falling within the measurement annulus. As a test, I compared the average  $A_{Ks}$  in a  $15''$  box to the median  $8\mu m$  extinction in the same box and the points with high  $A_{Ks}$  and low  $A_{8\mu m}$  were not present.

I determine  $I_{fg}$  by calculating Equation (4.17) at the position of each near-IR extinction measurement where  $A_{Ks} > 1$  and  $A_{8\mu m}$  is greater than the 1 sigma noise in the uncorrected optical depth map. Then I take the median value of  $I_{fg}$  and subtract it from the  $8\mu m$  image and recalculate the optical depth map. Then I run the comparison again on the corrected image and  $I_{fg}$  should be close to zero; graphically I check to see if the datapoints agree with the predicted relationship, usually  $I_{fg}$  will only need to be adjusted slightly from the initial value. I note that the regions of highest  $\tau'_8/A_{Ks}$  yield the best value of  $I_{fg}$  because the percentage error for these points is the least; there can be significant scatter at low  $\tau'_8/A_{Ks}$ . As shown in Figure 4.11, the correction to the optical depth measurements results in reasonable estimates of the foreground contribution. As highlighted in Section 4.4 this method lead to the simplifying conclusion that in all images the darkest part of the envelope is completely opaque within uncertainty limits of the images. This finding enables me to also correct the data which lack near-IR measurements or are not observed against a rich stellar field.

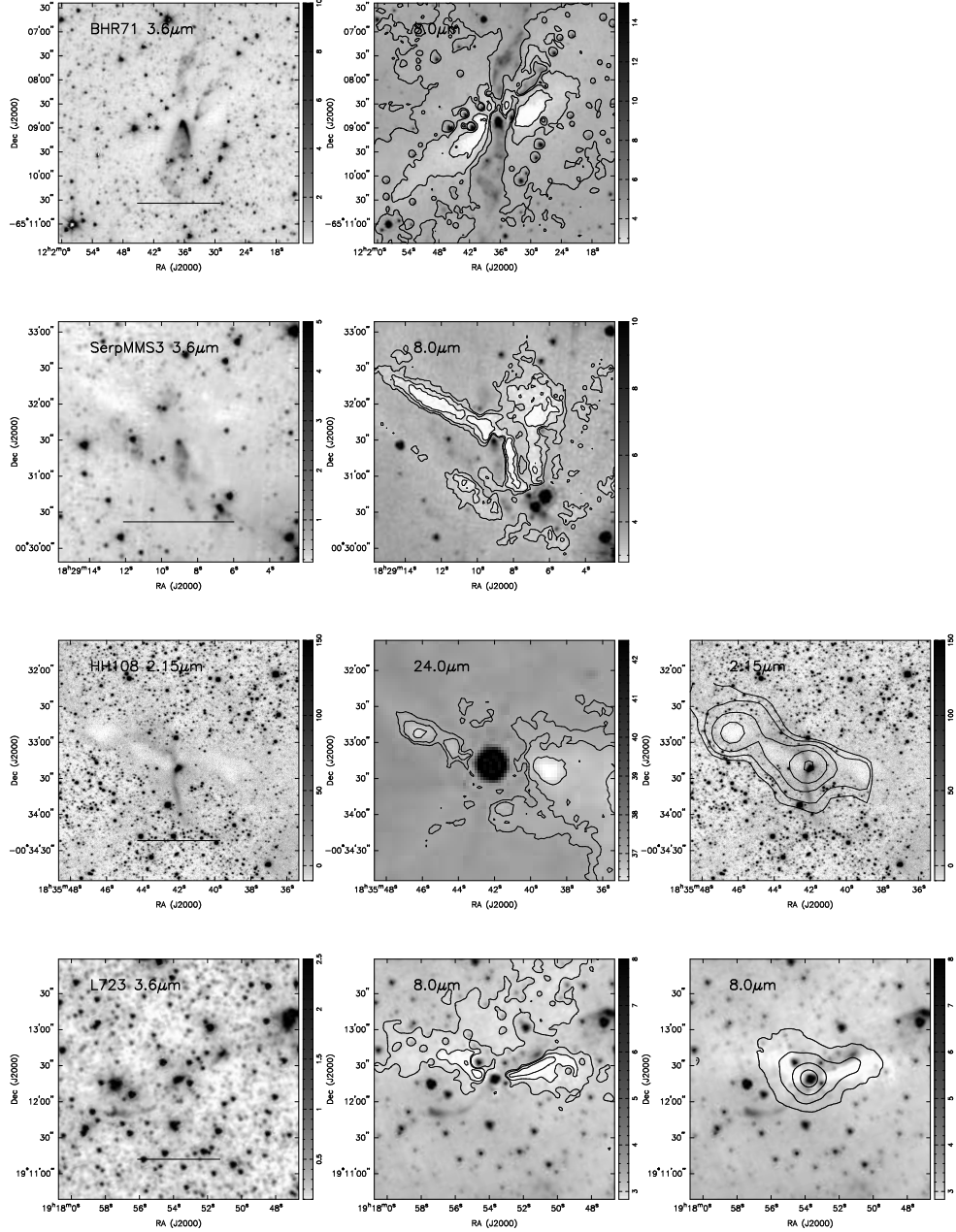


Figure 4.1 IRAC images of the sample of envelopes with flattened morphology. Left: IRAC  $3.6 \mu\text{m}$  or Ks-band images which highlight the scattered light cavities in these objects. Middle: IRAC  $8.0 \mu\text{m}$  images with the  $8.0 \mu\text{m}$  optical depth contours overlaid. Right: IRAC  $8.0 \mu\text{m}$  images with SCUBA  $850 \mu\text{m}$  contours. The line drawn in the left panel corresponds to  $0.1 \text{ pc}$  at the adopted distance. For HH108, I show the Ks-band image (left),  $24\mu\text{m}$  image with  $24\mu\text{m}$  optical depth contours (middle) highlighting structure, and SCUBA  $850\mu\text{m}$  data overlaid on the Ks-band image (right). The  $8.0 \mu\text{m}$  optical depth contours correspond to  $\tau_{8\mu\text{m}}$  values for BHR71: 0.6, 1.28, 2.75; L723: 0.2, 0.3, 0.45; L673: 0.3, 0.6, 1.2; SerpMMS3: 0.75 1.06 1.5; L1157: 0.5, 1.09, 2.4.

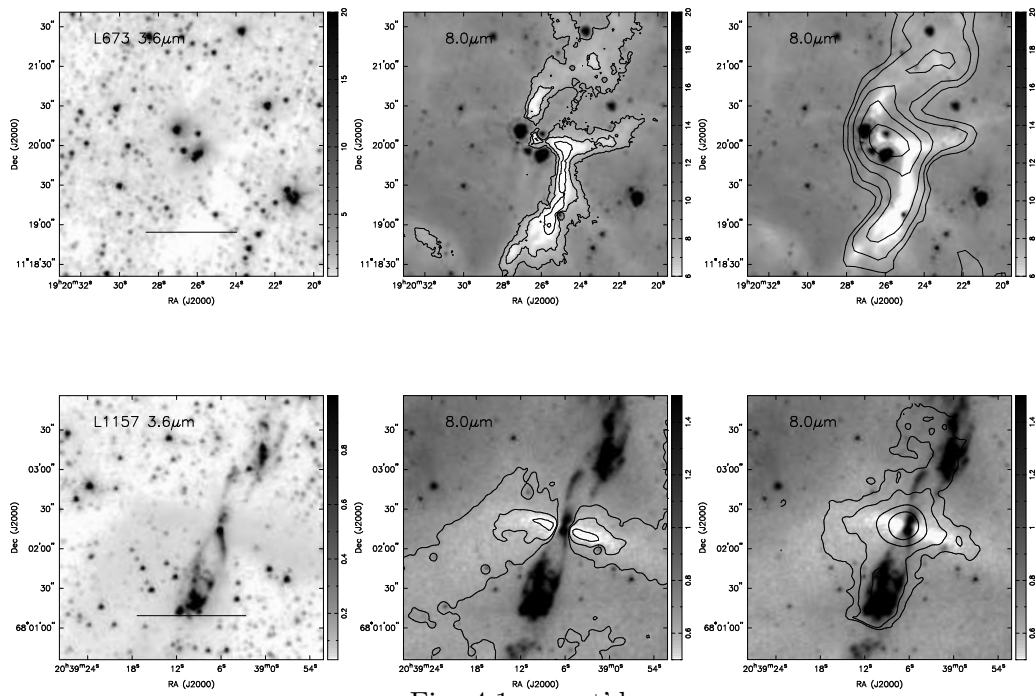


Fig. 4.1 —cont'd.

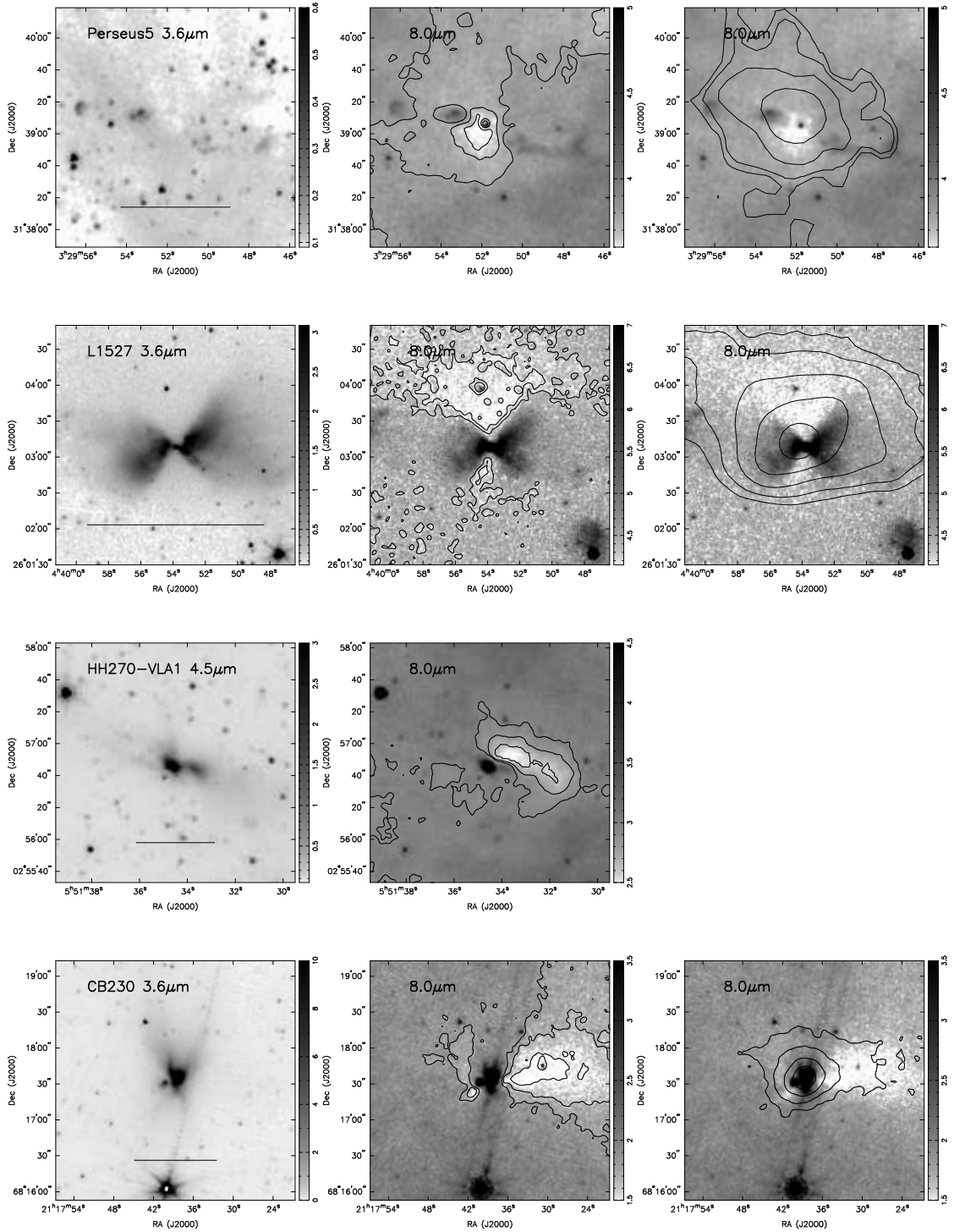


Figure 4.2 Same as Figure 4.1 except one-sided envelopes are shown. The 8.0  $\mu\text{m}$  optical depth contours correspond to the following values of  $\tau_{8\mu\text{m}}$  for Perseus 5: 0.75, 1.22, 2.0; L1527: 0.1 0.375, 1.4; HH270 VLA1: 0.34, 0.6, 2.4; CB230: 0.3, 0.67, 1.5.

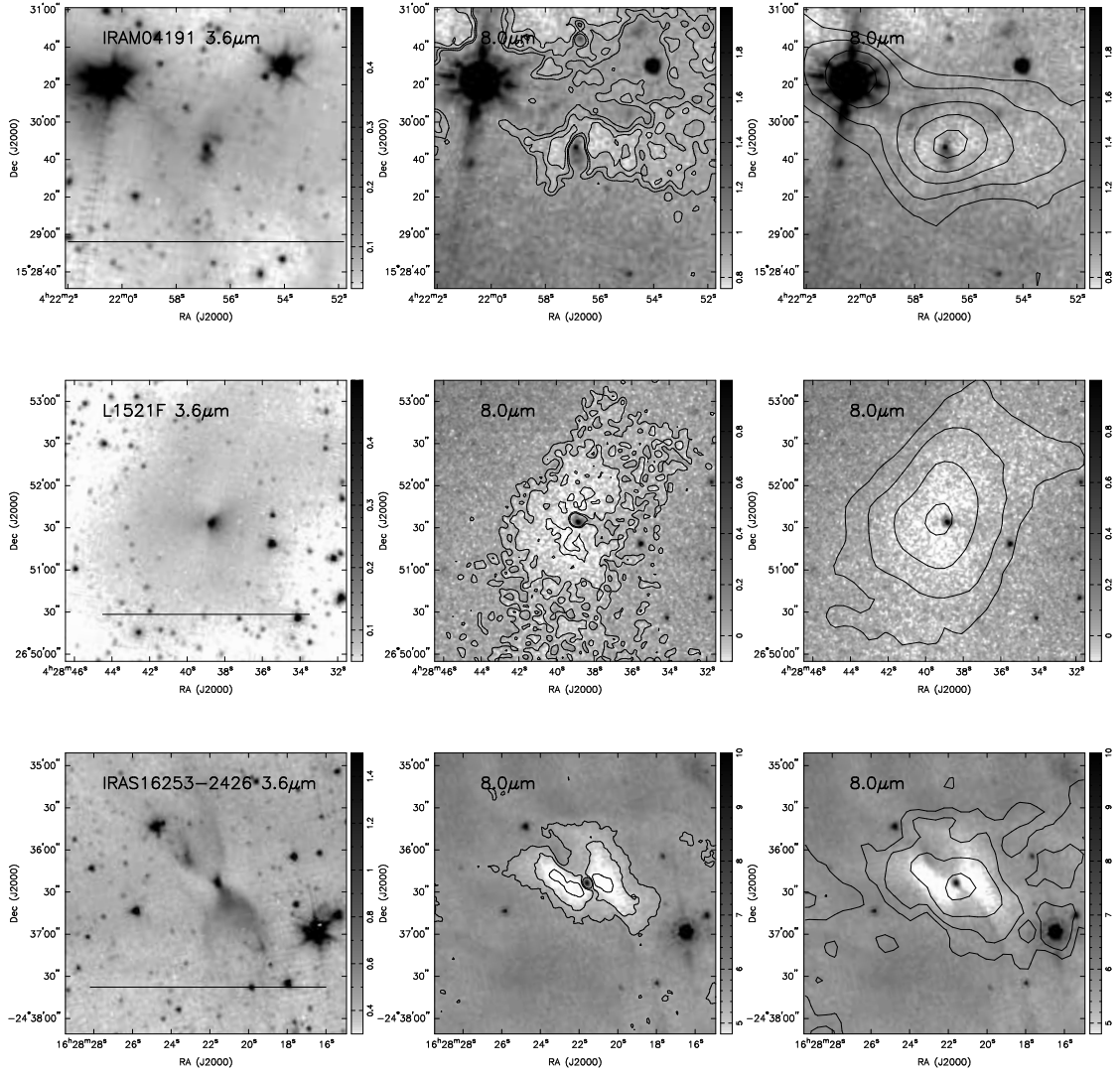


Figure 4.3 Same as Figure 4.1 except spheroidal envelopes are shown. The  $8.0 \mu\text{m}$  optical depth contours correspond to the following values of  $\tau_{8\mu\text{m}}$  for IRAM 04191: 0.4, 0.57, 0.8; L1521F: 0.6, 0.85, 1.2; IRAS 16253-2429: 0.3, 0.53, 0.95.

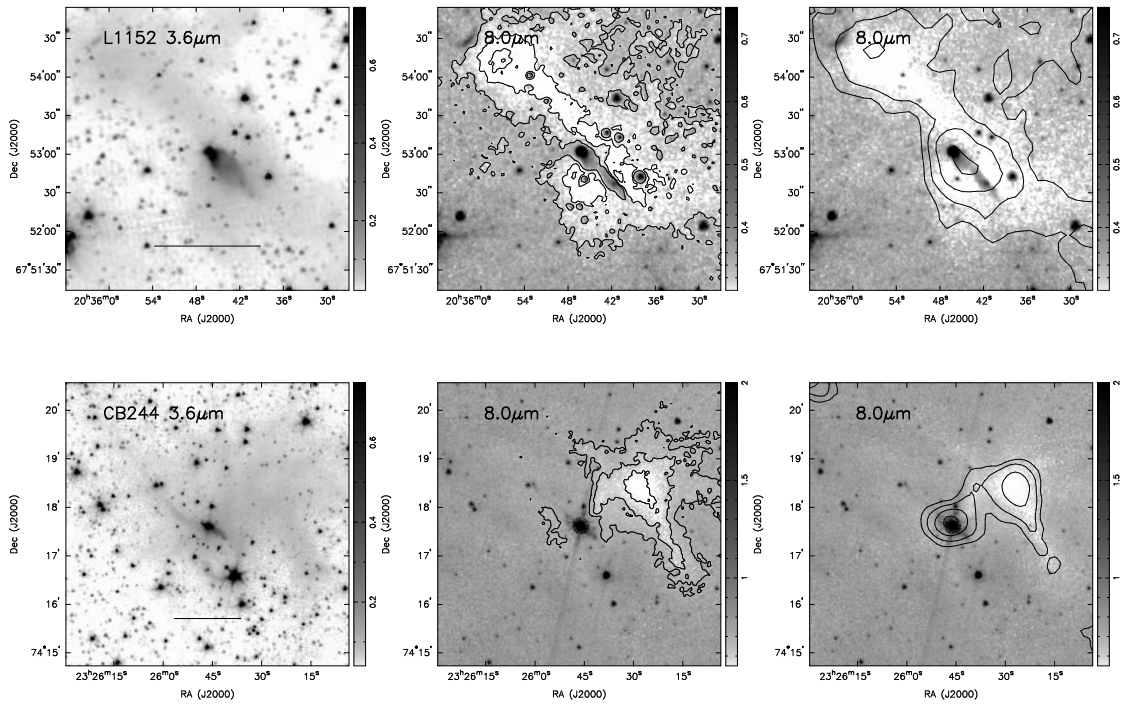


Figure 4.4 Same as Figure 4.1 except binary envelopes are shown. The 8.0  $\mu\text{m}$  optical depth contours correspond to the following values of  $\tau_{8\mu\text{m}}$  for CB244: 0.3, 0.72, 1.75; L1152: 0.45, 0.91, 1.85.

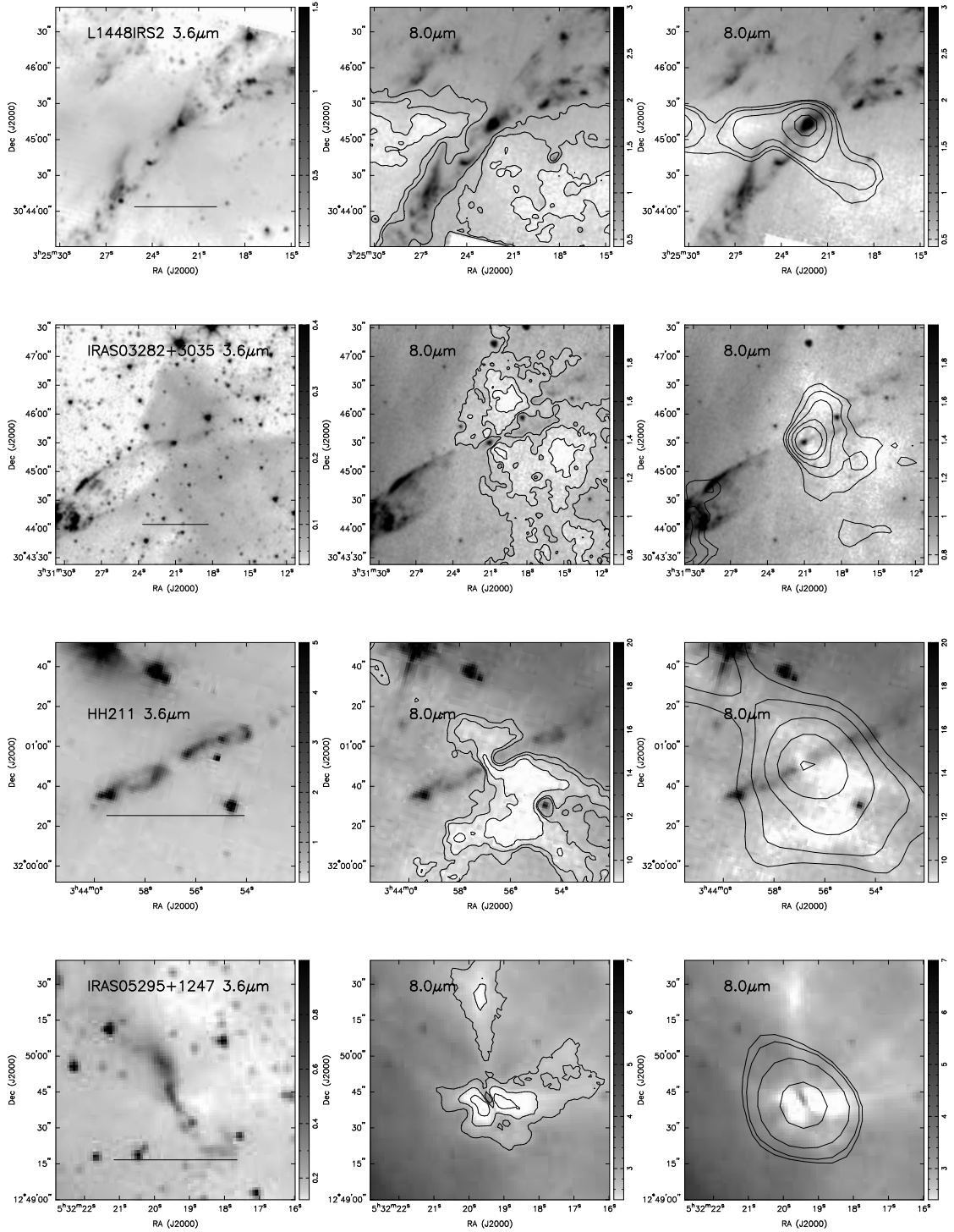


Figure 4.5 Same as Figure 4.1 except irregular envelopes are shown. The 8.0  $\mu\text{m}$  optical depth contours correspond to the following values of  $\tau_{8\mu\text{m}}$  for L1448 IRS2: 0.6, 1.02, 1.75; IRAS 03282+3035: 0.9, 1.34, 2.0; HH211 0.3, 0.57, 1.1; IRAS 05295+1247 0.275, 0.74, 2.0; IRAS 09449-5052: 0.25, 0.56, 1.25; L483: 0.5, 0.82, 1.35; L1165: 0.3, 0.54, 1.0.

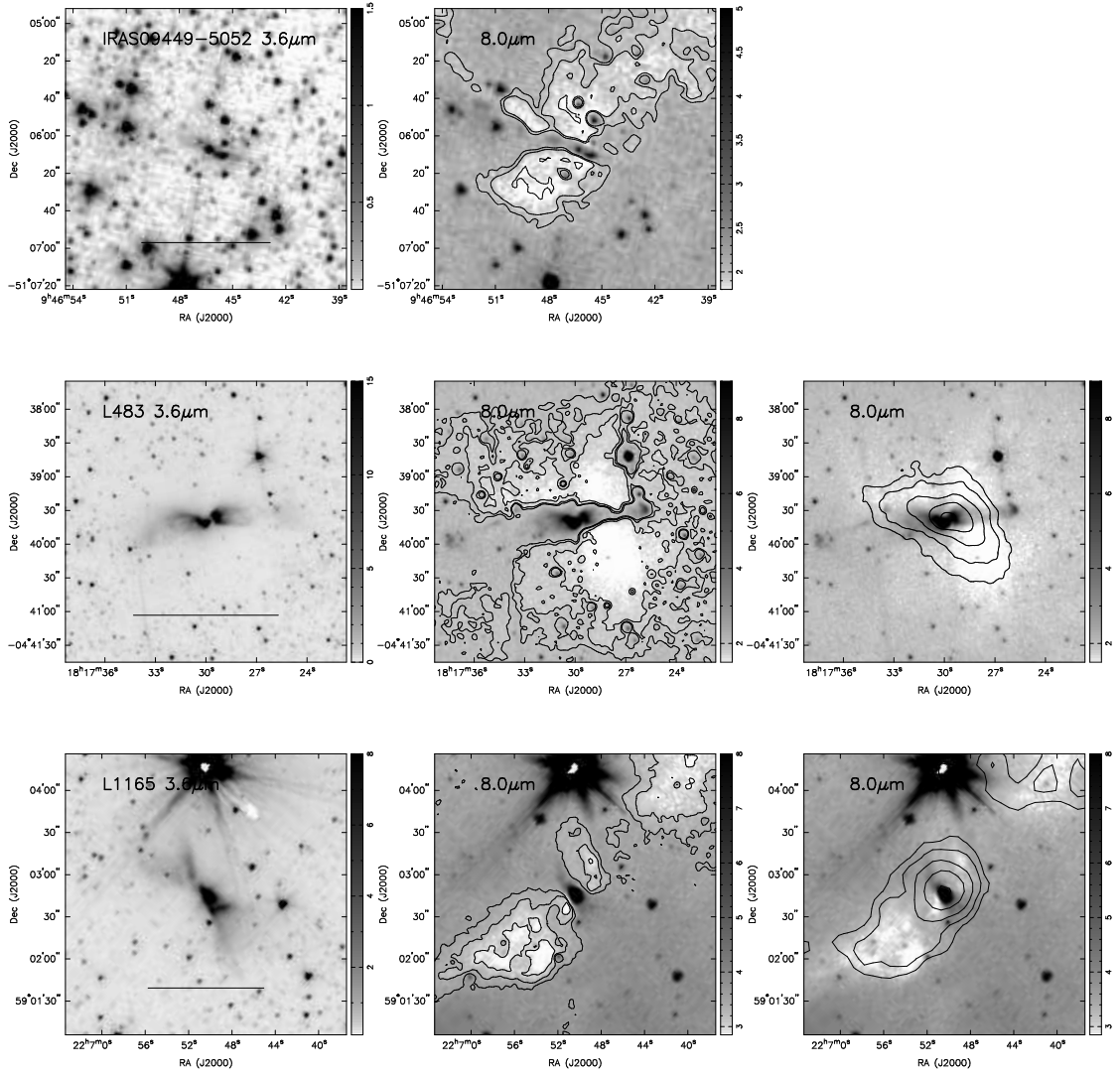


Fig. 5.5 —

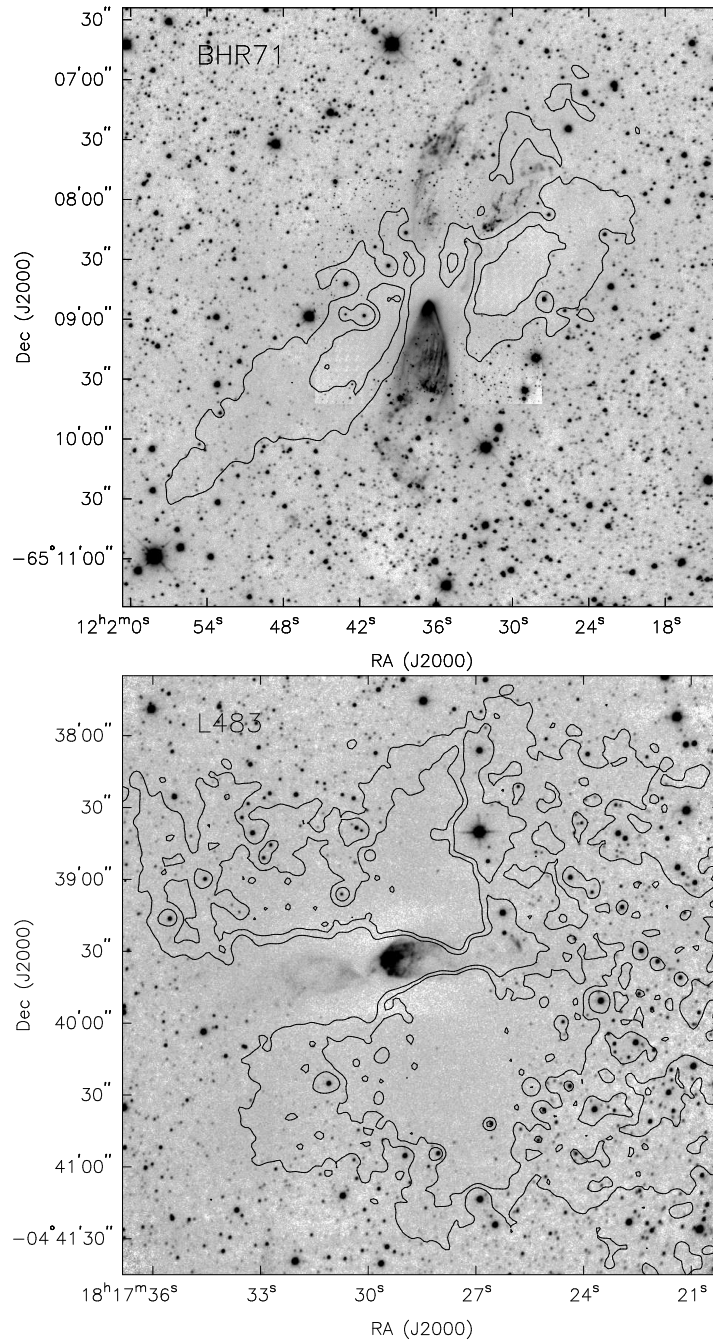


Figure 4.6 Ks-band images of BHR71 and L483 with the two highest optical depth contours from Figures 1 and 5 overlaid. As detailed in the text and Appendix, a number of background stars in the near-IR can be detected through the dense envelope enabling the correction of the  $8\mu\text{m}$  optical depth maps. The BHR71 image was taken with ISPI and the smaller PANIC image is inserted at the center. The L483 data was taken with TIFKAM at MDM observatory.

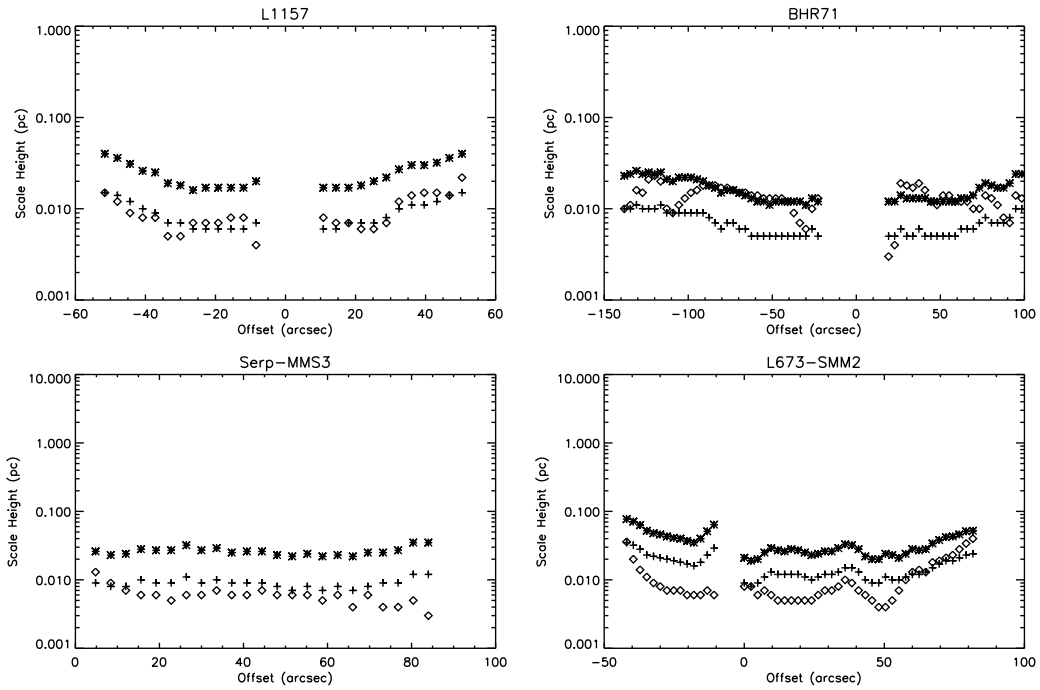


Figure 4.7 Plots of scale height versus radius for flattened envelopes. The diamonds are the measured scale heights determined by fitting Gaussians to the data, the plus signs are the predicted scale height of an infinite filament with peak surface density computed from the peak optical depth, asterisks are the computed scale heights for a sheet. In the case of filaments and sheets, the scale height computed in Section 4.3 does not correspond to the scale height of a Gaussian, to correct for this I integrated through a filament and fit a Gaussian to the surface density profile. The Gaussian scale height is always  $\sim 1.5 \times H$ .

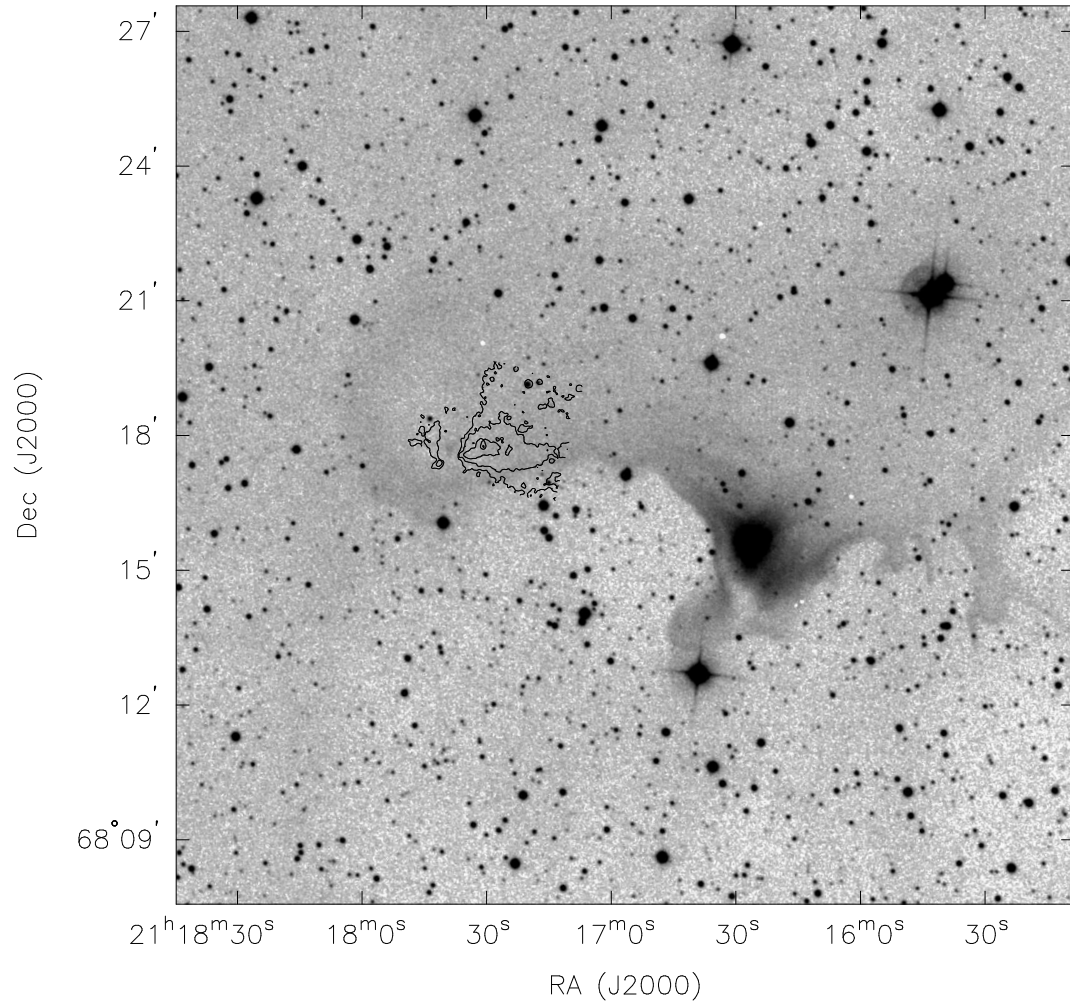


Figure 4.8 DSS2 red image of CB230 region. The overlaid contours are same optical depth contours as shown in Figure 4.2 for CB230. The protostar in CB230 has formed on the far eastern side of the cloud while on the western side there is an optical reflection nebula possibly from another recently formed star.

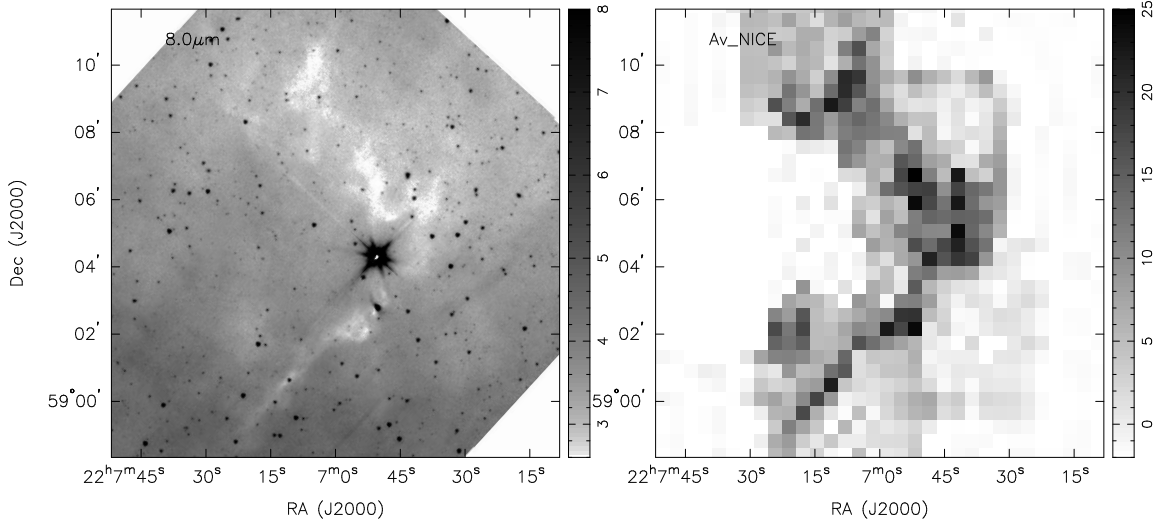


Figure 4.9 Left:  $8\mu\text{m}$  image of L1165 region surrounding the protostar(s). The large scale cloud structure shows a highly filamentary structure with a  $90^\circ$  bend near the protostar(s). Right: Extinction map of L1165 region constructed from H and Ks-band imaging taken with TIFKAM, units are in  $A_V$ . Despite the lower resolution of the map, the large scale structure is clearly well matched between the two techniques of extinction measurement. The large angular coverage of the dark cloud enabled good calibration of the  $8\mu\text{m}$  optical depths using the near-IR extinction measurements.

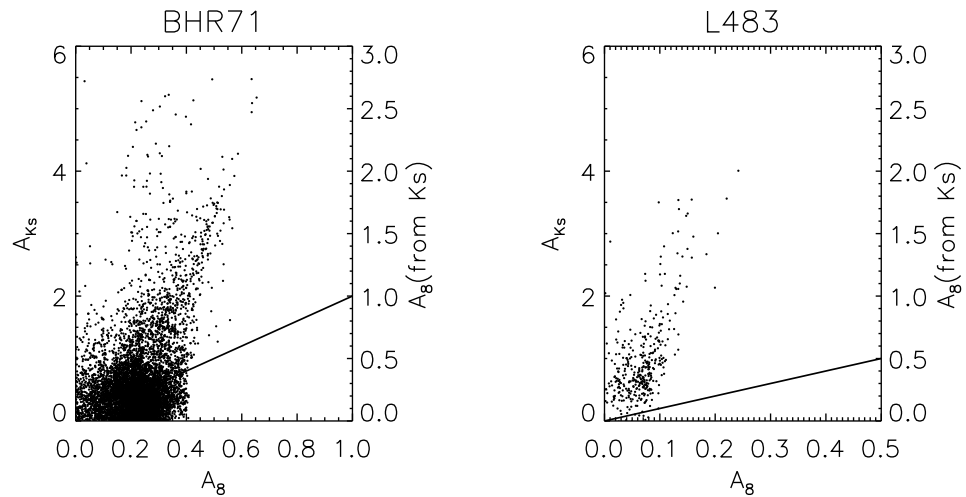


Figure 4.10 Uncorrected comparison of extinction from NICE method and  $8\mu\text{m}$  maps for BHR71 (Left) and L483 (Right). Solid line represents the predicted relationship between  $A_{K_s}$  and  $A_8$ .

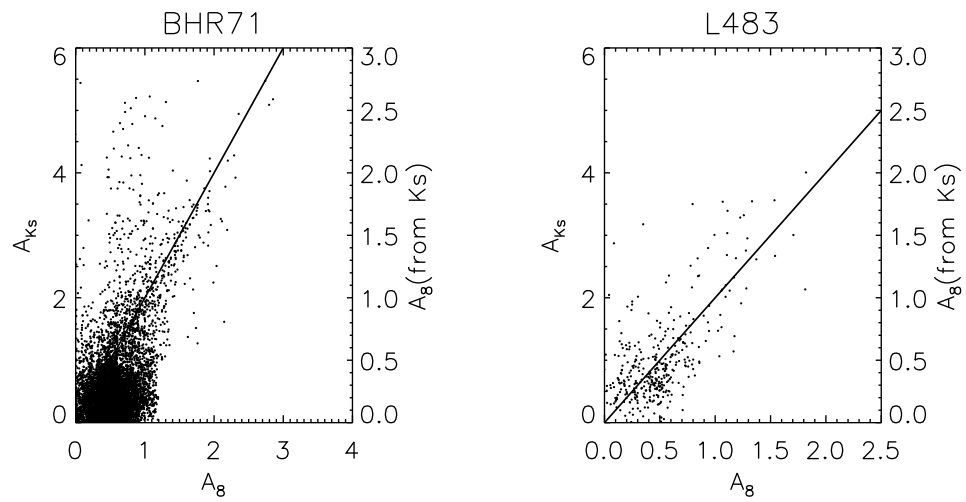


Figure 4.11 Comparison of extinction from NICE method and *corrected*  $8\mu\text{m}$  maps for BHR71 (Left) and L483 (Right). The points with high  $A_{Ks}$  and low  $A_8$  for BHR71 are likely due to a bright  $8\mu\text{m}$  star at the location of the near-IR measurement or scattered light and outflow emission at  $8\mu\text{m}$  coincident with the near-IR measurement.

Table 4.1: Spitzer IRAC Observations

Designation	RA (J2000)	Dec. (J2000)	Date(s) Obs.	Int. Time (s)	AORKEY/Program	Near-IR data (Obs./Inst.)
L1448 IRS2	03 25 22.5	+30 45 10.5	2005-02-25	900	12250624/P03557	
Perseus 5	03 29 51.6	+31 39 04	2005-01-29	900	12249344/P03557	
IRAS 03282+3035	03 31 21.0	+30 45 28	2006-09-28	900	18326016/P30516	
HH211-mm	03 43 56.8	+32 00 52	2004-08-09	24	5790976	
IRAM 04191	04 21 56.9	+15 29 46.1	2005-09-18	480	14617856, 14618112	
L1521F	04 28 39	+26 51 35	2006-03-25	480	14605824, 14605568	
L1527	04 35 53.9	+26 03 09.7	2004-03-07	90	3963648	
IRAS 05295+1247	05 32 19.4	+12 49 41	2006-10-26	900	18325248/P30516	
HH270 VLA1	05 51 34.5	+02 56 48	2005-03-25	360	10737920	
IRAS 09449-5052	09 46 46.5	-51 06 07	2004-04-29	48	5105152	CTIO/ISPI
BHR71	12 01 37.1	-65 08 54	2004-06-10	150	5107200	Magellan/PANIC, CTIO/ISPI
IRAS 16253-2429	16 28 22.2	-24 36 31	2004-03-29	48	5762816, 5771264	
L483	18 17 35	-04 39 48	2004-09-02,03	48	5149184,5149696	MDM/TIFKAM
Serp-MMS3 <sup>a</sup>	18 29 09.1	+00 31 28.6	2004-04-05	48	5710848, 5712384	
HH108	18 35 44.2	-00 33 15	2007-05-17	Med. Scan	14510336	CTIO/ISPI
L723	19 17 53.2	+19 12 16.6	2006-09-27	900	18326528/P30516	MDM/TIFKAM
L673-SMM2	19 20 26.3	+11 20 04	2004-04-30,22	48	5152256, 5151744	
L1157	20 39 06.2	+68 02 17.3	2006-08-13	900	18324224/P30516	MDM/TIFKAM
L1152	20 35 46.5	+67 53 04.2	2004-07-23,28	360	11390976, 11399424	MDM/TIFKAM
CB230	21 17 38.7	+68 17 32.9	2004-11-28	60	12548864	
L1165	22 06 51.0	+59 02 43.5	2004-07-03	48	5165056	MDM/TIFKAM
CB244	23 25 46.5	+74 17 39	2003-12-23	150	4928256	MDM/TIFKAM

<sup>a</sup>Source is identified as MMS3 in Djupvik et al. (2006).

Table 4.2: Source Properties

Designation	Distance (pc)	Mass ( $M_{\odot}$ ) ( $r < 0.15\text{pc}$ )	Mass ( $M_{\odot}$ ) ( $r < 0.1\text{pc}$ )	Mass ( $M_{\odot}$ ) ( $r < 0.05\text{pc}$ )	Mass <sub>obs</sub> ( $M_{\odot}$ )	$L_{bol}$ ( $L_{\odot}$ )	$\sigma\tau$	$\tau_{max}$	$I'_{bg}$ (MJy/sr)	$I_{fg}$ (MJy/sr)	Classification	References ( $M_{obs}$ , $L_{bol}$ )
L1448 IRS2	300	23.0	9.8	2.1	0.86 <sup>a</sup>	8.4	0.15	2.35	3.98	3.44	Flattened	13,1
Perseus 5	300	19.2	9.8	3.4	1.24 <sup>a</sup>	0.46	0.15	2.3	4.04	3.56	One-sided	3,2
IRAS 03282+3035	300	25.7	14.2	4.0	2.2 <sup>a</sup>	1.2	0.3	2.1	2.55	2.26	Irregular	4,2
HH211	300	5.5	3.4	1.8	1.5 <sup>a</sup>	3.02	0.15	1.7	10.1	8.57	Irregular	3,3
IRAM 04191	140	9.7	6.1	1.0	...	0.3	0.22	0.9	4.09	3.77	Spheroidal	...,7
L1521F	140	5.9	4.8	2.3	...	0.03	0.35	1.2	4.65	4.35	Spheroidal	...,8
L1527	140	1.9	1.5	0.84	2.4 <sup>b</sup>	2.0	0.2	1.5	4.37	4.0	One-sided	5,9
IRAS 05295+1247	400	2.9	2.4	1.5	...	12.5	0.05	3.3	5.2	4.02	Irregular	...,1
HH270 VLA1	420	7.8	5.7	1.9	...	7.0	0.12	2.4	4.2	3.72	One-sided	...,1
IRAS 09449-5052	300?	4.7	3.6	1.8	3.7 <sup>b</sup>	3.1	0.25	1.25	2.46	2.1	Irregular	6,6
BHR71	200	24.5	13.8	4.6	2.2 <sup>b</sup>	9.0	0.1	2.8	4.36	2.3	Flattened	6,6
IRAS 16253-2429	125	5.63	2.9	0.8	0.98 <sup>a</sup>	0.25	0.1	1.4	7.0	4.52	Spheroidal	10,2
L483	200	21.5	13.2	3.5	1.8 <sup>a</sup>	11.5	0.25	1.75	2.87	2.35	Irregular	4,1
Serp-MMS3	225	3.1	1.3	0.3	2.2 <sup>a</sup>	1.6	0.1	2.20	3.93	1.48	Flattened	2, 15
HH108	300				4.5, 3.6 <sup>a</sup>	~8.0, 1.0					Flattened	14
L723	300	4.0	2.1	0.6	1.6 <sup>a</sup>	4.6	0.03	3.1	3.22	2.55	Flattened	4,1
L673-SMM2	300	5.2	3.2	1.0	0.35 <sup>a</sup>	2.8	0.1	3.6	9.39	3.33	Flattened	12
L1157	250	12.0	6.0	0.6	2.2 <sup>a</sup>	3.0	0.1	2.5	0.71	0.45	Flattened	4,1
L1152	250	14.1	7.8	2.4	12.0 <sup>b</sup>	1.3	0.15	1.85	0.32	0.18	Binary Core	5,1
CB230	300	7.2	4.1	1.1	1.1 <sup>a</sup>	7.2	0.23	1.9	1.79	1.17	One-sided	11,1
L1165	300	6.9	3.8	1.1	0.32 <sup>a</sup>	28	0.1	3.0	3.76	2.6	Irregular	12,12
CB244	250	9.7	7.8	4.1	...	...	0.2	1.75	0.59	0.35	Binary Core	....

For HH108 the quoted values are given for IRS1 and IRS2 respectively. References: (1) This work, (2) Enoch et al. (2009), (3) Enoch et al. (2006), (4) Shirley et al. (2000), (5) Benson & Myers (1989), (6) Bourke et al. (1995a), (7) Dunham et al. (2006) (8) Terebey et al. (2009), (9) Tobin et al. (2008), (10) Young et al. (2006), (11) Kauffmann et al. (2008) (12) Visser et al. (2002), (13) O'Linger et al. (1999), (14) Chini et al. (2001), (15) Enoch et al. (2007).

<sup>a</sup>Mass is computed with sub/millimeter bolometer data assuming an isothermal temperature.

<sup>b</sup>Mass is computed from ammonia maps assuming an abundance relative to H<sub>2</sub> and excitation temperature.

Table 4.3. Moment of Inertia Ratios

Object	Radius (pc)	$I_{\perp}/I_{\parallel}$	$I_{\perp,t}/I_{\perp,r}$	$I_{\parallel,t}/I_{\parallel,r}$
Perseus 5	0.05	1.2	1.2	1.0
L1448 IRS2	0.05	0.6	1.0	1.7
IRAS 03282+3035	0.05	1.2	1.0	0.8
HH211	0.05	2.2	0.2	0.2
L1448-IRS2	0.05	1.7	0.6	1.0
IRAM 04191	0.03	1.5	2.5	1.2
L1521F	0.04	1.3	0.9	1.0
L1527	0.05	3.2	0.1	0.1
IRAS 05295+1247	0.05	1.3	0.5	0.5
HH270 VLA1	0.10	0.6	1.4	2.6
IRAS 09449-5052	0.05	1.7	0.8	1.0
BHR71	0.075	1.6	1.1	0.8
IRAS 16253-2429	0.05	1.1	0.9	1.0
L483	0.05	1.4	1.0	0.9
Serp-MMS3	0.05	1.0	1.9	1.5
L723	0.05	1.2	0.8	0.9
L673-SMM2	0.05	0.9	0.1	0.4
L1157	0.05	3.0	0.9	0.8
L1152	0.05	0.8	1.4	1.5
CB230	0.05	3.4	0.3	0.6
L1165	0.05	2.3	0.5	0.8

Note. —  $I_{\perp}$  measures material that is located away from the outflow/rotation axis along the abscissa and  $I_{\parallel}$  measures material located along the ordinate axis. CB244 does not appear in this table because most extinction in this system is associated with the neighboring starless core, not the protostar.

## CHAPTER 5

# Kinematic Structure of Complex Class 0 Protostellar Envelopes: Single-Dish and Interferometric Molecular Line Mapping

### 5.1 Introduction

Infall and rotation in dense cores and protostellar envelopes both play important roles in the formation of protostars and their surrounding disks. Infall must be taking place in the envelopes because newborn protostars are often observed to be embedded within their natal clouds. The two classic analytic theories of collapse describe infall as either being outside-in (Larson, 1969) or inside-out (Shu, 1977). The initial angular momentum of the protostellar cloud governs the formation and sizes of the protoplanetary disks (e.g. Cassen & Moosman, 1981; Terebey et al., 1984) and will affect the ability of the cloud core to fragment into multiple stellar systems (e.g. Burkert & Bodenheimer, 1993; Bonnell & Bate, 1994). The ubiquitous formation of protoplanetary disks (Haisch et al., 2001; Hernández et al., 2007) and the prevalence of binary systems (Raghavan et al., 2010) lends strong indirect evidence for the presence of rotation. Therefore, observing these two processes in protostellar envelopes has enormous potential for constraining star formation theory through comparisons to analytic models and numerical simulations. Dense protostellar cores are well known as sites of isolated, low-mass star formation (e.g. Shu et al., 1987; Benson & Myers, 1989;

---

Based on the paper by John J. Tobin, Lee Hartmann, Hsin-Fang Chiang, Leslie W. Looney, Edwin A. Bergin, Claire J. Chandler, Josep M. Masque, Sebastien Maret, Fabian Heitsch, ApJ, 2011, in press

McKee & Ostriker, 2007) and are the ideal place to study the kinematic structure from large, core/envelope scales ( $\sim 0.1$  pc) down to scales near the disk radius.

Several previous studies have attempted to characterize the rotation in dark clouds and dense cores. Arquilla & Goldsmith (1986) examined the kinematic structure of dark clouds using CO on  $\sim 10'$  ( $\sim 1$  pc) scales, finding that some exhibit possible rotation signatures derived from velocity gradients. Later, Goodman et al. (1993) and Caselli et al. (2002) used the dense molecular tracers  $\text{NH}_3$  and  $\text{N}_2\text{H}^+$  to examine rotation in the dense cores within dark clouds ( $\sim 2\text{--}3'$ ; 0.1 - 0.2 pc scales). Goodman et al. (1993) and Caselli et al. (2002) found typical velocity gradients of  $\sim 1$  to 2  $\text{km s}^{-1} \text{ pc}^{-1}$ , which were interpreted to be slow, solid-body core rotation. However, the observations had limited resolution ( $60''\text{--}90''$ ), nearly the size of the envelopes in some cases. Rotation is not necessarily solid-body; however, this assumption simplifies analysis in terms of equipartition and the early data did not warrant more sophisticated models.

Caselli et al. (2002) noted that their finer resolution as compared to Benson & Myers (1989) revealed clear deviations from linearity in the velocity gradients. This indicates that the velocity structure of cores may be more complex than simply axisymmetric, solid-body rotation. Chen et al. (2007) carried out a higher resolution study using interferometric observations of  $\text{N}_2\text{H}^+$  from OVRO on a sample of protostars in the Class 0 (Andre et al., 1993) and Class I phases (Lada, 1987). They found substantially larger velocity gradients in the inner envelopes, with complex velocity fields, only showing probable rotation signatures in a few cases.

While the possible rotation has been probed using optically thin tracers, the study of infall in protostellar envelopes has been limited to observations of optically thick tracers toward the envelope center. Zhou et al. (1993) and Myers et al. (1995) used observations of CS and  $\text{H}_2\text{CO}$  to infer the detection of infall in the envelope of the Class 0 protostar B335. The optically thick molecular lines are self absorbed at the line-center and the key signature of infall is the blue-shifted side of the line being brighter than the red-shifted side. Later, Di Francesco et al. (2001) found inverse-P Cygni line profiles in  $\text{H}_2\text{CO}$  that are interpreted as infall. Furthermore, infall at

large-scales may have been detected in the pre-stellar core L1544 (Tafalla et al., 1998).

These previous studies have interpreted the kinematic structure in terms of axisymmetric envelopes. However, recent studies (i.e. Tobin et al., 2010b; Looney et al., 2007) have revealed that the dense envelopes surrounding the youngest, generally Class 0, protostars often have complex, non-axisymmetric morphological structure (also see Benson & Myers, 1989; Myers et al., 1991; Stutz et al., 2009). Out of the 22 protostellar systems exhibiting extinction at  $8\mu\text{m}$ , only three appeared to be roughly axisymmetric. I suggested that the asymmetric envelope structure may play a role in the formation of binary systems by making fragmentation easier and that the initial disk structure may be perturbed from uneven mass loading. However, in order to understand the effects that complex envelope structure has on disk formation and fragmentation, the kinematics of the dense gas must be characterized.

Given the apparent prevalence of complex morphological structure in protostellar envelopes, the kinematics of the envelopes must also be studied on scales such that the morphological structure is spatially resolved. To examine the kinematic structure of morphologically complex envelopes, I have undertaken a molecular line survey focusing on nearby ( $d < 500$  pc), embedded protostars drawn from the sample of envelopes presented in Chapter 4. I have approached this study from two directions. First, I obtained new single-dish  $\text{N}_2\text{H}^+$  mapping of sixteen systems with the IRAM 30m, a factor of two improvement in resolution over Caselli et al. (2002). Secondly, I obtained new interferometric  $\text{N}_2\text{H}^+$  and  $\text{NH}_3$  observations of fourteen systems with resolutions between  $3.5''$  and  $6''$ . The analysis of both the single-dish and interferometric observations offers a comprehensive view of the kinematic and morphological structure from 0.1 pc scales down to  $\sim 1000$  AU. Complementary *Spitzer* imaging gives a clear view of the outflow angular extent and direction in all of these objects.

In this chapter, I am primarily presenting the dataset as a whole and give a basic analysis of each object; an upcoming chapter will give a more detailed interpretation of the velocity structures. The data for each object are quite rich and I find many envelopes with velocity gradients normal to the outflow on large-scales in the single-dish maps, persisting down to small-scales in the interferometer maps. I have

organized the chapter as follows: Section 5.2 discusses the sample, observations, data reduction, and analysis, Section 5.3 presents my general results and discusses each object in detail, and Section 5.4 discusses the basic overall properties of the sample as a whole.

## 5.2 Observations and Data Reduction

I mapped the protostellar envelopes in the dense gas tracers  $\text{NH}_3$  and  $\text{N}_2\text{H}^+$ , which are known to be present over a wide range of spatial scales and preferentially trace high density regions (critical densities of  $\sim 2 \times 10^3 \text{ cm}^{-3}$  Danby et al. (1988); Schöier et al. (2005) and  $\sim 1.4 \times 10^5 \text{ cm}^{-3}$  Schöier et al. (2005) respectively), where CO has depleted (e.g. Bergin et al., 2002; Tafalla et al., 2004). The single-dish data were all obtained using the IRAM 30m telescope, mapping  $\text{N}_2\text{H}^+$  ( $J = 1 \rightarrow 0$ ). The single-dish observations were followed by interferometric observations of  $\text{N}_2\text{H}^+$  ( $J = 1 \rightarrow 0$ ) using CARMA and the Plateau de Bure Interferometer, in addition to  $\text{NH}_3$  (1,1) observations using the VLA<sup>1</sup>, including VLA archival data for some objects. I will briefly describe the observations and the data analysis procedure for each data set.

### 5.2.1 The Sample

The sample of protostellar envelopes selected for kinematic study is directly drawn from the objects presented in Tobin et al. (2010b, hereafter Chapter 4). All protostellar systems observed have a surrounding envelope visible in  $8\mu\text{m}$  extinction. Much of the envelope sample was found within archival *Spitzer* data from the cores2disks (c2d) legacy program (Evans et al., 2009). Given that c2d and most other archival observations were short integrations, I was only able to detect very dense structures which happened to have a bright backgrounds at  $8\mu\text{m}$ . Thus, there may be a bias towards denser envelopes, but the range of bolometric luminosity is fairly broad with objects  $< 1 L_\odot$  and as much as  $\sim 14 L_\odot$ . These protostars are listed in Table 5.1 and are mostly Class 0 systems with a few Class Is. The requirement of having an

---

<sup>1</sup>The National Radio Astronomy Observatory is a facility of the National Science Foundation operated under cooperative agreement by Associated Universities, Inc.

envelope visible in extinction enables the envelope morphology to be considered in the interpretation of the kinematic data. I regard the  $8\mu\text{m}$  extinction to more robustly reflect the structure of high density material around the protostars on scales  $> 1000$  AU, as molecular tracers may have abundance variations which affect their spatial distribution. The requirement of  $8\mu\text{m}$  extinction also biases the sample to more isolated systems, only Serpens MMS3 and L673 have multiple neighbors  $< 0.1$  pc away.

### 5.2.2 IRAM 30m Observations

I observed the sample of protostellar envelopes in two observing runs at the IRAM 30m radio telescope on Pico Veleta in the Spanish Sierra Nevada. The first observing run took place between 2008 December 26 - 30; during this run I only observed four protostars due to poor weather. I used the AB receiver system and observed the protostars in the  $\text{N}_2\text{H}^+$  ( $J = 1 \rightarrow 0$ ) transition ( $\nu_{\text{rest}} = 93.1737637$  GHz;  $JF_1F = 123 \rightarrow 012$  component Keto & Rybicki, 2010); the half power beam width (HPBW) of the 30m at this frequency is  $\sim 27''$ . The second observing run took place between 2009 October 22-26 using the new Eight MIxer Receiver (EMIR). I observed thirteen protostars and revisited L1527 from the first run, using the VESPA auto-correlation spectrometer as the backend for all observations. Single-sideband system temperatures of 130 K at  $\nu = 93$  GHz were typical for both observing runs. During the 2008 run I used the 20 MHz bandwidth mode with 20kHz channels and in 2009 I used 40 MHz with 20kHz channels; see Table 5.2 the list of sources observed and more detail.

I conducted the observations using frequency-switched on-the-fly (OTF) mapping mode. The maps varied in size depending on the extent of the source being observed, most being  $3' \times 3'$ . Most maps were integrated down to at least  $\sigma_T \sim 150\text{mK}$  for the  $\text{N}_2\text{H}^+$  ( $J = 1 \rightarrow 0$ ) transition, noise levels for each map are listed in Table 5.2. I mapped the sources by scanning in the north-south direction and again in the east-west direction to minimize striping in the final map. The scan legs were stepped by  $5''$  and I repeated the maps to gain a higher signal-to-noise ratio. Calibration scans were taken about every 10 minutes between scan legs and the final maps took

approximately 2 hours to complete. Pointing was checked about every two hours, azimuth and elevation offsets were typically  $\pm 5''$ ; the pointing offset remained stable, typically within  $\sim 2''$  during an observation. These values agree well with the rms pointing accuracy of  $\sim 2''$ .

The initial calibration of the OTF data to the antenna temperature scale and CLASS data format was performed automatically on-site by the Multichannel Imaging and calibration software for Receiver Arrays (MIRA)<sup>2</sup> package. Further data reduction was done using CLASS (part of GILDAS<sup>2</sup>). For all molecular lines observed, the frequency switched spectra were folded and baseline subtracted using a second order polynomial. I then reconstructed the spectral map on a grid such that the FWHM of the beam was spanned by 3 pixels and each pixel is the average of all measurements within the FWHM of the beam.

### 5.2.3 CARMA Observations

The CARMA observations were taken in four observing semesters; most sources were observed solely in the D-array configuration (except L1527 and L1157 see below) which yields  $\sim 6''$  resolution. Three objects were observed in 2009 July and August. The correlator at this time only had three bands, operating dual side-band mode, giving 6 spectral windows and was configured for an IF frequency of 91.181 GHz.  $\text{N}_2\text{H}^+$  ( $J = 1 \rightarrow 0$ ) and  $\text{HCO}^+$  ( $J = 1 \rightarrow 0$ ) ( $\nu_{\text{rest}}=89.188518$  GHz; (Lovas, 1992)) were observed in opposite side-bands of one spectral window with 2MHz bandwidth and 63 channels giving  $\sim 0.1$  km/s velocity resolution. The  $\text{N}_2\text{H}^+$  ( $J = 1 \rightarrow 0$ ) emission spectrum comprises 7 hyperfine lines over  $\sim 17$  km s<sup>-1</sup>, consisting of two groups of three lines and a single isolated line. The 2MHz window is too narrow to observe all the lines; therefore, I observed the strongest set of three lines, rather than observing the isolated line to maximize the signal-to-noise. The multiple hyperfine transitions enables the optical depth and excitation temperature to be determined. The second band was also configured for 2 MHz bandwidth and was centered on the main hyperfine component of the HCN ( $J = 1 \rightarrow 0$ ) transition ( $\nu_{\text{rest}}=88.6318473$

<sup>2</sup><http://www.iram.fr/IRAMFR/GILDAS>

GHz; (Lovas, 1992)), and the third band was configured for continuum observations with 500 MHz bandwidth (1 GHz dual-side band).

Another set of sources was observed in 2010 April and May. During this time, a new correlator was being completed with higher velocity resolution over a wider bandwidth and more spectral windows; most data were taken with six bands (twelve spectral windows). For these observations, the IF frequency was set to 90.9027 GHz such that  $\text{N}_2\text{H}^+$  ( $J = 1 \rightarrow 0$ ) and  $\text{HCN}$  ( $J = 1 \rightarrow 0$ ) could be observed in opposite side-bands of the same correlator band. I also observed  $\text{HCO}^+$  ( $J = 1 \rightarrow 0$ ),  $\text{H}^{13}\text{CO}^+$  ( $J = 1 \rightarrow 0$ ) ( $\nu_{\text{rest}} = 86.754294$  GHz), ortho- $\text{NH}_2\text{D}$  ( $1_{1,1} \rightarrow 1_{0,1}$ ), ( $\nu_{\text{rest}} = 85.926263$  GHz), and continuum; rest frequencies for these transitions are taken from Lovas (1992). All spectral line observations used 8 MHz bandwidth with 385 channels yielding  $\sim 0.06$  km s $^{-1}$  velocity resolution, during reduction this was rebinned to 0.1 km s $^{-1}$  resolution to reduce noise. The continuum observations again had 500 MHz bandwidth (1 GHz dual-side band). See Table 5.3 for exact dates of observation for particular sources.

In addition, L1527 and L1157 were observed in E-array configuration in 2008 October and L1157 was again observed in D-array in 2009 March. These observations were taken in a three-point mosaic pattern to better recover the large-scale emission from the envelopes. The correlator was configured with one band for continuum, the other two bands were set to observe  $\text{N}_2\text{H}^+$  ( $J = 1 \rightarrow 0$ ) and  $\text{HCO}^+$  ( $J = 1 \rightarrow 0$ ). One band had 2MHz bandwidth and was centered on the isolated  $\text{N}_2\text{H}^+$  component. The other band was configured with 8 MHz bandwidth and 63 channels with 0.4 km s $^{-1}$  resolution to cover all 7  $\text{N}_2\text{H}^+$  ( $J = 1 \rightarrow 0$ ) hyperfine lines. However, I only use the 0.1 km s $^{-1}$  velocity resolution data for kinematics. The observations of L1157 are further detailed in Chiang et al. (2010).

All datasets were observed in a standard loop (calibrator–source–calibrator), a bright quasar within 15° was used for phase and amplitude calibration. The calibrator was integrated for 3 minutes while the source was integrated for 15 minutes in each cycle. Absolute flux calibration was obtained by observing standard flux calibration sources, see Table 5.3. Bandpass calibration for the continuum bands was

accomplished by observing a bright quasar, generally 3C454.3; the spectral line bands were bandpass corrected using the noise source.

Each dataset was processed using the MIRIAD software package (Sault et al., 1995). The raw visibilities were corrected for refined antenna baseline solutions and transmission line-length variation. The data were then edited to remove uncalibratable data (i.e. poor phase coherence, phase jumps, anomalous system temperatures/amplitudes). The bandpass corrections were computed using the *mfcal* routine. The absolute flux calibration was derived using the *bootflux* routine which determines the flux density of the gain calibrator relative to the flux calibration source (absolute calibration uncertainty is typically  $\sim 10\%$ ). The phases and amplitudes were calibrated using the *mselfcal* routine. The phase and amplitude solution calculated for the continuum bands was then transferred to the spectral line bands. Continuum images and spectral line cubes were generated by inverting the corrected visibilities with natural weighting, creating the dirty map. Then the dirty map is CLEANed using the *mossdi* routine using a clean box of  $60'' \times 60''$  which fits within the primary beam of the 10.4m dishes ( $\sim 72''$  at  $\lambda=3.2\text{mm}$ ). In this chapter, I will mainly interpret the  $\text{N}_2\text{H}^+$  data but will comment on the other molecules when relevant and the 3mm continuum data are presented in the Appendix.

#### 5.2.4 VLA Observations

The  $\text{NH}_3$  (1,1) observations were taken with EVLA transition system during the final semester of VLA correlator operation in D configuration. Eight-hour tracks were taken for 5 sources during 2009 October, November, and 2010 January (see Table 5.4). I used the 4 IF mode providing two tunings and dual-polarization to observe the  $\text{NH}_3$  (1,1) and (2,2) inversion transitions ( $\nu=23.6944955$ ,  $23.7226336$  GHz respectively (Ho & Townes, 1983)) with 1.5 MHz bandwidth and 127 channels yielding  $\sim 0.15$  km/s velocity resolution. This configuration was able to observe the main component and two sets of satellite lines for the  $\text{NH}_3$  (1,1) transition. I alternately observed the source and a calibrator within  $15^\circ$ . Two minutes were spent integrating on the calibrator while ten minutes were spent on the target during each cycle. Pointing was updated

every hour, 3C84 was observed as the bandpass calibrator and 3C48 or 3C286 was used for absolute flux calibration.

The raw visibility data from the VLA were reduced and calibrated using the CASA (Common Astronomy Software Applications)<sup>3</sup> package. The task *importvla* was used to convert the VLA data to a CASA measurement set. The visibility data were then inspected and edited, specifically flagging shadowed data and any VLA antennas. Only EVLA antennas were used in the final dataset because I used doppler tracking during the observations, which caused phase jumps between VLA and EVLA antennas. Antenna positions were corrected using the *gencal* task when necessary and the absolute flux scale was set using the *setjy* task (absolute calibration uncertainty is typically 10%). The phases and amplitudes were calibrated using the *gaincal* task; the bandpass correction was determined using the *bandpass* task. All the calibrations were then applied using the *applycal* task. I then inspected the corrected data to ensure proper phase correction; any severely outlying amplitude points in the source data were also flagged.

The final spectral datacubes were generated using the *clean* task. The clean task encompasses several individual processes including inverting the visibilities, CLEANing the image, and restoring the image. Since the VLA provides a 2' diameter primary beam (field of view), several additional steps were taken to increase the final image fidelity. I first performed a first-pass CLEANing of a spectral data cube over the 2' primary beam. Then I calculated the integrated intensity of the main component of the NH<sub>3</sub> (1,1) or (2,2) transition by summing the spectral line channels. Next, I created a mask image in which pixels below a 2 $\sigma$  intensity threshold were rejected and those above were kept. This isolated the area of NH<sub>3</sub> emission around a particular protostar enabling CLEANing down to near a 1 $\sigma$  threshold. Then for the NH<sub>3</sub> (1,1) images, the multi-scale CLEAN algorithm was employed (Rich et al., 2008); this algorithm models the sky as the sum of Gaussian components of various widths, which for extended sources works better than modeling the sky as the sum of many point source CLEAN components. In this chapter, I will only present the NH<sub>3</sub> (1,1) data.

---

<sup>3</sup><http://casa.nrao.edu>

In addition to my own observations, I include VLA archival data<sup>4</sup> for the sources L1527, L1521F, and L483. The data for L1521F and L483 were taken in different correlator configurations than my observations, see Table 5.4. The same reduction procedure was applied for these archival data as for my observations.

### 5.2.5 Plateau de Bure Interferometer Observations

L1157 was observed with the Plateau de Bure Interferometer on 2009 June 17 and 2009 July 8 in the D-array configuration with 5 antennas operating. It was observed again on 2009 November 13 in C-array configuration with 6 antennas. During the first track the weather conditions were average, with 5 to 10 mm of precipitable water vapor (pwv) and a RMS phase noise lower than  $64^\circ$ . During the last two tracks the weather conditions were better, with 3-6 mm and 5-7 mm of pwv and a RMS noise phase lower than  $41^\circ$  and  $24^\circ$ , respectively

The 3mm receivers were tuned to the  $\text{N}_2\text{H}^+$  ( $J = 1 \rightarrow 0$ ) transition in the lower-sideband. The correlator was configured with two windows for continuum observation, each having 320 MHz of bandwidth and one window with 20 MHz bandwidth for the  $\text{N}_2\text{H}^+$  ( $J = 1 \rightarrow 0$ ), yielding a velocity resolution of 0.125 km/s. Both the spectral line and continuum observations were taken in dual-polarization mode.

The raw data were calibrated using the CLIC program from the GILDAS software package. A standard calibration procedure was used. Visibilities amplitudes and phases for each baseline were inspected and bad data (e.g. affected by phase jumps or antenna shadowing) were flagged. Phases were then calibrated using observations of the 1927+739 calibrator. Absolute flux was derived from observations of MWC349, assuming a flux of 1.15 Jy at 3 mm for that source; uncertainty in the absolute flux is  $\sim 10\%$ .

The calibrated data were then reduced using the MAPPING program from GILDAS. A UV table was created for the 3mm continuum as well as for the  $\text{N}_2\text{H}^+$  ( $J = 1 \rightarrow 0$ ) line. The 3mm continuum visibilities were then subtracted from the line visibilities. Finally, a deconvolved map was produced using the the CLEAN algorithm. The syn-

---

<sup>4</sup><http://archive.nrao.edu>

thesized beam in the final map is roughly circular with a FWHM of  $\sim 3.4 \times 3.3''$  at PA 114°; further details of the observations are listed in Table 5.5.

## 5.2.6 Data Analysis

### 5.2.6.1 Hyperfine Fitting

The  $\text{N}_2\text{H}^+$  and  $\text{NH}_3$  molecular lines both have a hyperfine emission line spectrum. This allows the line-center velocity and full-width half-maximum (FWHM) linewidths to be robustly determined in each pixel by fitting all the hyperfine components simultaneously. The line-center velocities can be fit substantially better than native resolution of the observations. Goodman et al. (1993) approximates the observed velocity accuracy as

$$\sigma_v = 1.15 \left( \frac{\sigma_T}{T_{peak}} \right) (1.21 \delta_v \Delta v)^{1/2}. \quad (5.1)$$

This assumes that the lines have a Gaussian shape,  $\sigma_T$  is the rms noise,  $T_{peak}$  is the peak line intensity,  $\Delta v$  is the FWHM linewidth, and  $\delta_v$  is the velocity width of the channels. The additional factor 1.21 is the intrinsic error in the autocorrelation spectrometer with unity weighting (Thompson et al., 2001). Using this relationship for velocity accuracy, if a dataset had a signal-to-noise of 5, assuming  $\Delta v = 0.3 \text{ km s}^{-1}$  and  $\delta_v = 0.1 \text{ km s}^{-1}$ , the velocity accuracy would be  $0.043 \text{ km s}^{-1}$ . Note that this is the velocity accuracy for one line, using the multiple hyperfine components of  $\text{N}_2\text{H}^+$  and  $\text{NH}_3$  even greater accuracy can be obtained.

To fit the line kinematics, I applied the CLASS hyperfine fitting routines. The hyperfine frequencies and line ratios for  $\text{N}_2\text{H}^+$  ( $J = 1 \rightarrow 0$ ) were taken from Keto & Rybicki (2010) and the  $\text{NH}_3$  frequencies and line ratios that are built into CLASS were used (Rydbeck et al., 1977; Ho & Townes, 1983). A semi-automated routine was used for fitting the hyperfine structure across the entire spectral map. I first generated an integrated intensity map of the central three hyperfine lines, from this map I selected each pixel with  $3\sigma$  detection of  $\text{N}_2\text{H}^+$  or  $\text{NH}_3$  and then generated a CLASS script to fit the hyperfine structure at each point and write out a table containing these data. The fitting does not require all hyperfine components to have  $3\sigma$  detections,

only that there are clear detections of the strongest hyperfine lines. Points where the fitting failed due to inadequate signal-to-noise were removed from the final table. The table is then used for plotting maps of the velocity field, linewidth, optical depth, and excitation temperature, all of which are all determined from fitting the hyperfine structure. The zeroth-moment maps (integrated intensity) are computed simplistically by measuring the intensity of the hyperfine lines within a given velocity range, summing the emission, and multiplying by the channel velocity width. The basic emission properties of  $\text{N}_2\text{H}^+$  and  $\text{NH}_3$  are separated into three tables: Table 5.6 for the single-dish  $\text{N}_2\text{H}^+$ , Table 5.7 for the interferometric  $\text{N}_2\text{H}^+$ , and Table 5.8 for the VLA  $\text{NH}_3$  data. These tables list the line center velocities, linewidths, maximum integrated intensities, total optical depth of the transition (sum of optical depths for each component), excitation temperature, column density (following Goldsmith & Langer (1999) for  $\text{N}_2\text{H}^+$  and (Bourke et al., 1995b) for  $\text{NH}_3$ ), envelope mass as a function of assumed abundance, and approximate envelope radii.

### 5.2.6.2 Velocity Gradient Fitting

Using the line center velocities computed from the hyperfine fitting, the velocity gradients are computed for each object in three ways. First I simply computed the velocity difference between two points offset from the protostar by 10000 AU, normal to the outflow direction, and divided by the distance. Second, I computed a linear fit to cuts through the velocity data, taken normal to the outflow using points within  $\pm 30''$  of the protostar and/or within the region of the cloud directly associated with the protostar. Lastly, I fit a plane to the entire velocity field using the method described in Goodman et al. (1993), but using my own IDL implementation coupled with the MPFIT routines (Markwardt, 2009). The line-center velocity field was fit with the function

$$v_{LSR} = v_0 + a\Delta\alpha + b\Delta\delta \quad (5.2)$$

where  $v_0$  is the systemic velocity,  $\Delta\alpha$  and  $\Delta\delta$  are offsets in right ascension and declination (in arcseconds) and  $a$  and  $b$  are the velocity gradients per arcseconds in the

$\alpha$  and  $\delta$  directions respectively. The total velocity gradient is then given by

$$g = (a^2 + b^2)^{1/2} \times \frac{206264.98}{D} \quad (5.3)$$

with a position angle (PA) east of north (toward increasing velocity) given by

$$\theta_g = \tan^{-1} \frac{b}{a} \quad (5.4)$$

where  $D$  is the distance in parsecs and the constant is the number of arcseconds per radian. All three methods are used on the single-dish data and only the latter two methods on the interferometer data since the extent of  $\text{N}_2\text{H}^+$  and  $\text{NH}_3$  emission varies widely from object to object.

### 5.2.7 Extended Structure Sensitivity

As a general rule, interferometers filter-out large-scale emission; however, if there is a velocity gradient and the lines are well-resolved, the largest scale of emission in a given channel may only be a fraction of the full structure. Thus, different portions of the envelopes become visible in different velocity channels and the integrated intensity maps (zeroth-moment) build a picture of the envelope emission from the multiple velocity components. If all of this emission had resided in one velocity channel, substantially more emission would have been filtered-out. Furthermore, the filamentary nature of many envelopes enabled them to be viewed over a larger area than an envelope that fills the primary beam more evenly.

I do not combine the single-dish and interferometer data because each probe different size scales and it is often advantageous to have the large-scale emission resolved-out of the interferometer maps. Resolving-out the large-scale emission isolates the regions of compact emission in the inner envelope where there may be significant detail in the velocity field. Furthermore, the analysis of only the kinematic structure does not necessitate recovery of all flux; a detailed summary of the steps needed to combine single-dish data with CARMA observations is given in Koda et al. (2011).

### 5.3 Results

I mapped the regions around each protostar where the presence of  $8\mu\text{m}$  extinction was detected in Chapter 4. Each envelope was observed to be a bright source of  $\text{N}_2\text{H}^+$  ( $J = 1 \rightarrow 0$ ) (hereafter  $\text{N}_2\text{H}^+$ ) emission in the single-dish data;  $\text{N}_2\text{H}^+$  emission was present over much of the area where extinction at  $8\mu\text{m}$  is detected in each map, shown in Figures 5.1 through 5.23.  $\text{N}_2\text{H}^+$  or  $\text{NH}_3$  (1,1) (hereafter  $\text{NH}_3$ ) is also detected toward all sources in the interferometer data. The interferometer observations select out the regions of brightest, compact emission which are usually associated with the densest regions of the protostellar envelope. Furthermore, there are many cases where the  $\text{N}_2\text{H}^+$  or  $\text{NH}_3$  emission peak is not centered on the protostar in the single-dish and/or interferometer observations (see Section 5.4.5). The protostar positions in Figures 5.1 through 5.23 are derived from their 3mm continuum source, which is often coincident with the  $8\mu\text{m}$  point source (see Appendix), or the  $24\mu\text{m}$  source where continuum data were not available.

The outflow direction and the angular width of the cavity is known for all objects in the sample from the *Spitzer* IRAC data. This gives an observational constraint on the region in which the outflow may impact the envelope. These data enable the characterization of kinematic properties of the envelopes and determination of the origin of the kinematic structure. It can determine whether the kinematics reflect the intrinsic velocity structure of the core/envelope or if the outflow is likely affecting the observed kinematics. Such distinction is critical to ensure that I am not misled in further interpretation. While kinematic information is missing from the *Spitzer* images (i.e. blue and red-shifted sides traced by CO emission), this information is readily available in the literature for most objects (Table 5.1). Note that the blue and red-shifted outflow directions can also be inferred from the scattered light morphology and intensity (Whitney et al., 2003a).

#### 5.3.1 Similarity of $\text{N}_2\text{H}^+$ and $\text{NH}_3$ Emission Properties

Since the interferometric observations mapped either  $\text{NH}_3$  or  $\text{N}_2\text{H}^+$  for most protostars and the single-dish data solely mapped  $\text{N}_2\text{H}^+$ , it is important to demonstrate

that the kinematic structure observed in the two tracers is consistent. I have observed the envelope around L1157 in  $\text{N}_2\text{H}^+$  with the IRAM 30m, CARMA (Chiang et al., 2010), and the PdBI, while observing it in  $\text{NH}_3$  with the VLA. The  $\text{NH}_3$  and  $\text{N}_2\text{H}^+$  emission both closely follow the regions of  $8\mu\text{m}$  extinction as shown in Figures 5.1 and 5.2 and the velocity maps have a very similar structure. The similar spatial emission and kinematic properties indicate that emission from these molecular species arises from approximately the same region of the envelope (from 0.1 pc to 1000 AU). Further comparisons of the sample can be made to data in the literature: Chen et al. (2007) for CB230 and IRAS 03282+3035, L1527 with Goodman et al. (1993), HH211 with Tanner & Arce (2011), and L483 with Fuller & Wootten (2000). In all these cases, the  $\text{N}_2\text{H}^+$  and  $\text{NH}_3$  emission is detected in the same regions of the envelope with similar kinematic properties. This confirms that  $\text{N}_2\text{H}^+$  and  $\text{NH}_3$  trace similar physical conditions at the level of precision probed in these data, in agreement with the results from Johnstone et al. (2010). Section 5.4.5 further discusses the impact of chemistry on these species.

### 5.3.2 Velocity Gradients

I have computed velocity gradients for all objects using both the single-dish and interferometer data with the methods described in Section 5.2.6.2. The velocity gradients calculated from the single-dish data are given in Table 5.9 and the interferometric ( $\text{N}_2\text{H}^+$  and  $\text{NH}_3$ ) velocity gradients are listed in Table 5.10. The gradient directions from the 2D fitting are plotted in Figures 5.1 - 5.23 and also listed in Tables 9 and 10. The one-dimensional (1D) cuts through the velocity fields, normal to the outflow and across equatorial plane of each envelope, are shown in Figure 5.24 presenting an alternative view of the envelope velocity structure. Linear fits to the single-dish and interferometer data are overlaid on the plots. Notice that in some cases the velocity of the interferometer data diverges from the single-dish data. This results from the interferometer filtering-out larger-scale emission that dominated the single-dish data and the increased resolution picking out smaller-scale velocity structure.

The gradients calculated for the single-dish data with each method are compara-

ble. The median single-dish velocity gradients from the different fitting methods are:  $2.1 \text{ km s}^{-1} \text{ pc}^{-1}$  (1D fitting),  $1.7 \text{ km s}^{-1} \text{ pc}^{-1}$  (1D two points), and  $2.2 \text{ km s}^{-1} \text{ pc}^{-1}$  (2D fitting); the mean gradients are 2.3, 2.2, and  $2.04 \text{ km s}^{-1} \text{ pc}^{-1}$  respectively. The distribution of single-dish velocity gradients from the three methods is shown in Figure 5.25. The lower values of the two point method reflect that the region inside the 10000 AU radius of some sources has a higher velocity gradient; there are velocity decreases toward the edges of some envelopes that are reflected in the plots in Figure 5.24, yielding a preference toward lower gradients in Figure 5.25.

The mean velocity gradient of the single-dish sample ( $\sim 2.2 \text{ km s}^{-1} \text{ pc}^{-1}$ ) is about twice the average gradient in Goodman et al. (1993) and slightly higher than Caselli et al. (2002), but the sample of 16 objects is smaller than their larger samples. Larger observed velocity gradients are expected with the higher resolution data because the lower resolution data in Goodman et al. (1993) and Caselli et al. (2002) tend to smear velocity components together. L483 was common between my work and the two previous studies, with very similar gradient magnitudes and PAs. L1527 and L1152 were also common between my work and Goodman et al. (1993). The gradient directions fit for these sources were similar, but the magnitude of the gradients are different. I regard my values as being more reliable because my maps are comprised of substantially more independent points.

The interferometric sample has a median velocity gradient of  $8.1 \text{ km s}^{-1} \text{ pc}^{-1}$  from 2D fitting and  $10.7 \text{ km s}^{-1} \text{ pc}^{-1}$  from 1D fitting, both having a mean gradient of  $8.6 \text{ km s}^{-1} \text{ pc}^{-1}$ . The distribution of interferometric velocity gradients from the two methods is shown in Figure 5.26. The interferometric gradients are often larger than the single-dish gradients by factors of several. The 2D fitting method was less reliable for the interferometric data given the often complex velocity fields present within the data. Reliable 2D fits could not be obtained for L1157 (PdBI data) or Serpens MMS3 due to lack of convergence on their complex velocity fields. The range of observed velocity gradients is comparable to what Chen et al. (2007) found; however, they found three protostellar systems with gradients  $> 20 \text{ km s}^{-1} \text{ pc}^{-1}$ , such large gradients are not found in these data.

Using the outflow PAs derived from the *Spitzer* imaging and CO data from the literature, I have compared the gradient PAs (the angle toward increasing velocities) with the outflow PAs in Figure 5.27. The gradient position angles are also marked in Figures 5.1 - 5.23 with solid arrow; the majority of the velocity gradients are within  $45^\circ$  of normal to the outflow. The distribution of interferometric velocity directions strongly shows a trend for being oriented normal to the outflow axis. The gradient directions also generally reflect what is seen at large-scales in the single-dish data. Table 5.10 and Figure 5.28 show that only three systems have velocity gradient directions which differ by more than  $45^\circ$  between the single-dish and interferometric measurements.

The majority of envelopes in the interferometric sample have an ordered velocity structure, despite their often complex morphological structure. In contrast to Volgenau et al. (2006) and Chen et al. (2007), many systems have velocity gradients roughly normal to the outflow direction, this likely results from my larger sample of observations as compared to the Chen et al. (2007) and especially Volgenau et al. (2006). In addition, visual inspection of the data shows that the large and small-scale velocity gradient directions are generally consistent with one another, a feature which Volgenau et al. (2006) also sees in their sample. The interferometer observations often reveal small-scale kinematic detail near the protostar that is smeared-out in the lower-resolution single-dish data.

### 5.3.3 Description of Individual Sources

I will describe the dataset for each source individually in the following subsections and discuss the results as a whole in Section 5.4.

#### 5.3.3.1 L1157

The flattened, filamentary envelope of L1157 has been extensively studied in recent years (e.g. Looney et al., 2007; Chiang et al., 2010, Chapter 4). Its velocity field was first studied in Chiang et al. (2010), which showed a weak velocity gradient along the filament, normal to the outflow. I subsequently observed L1157 with the IRAM 30m, the PdBI, and the VLA. Figure 5.1 shows the data from the IRAM 30m and

PdBI and Figure 5.2 shows the data from the VLA and CARMA. The 30m data detects a large-scale velocity gradient normal to the outflow and this gradient follows the long axis of the envelope. On the east side of the envelope, where the emission curves downward, the  $\text{N}_2\text{H}^+$  continues to trace dense material as it becomes more blue-shifted.

The PdBI data are shown in the bottom panels of Figure 5.1. The  $\text{N}_2\text{H}^+$  emission appears double-peaked on small-scales. The 3mm dust continuum shows that the protostar resides between the peaks (see Appendix); the peaks are at radii of  $\sim 1000$  AU ( $\sim 3.5''$ ). The velocity field on scales  $> 15''$  reflects what has been seen with the CARMA, 30m, and VLA data. On the other hand, the velocity of the gas becomes highly red-shifted ( $\sim 1 \text{ km s}^{-1}$ ) at the  $\text{N}_2\text{H}^+$  peaks as compared to the surrounding gas at  $\sim 1000$  AU from the protostar. The high-velocity gas was observed in Chiang et al. (2010); however, its spatial location was not well-resolved in the CARMA data due to having a factor of  $\sim 2$  lower resolution than the PdBI data. Note that the 2D velocity gradient fits for the VLA and CARMA data have position angles that differ by  $80^\circ$ . This results from the north-south gradient being more prominent in the CARMA  $\text{N}_2\text{H}^+$  data while the east-west gradient appears more prominent in the  $\text{NH}_3$  data. A 2D gradient could not be fit to the PdBI data due to the highly complex velocity field present on small-scales.

The single-dish velocity and linewidth maps show a gradual large-scale velocity gradient in L1157 with broad linewidth in the inner envelope, consistent with the PdBI linewidth map in Figure 5.1. The broad linewidths were also shown in lower resolution data from Chiang et al. (2010). Both the east and west peaks in the PdBI maps have velocity wings toward the red and are not significantly extended toward blue-shifted velocities. Chiang et al. (2010) attributed the broad inner envelope line wings to infall. However, close examination of the higher-resolution PdBI data indicate that the blue and red-shifted line wings may result from outflow interaction effects. Figure 5.3 shows that the most red-shifted emission is slightly shifted to the southeast, along the outflow and traces one edge of the northern outflow cavity. Furthermore, the blue-shifted emission also seems to outline the southern outflow cavity

quite well. Thus, it appears that the outflow is entraining inner envelope material, while at larger scales the velocity structure appears unaffected by the outflow, tracing the intrinsic kinematic structure of the envelope. The spatial overlap of red and blue-shifted  $\text{N}_2\text{H}^+$  southeast of the protostar on the blue-shifted side of the outflow can be understood if the outflow is entraining material within a symmetric cavity in the inner envelope, producing both a blue and red-shifted component. There also appear to be outflow effects in the  $\text{N}_2\text{H}^+$  emission on the northwest side of the protostar but to a lesser extent. This is the first example of possible outflow entrainment in such a dense gas tracer. However, I note that rather than entrainment, the broad  $\text{N}_2\text{H}^+$  emission could also result from an outflow shock at that location.

### 5.3.3.2 L1165

The protostar L1165IRS is located within a  $\sim 1.5$  pc ( $17'$ ) long filamentary dark cloud (Chapter 4). The narrow filament, from which the protostar has formed, is normal to the protostellar outflow. I mapped a  $4'$  section of the dark cloud surrounding the protostar, as shown in the left panels of Figure 5.4. The  $\text{N}_2\text{H}^+$  emission is highly peaked very near the protostar, it is slightly offset  $4.87''$  ( $\sim 1462$  AU) to the southeast, and there is low-level extended emission associated with regions of  $8\mu\text{m}$  extinction. The velocity field from the single-dish  $\text{N}_2\text{H}^+$  data shows a fairly linear gradient nearly normal to the outflow; in areas away from the protostar the filament generally seems to have a fairly constant velocity with little variation and small linewidth.

The  $\text{N}_2\text{H}^+$  data from CARMA reveal a small-scale structure that is extended in the direction of the filament axis and the emission is strongly correlated with the small-scale  $8\mu\text{m}$  extinction shown in Figure 5.4. At the edges of detected emission, the velocity field of the interferometer map is consistent with the single-dish data. However, near the protostar there is a  $0.35$  km/s velocity shift between the blue and red-shifted velocity peaks that are on opposite sides of the protostar. I note that this velocity gradient is not perfectly normal to the outflow, but rather offset by about  $\sim 30^\circ$ . However, the most red-shifted emission is slightly extended in the direction of the outflow, but the linewidth peak is extended normal to the outflow and the

red-shifted emission at this location does not appear to be outflow affected. Thus, the gradient from the envelope itself appears to be normal to the outflow and tracing gravitationally dominated motion.

I show the  $\text{HCO}^+$  emission in Figure 5.5, in which the red and blue-shifted emission is confined to two clumps, that are oriented normal to the outflow and offset from the protostar by  $3''$ . The position-velocity plot of these data show the blue and red-shifted emission extending  $\sim 2$  and  $\sim 1.5 \text{ km s}^{-1}$  away from the systemic velocity respectively. Given the orientation of the blue and red-shifted emission normal to the outflow and a lack of emission along the outflow, the  $\text{HCO}^+$  emission appears to be originating from the inner envelope. Assuming that the  $\text{HCO}^+$  emission indicates rotationally supported motion, the enclosed mass can be calculated using  $M = R\Delta v^2/G$  which gives  $M_{enc} \sim 2.0M_{\odot}$ . This is not unreasonable for this source which has  $L_{bol} \sim 14L_{\odot}$  assuming a distance of 300 pc. However, if the velocities result from equal contributions of rotation and infall, then the enclosed mass would be a more modest  $0.5 M_{\odot}$ . I have overlaid lines representing Keplerian rotation (or infall) on Figure 5.5, the  $0.5 M_{\odot}$  curve matches the data much better than the  $2.0 M_{\odot}$  curve.

### 5.3.3.3 CB230

CB230 is an isolated protostar that formed at one end of its natal globule (Chapter 4). This protostar was discovered to be a wide binary system by Yun (1996) with a separation of  $\sim 10''$ , the companion is evident in the  $8\mu\text{m}$  images shown in Figure 5.6. The envelope around CB230 was classified as a “one-sided” envelope in Chapter 4 due to the  $60''$  (30000 AU) extension of the extinction envelope to the west, while the  $8\mu\text{m}$  extinction terminates just  $\sim 25''$  (6000 AU) on the eastern side. The single-dish  $\text{N}_2\text{H}^+$  emission is consistent with the  $8\mu\text{m}$  extinction observations, the emission falling off steeply to the east and more extended to the west. The large-scale extension of material beyond the region of detected  $\text{N}_2\text{H}^+$  emission suggests that it has lower density and has not formed  $\text{N}_2\text{H}^+$  at detectable levels, see Section 5.4.5 for further discussion.

The  $\text{NH}_3$  emission from the VLA is strongest in a “bar,” about  $10^\circ$  from normal

to the outflow. Notably, at the location of the protostar there is a "hole" in the ammonia emission; a similar depression of emission is seen in  $\text{N}_2\text{H}^+$  ( $J = 1 \rightarrow 0$ ) by Chen et al. (2007) and Launhardt et al. (2001). The region of decreased emission is  $\sim 2200\text{AU}$  in diameter, similar in size to the double-peaked  $\text{N}_2\text{H}^+$  emission in L1157. The lower level emission on the eastern side of the protostar extends northward along the outflow cavity. Incidentally, the northward extension is also where the scattered light emission in the near-IR and *Spitzer*  $3.6\mu\text{m}$  is brightest (Chapter 4; Launhardt et al., 2010).

The velocity field of the single-dish  $\text{N}_2\text{H}^+$  shows a fairly linear gradient, normal to the outflow, with a "plateau" of the most highly red/blue-shifted emission  $\pm 30''$  from the protostar. South of the protostar, the  $\text{N}_2\text{H}^+$  linewidth peaks, similar to L1157. The  $\text{NH}_3$  velocity gradient from the VLA data is in the same direction as the single-dish gradient and similar to the interferometric  $\text{N}_2\text{H}^+$  map from Chen et al. (2007). While the single-dish gradient is fairly gradual, the gradient from the VLA observations has an abrupt shift from blue to red-shifted emission coincident with the protostar. The VLA  $\text{NH}_3$  data also show a velocity "plateau" in the blue and red-shifted emission, with the highest relative-velocity emission being  $\pm 15''$  from the protostar. The linewidth remains fairly constant throughout the regions near the protostar, peaking at  $0.5\text{ km/s}$ . The region of highest linewidth also corresponds to the region of strongest ammonia emission. The large linewidth seen near the protostar in the single-dish data is not reflected in these  $\text{NH}_3$  data nor the  $\text{N}_2\text{H}^+$  data of Chen et al. (2007). The line-center velocity changes quite rapidly at the location of the large single-dish linewidth; therefore, the linewidth peak is likely due to the unresolved velocity gradient. This means that the outflow is not likely to be affecting the kinematics of the inner envelope in this protostar.

#### 5.3.3.4 HH108IRS

The protostar HH108IRS, the driving source of HH108, is located within a large-scale filament,  $\sim 0.5\text{ pc}$  in length,  $1.75^\circ$  south of the Serpens star forming region (Harvey et al., 2006). There are at least two protostars forming in the filament: the

higher luminosity object HH108IRS and the deeply embedded source HH108MMS (Chini et al., 2001). The single-dish  $\text{N}_2\text{H}^+$  map in Figure 5.7 shows an emission peak coincident with HH108IRS, but slightly offset from the protostar  $\sim 5''$  (1500 AU). The  $\text{N}_2\text{H}^+$  map from CARMA reveals that the  $\text{N}_2\text{H}^+$  peak emission is truly offset from the protostar and emission is extended normal to the outflow direction, forming a flattened structure across the protostar.

The single-dish  $\text{N}_2\text{H}^+$  velocity map indicates that there may be a slight gradient normal to the outflow. The CARMA  $\text{N}_2\text{H}^+$  velocity map reveals that there is indeed a velocity gradient normal to the outflow, though its structure is complex. Southeast of the protostar the velocities are red-shifted and moving toward the protostar the velocities are becoming more blue-shifted. This trend continues after crossing the protostar and moving northwest, but then the trend reverses itself rapidly and becomes more red-shifted. I also note that the linewidth is  $\sim 0.6$  km/s within  $\pm 10''$  (3000 AU) around the protostar, indicative of a dynamic environment near the protostar. The single-dish linewidth is consistent with this value as well.

### 5.3.3.5 HH108MMS

HH108MMS is the nearby neighbor to HH108IRS, separated by  $\sim 60''$  ( $\sim 0.09$  pc). This protostar is deeply embedded and invisible at  $24\mu\text{m}$ , only becoming visible at  $70\mu\text{m}$  (Chapter 4). There are no IRAC data available for this object, therefore the ISPI Ks-band ( $2.15\mu\text{m}$ ) image from Chapter 4 is shown. Despite the lack of  $8\mu\text{m}$  extinction observations, it can clearly be seen that the dense material of the envelope is blocking out the rich background star field. The single-dish  $\text{N}_2\text{H}^+$  in Figure 5.8 shows a slight extension toward the location of the protostar (derived from  $70\mu\text{m}$  and 3mm continuum), while the CARMA  $\text{N}_2\text{H}^+$  observations clearly show the  $\text{N}_2\text{H}^+$  emission centrally peaked on the protostar.

The single-dish velocity field does not show much structure, the region within  $\pm 30''$  (0.045 pc) of the protostar has a roughly constant velocity. The filament that HH108MMS is forming within has a velocity gradient of  $1.6$  km s $^{-1}$  pc $^{-1}$  running from southwest to northeast. The CARMA  $\text{N}_2\text{H}^+$  velocity map on the other hand

shows significant structure on  $\sim 10''$  scales within  $\pm 15''$  ( $\sim 0.02$  pc) of the protostar. Southeast of the protostar the emission is red-shifted and northwest there is blue-shifted emission, along the presumptive outflow axis and HCN emission mapped with CARMA (Tobin et al. 2011 in preparation). The outflow axis is determined from faint diffuse emission seen in Ks-band. The CARMA map also shows increased linewidth along the outflow; there is no indication of such an increase in the single-dish map, likely due to beam dilution. HH108MMS appears to be a prime example of the outflow impacting the envelope of a deeply embedded protostar.

### 5.3.3.6 Serpens MMS3

Serpens MMS3 is located within a complex network of filamentary structure in the Serpens B cluster (Djupvik et al., 2006; Harvey et al., 2006), shown in Figure 5.9. One of the most prominent filaments runs  $\sim 0.1$  pc in length into Serpens MMS3, see left panels of Figure 5.9. Directly west of the protostar the filament turns southward toward a small clustering of bright young stars. I also noticed that Serpens MMS3 has a faint companion separated by  $\sim 7''$ .

The single-dish  $\text{N}_2\text{H}^+$  map shows that the emission is highly pervasive throughout the region. The emission is peaked near the clustering of young stars in the southwest corner of the image in Figure 5.9. However, the emission is extended toward Serpens MMS3 and there is enhancement emission coincident with the large scale filament seen in  $8\mu\text{m}$  extinction. The VLA  $\text{NH}_3$  map reveals the structure of the region in substantially more detail. The interferometer resolved out whatever diffuse  $\text{NH}_3$  emission was in the region and the remaining emission directly correlates to the highest extinction regions seen in the  $8\mu\text{m}$  image, with a peak coincident with the Serpens MMS3 protostar. The  $\text{NH}_3$  emission is still extended toward the clustering of young stars in the southwest, but it is at the edge of the primary beam.

The overall velocity structure of this region is confusing in the single-dish  $\text{N}_2\text{H}^+$  velocity map because of the multitude of high-density structures in the region; however, there is a large scale gradient along the filament that Serpens MMS3 resides in and there is also a pocket of red-shifted emission next to the protostar. The VLA  $\text{NH}_3$

(1,1) map also shows this large scale gradient along the filament of Serpens MMS3 and red-shifted emission next to the protostar. The red-shifted emission appears over a region  $15''$  from the protostar and is extended in the direction of the outflow. I also detected an increased linewidth ( $\sim 1 \text{ km s}^{-1}$ ) next to the protostar. Directly southwest of the protostar the velocity gradient appears to resume the large-scale velocity trend exhibited northeast of the protostar. It is presently unclear if the kinematic structure near the protostar is related to the outflow or infall, but its proximity and extension along the outflow makes me suspicious. However, the broad linewidth is quite localized to the east of the protostar.

### 5.3.3.7 HH211

HH211MMS is a deeply embedded protostar on the outskirts of the IC348 cluster in the Perseus molecular cloud; emission from the central protostar itself only becomes evident at  $70\mu\text{m}$  (Rebull et al., 2007) and has been found to be a proto-binary in the submillimeter (Lee et al., 2009). There is a large absorbing structure in the  $8\mu\text{m}$  extinction map shown in Figure 5.10, as well as its powerful outflow (McCaughrean et al., 1994; Gueth & Guilloteau, 1999). The single-dish  $\text{N}_2\text{H}^+$  emission associated with HH211MMS is very strong, peaked to the southwest of the protostar itself. The  $\text{N}_2\text{H}^+$  emission also appears extended in the direction of the higher extinction areas. The  $\text{N}_2\text{H}^+$  emission mapped with CARMA detects emission on small scales around the protostar, with the emission peak offset  $\sim 2''$  southwest of the protostar (not coincident with the single-dish  $\text{N}_2\text{H}^+$  peaks). The emission is more extended along the northwestern side of the outflow, consistent with the extinction seen in the  $8\mu\text{m}$  image.

The single-dish  $\text{N}_2\text{H}^+$  velocity map shows a linear velocity gradient normal to the outflow and south of the protostar there is another velocity component in the dense gas. The transition between these two velocity components appears as an area of artificially large linewidth (an artifact from fitting); however, there are two sets of narrow emission lines present, not broad lines. The CARMA  $\text{N}_2\text{H}^+$  velocity map also finds a linear gradient normal to the outflow as well as the second velocity component

to the south. I also note that near the protostar the gradient is not perfectly linear at all scales. The deviance from a linear gradient is slight; however, it is present where there is excellent signal-to-noise and this agrees with the velocity map by Tanner & Arce (2011).

The linewidths in the single-dish data were quite low across the source, only 0.3 - 0.4 km s<sup>-1</sup> with similar levels seen in the CARMA N<sub>2</sub>H<sup>+</sup> map. I note that there is an area of increased linewidth just southeast of the protostar, apparently at the base of the outflow. I suggest that the increased linewidth in this region is due to outflow interaction, in agreement with Tanner & Arce (2011). In addition, the filament northeast of the protostar has a very narrow linewidth, <0.2 km s<sup>-1</sup>, appearing both the single-dish and interferometer maps.

### 5.3.3.8 IRAS 16253-2429

IRAS 16253-2429 is a low-luminosity ( $L_{Bol} = 0.25L_{\odot}$ ) Class 0 protostar in the  $\rho$  Ophiuchus star forming region; it is also identified as Oph MMS 126 (Stanke et al., 2006). I noted in Chapter 4 that this was one of the more “symmetric” envelopes seen in the 8 $\mu$ m extinction study. Its symmetric bipolar outflow has been traced in CO by Stanke et al. (2006) as well as in shocked H<sub>2</sub> emission from *Spitzer* IRS spectral mapping (Barsony et al., 2010).

The single-dish N<sub>2</sub>H<sup>+</sup> shown in Figure 5.11 correlates quite well with the 8 $\mu$ m extinction. The emission peak is slightly offset from the location of the protostar and the N<sub>2</sub>H<sup>+</sup> emission appears to be depressed at the location of the outflow cavities. The CARMA N<sub>2</sub>H<sup>+</sup> emission shows similar features in that it strongly correlates with the regions of 8 $\mu$ m extinction and there is less emission in regions occupied by the outflow cavities. The lack of emission within the outflow cavities is likely due to evacuation of envelope material and/or destruction of N<sub>2</sub>H<sup>+</sup> by CO in the outflow (section 5.4.2); there may also be some interferometric filtering-out of emission in this region. Furthermore, there appears to be a deficit of N<sub>2</sub>H<sup>+</sup> emission near the protostar.

The velocity field of the single-dish N<sub>2</sub>H<sup>+</sup> map indicates that there is a very small

velocity gradient across the envelope, approximately normal to the outflow; note the small velocity range occupied by the envelope and velocity gradient. The velocity map from the CARMA  $\text{N}_2\text{H}^+$  data is more complex with several gradient reversals throughout the emitting region. However, the global gradient still seems to be present in interferometer data. Furthermore, a VLA  $\text{NH}_3$  map shows a velocity structure very similar to the CARMA  $\text{N}_2\text{H}^+$  map (J. Wiseman, private communication).

The single-dish  $\text{N}_2\text{H}^+$  linewidth is quite small and constant across the envelope, whereas many other objects in the sample have linewidths which peak near the protostar. I also note that the linewidth is increasing in this source toward the edge of  $\text{N}_2\text{H}^+$  emission along the outflow; this is likely an outflow interaction effect. The CARMA  $\text{N}_2\text{H}^+$  map shows a similar small linewidth across the most of the envelope; however, there is a region of increased linewidth east and south of the protostar associated with an area of strong  $\text{N}_2\text{H}^+$  emission; at this location there is a slight enhancement of linewidth in the single-dish map.

### 5.3.3.9 L1152

The L1152 dark cloud is located in Cepheus, about 1.7 pc ( $20'$ ) away from L1157 on the sky. L1152 hosts three young stars; however, only one (IRAS 20353+6742) is classified as a Class 0 object and it is the only one embedded in the main core of L1152 (Chapman & Mundy, 2009). Chapter 4 found that the main core of L1152 appears to have a “dumbbell” morphology in which the northeastern core (see Figure 5.12) appears to be starless and the southeastern core harbors IRAS 20353+6742 (hereafter L1152). These two concentrations are connected by what appears to be a thinner filament of high density material.

The single-dish  $\text{N}_2\text{H}^+$  ( $J = 1 \rightarrow 0$ ) emission shown in Figure 5.12 exactly matches the morphology of the extinction in the  $8\mu\text{m}$  images. However, the peak  $\text{N}_2\text{H}^+$  emission in the southwestern core is offset from the protostar by  $\sim 20''$  (6000 AU). The  $\text{N}_2\text{H}^+$  map from CARMA shown in the right panel of Figure 5.12 only observed the southeastern core. The map confirms that the  $\text{N}_2\text{H}^+$  is substantially offset from the protostar and there is no sub-peak at its location. However, the  $\text{N}_2\text{H}^+$  emission

appears to extend toward the protostar.

The single-dish  $\text{N}_2\text{H}^+$  velocity field exhibits a velocity gradient normal to the outflow of L1152, noting that the protostar appears at the edge of the region exhibiting the gradient. The rest of the cloud, including the star-less core, has a fairly constant velocity; only varying by  $\sim 0.1$  km/s. However, increased linewidths northeast and southwest of the protostar are noted. Southwest of the protostar the jet from the protostar can clearly be seen, possibly interacting with envelope material, then in the northeast there is nothing obvious happening at this linewidth peak in the  $8\mu\text{m}$  image. However, the northeast linewidth peak is near the outflow axis and this could be the cause of the increased linewidth at this location.

The velocity map from the CARMA  $\text{N}_2\text{H}^+$  data tells a remarkably similar story to the single-dish data; the velocity gradient is only slightly better resolved. However, the most remarkable feature is in the linewidth map, where there is an increase in linewidth on the axis of the jet that is visible in the  $8\mu\text{m}$  maps. This appears to be another very clear example of the outflow interacting with the envelope material, though the velocity field does not seem to show outflow effects.

### 5.3.3.10 L1527

L1527 (IRAS 04368+2557) is an extensively studied protostar in Taurus. Benson & Myers (1989) observed its compact  $\text{NH}_3$  core, from which Goodman et al. (1993) derived its velocity gradient. Subsequent observations indicated the possibility of infall in the envelope from  $\text{H}_2\text{CO}$  observations by Myers et al. (1995). Furthermore, detailed modeling of its scattered light cavities observed in *Spitzer* IRAC imaging have been done by Tobin et al. (2008) and Gramajo et al. (2010). High-resolution mid-infrared imaging by Tobin et al. (2010a) found the signature of a large ( $R\sim 200$  AU) disk in scattered light.

IRAC  $8\mu\text{m}$  imaging of this source revealed an asymmetric distribution of extinction, the northern side of the envelope is substantially more extended than the southern side. This asymmetry is also exhibited in the single-dish  $\text{N}_2\text{H}^+$  data shown in Figure 5.13; in addition, the peak emission is also offset to the north of the protostar

by  $\sim 25''$  (3500 AU). The VLA  $\text{NH}_3$  and CARMA  $\text{N}_2\text{H}^+$  maps both show emission associated with the protostar, but the maps are somewhat difficult to interpret due to the likelihood of spatial filtering. In addition, the CARMA observation was done as a mosaic in order to cover the entire region of emission as the primary beam is only  $70''$ ; both maps seem to detect emission in the same general areas.

The velocity field from the single-dish  $\text{N}_2\text{H}^+$  map has a complicated morphology. There appear to be two velocity gradients in the map, one along the outflow (pointed out by Myers et al. (1995)) and another normal to the outflow isolated by Goodman et al. (1993). However, the gradient along the outflow is not linear, the velocities go from red to blue and back to red. The linewidth remains fairly constant throughout the map, with a minimum at the northeast and southwest edges of the map.

The velocity fields from both the VLA and CARMA reveal further kinematic complexity in this system. The consistency with the single-dish velocity map on large-scales can be seen; however, the  $\text{N}_2\text{H}^+$  and  $\text{NH}_3$  maps show that there is a small-scale velocity gradient near the protostar. Notice that this small-scale velocity gradient is in the opposite direction as compared to the large-scale gradient. The linewidths of the  $\text{N}_2\text{H}^+$  and  $\text{NH}_3$  exhibit a corresponding increase in the inner envelope, near these small-scale velocity gradients. This is the only protostellar envelope that where a velocity gradient reversal is seen going from large to small-scales.

### 5.3.3.11 RNO43

RNO43 is protostar forming within the  $\lambda$  Ori ring. On large scales the envelope is quite asymmetric, with several filamentary structures appearing to converge at the location of the protostar as shown in the left panels of Figure 5.14. RNO43 also drives a powerful, parsec-scale outflow; CO emission has been mapped on small scales by Arce & Sargent (2005) tracing an outflow cavity and on large-scales, tracing a  $\sim 5$  pc long outflow (Bence et al., 1996). The  $\text{N}_2\text{H}^+$  emission is mostly unresolved in the single-dish map as shown in Figure 5.14. The peak emission is located near the location of the protostar and there are slight extensions in the direction of the outflow.

The CARMA  $\text{N}_2\text{H}^+$  ( $J = 1 \rightarrow 0$ ) map traces the small-scale structure seen in

8 $\mu$ m extinction very well. Note the depression of N<sub>2</sub>H<sup>+</sup> emission at the location of the protostar, consistent with observations of other protostars in the sample; see Section 5.4.5 for further discussion of this feature. East of the protostar there is a ridge of N<sub>2</sub>H<sup>+</sup> emission which is composed of the three bright knots almost running north-south in the image extending  $\sim 35''$ . The southern-most knot is associated with the highest column density region east of the protostar and the two northern knots correlate well with an extinction filament running from the north into the envelope of RNO43. In addition, this filament of 8 $\mu$ m extinction and N<sub>2</sub>H<sup>+</sup> emission are coincident with the brightest part of the outflow cavity in the *Spitzer* 3.6 $\mu$ m image (Chapter 4). Directly west of the protostar, there is another peak of N<sub>2</sub>H<sup>+</sup> emission and weaker N<sub>2</sub>H<sup>+</sup> emission extended further west, in agreement with the 8 $\mu$ m extinction. Chen et al. (2007) mapped this region in N<sub>2</sub>H<sup>+</sup> using OVRO, the data agree quite well with the observations. However, the map appears to have recovered more large-scale emission, likely due to better uv-coverage at short spacings.

The velocity field from the single-dish N<sub>2</sub>H<sup>+</sup> map shows a large scale velocity gradient that is nearly normal to the outflow axis and there is an area of enhanced linewidth southeast of the protostar. The CARMA data reveal significant kinematic detail in the velocity field of the N<sub>2</sub>H<sup>+</sup> gas. The CARMA velocity maps in Figure 5.14 clearly show red and blue-shifted sides of the envelope; however, separating those sides of the envelope is a sharp velocity jump from blue to red by  $\sim 0.7$  km s<sup>-1</sup>. Due to the overlapping lines at the location of the protostar, the N<sub>2</sub>H<sup>+</sup> linewidth forms a line marking the jump in velocity. There also appears to be a north-south gradient in the interferometer data as well (the single-dish map hints at this). Chen et al. (2007) ignored the western, red-shifted portion of the envelope thinking that it was a line-of-sight alignment with another clump; however, the envelope has density increasing in 8 $\mu$ m extinction toward the protostar on both sides (shown in Chapter 4), suggesting that the western side is indeed part of the same structure.

I note that the most highly blue-shifted gas is not located directly adjacent to the protostar; this is likely due to the absence of N<sub>2</sub>H<sup>+</sup> near the protostar, as mentioned earlier. Furthermore, small-scale emission of HCO<sup>+</sup> was also detected with similar

morphology to L1165 (Figure 5.5). Figure 5.15 shows that the centroid of blue and red-shifted emission are located normal to the outflow and are offset from each other by  $\sim 3''$  (1400 AU). In RNO43, the  $\text{HCO}^+$  line wings extend  $\pm \sim 2$  km/s from the systemic velocity. If it is assumed that the  $\text{HCO}^+$  emission reflects only rotation, its velocities would imply an enclosed mass of  $2.7M_{\odot}$ . If only half of this velocity is due to rotation then the enclosed mass would be  $0.67M_{\odot}$ . The bolometric luminosity of RNO43 is  $\sim 8.0L_{\odot}$ ; comparable to L1165 in both luminosity and mass. I have overlaid lines representing Keplerian rotation (or infall) on Figure 5.15, the  $0.67M_{\odot}$  curve matches the data much better than the  $2.67M_{\odot}$  curve.

Note that the outflow position axis has been redefined to be  $20^{\circ}$  east of north in contrast to the  $54^{\circ}$  found by Arce & Sargent (2005); my value is more accurate taking into account the outflow cavity observed by *Spitzer* (Figure 5.14) and CO maps from both Arce & Sargent (2005) and Bence et al. (1996). Furthermore, Chen et al. (2007) assumed the  $54^{\circ}$  outflow position axis, leading them to interpret the velocity gradient along the eastern ridge as symmetric rotation. The  $\text{N}_2\text{H}^+$  gradient across the protostar has a very similar direction to the  $\text{H}^{13}\text{CO}^+$  and  $\text{C}^{18}\text{O}$  velocity gradients found by Arce & Sargent (2005). However, my revised outflow axis and the observed  $\text{N}_2\text{H}^+$  velocity structure, in conjunction with the  $\text{H}^{13}\text{CO}^+$  and  $\text{C}^{18}\text{O}$  data, lead me to suggest that envelope material is not likely being “pushed out” in this system, as suggested by Arce & Sargent (2005). Thus, the  $\text{N}_2\text{H}^+$  velocity structure appears to reflect kinematic structure intrinsic to the envelope.

### 5.3.3.12 IRAS 04325+2402

IRAS 04325+2402, sometimes referred to as L1535, harbors a multiple Class I protostellar system in the Taurus star forming region. The primary is possibly a sub-arcsecond binary with a wider companion separated by  $8.2''$  (Hartmann et al., 1999). The  $8\mu\text{m}$  extinction around IRAS 04325 was found in the envelope study but not published in Chapter 4 due to its low signal-to-noise; however, Scholz et al. (2010) noticed the  $8\mu\text{m}$  extinction in their study of the system. These authors pointed out that there is a bright diffuse region of emission at  $3.6$  and  $4.5\mu\text{m}$ , at the peak of the

$8\mu\text{m}$  extinction. Furthermore, they noticed a dark band between the protostar and the  $4.5\mu\text{m}$  diffuse emission, suggesting a dense cloud; however, there is a lack of  $8\mu\text{m}$  extinction at the location of the dark band.

Emission throughout the core surrounding the protostar is seen in the single-dish  $\text{N}_2\text{H}^+$  map, with the peak emission coincident with the  $8\mu\text{m}$  extinction peak and the  $4.5\mu\text{m}$  diffuse scattered light peak. In fact, the  $\text{N}_2\text{H}^+$  is peaked  $\sim 60''$  northeast of the protostar, but the map does show a slight enhancement of  $\text{N}_2\text{H}^+$  emission west of the protostar. Given this emission morphology, I suggest that the dark band seen at  $4.5\mu\text{m}$  is really just a lack of material and that the diffuse emission is light from the protostar shining onto the neighboring star-less core. There are no interferometry data for this object, however it would not be expected to observe substantial  $\text{N}_2\text{H}^+$  emission peaked around the protostar, based on the single-dish map.

The velocity structure of the  $\text{N}_2\text{H}^+$  shows that there is a relatively smooth velocity gradient across the entire object with an increased gradient just southeast of the protostar. The linewidth of  $\text{N}_2\text{H}^+$  however shows large increase along the outflow axis of the protostar. Thus, the outflow from the protostar may be interacting with the dense material in the surrounding core producing the increased linewidth. On the other hand, the velocity field does not seem to show effects from the outflow, similar to L1152.

### 5.3.3.13 L483

L483 is an isolated globule harboring a Class 0 protostar (Tafalla et al., 2000). The envelope surrounding the protostar is quite large,  $\sim 0.15$  pc in diameter with at least  $10\text{-}20M_\odot$  of material measured from  $8\mu\text{m}$  extinction in Chapter 4. The densest regions seen in  $8\mu\text{m}$  extinction form a “tri-lobed” pattern that is also traced by  $850\mu\text{m}$  emission (Jørgensen, 2004). The single-dish  $\text{N}_2\text{H}^+$  also follows this same pattern with the peak emission coincident with the protostar, see Figure 5.17. The VLA  $\text{NH}_3$  emission is not peaked on the protostar, but also follows the “tri-lobed” morphology. The  $\text{N}_2\text{H}^+$  emission mapped with OVRO by Jørgensen (2004) is extended along the outflow; however, this observation appears to have resolved out a significant amount

of extended emission.

The velocity gradient from the single-dish  $\text{N}_2\text{H}^+$  map is not normal to the outflow but is at an angle of  $\sim 45^\circ$ . The VLA  $\text{NH}_3$  map shows a velocity gradient in the same direction as the single-dish data; however, the protostar is located in a pocket of blue-shifted emission. This is consistent with what Jørgensen (2004) observed. Furthermore, directly north of the protostar, there is an area of highly red-shifted emission seen in the  $\text{NH}_3$  map. The single-dish  $\text{N}_2\text{H}^+$  also shows red-shifted emission in this region, but it is not as prominent due to the larger beamsize. This emission appears to come from another distinct velocity component in the cloud, as evidenced by the large linewidths in the  $\text{NH}_3$  map at the transition to the red-shifted emission.

I also noticed that the  $\text{N}_2\text{H}^+$  linewidth map shows a region of enhanced linewidth running across the envelope, nearly normal to the outflow. This region connects to where there is the second velocity component in the VLA  $\text{NH}_3$  map and this is also where the velocity field is most rapidly changing in the single-dish  $\text{N}_2\text{H}^+$  map. Since the increased linewidth appears to be a global feature I do not attribute it to outflow effects and could be related to the initial formation of the dense core.

#### **5.3.3.14 L673**

The L673 dark cloud in the constellation Aquila has been the subject of a SCUBA survey by Visser et al. (2002) and two *Spitzer* studies by Tsitali et al. (2010) and Dunham et al. (2010). In Chapter 4, I highlighted a small region of the cloud exhibiting highly filamentary  $8\mu\text{m}$  extinction associated with L673-SMM2 as identified in Visser et al. (2002). There are more regions with  $8\mu\text{m}$  extinction within the cloud that I did not focus on in Chapter 4, but are apparent in the images shown by Tsitali et al. (2010). The *Spitzer* IRAC data around L673-SMM2, show four point sources closely associated with the sub-millimeter emission peak and another  $70\mu\text{m}$  source which may be a Class 0 protostar (Tsitali et al., 2010).

The filamentary region around L673-SMM2 is shown in Figure 5.18. The  $\text{N}_2\text{H}^+$  emission maps closely to the  $8\mu\text{m}$  extinction and the  $\text{N}_2\text{H}^+$  peak is centered on the small clustering of protostars. The peak  $\text{NH}_3$  emission from the VLA is located very

near the  $\text{N}_2\text{H}^+$  peak and the dense filament is further traced by the low-level  $\text{NH}_3$  emission; a substantial amount of extended emission is likely resolved out by the interferometer.

The velocity field traced by the single-dish  $\text{N}_2\text{H}^+$  appears to show a gradient along the filament going from north to south and there is an area of blue-shifted emission coincident with the southern protostar marked with an X in Figure 5.18. This southern-most protostellar source is comprised of three sources in higher-resolution Ks-band imaging (Tobin et al. in preparation). In the northeast part of the image, there is another velocity component of  $\text{N}_2\text{H}^+$  present. The linewidths are fairly low across the filament with about a factor of two increase at the location of the protostars; there is an area of artificially large linewidth due to the second velocity component.

The VLA  $\text{NH}_3$  map shows similar velocity structures that were present in the single-dish map; however, it is now clear that the protostar near  $\Delta\delta=0''$  is located in an area of red-shifted emission while the southern protostar is still in a localized area of blue-shifted emission. The line-center velocity shift between these components is 0.4-0.5 km/s. The linewidth peak falls between the two main protostars, coincident with the region of peak  $\text{NH}_3$  emission. Also, the northernmost, deeply embedded protostar appears to be associated with a fairly ordered velocity gradient, north of the two more obvious protostars.

### 5.3.3.15 L1521F

L1521F is a dense core found in the Taurus star forming region. Bourke et al. (2006) found a deeply embedded protostar within what was previously considered a star-less core (Crapsi et al., 2004, 2005). An approximately symmetric extinction envelope was found around L1521F, elongated normal to the outflow in Chapter 4. The  $\text{N}_2\text{H}^+$  integrated intensity correlates very well with the  $8\mu\text{m}$  extinction. The  $\text{NH}_3$  observations from the VLA are also centrally peaked and show a flattened structure normal to the outflow. However, there is an extension to the east, along the outflow.

The velocity structure of the core is complex and appears similar to that of L1527.

The  $\text{N}_2\text{H}^+$  velocity field shows that there is emission blue-shifted relative to the protostar normal to the outflow. Along the outflow there is red-shifted emission toward the edge of the envelope. Crapsi et al. (2004) examined the velocity structure of L1521F finding that the average gradient across the core was  $0.37 \text{ km s}^{-1} \text{ pc}^{-1}$  with a position angle of  $180^\circ$ . With the two dimensional fitting I derive a gradient of  $0.76 \text{ km s}^{-1} \text{ pc}^{-1}$  and a position axis of  $239^\circ$ . The differences between our results likely come from mapping a larger area around the core, which detects more red-shifted emission in the western side of the map, influencing the gradient fit. Otherwise, the emission and velocity structure are quite similar.

The  $\text{NH}_3$  velocity map shows similar structure to the  $\text{N}_2\text{H}^+$  map, and near the protostar there appears to be a gradient emerging normal to the outflow on small-scales. However, the  $\text{NH}_3$  emission is optically thick toward the center of L1521F: the satellite and main lines have approximately equivalent intensities. Therefore, I cannot obtain a better measure of the small-scale kinematic structure. The  $\text{N}_2\text{H}^+$  linewidth map shows a roughly constant  $0.2 - 0.3 \text{ km/s}$  linewidth across the map. The  $\text{NH}_3$  linewidth is similarly low, except at the southern end of the envelope where the blue-shifted emission is present.

### 5.3.3.16 Perseus 5

Perseus 5 is a relatively isolated core in the Perseus molecular cloud, just northeast of NGC1333 and observed by Caselli et al. (2002). The protostar is deeply embedded and is obscured shortward of  $8\mu\text{m}$  with only its outflow as a prominent signpost. It was discovered to have an asymmetric extinction envelope around it in Chapter 4. I did not have the opportunity to take single-dish  $\text{N}_2\text{H}^+$  observations of this object, but I did take data with CARMA as shown in Figure 5.20. The  $\text{N}_2\text{H}^+$  intensity image shows that the entire extinction region is not well traced by the interferometric  $\text{N}_2\text{H}^+$ . The data indicate that substantial emission around this source is resolved-out indicated by the strong negative bowls in the image. However,  $\text{NH}_2\text{D}$  (another molecule observed) does seem to fully trace the envelope seen in  $8\mu\text{m}$  extinction, since emission from this molecule is more spatially compact and not filtered-out by

the interferometer.

The velocity structure is complex in both  $\text{N}_2\text{H}^+$  and  $\text{NH}_2\text{D}$ , showing a blue-shifted feature east of the protostar along the outflow (Figure 5.20). Furthermore, both tracers show a similar gradient along the outflow direction;  $\text{NH}_2\text{D}$  shows increased linewidth through the envelope, close to the outflow direction and there are several regions of enhanced linewidth in  $\text{N}_2\text{H}^+$  along the outflow. Furthermore, there may be a gradient normal to the outflow as seen in both the  $\text{N}_2\text{H}^+$  and  $\text{NH}_2\text{D}$  velocity maps. However, the outflow seems to be significantly influencing the kinematics of the dense gas.

### 5.3.3.17 IRAS 03282+3035

IRAS 03282+3035 is an isolated, deeply embedded Class 0 protostar located in the B1-ridge of the Perseus star forming region (Jørgensen et al., 2006). Mid-infrared emission from the protostar itself is quite faint, but appears as a point-source at  $8\mu\text{m}$  and Chen et al. (2007) identified it as a binary in millimeter continuum emission. The IRAC  $8\mu\text{m}$  extinction toward this object in Chapter 4 highlights a rather complex morphology on large scales; however, near the protostar the extinction appears to be concentrated into a filamentary structure.

The single-dish  $\text{N}_2\text{H}^+$  observations in Figure 5.21 trace the large-scale extinction morphology very well and the emission is observed to be quite extended, with the emission peak slightly offset from the protostar along the outflow. The  $\text{N}_2\text{H}^+$  emission also ends at the northeast edge of the core where the extinction rapidly falls off. The VLA  $\text{NH}_3$  map traces a filamentary structure on large-scales north and south of the protostar. Furthermore, the emission is double-peaked, with the individual peaks located north and south of the protostar, in agreement with the  $\text{N}_2\text{H}^+$  emission shown by Chen et al. (2007).

The velocity field derived from the single-dish  $\text{N}_2\text{H}^+$  map shows a strong velocity gradient in the direction of the outflow; however, there also appears to be another gradient that is normal to the outflow on the southeast side of the envelope. I also note that there is a strong linewidth gradient in the direction of the outflow (same

direction as the line-center velocity gradient) with the largest linewidths appearing on the west side of the envelope. The  $\text{NH}_3$  velocity map from the VLA again finds the velocity gradient in the direction of the outflow along with blue-shifted emission north and south of the protostar. The linewidth of the  $\text{NH}_3$  emission is peaked just north and south of the protostar indicative of dynamic motion in the line of sight.

Chen et al. (2007) suggested that the outflow may be interacting with the envelope, causing the gradient along the outflow. However, the IRAC data show that the outflow is well-collimated and appears only able to affect the material extended to the northwest of the protostar. To further examine the kinematic structure of this system, I have overlaid the  $\text{NH}_3$  channel map contours on the CO map from Arce & Sargent (2006) in Figure 5.22. The top and bottom rows show the portions of the  $\text{NH}_3$  lines that are not blended while in the middle panel the two lines are blended. At red-shifted velocities in the top panel, notice how the different parts of the emission come into view going toward lower velocities. The top right panel shows the red-shifted emission being emitted from two very thin structures running north-south. In the bottom panels of Figure 5.22, it can be seen that there is more blue-shifted emission is still confined to a very thin structure running north-south; however, its location has shifted further to the east compared to the upper panels. Thus, I suggest that rather than an outflow interaction giving rise to the global velocity structure, a more probable explanation is that the envelope is filamentary and that the velocity shifts are flows along the filament toward the protostar. However, certain regions of the envelope that are spatially coincident with the outflow cavities may be affected by the outflow.

### 5.3.3.18 HH270 VLA1

HH270 VLA 1 is located in the L1617 cloud near Orion and is the driving source of the HH270 outflow (Reipurth et al., 1996; Rodríguez et al., 1998). This outflow in particular appears to be deflected and colliding with a neighboring core (the driving source of HH110 (Rodríguez et al., 1998)). In Chapter 4, I found that this protostar exhibits  $8\mu\text{m}$  extinction in a filamentary envelope that is extended along the outflow

and only on one side of the protostar. Furthermore, it was noted that the  $4.5\mu\text{m}$  scattered light is brighter at the edge of the extinguishing envelope, indicating that extinction structure is indeed extended along the outflow and not due to a complex line of sight projection effect. The single-dish  $\text{N}_2\text{H}^+$  emission from this source is peaked on the  $8\mu\text{m}$  extinction with no peak coincident with the protostar. The CARMA  $\text{N}_2\text{H}^+$  map is still tracing the  $8\mu\text{m}$  extinction and shows a sharp decline of emission at the location of the protostar; the emission still appears one-sided even at high resolution.

The single-dish  $\text{N}_2\text{H}^+$  velocity map shows a gradient along the outflow with a linewidth enhancement just southwest of the protostar. This region of high linewidth is likely an unresolved velocity gradient, which is then resolved in the CARMA velocity map. The pattern in the CARMA velocity map closely matches the shape of the scattered light outflow cavity visible at  $8\mu\text{m}$  in Figure 5.23. I suggest that these features are due to an outflow interaction with the surrounding material. Note that the data do not show a linewidth increase; therefore the outflow seems to be inducing bulk motion, but not an increase in linewidth.

## 5.4 Discussion

### 5.4.1 Large-Scale Velocity Field

The large-scale velocity gradients in dense molecular cores have long been interpreted as rotation (possibly solid-body) (e.g. Goodman et al., 1993; Caselli et al., 2002; Belloche et al., 2002; Belloche & André, 2004; Chen et al., 2007). If the large-scale motions are indeed rotation, then the circumstellar disk forming from the collapse of the surrounding envelope should be rotating in the same direction as the surrounding cloud, assuming axisymmetric collapse (e.g. Shu et al., 1987; Bodenheimer, 1995). However, if the core has fragmented, then the angular momenta of the individual disks could be misaligned, but the sum of the angular momenta would still be aligned with the cloud rotation. The direction of the jet and outflow of the system is commonly thought to reflect the current angular momentum vector of the protostar and disk

system. This is because outflows and jets are thought to be related to the magnetic field of the protostar and disk which should be along the rotation axis (Pudritz & Norman, 1983; Shu et al., 1994) and resolved observations of disks have shown that jets are oriented normal to the disk midplane. Thus, I have used the outflow direction and protostar locations as guideposts as to where I should measure the velocity gradients relative to and in which direction because the equatorial plane of the envelope is where one is most likely to observe rotation.

The 2D fitting method (see Section 5.2.6.2) shows that eleven out of sixteen systems have a gradient direction that is within  $45^\circ$  of normal to the outflow axis in the single-dish data; however, there is considerable spread in this distribution. I caution that the PA of the gradients calculated by this method may have systematic error due to the velocity fields not being uniform and the velocities are sampled over a region that is not symmetric, leading to a bias of data points in a particular direction. Visual inspection of the velocity fields does yield a similar result to the 2D fitting, with eleven normal to the outflow and five not normal; IRAS 03282+3035, HH270 VLA1, L1527, L1521F, and L483 were not normal to the outflow. In contrast to the 2D fitting, I visually identify L483 and HH270 VLA1 as not normal to the outflow and L1157 and Serpens MMS3 to be normal. I further caution that most velocity fields have structure not easily described by a single position angle or velocity gradient. Nevertheless, as a simple significance test of the gradient-outflow direction relation, the binomial distribution can be applied when considering the  $<45^\circ$  and  $\geq 45^\circ$  as two bins and that the gradient direction relative to the outflow may be oriented randomly between 0 and  $90^\circ$  with a mean of  $45^\circ$  (Bevington, 1969). Thus, the probability of the relative directions falling within  $<45^\circ$  or  $>45^\circ$  should be equal. The chance of eleven or more objects out of sixteen with randomly oriented velocity gradients falling within the  $\geq 45^\circ$  bin is only  $\sim 10\%$ .

I also attempted to see if there is any trend with envelope mass and velocity gradient, I compared the observed velocity gradients and linewidths with the escape velocity in Figure 5.29. The envelope mass is calculated from the dust mass measured from  $8\mu\text{m}$  extinction (Chapter 4, Table 5.1) plus  $1 M_\odot$  to account for the central ob-

ject; note that the central object masses may be overestimated while the envelope masses are likely underestimated (Chapter 4). There is no apparent trend of velocity gradients or linewidth with increasing envelope mass (in terms of escape velocity). This figure further demonstrates that these protostellar systems are consistent with being gravitationally bound and are not supported by rotation or turbulence, consistent with many previous studies (e.g. Goodman et al., 1993; Caselli et al., 2002; Chen et al., 2007).

Furthermore, the smallest velocity gradients in the sample appear to be coming from the most symmetric envelopes L1521F, IRAS 16253-2429, and L1157, and the largest gradients are found in the morphologically complex HH211 and IRAS 03282+3035 systems. This could be taken to mean that the velocity structure is not strongly influenced by complex projection effects in the symmetric systems and are observing slow envelope rotation, while the more complex systems have projection effects altering the observed velocity structure. However, despite this trend, I note that the envelope of the low-luminosity source IRAM 04191 is approximately symmetric (Chapter 4) and has a velocity gradient of  $17 \text{ km s}^{-1} \text{ pc}^{-1}$  (Belloche et al., 2002; Belloche & André, 2004), a clear counter-example to this morphological trend.

The simple interpretation of the velocity gradient data as a whole is that core rotation is observed in these systems and that they have a variety of angular momenta; some angular momenta being quite large (Figure 5.25). However, if pure rotation were observed on large-scales, then one would expect the velocity gradient directions to be much more clustered toward being orthogonal to the outflow rather than the broad distribution shown in Figure 5.27. Therefore, either the complex morphology makes the rotation ambiguous, causing the velocity gradients to not be orthogonal to the outflow or pure rotation is not being observed. In either case, the angular momenta derived from the velocity gradients will be suspect at best. Given these complicating factors, I regard the velocity gradients taken as 1D cuts normal to the outflow as most likely to be probing the velocity gradients due to rotation, but these values should be regarded as upper limits.

If pure rotation is not being observed, the only other dynamical process which

should give rise to ordered velocity structures are infall and/or outflow entrainment. The outflows from the protostars in the sample are highly collimated, limiting their ability to affect the large-scale kinematic structure, see Section 5.4.3 for further discussion, which leaves infall as the only other mechanism to contribute to the velocity field. This would require that infall is happening on large-scales and that collapse would need to be outside-in and not inside-out. Large-scale infall is shown to be possible in numerical simulations of complex, filamentary cores forming within a molecular cloud by Smith et al. (2011). Their simulations show that there is infall onto filaments (scales of 0.1 pc to 0.01 pc) from the surrounding molecular cloud, with subsequent infall from the filament to the protostar (sink particle) ( $< 0.01$  pc). Thus, infall convolved with rotation in real envelopes could lead to some of the complex velocity structures observed.

In summary, it is difficult to interpret the large-scale velocity gradients wholly being due to rotation since the envelopes are asymmetric and the gradients are often not normal to the outflow. Furthermore, flows or infall along a filament could give a similar signature to rotation simply from geometric projection, and if an envelope is filamentary, infall along the envelope would also produce a velocity gradient normal to the outflow. I therefore suggest that a component of infall velocity could be projected along the line of sight, entangled with the rotation velocity, resulting in the large velocity gradients. This issue of rotation versus projected infall will be further explored in the next chapter.

#### **5.4.2 Small-scale Velocity Structure**

The high-resolution interferometer data are essential for probing the kinematics of the envelope at scales smaller than 5000 AU. These data enable me to localize the gas in the envelope and to assess the dynamical processes at work. Small-scale velocity substructure, beyond an ordered/linear velocity gradient, is found in the interferometric observations of most envelopes, including L1157, L1165, HH108IRS, Serpens MMS3, L1527, CB230, IRAS 03282+3035, and RNO43. These features are sometimes apparent in the velocity maps or profiles shown in Figure 5.24, but they also appear

as increased linewidth in the inner envelope. The small-scale velocity structure is generally found on  $\sim 2000$  AU scales in the envelopes. This radius could possibly be the centrifugal radius where material can be rotationally supported against gravity and the increased rotation velocity makes this region stand out against the rest of the envelope in velocity. However, assuming the large-scale velocity gradients reflect rotation, there would not be enough angular momentum for material to be rotationally supported at this radius.

I found that the relationship between outflow axis and velocity gradient direction in the interferometer data trends even more strongly toward being normal to the outflow than in the single-dish data. Twelve of fourteen systems have gradients within  $45^\circ$  of the outflow in the right panel Figure 5.27, as found by the 2D fitting technique. Using the same statistical analysis as the single-dish gradients, this result being due to chance is  $\sim 0.6\%$ . Note that this plot is missing L1157 and Serpens MMS3 since their complex velocity fields could not be reliably fit. Visually, I find that twelve envelopes clearly have gradients normal to the outflow and four do not (HH108MMS, L483, IRAS03282, and HH270VLA1); L483 and HH270 VLA1 were counted as within  $45^\circ$  of normal to the outflow. Note that RNO43, Perseus 5, and L1521F appear to have gradients normal to the outflow, but they also have complex velocity fields. L1157 is left out of this analysis because the gradient directions from the CARMA and VLA data differ by  $\sim 80^\circ$ .

The velocity gradient direction is generally consistent between both large and small scales in the single-dish and interferometer data as shown in Figure 5.28. This could mean that the dynamical processes observed at large-scales are also responsible for the kinematics observed at small-scales. The protostellar systems which show substantial deviation from large to small-scales are L1527 and L1521F. The difference in L1527 marks a velocity gradient reversal from large to small-scale (as also shown in Figure 5.24) and the difference in L1521F reflects that the kinematic structure was not well-resolved in the single-dish data. The  $\text{N}_2\text{H}^+$  and  $\text{NH}_3$  lines in L1521F are also extremely optically thick making the velocity field derived from fitting uncertain since all the gas along the line of sight cannot be probed.

The preference for the vast majority of velocity gradients to be within  $45^\circ$  of normal to the outflow contrasts with Chen et al. (2007), where only two of nine targets had this feature. Moreover, in Volgenau et al. (2006), only one protostellar core of three observed had a well-ordered velocity structure. This result may be due to environment since the ordered structure was found in L1448 IRS3, a more isolated system, and the other sources were located in the more complex environment of NGC1333. The sources in this study are, in contrast, are generally isolated, like those in Chen et al. (2007). As noted in the preceding paragraphs, I find several objects with similarly complex velocity fields in the data; however, the greater number of observed systems in this study likely enabled me to find more with ordered velocity fields.

The velocity gradients fit for the interferometer data are systematically larger than those found for the single-dish data, with the average being  $8.6 \text{ km s}^{-1} \text{ pc}^{-1}$  from 1D fitting, the distribution is shown in Figure 5.26. This factor is nearly equal to the increase in resolution in the interferometer data as compared to the IRAM 30m, but the object-to-object increase is more varied. Some of the small-scale velocity structure is due to outflow interactions in the inner envelope as I will discuss in more detail in the following section; however, I have attempted to mask out these regions when fitting the velocity gradients. Like the single-dish data, I regard the 1D fitting method to more accurately reflect the velocity gradient intrinsic to the envelope itself since the 2D method will be more susceptible to outflow effects on the envelope kinematics. The only objects not showing large increase in the velocity gradient on small-scales are HH211 and IRAS 16253-2429 whose small-scale velocity gradient may be slightly overestimated.

I strongly cautioned in the previous section about interpreting the velocity gradients as rotation on large-scales and I am again hesitant to interpret the small-scale gradients as rotation and/or spin-up. This is because most envelopes are highly filamentary and on small-scales projections effects on the velocity structure will be even more apparent since both infall and rotation velocities increase at small radii. The velocity fields themselves on small-scales are not well-ordered as one might expect

from rotationally dominated motion. Highlighting a few examples from Section 5.3.2: Serpens MMS3 shows deep red-shifted emission and increased linewidth only on one side of the protostar, the velocity gradient in HH108IRS reverses itself just past the protostar, the gradient in L1527 on small-scales is opposite of large scales, and RNO43 has an abrupt velocity jump across the envelope. The complex nature in the velocity fields of many sources do not necessitate an interpretation as rotation. Furthermore, infall velocities will always be necessarily be larger than rotation since the envelopes are not rotationally supported (Chen et al., 2007). Thus, the only way to robustly separate infall velocities from rotation is at  $< 1000$  AU scales, near the centrifugal radius where material can be rotationally supported.

Two systems in the sample (L1165 and RNO43) show high-velocity line wings in the inner envelope that could indeed reflect significant rotation. In both sources, the emission appears to be coming from a radius of  $\sim 600$  AU. My data indicate that the observed velocities could reflect rotationally supported motion around  $\sim 0.5M_{\odot}$  central objects. Higher resolution and higher signal-to-noise data are needed to accurately centroid the high velocity emission in order to more precisely constrain the enclosed masses. In the future, ALMA could be used to spatially resolve the high-velocity emission in order to fully separate rotation from infall. Further analysis and modeling of the velocity structures observed with the interferometric data with the goal of determining the kinematic processes at work in the envelopes will be presented in the next chapter.

### 5.4.3 Outflow Induced Kinematic Structure

Knowledge of protostellar outflows has been greatly enhanced in recent years (e.g. Bachiller, 1996; Arce et al., 2007, and references therein) and their possible effects on the surrounding envelope have been characterized (Arce & Sargent, 2006). Furthermore, IRAC imaging from the *Spitzer Space Telescope*, in addition to near-IR imaging from the ground, can give a strong constraint on the outflow axis and cavity width (e.g. Seale & Looney, 2008). These data complement observations of outflow tracers such as CO and give a more complete picture of how the outflow may be impacting

the protostellar envelope.

Several protostars in the sample have velocity structures that are strongly suggestive of outflow effects on the  $\text{N}_2\text{H}^+$  and  $\text{NH}_3$  gas kinematics. L1157, HH108MMS, and Perseus 5 appear to be significantly affected by the outflow, while HH108IRS, HH211, IRAS 03282+3035, L1152, and IRAS 04325+2402 only appear to be mildly affected. In the mildly affected cases, the large-scale bulk motion of the envelopes (line-center velocity) does not appear to be affected by the outflow, rather I see the effects in the linewidth at both large-scales and small-scales. This probably means that only a small portion of the total cloud mass is being affected by the outflow. The bulk motion effects are revealed in the strongly affected cases, generally on small-scales and only visible in the interferometer data.

Arce & Sargent (2006) presented an empirical model for how the outflow will affect the envelope during protostellar evolution, concluding that the outflow is ultimately responsible for disrupting the protostellar envelopes. The number of objects I find showing outflow effects in the kinematic data strongly support the outflow-envelope interaction framework put forward by Arce & Sargent (2006) and enable me to offer some further input to this empirical framework.

Perseus 5 and HH108MMS appear to be some of the youngest objects in the sample, as evidenced by their deeply embedded nature and lack of visible outflow cavities in  $3.6\mu\text{m}$  or Ks-band imaging. In these systems, the outflow seems to be having the greatest impact on the kinematics in both line-center velocity and linewidth. Therefore, the effects of the outflow on the kinematic structure may be most prominent during its initial breakout of the envelope, early in the Class 0 phase. Smaller-scale effects on the envelope can clearly be seen in the case of L1157 where the envelope material may be entrained at 1000 AU scales. Thus, the outflows could be carrying significant momentum at wide angles near the protostar in order to be actively forcing inner envelope material out. If the outflows are impacting the envelope at small-scales and wide angles, an important question remains as to how much the outflow can quench infall in filamentary envelopes. In L1157, the amount of entrained gas appears tenuous, only  $\sim 0.04 M_\odot$  out of  $0.7 M_\odot$  in the inner envelope, following

a simple analysis (Goldsmith & Langer, 1999) assuming an  $\text{N}_2\text{H}^+$  abundance of  $10^{-9}$  per  $\text{H}_2$ . On larger-scales ( $> 1000\text{AU}$ ), I expect that material extended normal to the outflow in filamentary envelopes will not be strongly influenced by the outflow, as the outflows appear to stay well collimated throughout the Class 0 phase.

#### 5.4.4 Linewidths

The linewidths in the envelopes are generally quite small away from the protostar. In most cases, the linewidths are  $0.2 - 0.5 \text{ km s}^{-1}$  in the single-dish data; linewidths averaged over the entire source are given Table 5.3. Note that these linewidths are substantially broader than the 10K thermal linewidth of  $\text{N}_2\text{H}^+$  which is  $\sim 0.13 \text{ km/s}$ , and is generally attributed to turbulent motions and/or unresolved velocity gradients along the line of sight. However, these linewidths are not large enough to make the envelope unbounded, as shown Figure 5.29.

The interferometer data find even smaller linewidths toward the outer edges of the envelopes; there were several cases where the lines are less than 2 channels wide. The narrow line-widths in the interferometer data likely stem from the larger scale structure being resolved out; the larger scale emission may have some turbulent or large-scale infall velocity component. The regions of broad linewidth in the interferometer observations appear to be directly related to the outflow, increased line-of-sight motion, and/or heating from the protostar; not a transition to a turbulent core (cf. Chen et al., 2007).

$\text{NH}_3$  linewidths were used by Pineda et al. (2010) to probe the kinematics of the large-scale molecular core, detecting a transition from the quiescent core to the turbulent cloud. I looked for such an effect in the sensitive  $\text{N}_2\text{H}^+$  data but did not find similar structure. I also did not detect  $\text{N}_2\text{H}^+$  emission on the scales for which Pineda et al. (2010) were able to detect  $\text{NH}_3$ , despite the high sensitivity. I believe that this is likely due to the differing critical densities between  $\text{N}_2\text{H}^+$  and  $\text{NH}_3$  ( $\sim 2 \times 10^3 \text{ cm}^{-3}$  for  $\text{NH}_3$  (1,1) and  $\sim 1.4 \times 10^5 \text{ cm}^{-3}$  for  $\text{N}_2\text{H}^+$  ( $J = 1 \rightarrow 0$ )).

I did, however, find that some maps (i.e. L673, HH211, HH108, RNO43) had regions with two distinct velocity components. The regions of overlap between the

components appear as artificially large linewidths in the maps generated by the hyperfine fitting routine (Section 5.2.6.1). I show three  $\text{N}_2\text{H}^+$  spectra from HH211 taken at three positions showing the different velocity components in Figure 5.30; this is indicative of what takes place in the other regions showing this feature. Notably, the additional velocity components tend to appear toward the edge of the maps, except in RNO43 where the transition takes place near the protostar. The distinct velocity components are located in regions that appear form a contiguous structure when viewed in  $8\mu\text{m}$  extinction. The second velocity component generally appears about  $\sim 0.05$  pc from the nearest protostar. Thus, the reason for multiple components could have to do with the initial conditions of the clouds themselves. Recent simulations have suggested that colliding clouds could be an important component to setting up the initial conditions for star formation (e.g. Heitsch et al., 2006).

#### 5.4.5 Chemical Effects on Molecular Tracers

The kinematic data presented are based on the molecular tracers  $\text{N}_2\text{H}^+$ ,  $\text{NH}_3$ , and  $\text{HCO}^+$ . I have used  $\text{N}_2\text{H}^+$  and  $\text{NH}_3$  relatively interchangeably, since they appear to trace the same kinematics and physical conditions (see Section 5.3.1 and Johnstone et al. (2010)). This makes sense because it is known that in the pre-stellar phase, the formation of  $\text{N}_2\text{H}^+$  and  $\text{NH}_3$  appear to be linked given their similar abundance distributions and only deplete onto dust grains at very high densities (Bergin & Tafalla, 2007). In many of the observations,  $\text{N}_2\text{H}^+$  and  $\text{NH}_3$  only appear to trace the gas on scales  $>1000$  AU from the protostar; the emission generally peaks near the protostar, but not directly on it. This indicates a drop in abundance either due to depletion or destruction of the molecules. Several of the protostars for which there are both interferometric  $\text{NH}_3$  and  $\text{N}_2\text{H}^+$  observations (in this chapter or in the literature) show decreased emission at the location of the protostar in both  $\text{N}_2\text{H}^+$  and  $\text{NH}_3$ . Observations of CB230 and IRAS 03282+3035 in  $\text{NH}_3$  (Figures 5.6 and 5.21) and  $\text{N}_2\text{H}^+$  (Chen et al., 2007) are clear examples of  $\text{NH}_3$  and  $\text{N}_2\text{H}^+$  not being peaked coincident with the protostar. L1157 also exhibits this effect in  $\text{N}_2\text{H}^+$  from the PdBI observations and also does in  $\text{NH}_3$  if the longer baselines are given more weight

in the VLA map. Finally, the low-luminosity source IRAM 04191 shows a similar depletion pattern in both of these tracers (Belloche & André, 2004, J. Mangum, Private Communication).

The decrease in  $\text{N}_2\text{H}^+$  emission can be understood in terms of molecular destruction by reactions with other molecules. In the inner envelope, where the temperatures rise above 20K, the CO that has depleted onto the dust grains (Bergin et al., 2002) is released back into the gas phase. CO and  $\text{N}_2\text{H}^+$  rapidly react to form  $\text{HCO}^+$ ; this is the dominant destruction mechanism for  $\text{N}_2\text{H}^+$  (Aikawa et al., 2001; Lee et al., 2004). This is the same reason that  $\text{N}_2\text{H}^+$  is not seen in outflows and why the  $\text{N}_2\text{H}^+$  is often not centrally peaked on the protostars in the interferometric observations.  $\text{NH}_3$  however, is not directly destroyed by CO, but rather  $\text{HCO}^+$  (Lee et al., 2004).  $\text{HCO}^+$  will readily form within the region of CO evaporation making it available to react with  $\text{NH}_3$ . Alternatively,  $\text{NH}_3$  could also become depleted onto dust grains in an ice mantle, and if it is well-mixed with the water ice, then it would only be evaporated at temperatures  $\geq 100\text{K}$ .  $\text{NH}_3$  ice is frequently observed in the envelopes surrounding protostars (Bottinelli et al., 2010) via mid-infrared spectroscopy. The absorbing  $\text{NH}_3$  ice should be in the inner envelope since  $\text{NH}_3$  only depletes onto grains at high densities. If any of the  $\text{NH}_3$  ice were released into the gas phase, then  $\text{HCO}^+$  would be present to destroy it.

Since both  $\text{NH}_3$  and  $\text{N}_2\text{H}^+$  are not present on scales  $< 1000$  AU, other tracers must be used to probe the kinematic structure on these scales. In two protostars,  $\text{HCO}^+$  is able to be used to trace the small-scale kinematic structure. The  $\text{HCO}^+$  emission from L1165 and RNO43 show high-velocity wings on small-scales inside the innermost  $\text{N}_2\text{H}^+$  emission; the centroids of the red and blue-shifted emission are offset from the protostar, normal to the outflow direction, at radii of  $\sim 600\text{AU}$ .

Chemical models of an infalling protostellar envelope have been calculated by Lee et al. (2004), showing that  $\text{HCO}^+$  becomes enhanced at small-scales after formation of the protostar. This reflects the evaporation of CO ice, releasing CO back into the gas phase where  $\text{HCO}^+$  is readily formed. In addition, the primary destruction pathway of  $\text{N}_2\text{H}^+$  from CO results in the formation of  $\text{HCO}^+$  and  $\text{N}_2$ . Thus, it is

clear why the  $\text{N}_2\text{H}^+$  is tracing the gas at larger radii and lower velocities, while in the inner envelope  $\text{HCO}^+$  is readily being formed and can then trace the small-scale high-velocity gas.

My dataset explicitly shows how multiple tracers can be used to gain a more complete picture of the kinematics in protostellar envelopes.  $\text{N}_2\text{H}^+$  and  $\text{NH}_3$  are excellent tracers of the cold, dense gas on scales from  $\sim 1000$ - $2000$  AU out to  $\sim 10000$ - $20000$  AU. Inside of  $1000$  AU, an abundant tracer of the warm, inner envelope tracer must be observed;  $\text{HCO}^+$  works quite well in two out of nine sources observed with CARMA and other tracers and/or higher- $J$  transitions of  $\text{HCO}^+$  may work as well (see Lee et al. (2009) and Brinch et al. (2007)). However, these other tracers are often found in outflows and they must be observed with sufficiently high resolution to confirm their origin in the envelope and not the outflow. In the future, ALMA may be able to observe inner envelope tracers to resolve the motion of the dense gas in the inner envelope, tracing infall onto the disk.

## 5.5 Summary

I have conducted a single-dish and interferometric survey mapping emission of the dense gas tracers  $\text{N}_2\text{H}^+$  ( $J = 1 \rightarrow 0$ ) and/or  $\text{NH}_3$  (1,1) in envelopes around low-mass protostars. Many of these envelopes are known to be morphologically complex from  $8\mu\text{m}$  extinction mapping. These data have been used to map the line-center velocity and linewidth across these envelopes. The velocity gradients and their directions have been quantitatively measured in order to characterize the dense gas kinematics in the complex protostellar envelopes, my specific results are as follows.

1. Ordered velocity fields are present on large-scales in most protostellar envelopes from the single-dish sample. In eleven out of sixteen cases, the velocity gradients appear to be within  $45^\circ$  of normal to the outflow axis with an average gradient of  $\sim 2.3 \text{ km s}^{-1} \text{ pc}^{-1}$ , depending on fitting method. The velocity gradients could be due to core rotation; however, the velocity gradient position angles do have a broad distribution with respect to the outflow direction. Furthermore, the strongly asymmetric nature of the envelopes and the fact that most envelopes in the sample

are substantially bound leads me to suggest that a component of infall projected along the line of sight is entangled with rotation. Evidence is found for multiple components of  $\text{N}_2\text{H}^+$  emission in several clouds, possibly relating the observations to a colliding-cloud formation scenario.

2. The small-scale kinematic structure observed by the interferometers appears to be gravitationally dominated by the central protostar and it likely originates from a combination of infall and rotation in some cases. The average velocity gradient in the interferometer data is  $8.6 \text{ km s}^{-1} \text{ pc}^{-1}$ , with gradient directions within  $45^\circ$  of normal to the outflow in twelve out of fourteen cases. The complex velocity fields in many systems suggest that interpreting the velocity gradients as pure rotation is incorrect. Only on the smallest scales ( $<1000 \text{ AU}$ ) will rotation differentiate itself from infall. Furthermore, multiple tracers must be used to gain a complete picture of the kinematic structure of the envelope down to sub-1000 AU scales due to depletion of the cold gas tracers within  $\sim 1000 \text{ AU}$ . In the cases of RNO43 and L1165,  $\text{HCO}^+$  ( $J = 1 \rightarrow 0$ ) was able to be used to trace inner envelope kinematics on scales of  $\sim 600 \text{ AU}$ .

3. Outflows do impact the envelope kinematics derived from  $\text{NH}_3$  and  $\text{N}_2\text{H}^+$  in some systems and their effects are most prominent at  $\sim 1000\text{-}2000 \text{ AU}$  scales. Clear outflow effects on the large-scale kinematics in the single-dish data are only seen for five systems, but the only evident kinematic effect is increased linewidth along the outflow. The effects are most pronounced in the interferometer data for the deeply embedded sources HH108MMS and Perseus 5. Furthermore, there is a remarkable case of the outflow possibly entraining the inner envelope of L1157 on  $\sim 1000 \text{ AU}$  scales.

## 5.6 Appendix: Continuum Data

In conjunction with the CARMA and PdBI  $\text{N}_2\text{H}^+$  observations, the 3mm continuum emission was observed for those 11 sources. The continuum data are overlaid on the IRAC  $8\mu\text{m}$  images for all but HH108IRS/MMS ( $70\mu\text{m}$  data is shown due to lack of IRAC imaging) in Figure 5.31. The 3mm continuum sources are point-like

in most cases, HH108IRS and HH211 appear to show extended structure at the  $3\sigma$  level, consistent with envelope dust emission. L1157, L1165, and HH270 are also slightly extended, but in the direction of their outflows, indicating that there may be a component of free-free jet emission or heated dust along the outflow in the 3mm continuum data. In all cases, the continuum sources are coincident with the  $8\mu\text{m}/70\mu\text{m}$  point sources. There are a few cases (L1157, HH211, and RNO43) where there is not a clear point source at  $8\mu\text{m}$  and the 3mm emission is located between the outflow cavities where there is significant extinction. In these cases, the  $24\mu\text{m}$  point source is then found to peak at the same location of the 3mm source. Note that the protostar IRAS 16253-2429 shows a slight offset between the  $8\mu\text{m}$  point source and the continuum detection; however, the detection is barely  $3\sigma$ , thus, I do not believe that this offset is real. The continuum fluxes at 3mm are listed in Table 5.11.

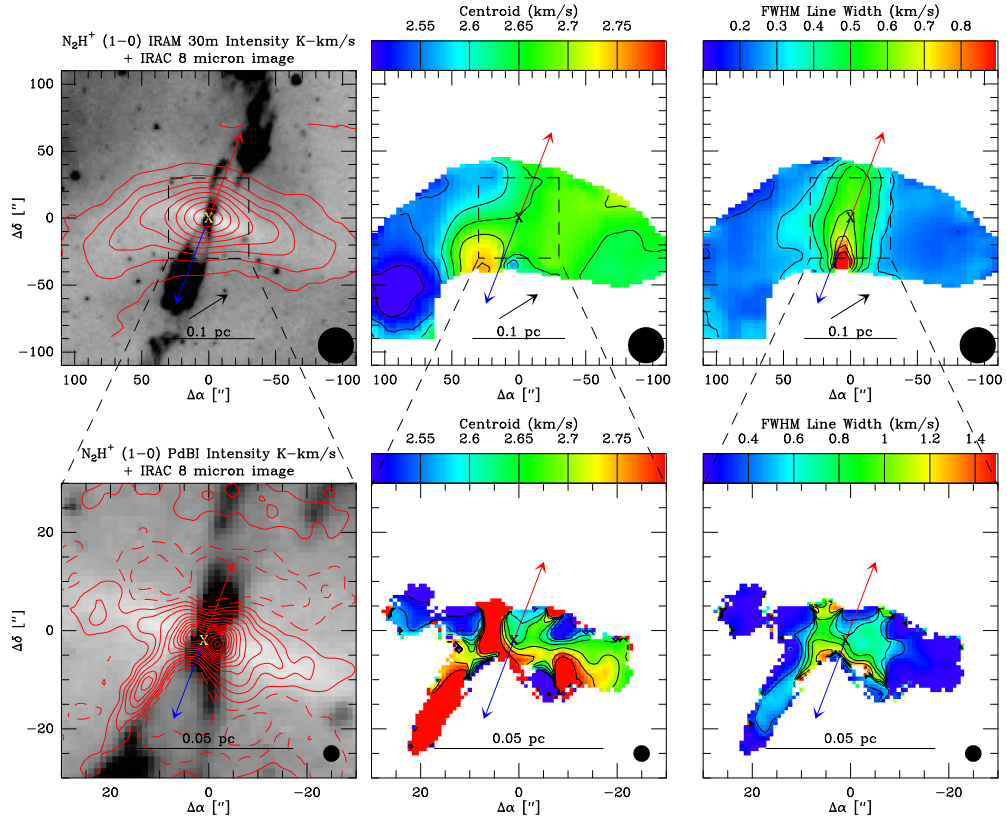


Figure 5.1 L1157– The *top* row shows the data from the IRAM 30m and the *bottom* row shows the PdBI data. In the *left* column, the  $8\mu\text{m}$  IRAC images with  $\text{N}_2\text{H}^+$  ( $J = 1 \rightarrow 0$ ) integrated intensity contours overlaid. The IRAM 30m contours start at the  $10\sigma$  level and increase in  $20\sigma$  increments while the PdBI data start at the  $\pm 5\sigma$  level and increase in  $20\sigma$  increments, see Tables 5.6 - 5.8 for values of  $\sigma_I$ . The *middle* column shows the line-center velocity fit of the  $\text{N}_2\text{H}^+$  emission across the envelope and the *right* column shows the FWHM linewidth. The *red and blue* lines mark the central axis of the outflow and their respective orientation in the plane of the sky; the X marks the position of the protostar from dust continuum and/or  $24\mu\text{m}$  emission and the *black arrows* indicate the direction of the velocity gradient derived from the velocity field. The velocity gradient direction for the PdBI data could not be fit for L1157. The single-dish data show an ordered velocity gradient along the filamentary envelope, following the high density region as it curves south. The interferometer map also reflects this velocity gradient, but there is a reversal with red-shifted emission just east of the protostar. There is also a red-shifted feature that appears in the interferometer and single-dish map just southeast of the protostar, this appears to be due to outflow interaction given its location along the cavity wall. Both the single-dish and interferometer maps have large linewidths near the protostar, which appears to be due to outflow interaction. Reference positions for the observations are listed in Tables 5.2 and 5.5.

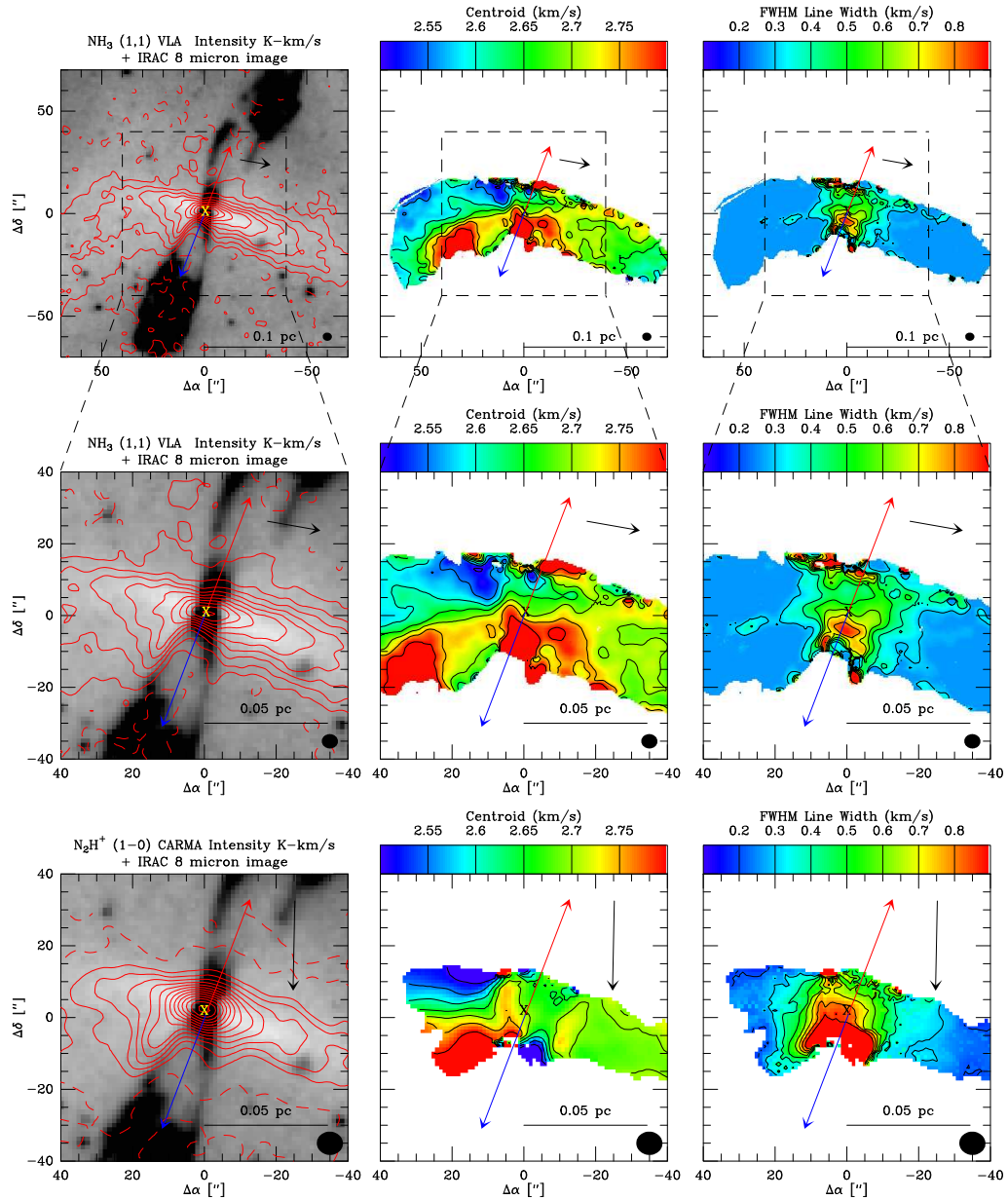


Figure 5.2 L1157– Same as Figure 5.1, but the *top and middle* rows show the VLA  $\text{NH}_3$  (1,1) data while the *bottom* row shows the CARMA  $\text{N}_2\text{H}^+$  ( $J = 1 \rightarrow 0$ ) data. The VLA contours start at the  $\pm 3\sigma$  level and increase in  $6\sigma$  increments while the CARMA data start at the  $\pm 3\sigma$  level and increase in  $3\sigma$  increments, see Tables 5.6 - 5.8 for values of  $\sigma_I$ . Notice the close correspondence of the line intensity and kinematics between the  $\text{NH}_3$  and  $\text{N}_2\text{H}^+$  maps, indicating that they are likely tracing the same material.

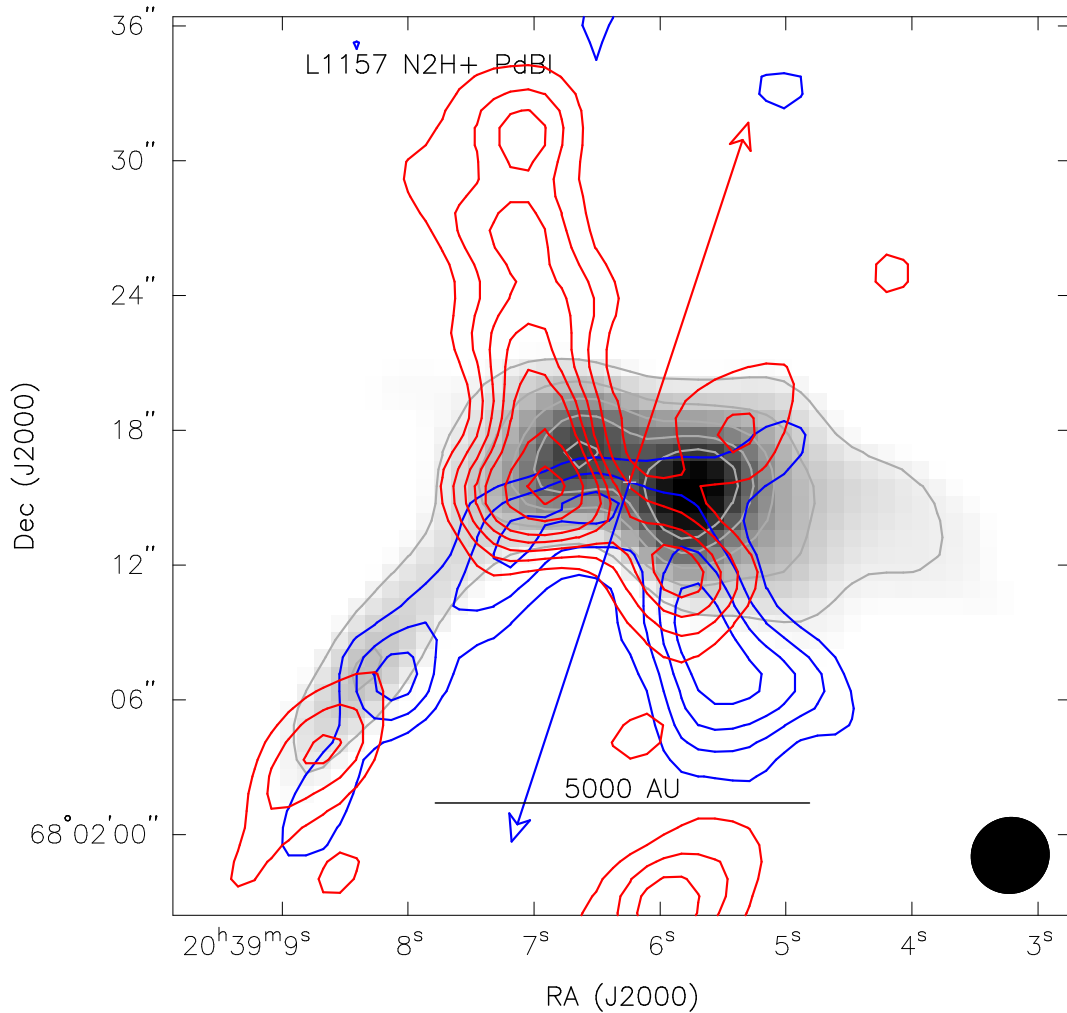


Figure 5.3 L1157– Maps of  $\text{N}_2\text{H}^+$  emission from the PdBI in L1157 in three velocity ranges; the blue and red lines denote the blue and red-shifted sides of the outflow (Jørgensen et al., 2007). The line-center emission from  $2.33\text{--}3.1\text{ km s}^{-1}$  is plotted as grayscale with light gray contours in units of 15, 30, 25, 60,  $75\sigma$  where  $\sigma=0.027\text{ K km s}^{-1}$ . The red contours are emission between  $3.2$  and  $4\text{ km s}^{-1}$  and the blue contours are emission between  $1.57$  and  $2.2\text{ km s}^{-1}$  and plotted in units of 3, 6, 9, 12, 15, 21,  $27\sigma$ . The red- and blue-shifted emission near the protostar is clearly shifted along the blue-shifted side of the outflow and both the blue and red-shifted emission seem to outline the outflow cavity wall. The spatial shifts along the outflow in the blue and red-shifted emission strongly suggest that the outflow is entraining material from the inner envelope.

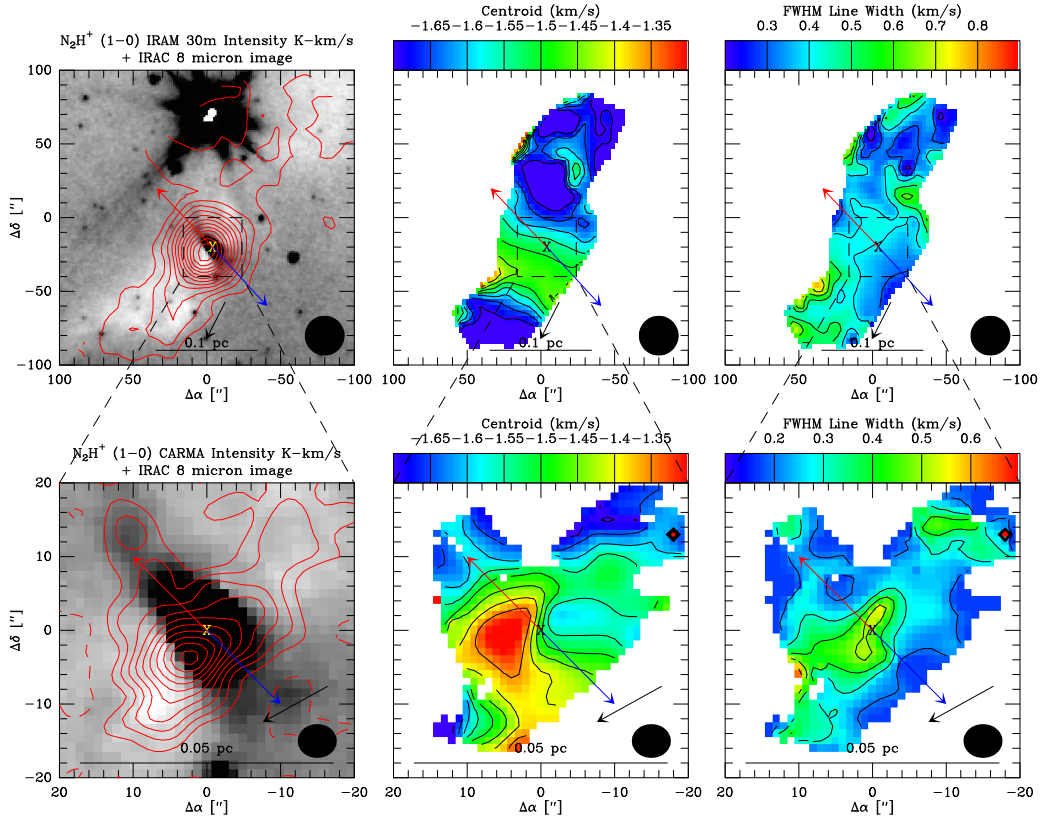


Figure 5.4 L1165– Same as Figure 5.1 but with CARMA data in the *bottom* row. The IRAM 30m contours start at  $5\sigma$  with  $5\sigma$  intervals; the CARMA data start at  $\pm 3\sigma$  with  $3\sigma$  intervals. The single-dish data show that the cloud has a fairly constant velocity away from the protostar, but near the protostar the kinematic structure is distinct; however, the single-dish linewidth map shows no indication of enhancement near the protostar. The velocity field from the interferometer map shows considerable detail, with a velocity gradient across the protostar nearly normal to the outflow. There is also enhanced linewidth near the protostar in the central envelope. Reference positions for the observations are listed in Tables 5.2 - 5.5.

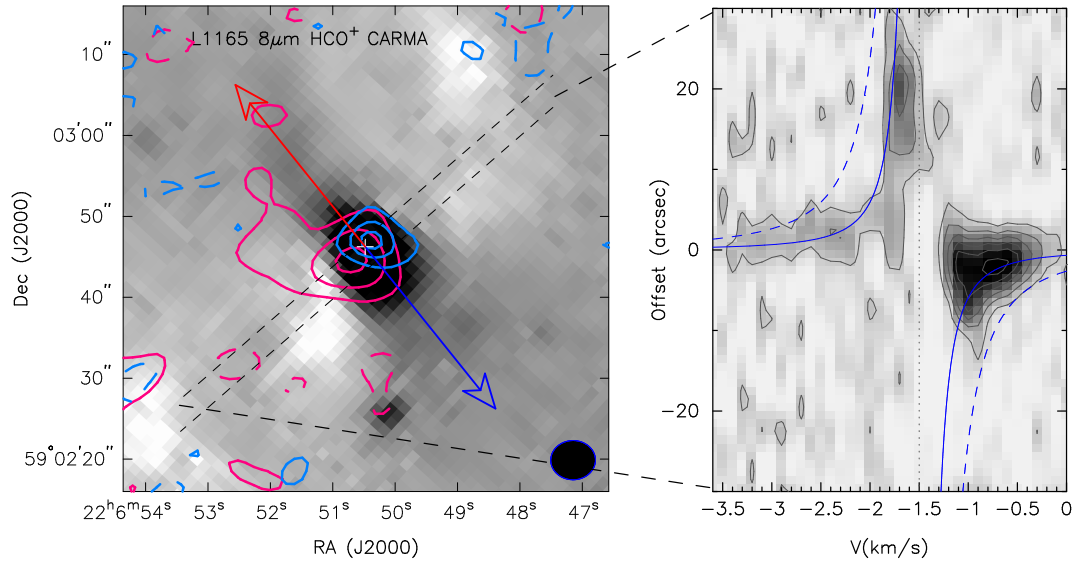


Figure 5.5 L1165– The *left panel* shows the IRAC  $8\mu\text{m}$  image with CARMA  $\text{HCO}^+$  blue and red-shifted emission, summed over  $-3.5$  to  $-2 \text{ km s}^{-1}$  and  $-1.0$  to  $0 \text{ km s}^{-1}$ , plotted as blue and red contours respectively. The contours levels are  $\pm 3$ ,  $6$ , and  $8.25\sigma$  ( $\sigma=0.175 \text{ K}$ ) for the blue-shifted emission and  $\pm 3$ ,  $9$ ,  $18$ , and  $27\sigma$  ( $\sigma=0.212 \text{ K}$ ) for the red-shifted emission. The blue and red-shifted emission from  $\text{HCO}^+$  is located symmetrically about the protostar, normal to the outflow. The dashed lines mark the regions where the position-velocity cut was taken and point to respective ends of the PV plot in the *right panel*. The position of the protostar/continuum source is marked with a white cross. The position-velocity cut shows that the blue and red-shifted emission traces higher velocity material and there is a slight gradient of material going to higher velocity closer to the continuum source. The PV plot contours start at  $3\sigma$  and increase in  $3\sigma$  intervals ( $\sigma=0.2$ ). The *solid-blue* curve represents Keplerian rotation (or infall) for a  $0.5 M_{\odot}$  central object and the *dashed-blue* curve is for a  $2.0 M_{\odot}$  central object.

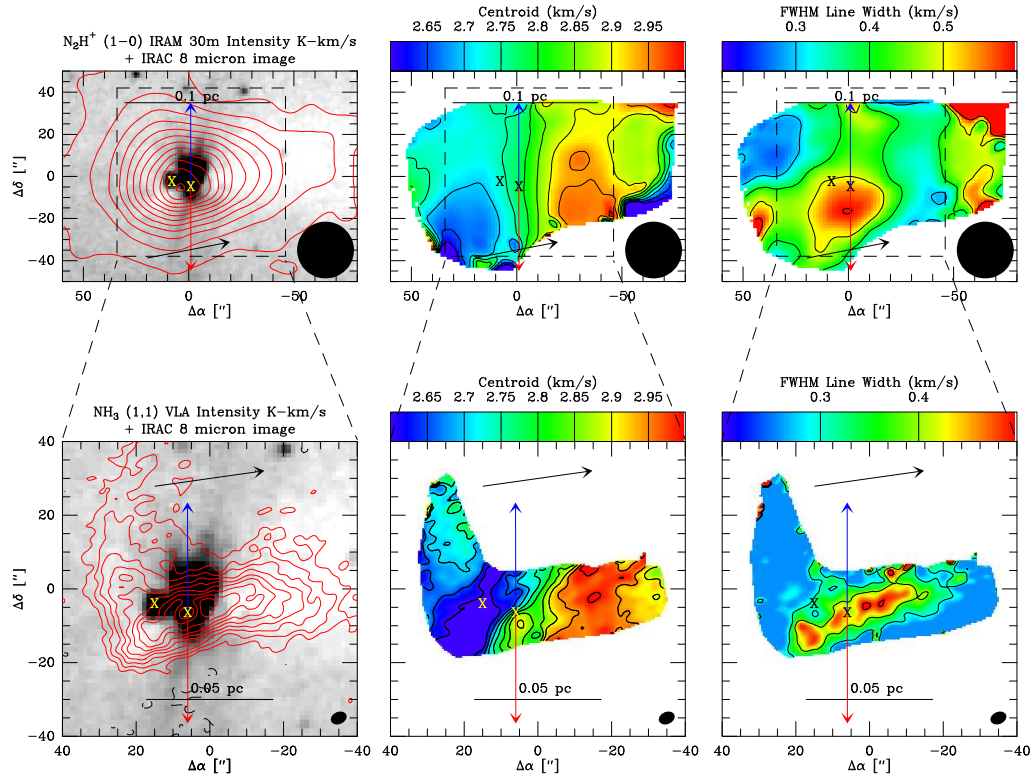


Figure 5.6 CB230– Same as Figure 5.1, but the interferometer data are VLA  $NH_3$  (1,1) observations. The IRAM 30m contours start at  $3\sigma$  with  $10\sigma$  intervals; the VLA data start at  $\pm 3\sigma$  with  $3\sigma$  intervals. The line-center velocity from the single-dish data traces a fairly smooth velocity gradient across the envelope with enhanced linewidth near the protostar. The  $NH_3$  intensity is less extended directly east of the protostar associated with the cutoff of  $8\mu m$  extinction, the rest of the envelope appears fairly flat. The line-center velocity from the  $NH_3$  emission traces a velocity gradient similar to the single-dish data; however, the shift from red to blue-shifted emission is quite abrupt and the transition region itself is curved. The  $NH_3$  line-width does not show much detail other than having its peak coincident with the highest intensity  $NH_3$  emission.

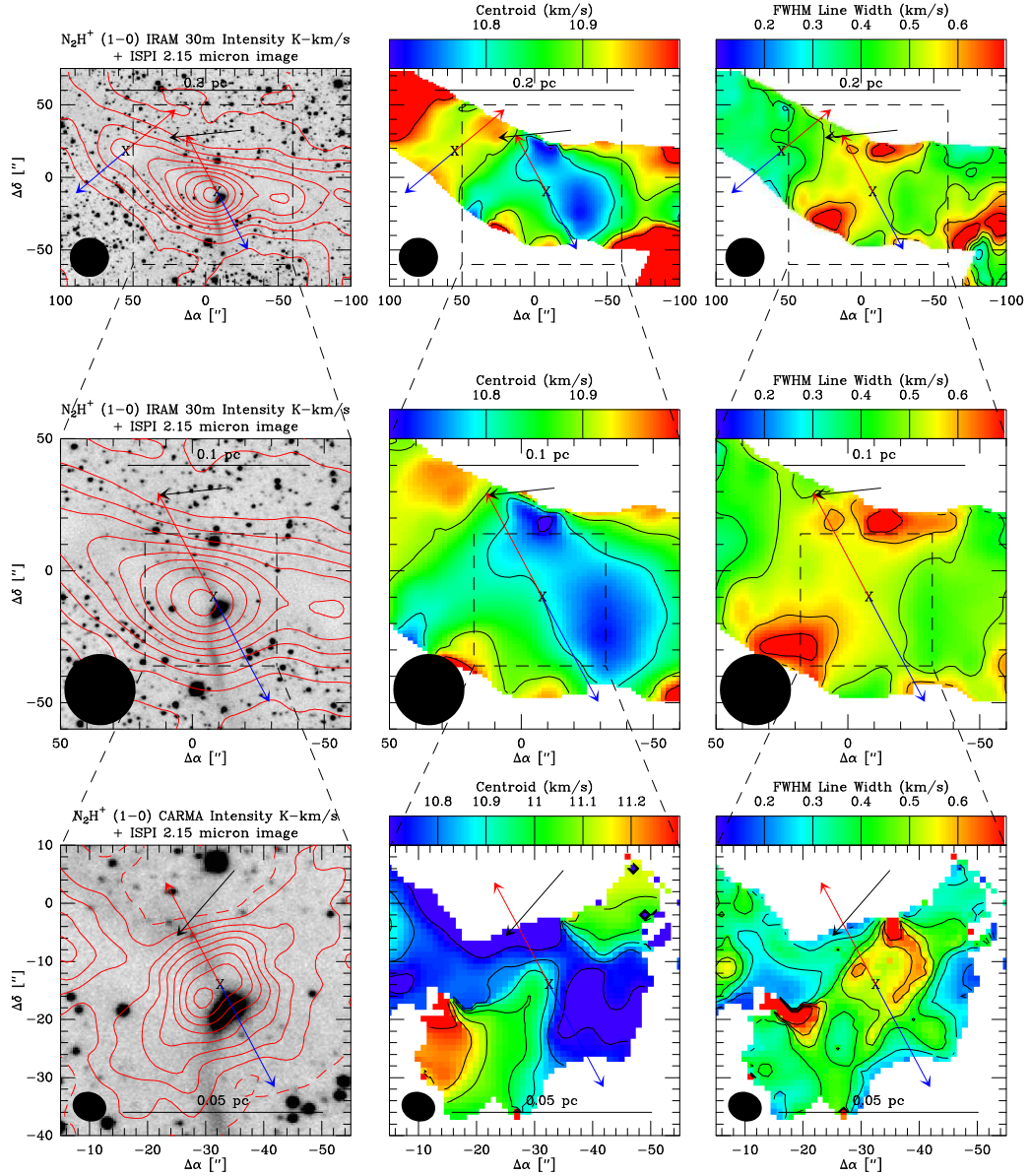


Figure 5.7 HH108IRS— Same as Figure 5.4, but zooming in on the single-dish data in the *middle row* and then the interferometer data in the *bottom row*. The IRAM 30m contours start at  $3\sigma$  with  $10\sigma$  intervals; the CARMA data start at  $\pm 3\sigma$  with  $6\sigma$  intervals. The  $N_2H^+$  peak in this object appears offset from the protostar in the single-dish and interferometer map. The interferometer map further appears to be elongated normal to the outflow. The single-dish line-center velocity map appears to show a slight gradient normal to the outflow, but the interferometric velocity field starts red-shifted, becomes blue-shifted and then goes back to red-shifted. The single-dish linewidth maps show a slight enhancement near the protostar; the interferometer data on the other hand show a highly increased linewidth near the protostar as compared to the surrounding region.

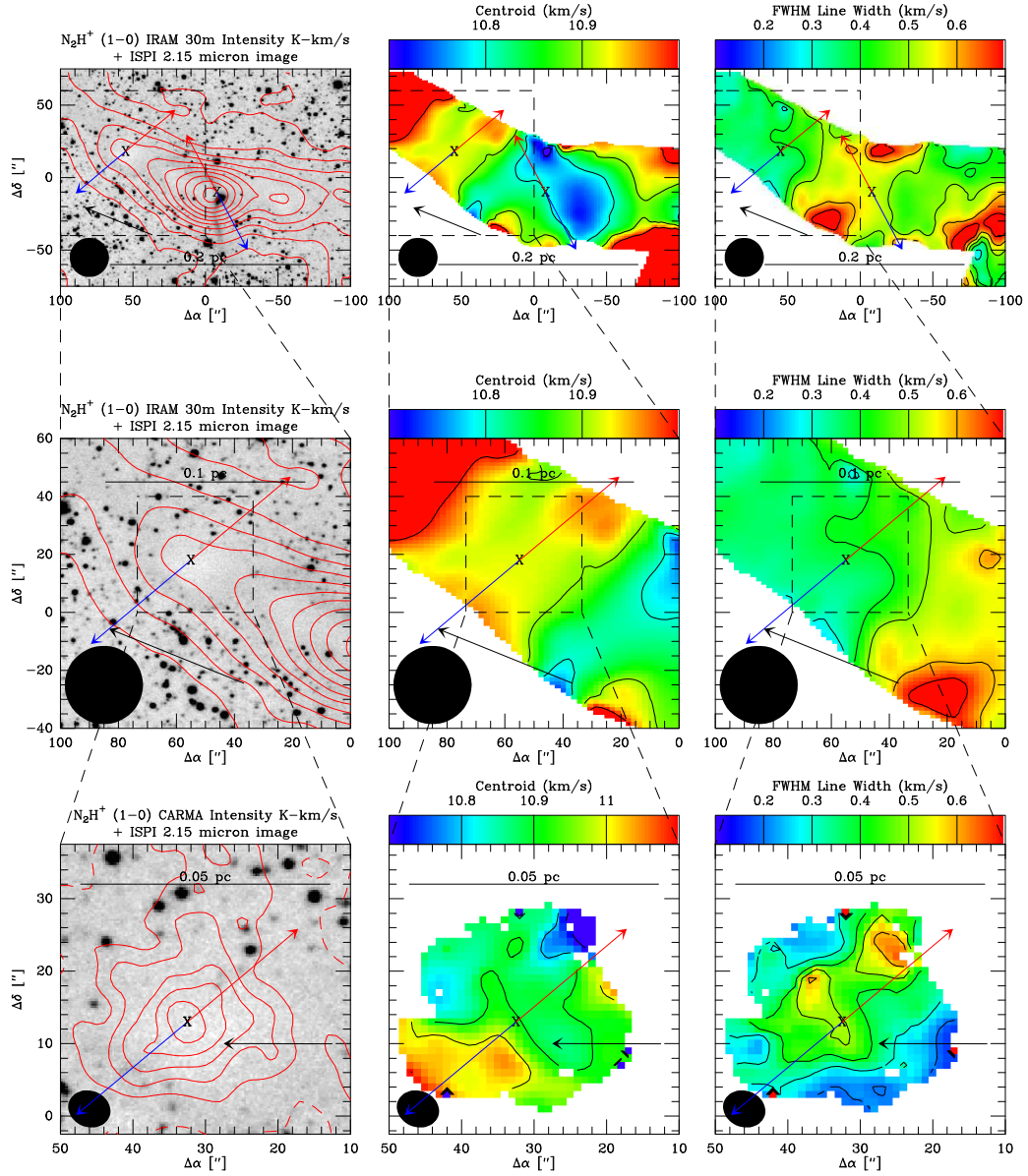


Figure 5.8 HH108MMS– Same as Figure 5.7. The IRAM 30m contours start at  $3\sigma$  with  $10\sigma$  intervals; the CARMA data start at  $\pm 3\sigma$  with  $3\sigma$  intervals. The single-dish integrated intensity map shows HH108MMS as an extension along a large-scale filamentary structure that connects with HH108IRS. However, the interferometer map finds the  $N_2H^+$  peak directly coincident with the protostar. The single-dish velocity field is fairly constant throughout the region of the envelope, but the large scale gradient is normal to its outflow. The CARMA velocity map then shows that there is a gradient along the outflow and the linewidth map shows increased linewidth along the outflow, this detail was absent in the single-dish map.

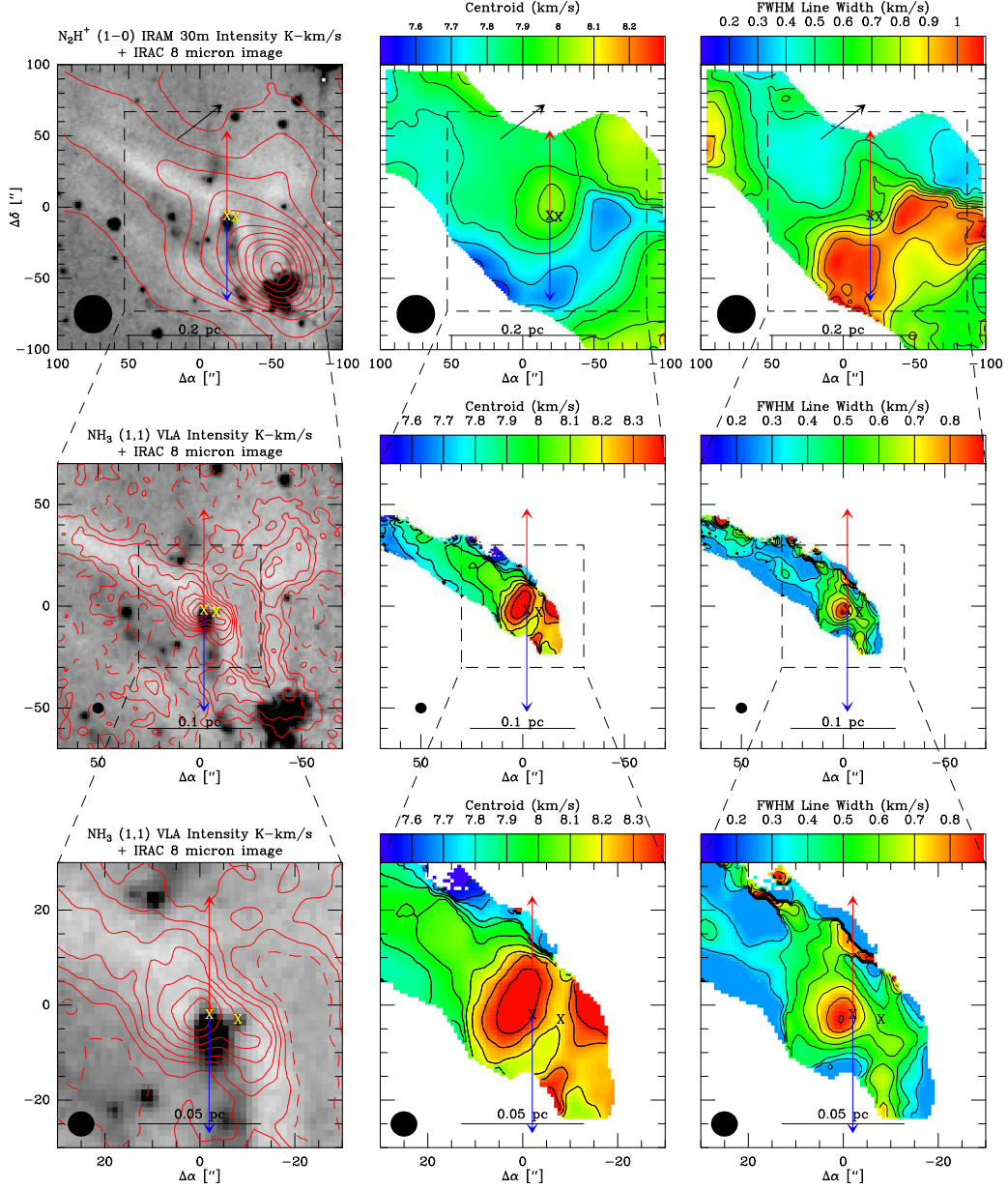


Figure 5.9 Serpens MMS3– Same as Figure 5.1 but with VLA  $\text{NH}_3$  (1,1) data and an additional zoom-in of the  $\text{NH}_3$  data in the bottom row. The IRAM 30m contours start at  $5\sigma$  with  $10\sigma$  intervals; the VLA data start at  $\pm 3\sigma$  with  $5\sigma$  intervals. The  $\text{N}_2\text{H}^+$  peak in the single-dish data is not on Serpens MMS3 but rather near a small cluster of young stars to the southwest, but there is an extension toward MMS3. The single-dish velocity field near MMS3 shows a red-shifted pocket associated with its position with a gradient extending along the large-scale filament. The VLA  $\text{NH}_3$  map reveals more detail as the emission closely follows the filamentary structures in the region. The  $\text{NH}_3$  velocity map also shows the deep red-shifted pocket of emission next to the protostar and reveals more detail in the gradient along the filament. There is a corresponding increase in linewidth to the east of the protostar at the location of the red-shifted emission.

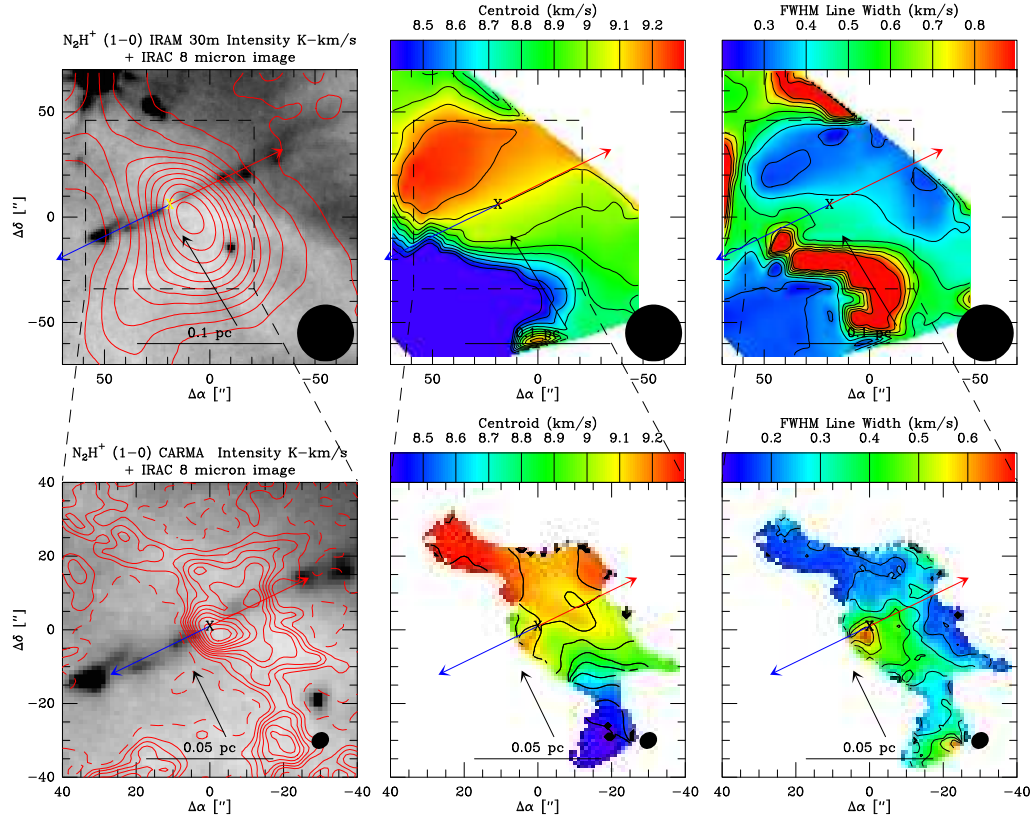


Figure 5.10 HH211– Same as Figure 5.4. The IRAM 30m contours start at  $3\sigma$  with  $10\sigma$  intervals; the CARMA data start at  $\pm 3\sigma$  with  $3\sigma$  intervals. As shown in the left panels, the  $\text{N}_2\text{H}^+$  emission mapped by the 30m and CARMA correlates very well with the  $8\mu\text{m}$  extinction in the region. Notice that the  $\text{N}_2\text{H}^+$  peak is offset from the protostar to the southwest in the single-dish and interferometer data. The velocity field shows a linear gradient normal to the outflow of HH211; however, south of the protostar there is another  $\text{N}_2\text{H}^+$  velocity component blue-shifted from the rest of the gas in the region. Tanner & Arce (2011) referred to this as the southwest extension. This transition region appears as artificially large line-width in the top right panel. The velocity field in the CARMA data also shows the linear gradient with a slight increase in linewidth near the protostar.

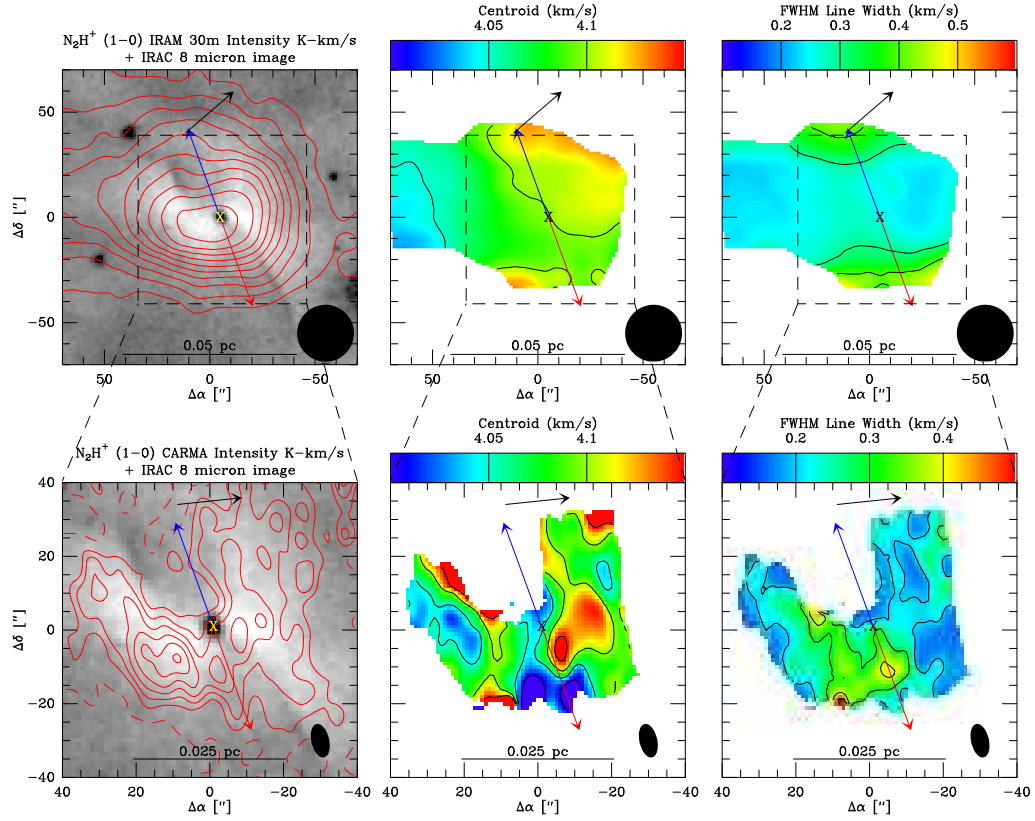


Figure 5.11 IRAS 16253-2429– Same as Figure 5.4. Both the IRAM 30m and CARMA contours start at  $3\sigma$  with  $3\sigma$  intervals. The single-dish  $\text{N}_2\text{H}^+$  emission traces the roughly symmetric envelope of IRAS 16253-2429 quite well with the peak emission just east of the protostar. The CARMA  $\text{N}_2\text{H}^+$  map also traces the envelope well and the northern outflow cavity is prominent as an evacuated region, probably due to resolved-out emission. The single-dish velocity field shows a very small velocity gradient roughly normal to the outflow. The CARMA velocity map shows complex structure, but there is an overall gradient in the same direction as the single-dish map. In addition, there is a red-shifted feature at the same location of as the outflow cavity wall. The single-dish and interferometer linewidth maps show slight enhancements at the same locations, where the peak emission is present, but there also is a linewidth increase toward the edge of the envelope along the outflow in the single-dish map. Note that the linewidth in the envelope is extremely narrow, only  $\sim 0.2 \text{ km s}^{-1}$  over the regions where the outflow could not be interacting.

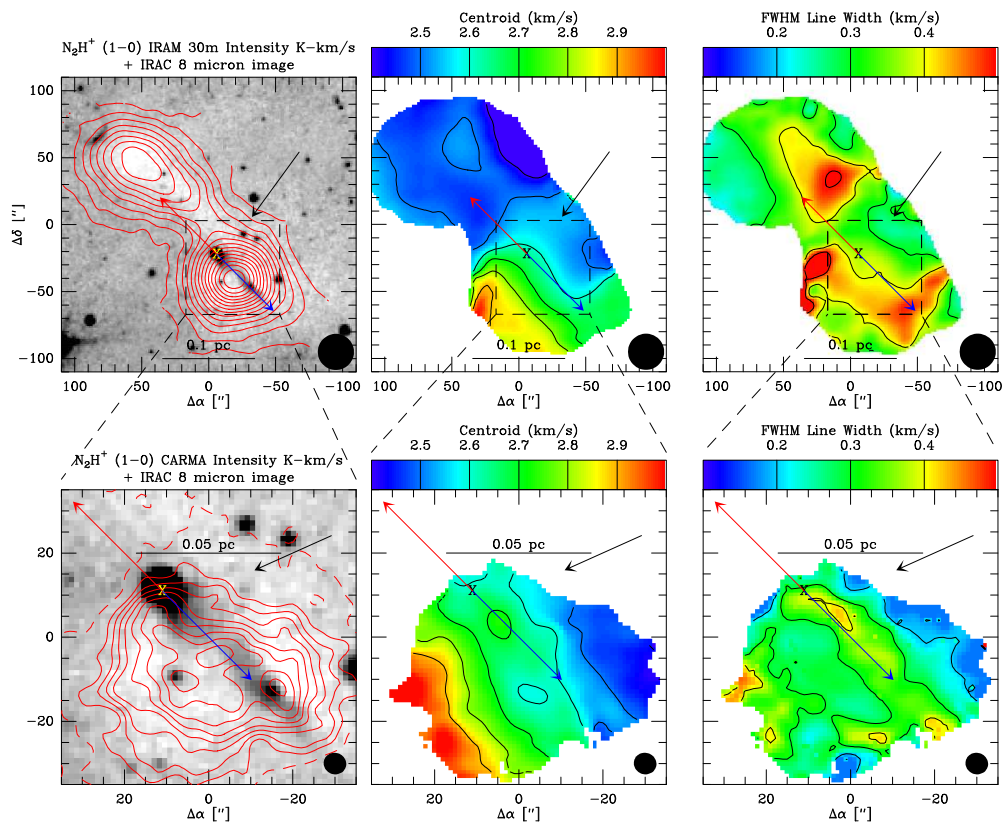


Figure 5.12 L1152– Same as Figure 5.4. The IRAM 30m contours start at  $10\sigma$  with  $10\sigma$  intervals; the CARMA data start at  $\pm 3\sigma$  with  $3\sigma$  intervals. The single-dish  $N_2H^+$  emission traces two connected peaks over  $\sim 0.1$  pc; one is star-less the other is adjacent to the protostar. The CARMA  $N_2H^+$  map focuses on the protostellar clump and clearly shows that the protostar is offset from most of the  $N_2H^+$  emission. Both velocity maps show a strong gradient normal to the outflow, while the star-less clump does not have much velocity structure. The linewidth maps show increases along the outflow; there is a feature in the single-dish map which is not exactly along the outflow but quite near it. The CARMA linewidth map shows increased linewidth that correlates very strongly with the jet-like emission shown in the  $8\mu m$  image.

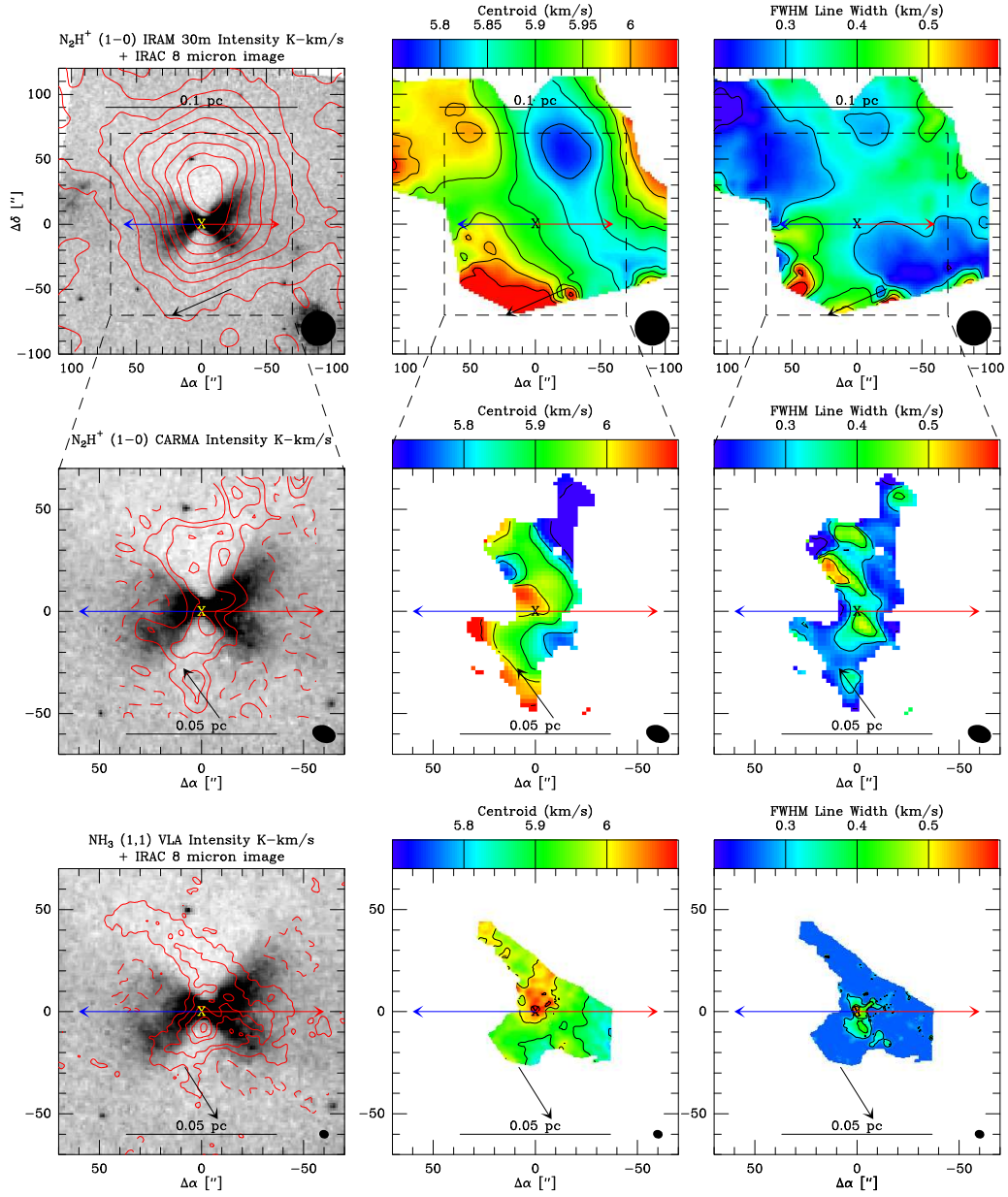


Figure 5.13 L1527– Same as Figure 5.4, but VLA  $\text{NH}_3$  data are also shown in the *bottom row*. The IRAM 30m contours start at  $5\sigma$  with  $10\sigma$  intervals; both the CARMA and VLA contours start at  $\pm 3\sigma$  with  $3\sigma$  intervals. The single-dish  $\text{N}_2\text{H}^+$  data are peaked north of the protostar, which is also the case for the CARMA data, but the VLA data are peaked south of the protostar. The single-dish velocity field appears to have a component along the outflow and normal to it. The interferometer velocity maps reflect the single-dish velocities on the largest scales, but near the protostar there is a small-scale velocity gradient in the opposite direction of the large-scale gradient. There is little increase in linewidth in the single-dish data, but there appears to be increased linewidth near the protostar in both sets of interferometer data.

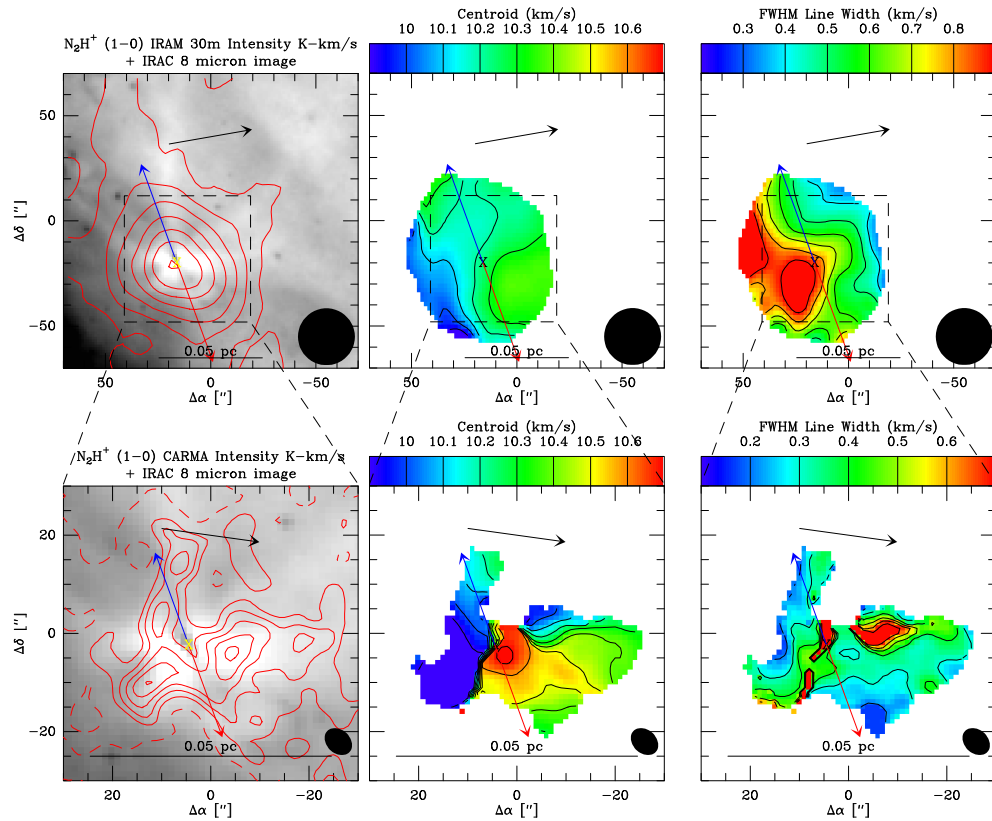


Figure 5.14 RNO43– Same as Figure 5.4. The IRAM 30m contours start at  $3\sigma$  with  $10\sigma$  intervals; the CARMA contours start at  $\pm 3\sigma$  with  $3\sigma$  intervals. The single-dish intensity map appears mostly unresolved, while the CARMA data trace the  $8\mu\text{m}$  extinction structures closely with a depression of emission coincident with the protostar. The single-dish velocity field shows a gradient mostly normal to the outflow and the interferometer data reveal a sharp velocity shift between the east and west sides of the envelope. This appears as a line of broad linewidth (an artifact from fitting) where the two components are viewed on top of each other; this is associated with a region of large linewidth in the single-dish map.

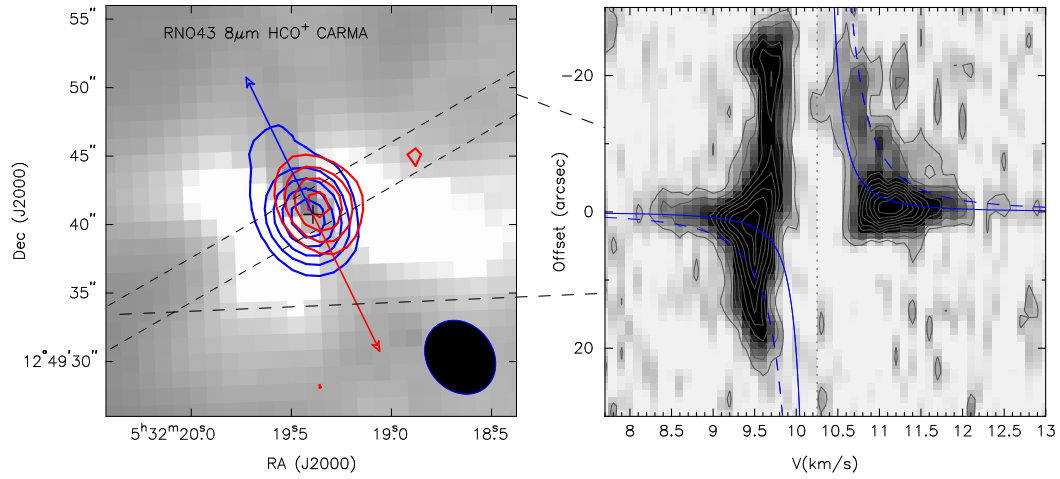


Figure 5.15 RNO43– Same as Figure 5.5. The contours levels are  $\pm 5, 8, 11, 14,$  and  $17\sigma$  ( $\sigma = 0.12$  K) for the red and blue-shifted emission. The emission morphology of the HCO<sup>+</sup> in both the integrated intensity map on the left and in the PV plot are quite similar to L1165. The total velocity extent of  $\sim \pm 2$  km s<sup>-1</sup> is similar in magnitude to L1165. However, the red and blue peaks are much closer together due to the increased distance of RNO43. The PV plot contours start at  $3\sigma$  and increase in  $3\sigma$  intervals ( $\sigma=0.2671$ ). The *solid-blue* curve represents Keplerian rotation (or infall) for a  $0.67 M_{\odot}$  central object and the *dashed-blue* curve is for a  $2.67 M_{\odot}$  central object.

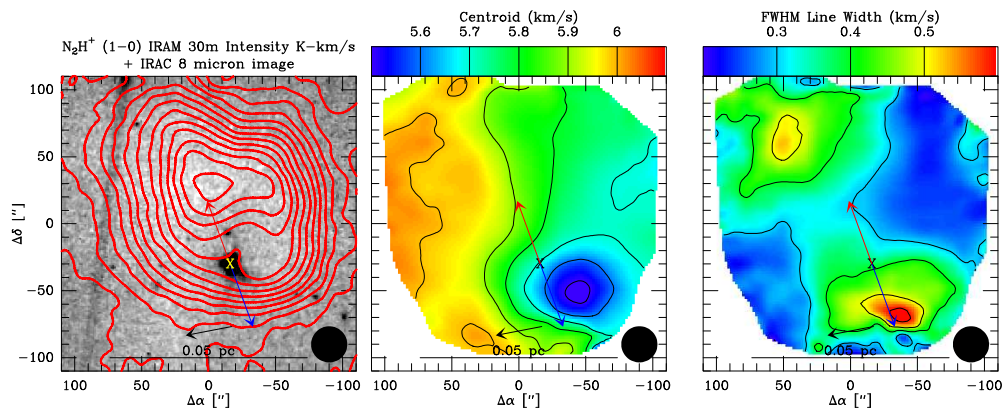


Figure 5.16 IRAS 04325+2402– Same as Figure 5.1, but I only have single-dish data for this object. The IRAM 30m contours start at  $10\sigma$  with  $10\sigma$  intervals. The N<sub>2</sub>H<sup>+</sup> contours correlate very well with the  $8\mu\text{m}$  extinction and the peak is actually on an apparent star-less core north of the protostar. There is a tail of emission wrapping towards the protostar, but at lower intensity levels. The velocity field shows a gradient roughly normal to the outflow and there appears to be smaller-scale structure in the velocities near the protostar. The linewidth map does not show a large increase near the protostar but shows two peaks that are located along the outflow indicating a possible interaction.

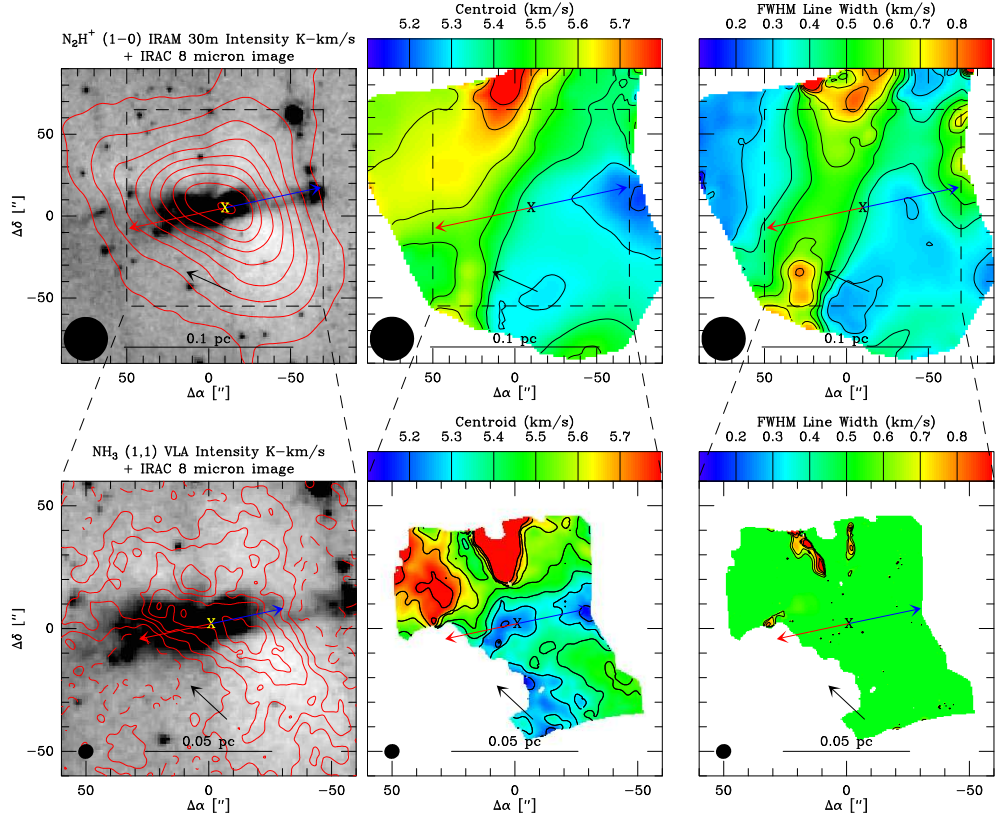


Figure 5.17 L483– Same as Figure 5.6, using archival  $NH_3$  data from Fuller & Wootten (2000). The IRAM 30m contours start at  $20\sigma$  with  $20\sigma$  intervals; the VLA contours start at  $\pm 3\sigma$  with  $6\sigma$  intervals. The  $N_2H^+$  and  $NH_3$  emission trace the envelope seen in  $8\mu m$  extinction quite closely. The velocity field shows a gradient that is at an angle  $45^\circ$  from the outflow in the single-dish map. The VLA velocity map shows a similar large-scale feature but there is a pocket of blue-shifted gas coincident with the protostar and there is a red-shifted pocket directly north of the protostar. The single-dish linewidth map shows increased linewidth at the location of the most rapid velocity changes; the VLA linewidth map only shows a couple of features where there is a sharp transition in the velocity components. This is due to only having  $0.3 \text{ km s}^{-1}$  channel width in the  $NH_3$  data.

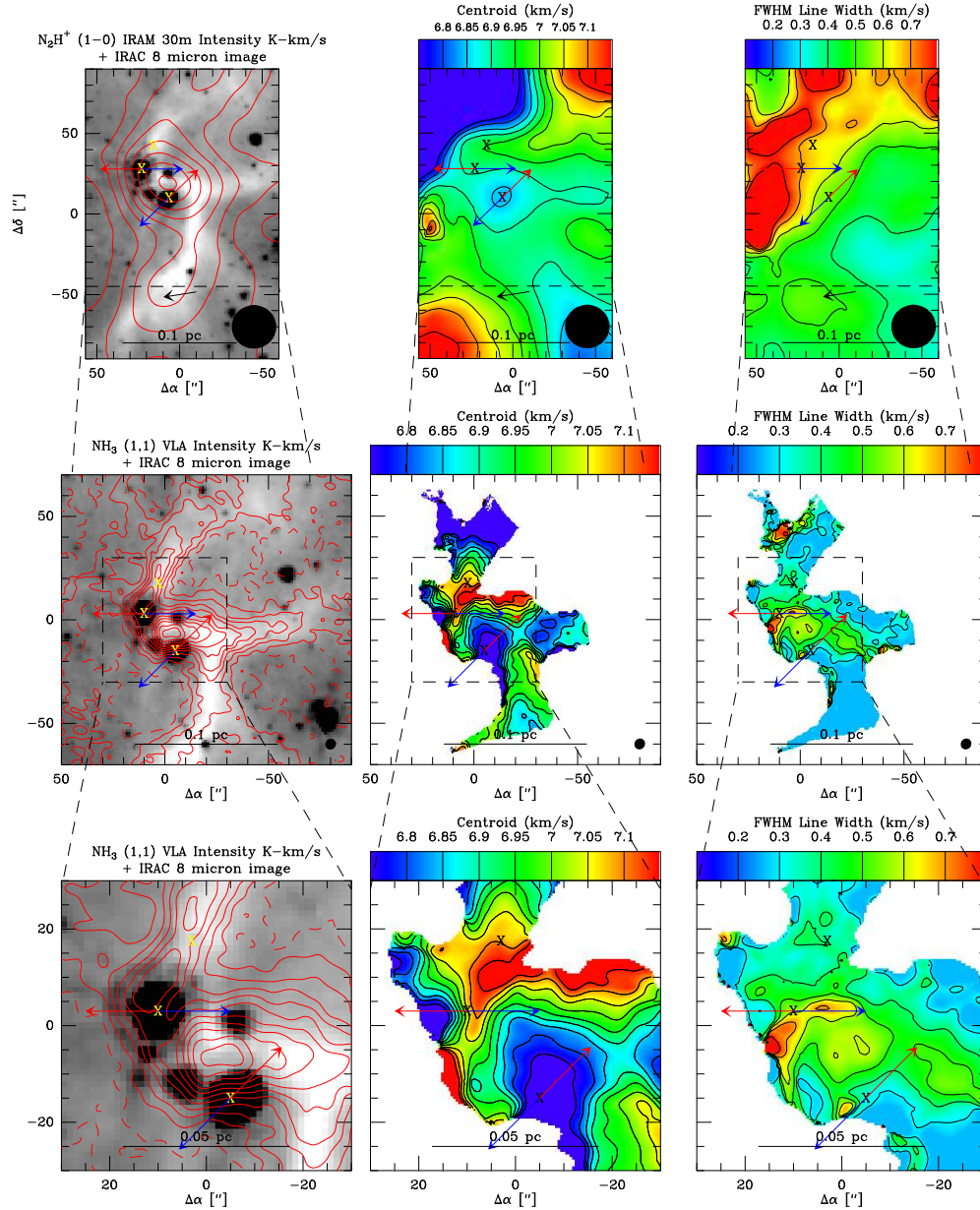


Figure 5.18 L673– Same as Figure 5.6 with an additional zoom-in on the  $\text{NH}_3$  data in the bottom row. The IRAM 30m contours start at  $20\sigma$  with  $20\sigma$  intervals; the VLA contours start at  $\pm 3\sigma$  with  $6\sigma$  intervals. Though only three protostars are marked; there are likely seven in the region (Tsitali et al., 2010); the southern-most protostar appears to be a triple (Tobin et al. in prep.). The single-dish  $\text{N}_2\text{H}^+$  emission fills the map, but there is increased emission where the  $8\mu\text{m}$  extinction is most prominent. The  $\text{NH}_3$  map only picks up the densest regions around the protostars. There is a gradient in the velocity map along the filament, though there appears to be features associated with the two marked protostars in both the single-dish and VLA maps. Both velocity maps also show a second velocity component to the north and the transition region appears as increased linewidth.

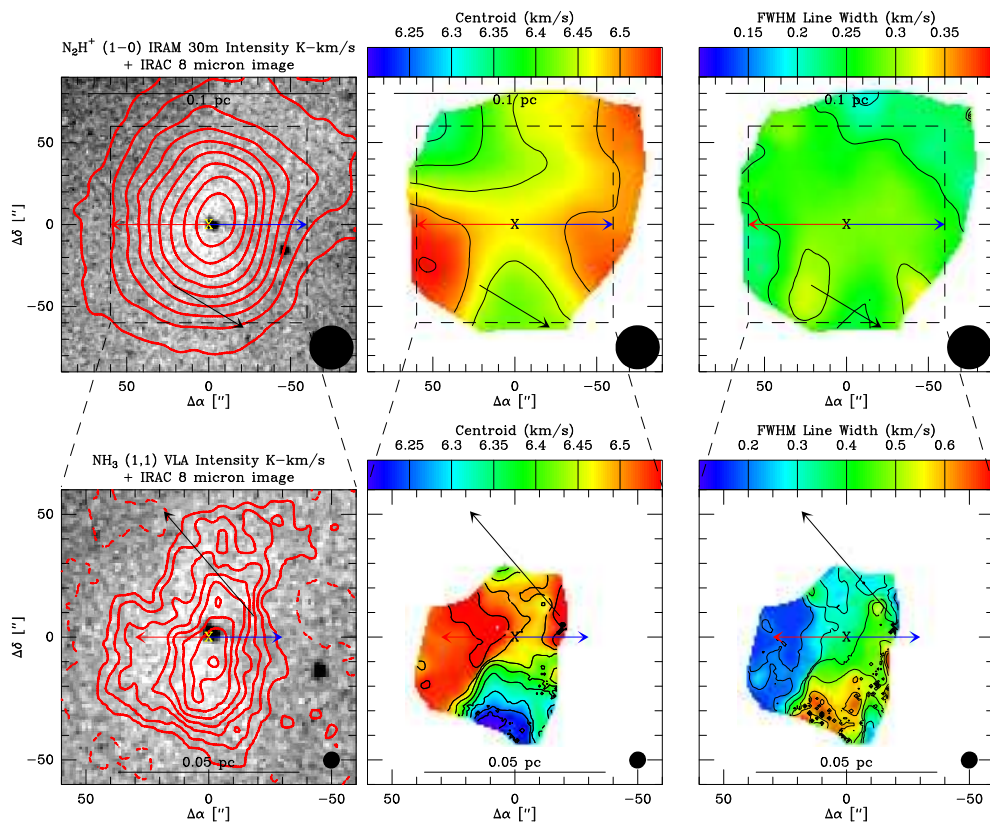


Figure 5.19 L1521F– Same as Figure 5.6. The IRAM 30m contours start at  $3\sigma$  with  $3\sigma$  intervals; the VLA contours start at  $\pm 3\sigma$  with  $3\sigma$  intervals. The single-dish data trace the region of  $8\mu\text{m}$  extinction well and the  $\text{NH}_3$  data trace the inner, high density regions. The velocity structure from the single-dish map shows weak evidence for a gradient normal to the outflow. The  $\text{NH}_3$  data do show a gradient, but the emission near the protostar is all red-shifted and the blue-shifted emission is far ( $10''$  1400 AU) from the protostar. However, as noted in the text, the  $\text{NH}_3$  emission is optically thick and may not fully trace the inner envelope kinematics. The single-dish linewidth map has very little structure while the  $\text{NH}_3$  linewidths are peaked coincident with the blue-shifted area of the velocity field.

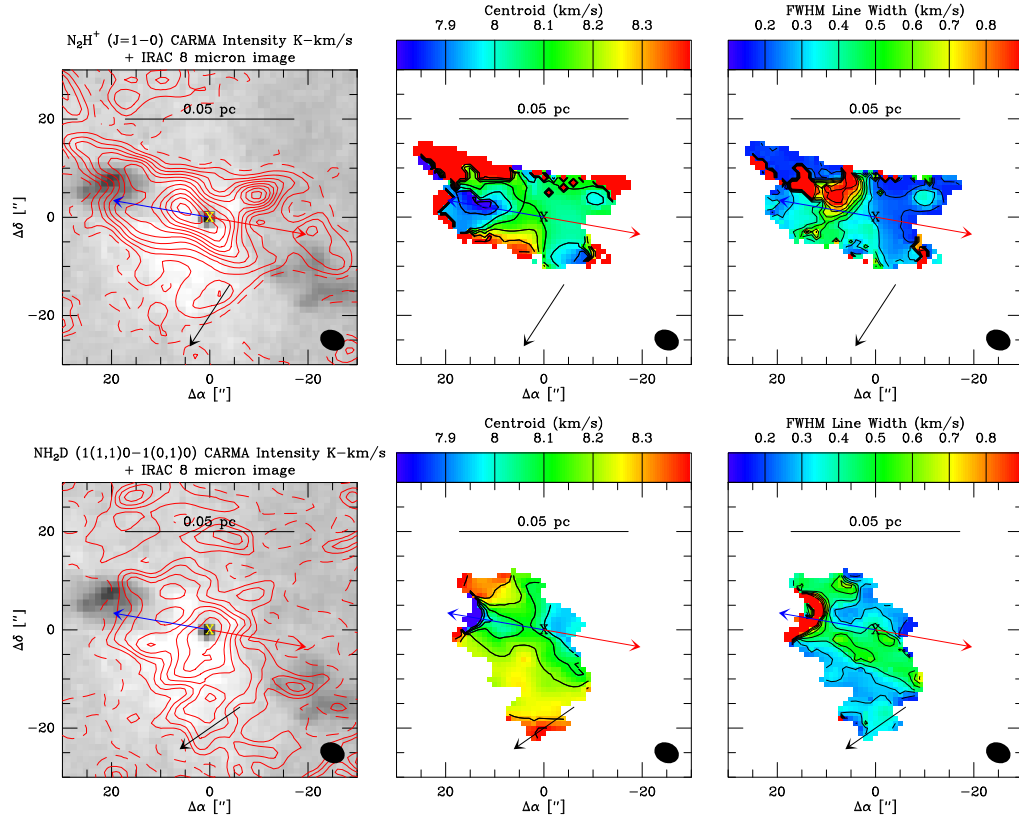


Figure 5.20 Perseus 5– The *top row* shows the CARMA  $N_2H^+$  ( $J = 1 \rightarrow 0$ ) data and the *bottom row* shows the  $NH_2D$  ( $1_{1,1} \rightarrow 1_{0,1}$ ) data also from CARMA; the contours start at  $\pm 3\sigma$  with  $6\sigma$  intervals for  $N_2H^+$  and  $\pm 3\sigma$  with  $3\sigma$  intervals for  $NH_2D$ . Both molecules have approximately the same noise level. The integrated intensity data for both molecules are overlaid on the IRAC  $8\mu m$  images.  $NH_2D$  appears to trace the  $8\mu m$  extinction best while  $N_2H^+$  is centrally peaked. The line-center velocity of each molecular line is shown in the center column,  $N_2H^+$  and  $NH_2D$  indicate that there may be a gradient normal to the outflow, but that there is also a gradient in the direction of the outflow. The linewidth plots in the right panels are complex, all show an enhancement away from the protostar along the outflow;  $NH_2D$  in particular shows an increase through the envelope near the outflow axis.

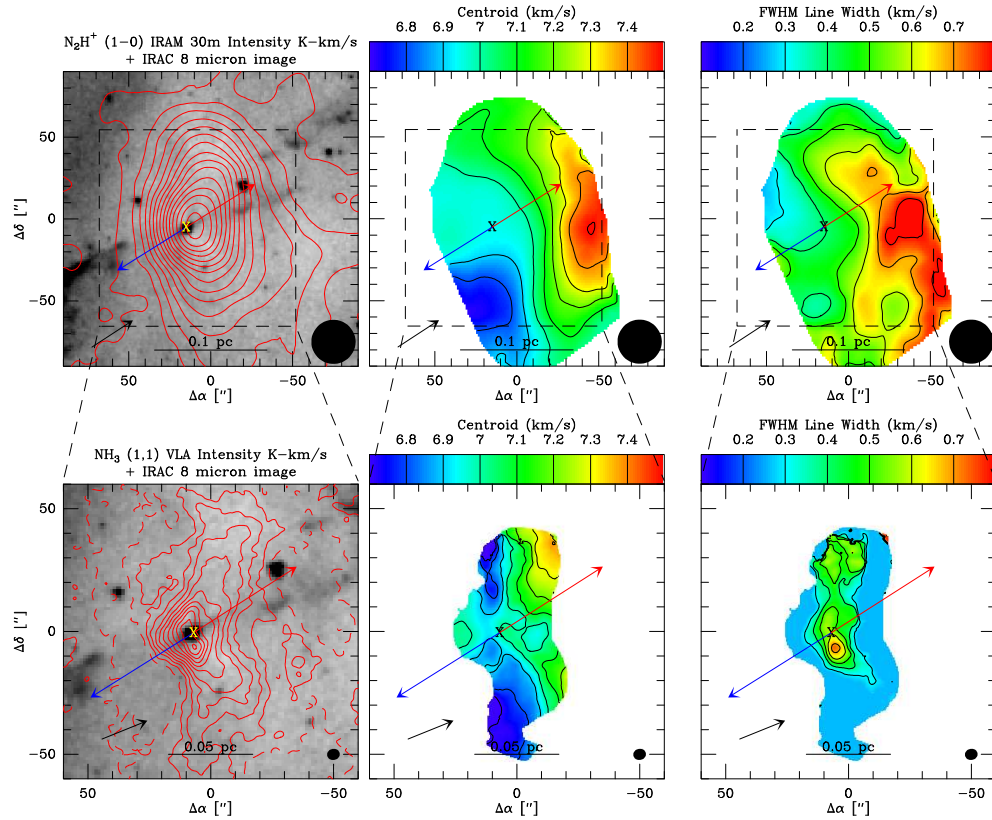


Figure 5.21 IRAS 03282+3035– Same as Figure 5.6. The IRAM 30m contours start at  $3\sigma$  with  $10\sigma$  intervals; the VLA contours start at  $\pm 3\sigma$  with  $5\sigma$  intervals. The single-dish  $\text{N}_2\text{H}^+$  emission closely traces the entire area viewed in  $8\mu\text{m}$  extinction, peaking near the protostar. The VLA  $\text{NH}_3$  data are picking up the densest region near the protostar. The velocity gradient is mostly along the outflow in the single-dish and VLA  $\text{NH}_3$  velocity map. The linewidth in the single-dish data peaks to the west of the protostar, somewhat along the outflow. The  $\text{NH}_3$  linewidth map has peaks about the protostar, normal to the outflow, and directly north, while the rest of the map has a small linewidth.

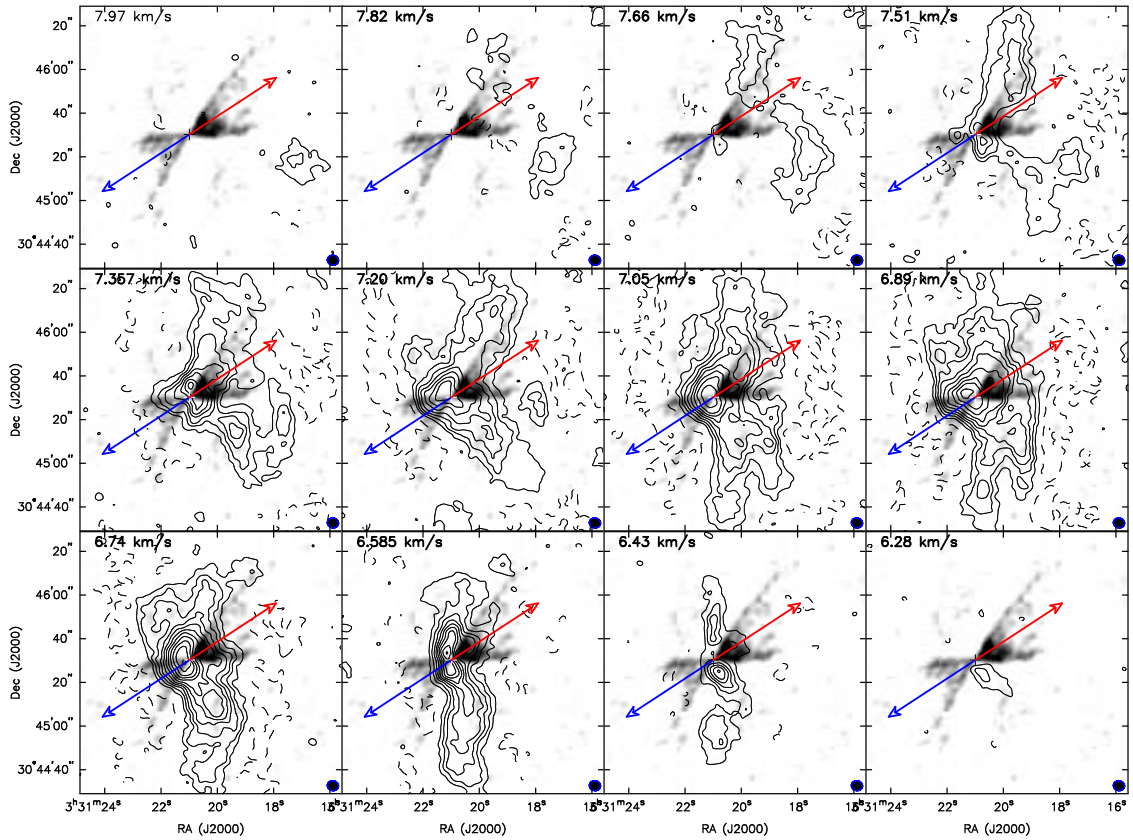


Figure 5.22 Channel maps of  $\text{NH}_3$  (1,1) emission (*contours*) overlaid on CO ( $J = 1 \rightarrow 0$ ) emission from Arce & Sargent (2006), showing the relationship between  $\text{NH}_3$  emission and the outflow cavity. The top and bottom rows show the red- and blue-shifted component that are unblended; the  $\text{NH}_3$  emission in the middle panels is blended. Contours start at  $\pm 3\sigma$ , and then increase in  $3\sigma$  intervals. The negative contours are plotted as dashed lines, reflecting the loss of large-scale structure. The unblended velocity channels show very narrow structures and in the bottom row, the blue-shifted components are almost north-south in orientation. Much of the  $\text{NH}_3$  emission south of the protostar appears unlikely to be influenced by the outflow. The position of the protostar is marked with the cross and the outflow axis is marked by the blue and red lines denoting the outflow orientation within the plane of the sky.

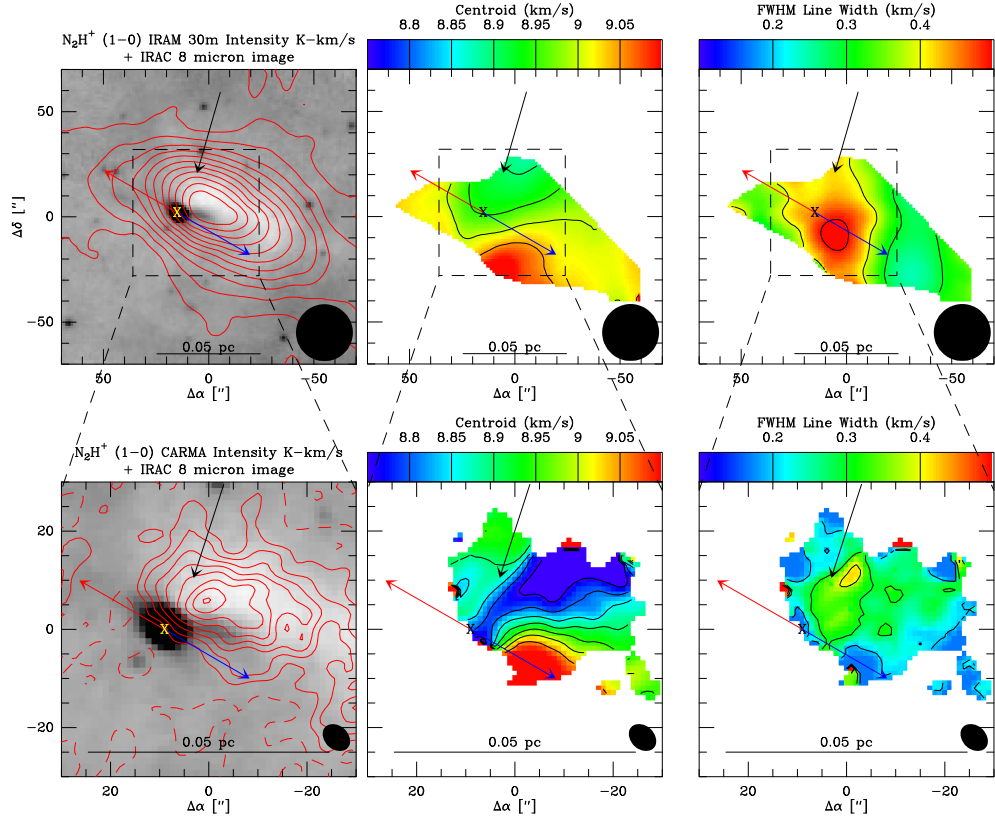


Figure 5.23 HH270 VLA1– Same as Figure 5.4. The IRAM 30m contours start at  $3\sigma$  with  $6\sigma$  intervals; the CARMA contours start at  $\pm 3\sigma$  with  $3\sigma$  intervals. The single-dish map shows strong emission coincident with the  $8\mu\text{m}$  extinction extended along the outflow. The CARMA  $\text{N}_2\text{H}^+$  map shows a similar morphology, with no emission coincident with the protostar. The single-dish velocity field shows a gradient normal to and along the outflow; however, the CARMA velocity map shows that the gas velocity is relatively constant normal to the outflow, but along the outflow axis there is a clear gradient with more red-shifted emissions toward the outflow axis. The velocity contours trace a similar shape as the outflow cavity; the faint scattered light of the outflow cavity can be seen in the  $8\mu\text{m}$  image. The single-dish linewidth map shows a peak along the outflow southwest of the protostar, this appears to be the unresolved velocity gradient along the outflow as the CARMA map does not have increased linewidth along at the same location.

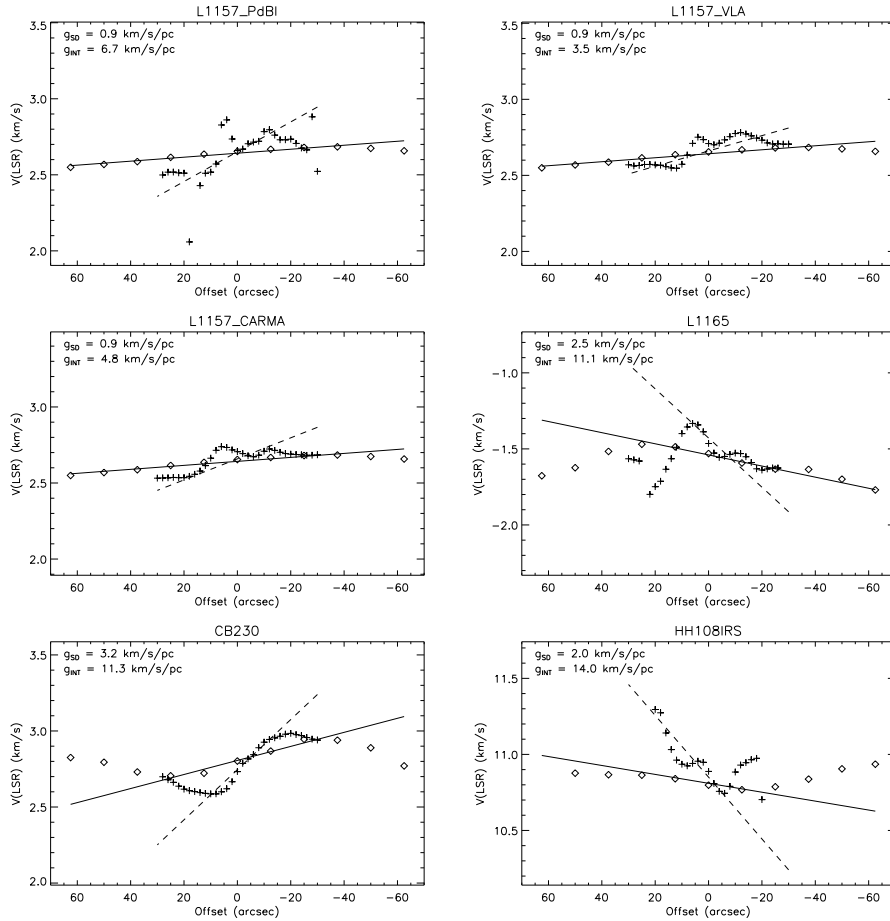


Figure 5.24 Line center velocity cuts taken across each protostellar envelope, normal to the outflow. The diamonds are the single-dish data and the plus-signs are the interferometer data. Each point for the single-dish data is the average of the  $27''$  beam surrounding each point. Each interferometer point is the average of points within the semi-major axis of the synthesized beam. The velocity errors at each point are generally  $<0.05 \text{ km s}^{-1}$ , approximately the size of the symbols. The solid-lines are the linear fits to the single-dish velocity data between  $\pm 30''$  for most sources. Serpens MMS3 was fit between  $60''$  and  $0''$  and L1152 was fit between  $40''$  and  $-20''$ .

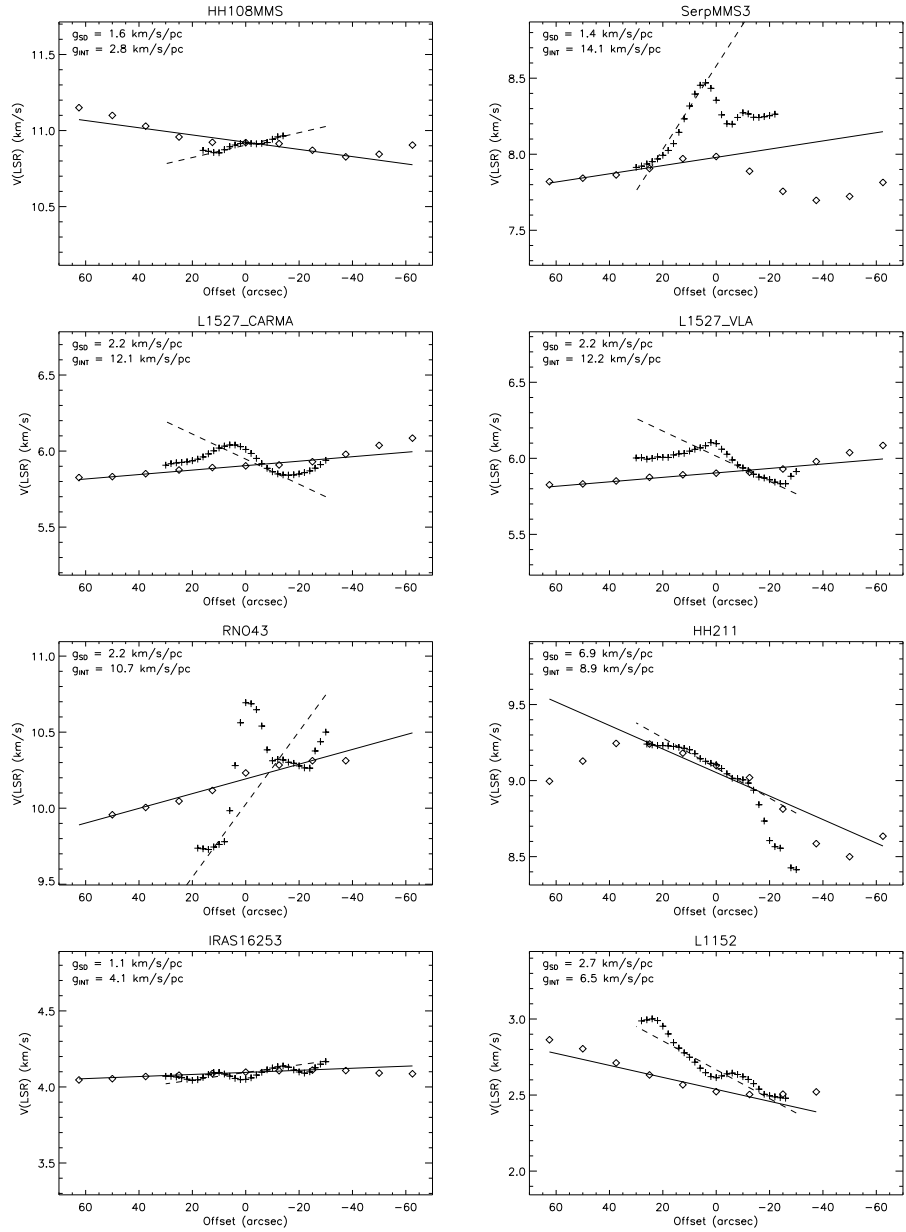


Fig. 5.24 — cont'd.

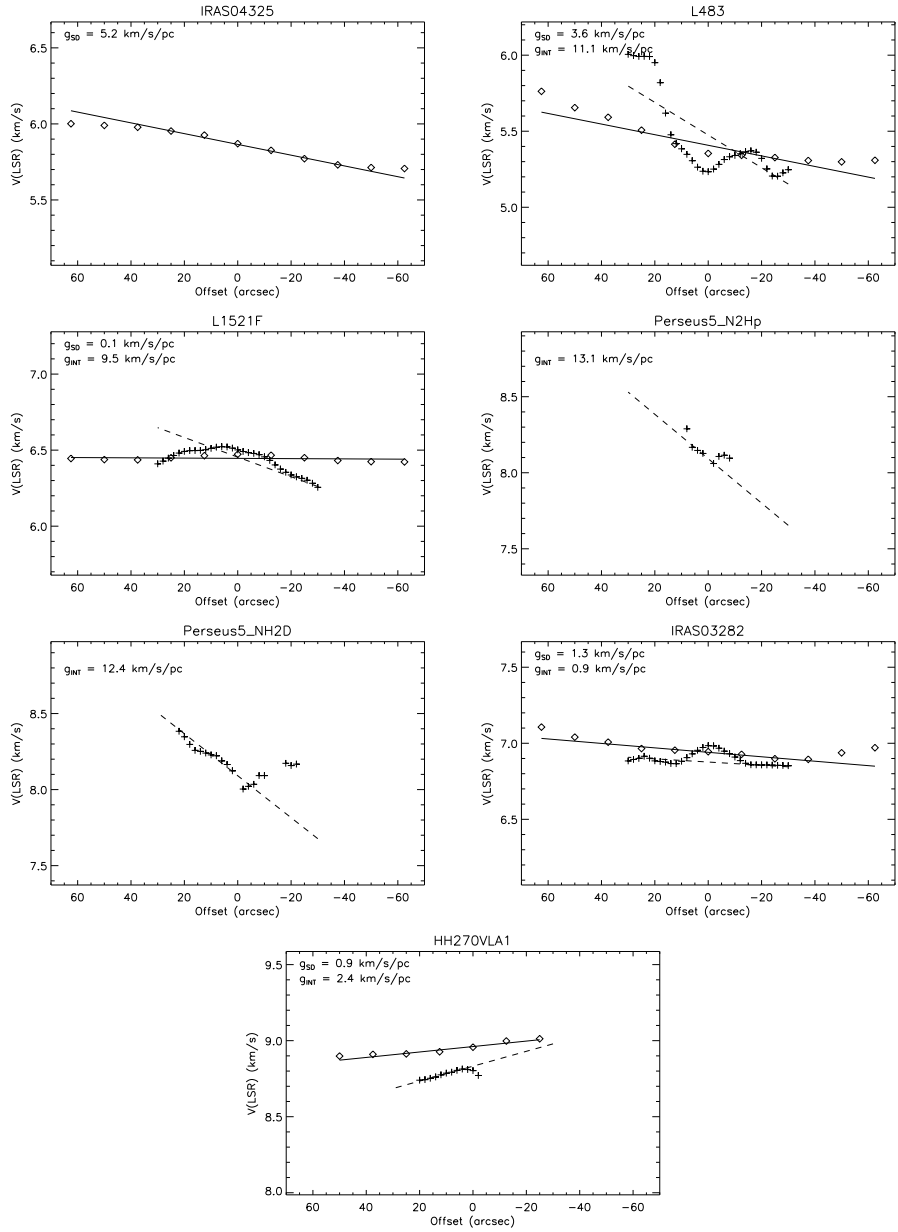


Fig. 5.24 — cont'd.

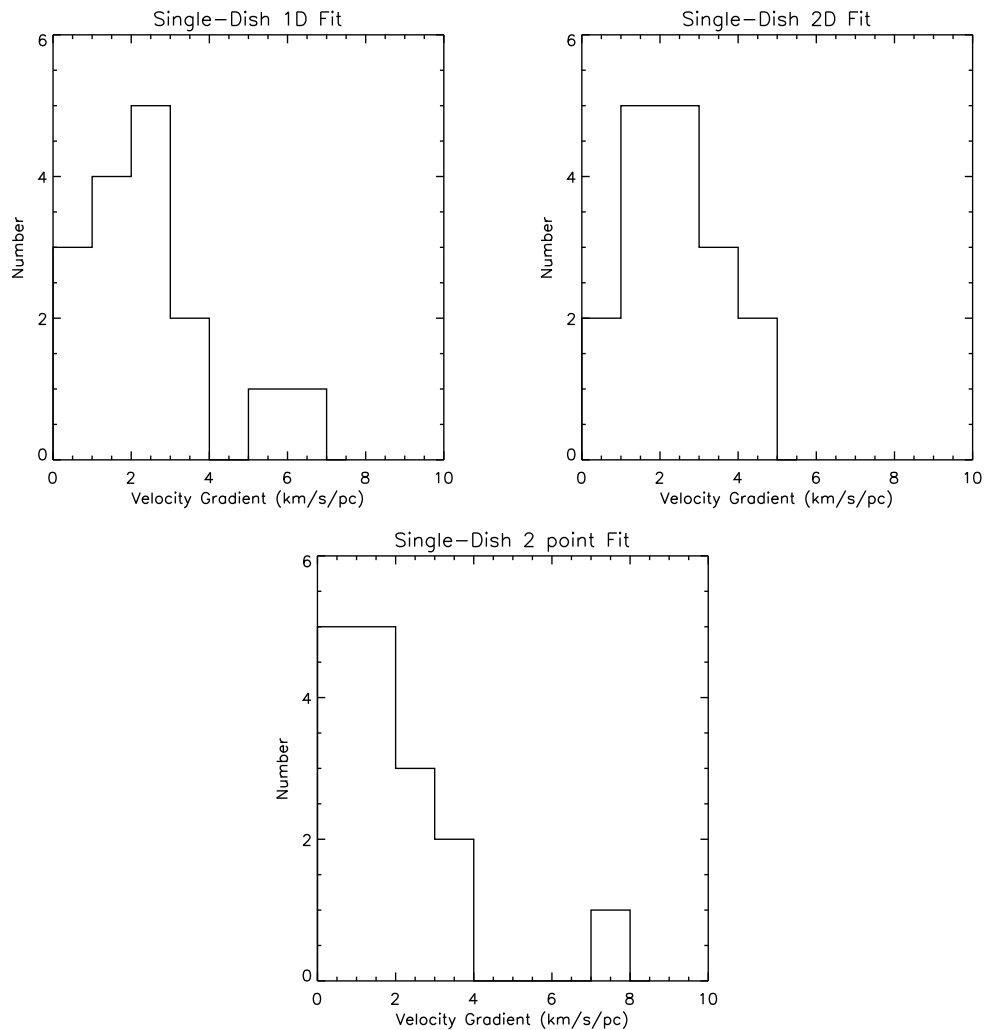


Figure 5.25 Histogram plots of measured velocity gradients from single-dish data. The top left panel shows the velocity gradients derived from one-dimensional cuts across the velocity field, taken normal to the outflow. The top right middle panel shows the velocity gradients derived from a two-dimensional fit to the velocity field. The bottom panel shows the velocity gradients derived from the velocity difference at  $\pm 10000$  AU from the protostar, also normal to the outflow. The distributions from the one- and two-dimensional fits are comparable while the two point method is skewed toward smaller gradients; this difference is likely due to the gradients fits picking up on higher velocity emission that sometimes turns over toward lower velocities by  $\sim 10000$  AU. The middle panel include the two-dimensional fit for L673 which is absent from the left and right panels.

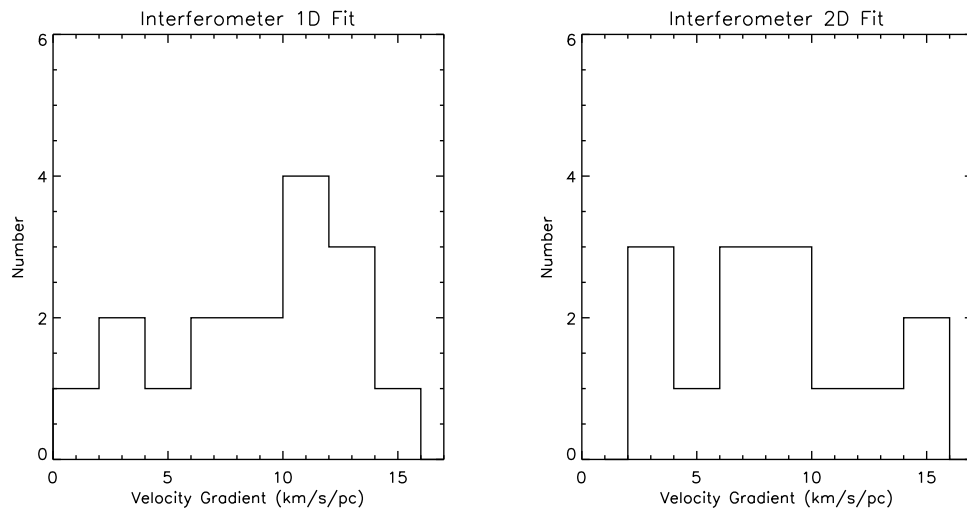


Figure 5.26 Histogram plots of measured velocity gradients from interferometer data. The left panel shows the velocity gradients derived from one-dimensional cuts across the velocity field, taken normal to the outflow. The right panel shows the velocity gradients derived from a two-dimensional fit to the velocity field. The differences in these distributions likely result from the two-dimensional method having to fit all the data where complexities in the velocity field may reduce the gradient fit. The left panels include L1157 and Serpens MMS3 while they are absent from the right panels.

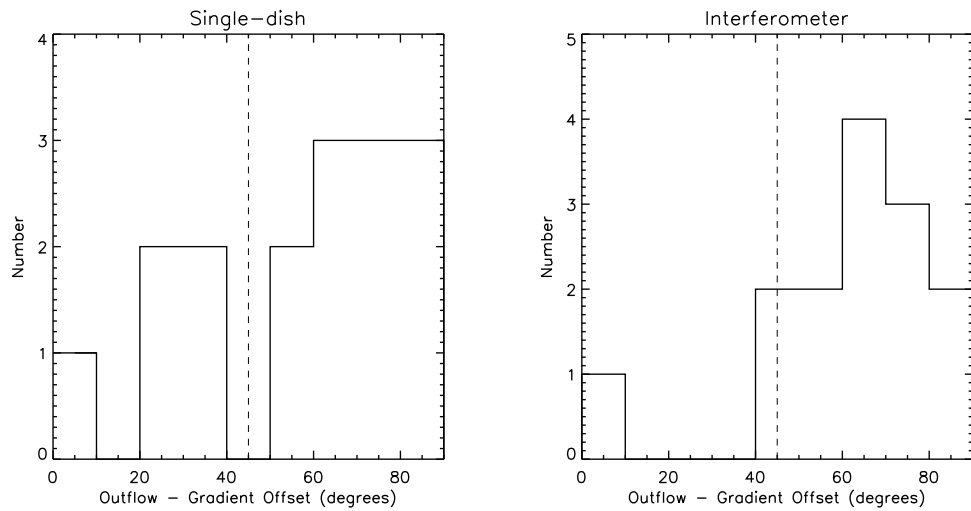


Figure 5.27 Histogram plots of velocity gradient position angle offset relative to outflow position angle for single-dish (*left panel*) and interferometric (*right panel*) velocity gradient measurements. An offset of  $90^\circ$  indicates that the gradient is normal to the outflow and most of the velocity gradients are within  $45^\circ$  of normal to the outflow (*dashed line*); however, there is substantial dispersion in this relationship. The shift in number toward  $90^\circ$  in the interferometer observations may reflect that smaller-scale motion is becoming more ordered. The left panels include L1157 and Serpens MMS3 while they are absent from the right panels.

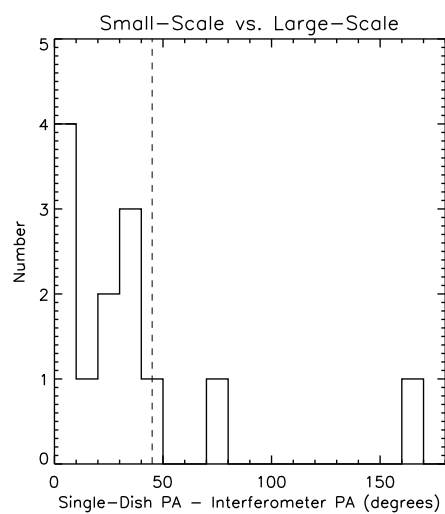


Figure 5.28 Histogram plot of single-dish velocity gradient position angle minus the interferometric velocity gradient position angle. Most velocity gradients at large and small-scales are within  $45^\circ$  of each other, indicating that the line of sight velocities at large-scales reflect similar velocity structure at small-scales. This plot does not include L1157, Serpens MMS3, or L673.

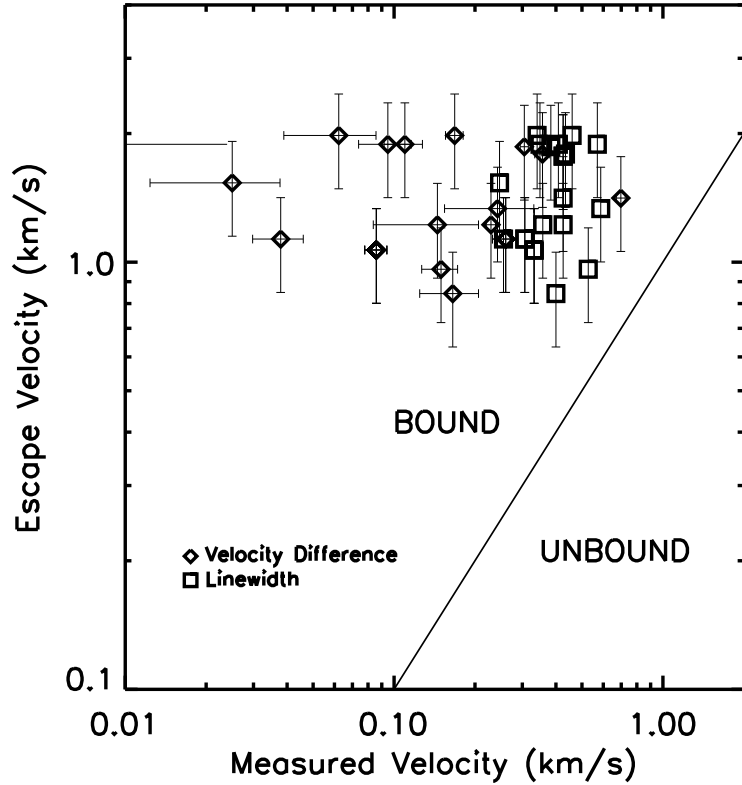


Figure 5.29 Plot of escape velocity at 10000 AU versus velocity shifts measured at 10000 AU radii (*diamonds*) and the average  $\text{N}_2\text{H}^+$  FWHM from the single-dish data (*squares*). The escape velocity is calculated using the total mass of the envelope from the  $8\mu\text{m}$  extinction data in Chapter 4 plus a  $1 M_\odot$  solar mass central object; the error bars in the calculated escape velocity reflect a 50% uncertainty in total mass. This shows that the envelopes are consistent with being gravitationally bound on large-scales and that the envelopes are not supported by rotation, turbulence, and/or thermal pressure. The protostar closest to rotational support is HH211; its substantial rotation was also highlighted by Tanner & Arce (2011).

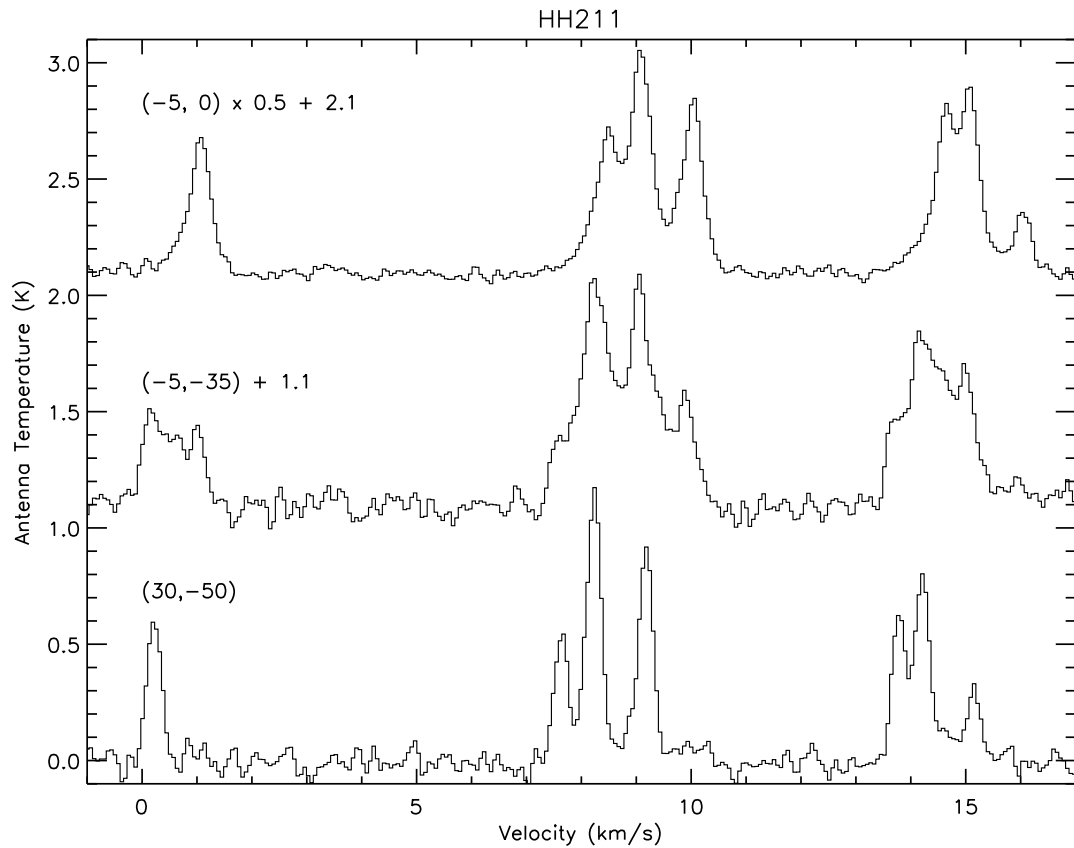


Figure 5.30 Plot of single-dish  $\text{N}_2\text{H}^+$  line profiles at three positions in HH211 showing the transition between different velocity components. The middle spectrum is in the region where the two components are blended, demonstrating that the lines are not extremely wide.

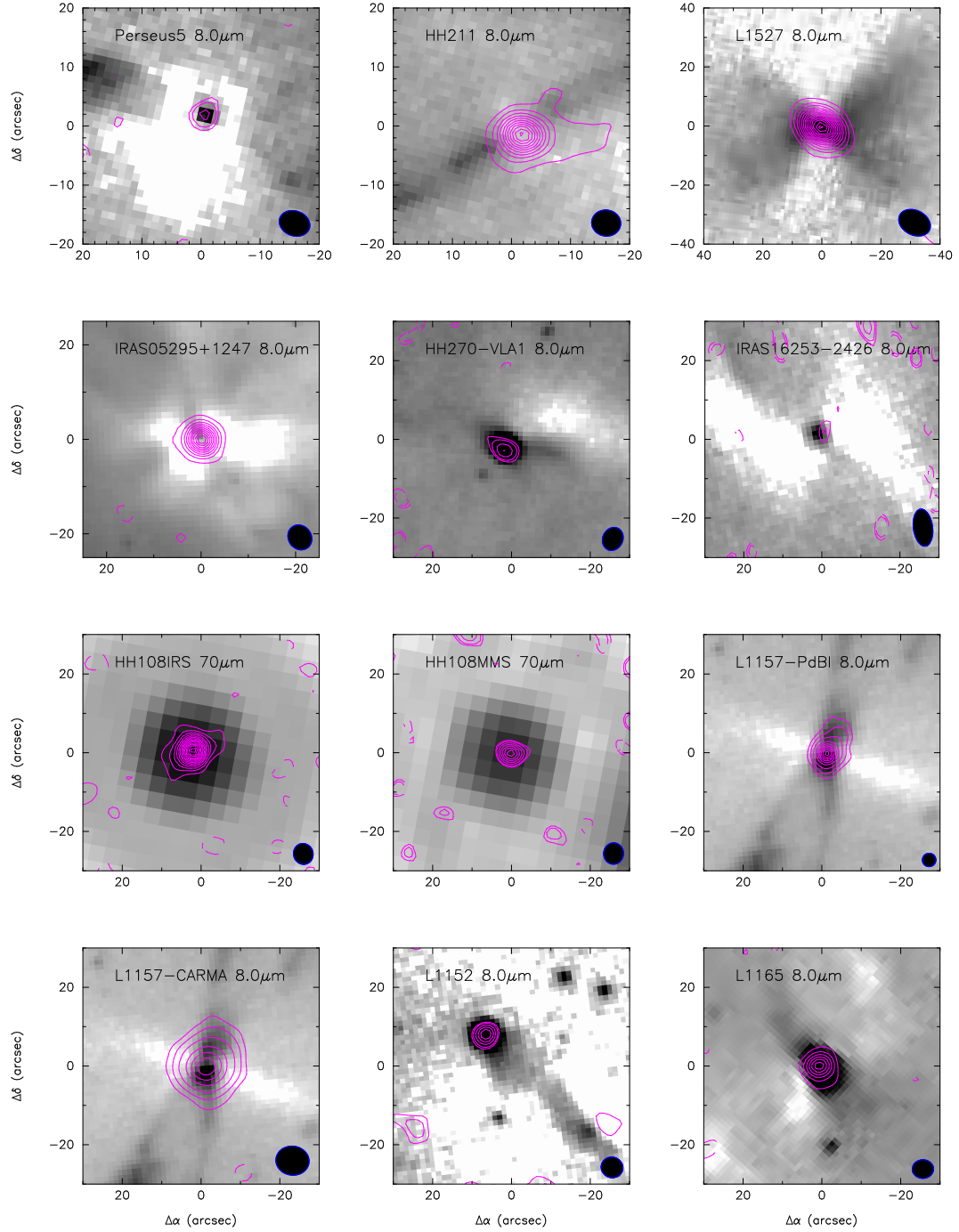


Figure 5.31 IRAC  $8\mu\text{m}$  images of sources observed, with CARMA  $\lambda=3\text{mm}$  continuum contours overlaid. For most protostars, the continuum emission is directly coincident with the  $8\mu\text{m}$  point sources;  $70\mu\text{m}$  in the case of HH108IRS/MMS. The contours for Perseus 5, HH270, IRAS 16253-2429, HH108MMS, and L1152 are  $\pm 2.5\sigma$ ,  $3, 4, 5, \dots, 9\sigma$  and then increase in  $3\sigma$  intervals. The contours for HH211, L1527, RNO43, HH108IRS, and L1165 start at  $\pm 3\sigma$  and increase by  $3\sigma$ . The contours for L1157 are  $\pm 3, 6, 12, 24, 36, 48, 60, 72, 84, \text{ and } 96\sigma$ .

Table 5.1. Source Properties

Source	RA (J2000)	Dec (J2000)	Distance (pc)	Mass $_{8\mu m}$ ( $M_{\odot}$ ) ( $r < 0.05\text{pc}$ )	Mass $_{submm}^*$ ( $M_{\odot}$ )	$L_{bol}$ ( $L_{\odot}$ )	$T_{bol}$ (K)	Morphological Classification	Outflow PA ( $^{\circ}$ )	References (Distance, $M_{ref}$ , $L_{bol}$ , ( $T_{bol}$ , Outflow PA)
Perseus 5	03:29:51.88	+31:39:05.7	230	2.0	1.24	0.46	41	One-sided	80	23, 17, 3, 3, 1
IRAS 03282+3035	03:31:21.10	+30:45:30.2	230	2.4	2.2	1.2	33	Irregular	122	23, 4, 3, 3, 26
HH211	03:43:56.78	+32:00:49.8	230	1.1	1.5	3.02	24	Irregular	116	23, 3, 3, 3, 6
L1521F	04:28:39.03	+26:51:35.0	140	2.3	1.0	0.03	$\sim 20$	Spheroidal	270	20, 10, 8, 1, 7
IRAS 04325+2402	04:35:35.39	+24:08:19.0	140	-	-	0.97	73	Binary Core	200	20, -, 15, 15, 16
L1527	04:39:53.86	+26:03:09.5	140	0.8	2.4	0.9	56	One-sided	90	20, 4, 9, 15, 31
RNO43	05:32:19.39	+12:49:40.8	460	2.8	2.6	12.5	56	Irregular	20	21, 10, 2, 15, 21 & 1
HH270 VLA1	05:51:34.64	+02:56:45.8	420	1.9	-	7.0	32	One-sided	240	22, -, 2, 1, 1
IRAS 16253-2429	16:28:21.42	-24:36:22.1	125	0.8	0.98	0.25	35	Spheroidal	20	19, 10, 3, 3, 26
L483	18:17:29.93	-04:39:39.6	200	3.5	1.8	11.5	$< 54$	Irregular	282	25, 4, 3, 15, 30
Serpens MMS3	18:29:09.13	+00:31:31.6	400	0.95	2.2	1.6	39	Flattened	180	18, 3, 14, 3, 1
HH108IRS	18:35:42.14	-00:33:18.5	300	-	4.5	$\sim 8.0$	28	Flattened	208	17, 14, 14, 1, 1
HH108MMS	18:35:46.46	-00:32:51.2	300	-	3.6	0.7	18	Flattened	130	17, 17, 1, 1, 1
L673-SMM2	19:20:25.96	+11:19:52.9	300	1.0	0.35	2.8	-	Flattened	270, 135	24, -, -, 12, 1 & 12
L1152	20:35:46.22	+67:53:01.9	300	3.4	12.0	1.0	33	Binary Core	225	5, 10, 3, 1, 13
L1157	20:39:06.25	+68:02:15.9	300	0.86	2.2	3.0	29	Flattened	150	5, 4, 3, 15, 27
CB230	21:17:38.56	+68:17:33.3	300	1.1	1.1	7.2	69	One-sided	0	5, 11, 3, 15, 28
L1165	22:06:50.46	+59:02:45.9	300	1.1	0.32	13.9	46	Irregular	225	5, 1, 12, 1, 12

Note. — Properties of sources observed in the single-dish and/or interferometric sample. The  $8\mu m$  extinction masses are taken within 0.05 pc of the protostar and note that some of the masses have been rescaled to account for a different distance estimate as compared to Paper I. Positions are reflect the coordinates of the  $24\mu m$  point source from *Spitzer* data or the 3mm continuum position for protostars observed with CARMA. The Outflow position axes (PA) are not well constrained since the outflows are known to precess they can have fairly large angular width; a conservative estimate of uncertainty would be  $\pm 10^{\circ}$ . References: (1) This work, (2) Tobin et al. (2010b), (3) Enoch et al. (2009), (4) Shirley et al. (2000), (5) Kirk et al. (2009), (6) Lee et al. (2009), (7) Bourke et al. (2006) (8) Terebey et al. (2009), (9) Tobin et al. (2008), (10) Young et al. (2006), (11) Kauffmann et al. (2008) (12) Visser et al. (2002), (13) Chapman & Mundy (2009), (14) Enoch et al. (2007), (15) Froebrich (2005), (16) Hartmann et al. (1999), (17) Chini et al. (2001), (18) Dzib et al. (2010), (19) Loinard et al. (2008), (20) Loinard et al. (2007), (21) Bence et al. (1996), (22) Menten et al. (2007), (23) Hirota et al. (2011), (24) Herbig & Jones (1983), (25) Jørgensen (2004), (26) Arce & Sargent (2006), (27) Gueth et al. (1996), (28) Launhardt et al. (2001), (29) Stanke et al. (2006), (30) Fuller et al. (1995), (31) Hogerheijde et al. (1998).

\*Mass was computed with sub/millimeter bolometer data assuming an isothermal temperature.

Table 5.2. IRAM 30m Observations

Source	RA (J2000)	Dec (J2000)	Receiver	Date (UT)	$\sigma_T$ (mK)	$\Delta v$ (km s <sup>-1</sup> )
IRAS 03282+3035	03:31:19.8	+30:45:37	EMIR E090	25 Oct 2009	60	0.067
HH211-mm	03:43:55.3	+32:00:46	EMIR E090	24 Oct 2009	70	0.067
L1521F	04:28:39.0	+26:51:37	EMIR E090	24 Oct 2009	200	0.067
IRAS04325+2402	04:35:36.6	+24:08:54	EMIR E090	25 Oct 2009	60	0.067
L1527 <sup>a</sup>	04:39:54.0	+26:03:22	EMIR E090	26 Oct 2009	50	0.067
RNO43	05:32:18.2	+12:50:01	EMIR E090	24 Oct 2009	50	0.067
HH270 VLA1	05:51:33.6	+02:56:46	AB100	27 Dec 2008	50	0.067
IRAS 16253-2429	16:28:21.9	-24:36:22	AB100	29 Dec 2008	170	0.067
L483	18:17:30.3	-04:39:40.6	EMIR E090	25 Oct 2009	75	0.067
Serpens MMS3	18:29:10.2	+00:31:18	EMIR E090	24 Oct 2009	200	0.067
HH108	18:35:42.7	-00:33:07	EMIR E090	23 Oct 2009	80	0.067
L673-SMM2	19:20:25.4	+11:19:44	EMIR E090	23/24 Oct 2009	65	0.067
L1152	20:35:47.17	+67:53:22	EMIR E090	24 Oct 2009	55	0.067
L1157	20:39:05.6	+68:02:13.2	EMIR E090	25 Oct 2009	30	0.067
CB230	21:17:28.7	+68:17:42.8	AB100	26 Dec 2008	50	0.067
L1165	22:06:50.8	+59:03:06.5	EMIR E090	25 Oct 2009	60	0.067

Note. — Observations of protostellar envelopes taken with the IRAM 30m telescope. The positions reflect the map center and not necessarily the protostar position.

<sup>a</sup>Source was observed in both observing runs; however, the data taken in the 2009 EMIR run were significantly better quality and we only use those data for analysis.

Table 5.3. CARMA Observations

Source	RA (J2000)	Dec (J2000)	Config.	Date (UT)	Calibrators (Gain, Flux)	Beam (")	$\sigma_T$ (mK)	$\Delta v$ (km s <sup>-1</sup> )
Perseus 5	03:29:51.84	+31:39:06.2	D-array	10 Apr 2010	0336+323, Uranus	5.2×4.1	450	0.067
HH211-mm	03:43:56.8	+32:00:50.3	D-array	16 Apr 2010	0336+323, Uranus	5.0×4.3	400	0.067
L1527	04:39:53.9	+26:03:09.6	E-array	02/05/06 Oct 2008	3C111, 3C84	11.1×8.2	100	0.1
RNO43	05:32:19.1	+12:49:43.1	D-array	18/22 Apr 2010	0532+075, Mars	5.5×4.6	300	0.067
..	..	..	..	2 Sept. 2010	0532+075, Uranus	..	..	0.067
HH270 VLA1	05:51:33.6	+02:56:47.2	D-array	24/25/26 Jul 2009	0532+075, Mars	5.9×5.0	500	0.1
IRAS 16253-2429	16:28:21.6	-24:36:23.1	D-array	12 Aug 2009	1625-254, MWC349	9.3×4.9	500	0.1
HH108 IRS	18:35:42.17	-00:33:18.3	D-array	10 Apr 2010	1830+063, Neptune	5.9×5.0	500	0.067
HH108 MMS	18:35:46.53	-00:32:51.4	D-array	14/15 Apr 2010	1830+063, MWC349	5.9×5.0	450	0.067
L1152	20:35:44.14	+67:52:51.3	D-array	11 Apr 2010	1927+739, MWC349	5.4×5.1	600	0.067
L1157	20:39:06.3	+68:02:15.8	D-array	19/29 Mar 2009	1927+739, MWC349	7.3×6.6	150	0.1
..	..	..	E-array	02 Oct 2008	1927+739, MWC349	..	..	0.1
L1165	22:06:50.32	+59:02:45.5	D-array	25 Jul 2009	2038+513, MWC349	5.3×4.7	400	0.1

Note. — Observation parameters of protostars observed with CARMA, the coordinates listed for each protostar denote the phase center of the observation, not necessarily the position of the protostar. The frequency resolution for the 2010 observations was 0.067 km s<sup>-1</sup>; however, this was rebinned to 0.1 km s<sup>-1</sup> to increase signal-to-noise. The observations of L1165, IRAS 16253-2429, and HH270 VLA 1 only observed the central three hyperfine N<sub>2</sub>H<sup>+</sup> lines, while the observation of L1157 and L1527 observed the isolated N<sub>2</sub>H<sup>+</sup> line. All other observations observed all 7 N<sub>2</sub>H<sup>+</sup> hyperfine transitions.

Table 5.4. Very Large Array Observations

Source	RA (J2000)	Dec (J2000)	Config.	Date (UT)	Calibrators (Gain, Flux)	Beam ( $''$ )	$\sigma_T$ (mK)	$\Delta v$ (km s $^{-1}$ )
IRAS 03282+3035	03:31:20.34	+30:45:32.0	D-array	12 Nov 2009	0336+323, 3C48	5.2 $\times$ 4.6	240	0.15
L1521F	04:28:38.9	+26:51:35.0	D-array	19 Mar 2007	0418+380, 3C48	7.1 $\times$ 6.7	125	0.075
L1527	04:39:53.9	+26:03:09.6	D-array	07 Mar 2003	0510+180, 3C48	4.8 $\times$ 4.1	300	0.15
L483	18:17:29.83	-04:39:38.3	D-array	18 Apr 1995	1751+096, 3C286	6.3 $\times$ 5.9	300	0.3
Serpens MMS3	18:29:09.1	+00:31:34.0	D-array	11/12 Nov 2009	1851+005, 3C48	5.6 $\times$ 5.3	270	0.15
L673-SMM2	19:20:26.27	+11:20:08.2	D-array	6 Nov 2009	1925+211, 3C286	5.4 $\times$ 5.0	250	0.15
L1157	20:39:06.3	+68:02:15.0	D-array	2/3 Jan 2010	1927+739, 3C48	4.6 $\times$ 4.0	250	0.15
CB230	21:17:37.59	+68:17:38.5	D-array	18/20 Oct 2009	2022+616, 3C48	4.5 $\times$ 3.3	325	0.15

Note. — Observation parameters of protostars observed with VLA, the coordinates listed for each protostar denote the phase center of the observation, not necessarily the position of the protostar. The frequency resolution of the L1521F observation was 0.075 km s $^{-1}$ ; however, this was rebinned to 0.15 km s $^{-1}$  to increase signal-to-noise.

Table 5.5. Plateau de Bure Interferometer Observations

Source	RA (J2000)	Dec (J2000)	Config.	Date (UT)	Calibrators (Gain, Flux)	Beam ( $''$ )	$\sigma_T$ (mK)	$\Delta v$ (km s $^{-1}$ )
L1157	20:39:05.6	+68:02:13.2	D-array	17 Jun, 07 Jul 2009	1927+739, MWC349	3.4 $\times$ 3.3	80	0.125
..	..	..	C-array	13 Nov 2009	1927+739, MWC349	..	..	0.125

Note. — Observation parameters of the protostar observed with the PdBI, the coordinates listed denote the phase center of the observation, not necessarily the position of the protostar.

Table 5.6. Single-Dish  $N_2H^+$  Properties

Source	$V_{lsr}$ (km s $^{-1}$ )	FWHM (km s $^{-1}$ )	$I_{max} \pm \sigma_I^\dagger$ (K km s $^{-1}$ )	$\tau_{tot}$	$T_{ex}$ (K)	$N(N_2H^+)$ (cm $^{-2}$ )	$N_2H^+$ Mass ( $10^{-9} M_\odot / X(N_2H^+)$ )	Radius ( $''$ )
IRAS 03282+3035	7.1	0.67	5.9 $\pm$ 0.04	4.9	6.4	1.8 $\times$ 10 $^{13}$	1.4	160 $\times$ 80
HH211-mm	9.1	0.5	5.8 $\pm$ 0.05	6.9	5.2	2.3 $\times$ 10 $^{13}$	1.4	120 $\times$ 110
L1521F	6.45	0.29	4.0 $\pm$ 0.14	17.5	4.7	4.1 $\times$ 10 $^{13}$	1.9	160 $\times$ 110
IRAS 04325+2402	5.9	0.45	5.4 $\pm$ 0.04	5.4	6.8	1.9 $\times$ 10 $^{13}$	2.4	180 $\times$ 160
L1527	5.9	0.36	3.1 $\pm$ 0.03	9.3	4.3	1.7 $\times$ 10 $^{13}$	0.9	180 $\times$ 160
RNO43	10.25	0.69	2.5 $\pm$ 0.04	0.9	5.6	2.3 $\times$ 10 $^{13}$	0.8	90 $\times$ 80
HH270 VLA1	8.9	0.41	2.5 $\pm$ 0.04	4.6	4.2	6.5 $\times$ 10 $^{12}$	1.2	135 $\times$ 65
IRAS 16253-2429	4.05	0.3	4.2 $\pm$ 0.13	6.6	5.6	1.7 $\times$ 10 $^{13}$	0.4	100 $\times$ 80
L483	5.5	0.51	10.3 $\pm$ 0.06	16.1	5.4	9.1 $\times$ 10 $^{13}$	10.4	200 $\times$ 150
Serpens MMS3-full	8.5	0.62	12.5 $\pm$ 0.12	6.6	6.9	6.1 $\times$ 10 $^{13}$	21.5	200 $\times$ 150
Serpens MMS3-proto	8.5	0.62	5.4 $\pm$ 0.12	3.5	6.1	1.5 $\times$ 10 $^{13}$	1.9	no boundary
HH108-full	11.0	0.54	4.7 $\pm$ 0.05	4.0	5.6	1.1 $\times$ 10 $^{13}$	2.35	160 $\times$ 50
HH108IRS	11.0	0.54	4.7 $\pm$ 0.05	4.0	5.6	1.1 $\times$ 10 $^{13}$	0.9	no boundary
HH108MMS	10.9	0.54	1.9 $\pm$ 0.05	2.5	5.1	3.0 $\times$ 10 $^{12}$	0.4	no boundary
L673-SMM2	7.1	0.48	7.1 $\pm$ 0.04	2.6	8.5	1.6 $\times$ 10 $^{13}$	5.3	$\sim$ 150 $\times$ 80
L1152	2.5	0.47	5.4 $\pm$ 0.04	7.3	5.5	2.4 $\times$ 10 $^{13}$	3.9	260 $\times$ 95
L1157	2.65	0.39	4.6 $\pm$ 0.02	4.5	4.8	1.4 $\times$ 10 $^{13}$	3.0	200 $\times$ 70
CB230	2.8	0.5	4.0 $\pm$ 0.04	3.6	5.0	8.9 $\times$ 10 $^{12}$	1.0	115 $\times$ 75
L1165	-1.50	0.42	2.5 $\pm$ 0.04	5.6	4.2	8.3 $\times$ 10 $^{12}$	0.6	90 $\times$ 60

Note. — The  $N_2H^+$  properties of each source are tabulated, column densities are scaled by 1.17 to account for beam efficiency. The FWHM linewidth is taken from the average single-dish spectrum over the entire envelope. The statistical uncertainty in the linewidth is less than 0.01 km s $^{-1}$ ; however, this value varies across the envelope and will vary depending on the region averaged. The optical depth,  $T_{ex}$ , column density are measured at the  $N_2H^+$  emission peak; however, multiple positions are quoted for HH108 and Serpens MMS3. The envelope mass is computed by summing the column density over the entire emitting region and assuming a constant  $N_2H^+$  abundance of  $1.0 \times 10^{-9}$  relative to  $H_2$ . The envelope radius is measured where the  $N_2H^+$  is 10% of the peak. The optical depths, column densities, and masses should only be regarded as accurate within factors of a few owing to systematic errors in calculation of optical depth and excitation temperature.

$^\dagger$ Sum of all hyperfine line emission, multiplied by channel velocity width on the  $T_A$  scale and  $\sigma_I = \sigma_T N_{ch}^{1/2} \Delta v$  where  $N_{ch}^{1/2}$  is the number of channels in the summed velocity range and  $\Delta v$  is the channel width;  $N_{ch}$  can be calculated from the information given in the table.

Table 5.7. Interferometric N<sub>2</sub>H<sup>+</sup> Properties

Source	$V_{lsr}$ (km s <sup>-1</sup> )	FWHM (km s <sup>-1</sup> )	$I_{max} \pm \sigma_I^\dagger$ (K km s <sup>-1</sup> )	$\tau_{tot}$	$T_{ex}$ (K)	N(N <sub>2</sub> H <sup>+</sup> ) (cm <sup>-2</sup> )	N <sub>2</sub> H <sup>+</sup> Mass (10 <sup>-9</sup> M <sub>⊙</sub> /X(N <sub>2</sub> H <sup>+</sup> ))	Radius <sup>c</sup> ( $''$ )
Perseus 5	8.06	0.29	6.1±0.28	3.1	13.1	3.0×10 <sup>13</sup>	0.3	20
HH211-mm	9.12	0.39	8.3±0.25	9.9	8.4	9.3×10 <sup>13</sup>	1.1	40
L1527 <sup>a</sup>	6.01	0.26	0.9±0.05 <sup>a</sup>	8.8	4.8	1.8×10 <sup>13</sup>	0.2	57
RNO43	9.87, 10.5	0.43, 0.32	3.0±0.19	5.5	6.7	1.8×10 <sup>13</sup>	0.4	23
HH270 VLA1 <sup>b</sup>	8.86	0.41	6.0±0.24	4.9	11.2	3.5×10 <sup>12</sup>	0.9	28
IRAS 16253-2429 <sup>b</sup>	4.12	0.21	4.4±0.24	7.4	7.6	3.2×10 <sup>13</sup>	1.5	36
HH108IRS	10.8	0.59	14.1±0.3	8.2	12.5	8.4×10 <sup>13</sup>	1.2	21
HH108MMS	10.9	0.40	5.0±0.3	8.4	6.4	4.3×10 <sup>13</sup>	0.7	12
L1152	2.63	0.34	9.6±0.36	10.1	10.7	1.3×10 <sup>14</sup>	4.3	29
L1157 (PdBI)	2.7	0.74	19.8±0.06	10.4	8.0	1.2×10 <sup>14</sup>	0.7	25
L1157 (CARMA)	2.7	1.0	16.7±0.06	4.8	8.5	4.7×10 <sup>13</sup>	0.8	41
L1165 <sup>b</sup>	-1.5	0.38	6.6±0.21	6.6	8.0	4.5×10 <sup>13</sup>	0.4	17

Note. — The N<sub>2</sub>H<sup>+</sup> properties of each source are tabulated. The  $V_{lsr}$  and FWHM linewidth are taken from the position of peak intensity. The statistical uncertainty in the linewidth is less than 0.01 km s<sup>-1</sup>; however, the linewidth varies across the envelope. The optical depth,  $T_{ex}$ , column density are measured at the N<sub>2</sub>H<sup>+</sup> emission peak. The envelope mass is computed by summing the column density over the entire emitting region and assuming a; regions of bad data toward edges are masked out of the measurement. The optical depths, column densities, and masses should only be regarded as accurate within factors of a few owing to systematic errors in calculation of optical depth and excitation temperature.

<sup>†</sup>Intensity quoted is summed the central three hyperfine lines of N<sub>2</sub>H<sup>+</sup> and multiplied by the channel velocity width.  $\sigma_I = \sigma_T N_{ch}^{1/2} \Delta v$  where  $N_{ch}^{1/2}$  is the number of channels in the summed velocity range and  $\Delta v$  is the channel width;  $N_{ch}$  can be calculated from the information given in the table.  $\sigma_I$  is the statistical uncertainty and does not take into account the ~10% absolute calibration uncertainty.

<sup>a</sup>The values for L1527 are highly uncertain due to only observing the isolated N<sub>2</sub>H<sup>+</sup> line and are scaled by a factor of 27/3 to approximate the flux from the other hyperfine components.

<sup>b</sup>The column density and masses are scaled by 27/15 since the bandwidth only enabled the central three hyperfine components of N<sub>2</sub>H<sup>+</sup> to be observed.

<sup>c</sup>The radii quoted are the radius of a circle which encompasses the detected regions of the envelope above the 3 $\sigma$  level in the integrated intensity map. Note that these radii do not reflect the dimensions of the entire core because they are highly influenced by the primary beam, uv-coverage, and sensitivity.

Table 5.8. Interferometric NH<sub>3</sub> Properties

Source	$V_{lsr}$ (km s <sup>-1</sup> )	FWHM (km s <sup>-1</sup> )	$I_{max} \pm \sigma_I^\dagger$ (K km s <sup>-1</sup> )	Optical Depth	$T_{ex}$ (K)	N(NH <sub>3</sub> ) (cm <sup>-2</sup> )	NH <sub>3</sub> Mass (10 <sup>-8</sup> M <sub>⊙</sub> /X(NH <sub>3</sub> ))	Radius <sup>b</sup> (")
IRAS 03282+3035	6.98	0.38	6.4±0.13	10.1	12.7	1.4×10 <sup>15</sup>	5.7	60
L1521F <sup>a</sup>	7.11	0.37	1.4±0.06	10.1	3.9	8.0×10 <sup>15</sup>	29.3	49
L1527	5.95	0.26	2.6±0.16	1.0	10.45	3.9×10 <sup>14</sup>	1.4	39
L483 <sup>a</sup>	5.41	0.51	5.8±0.18	6.8	8.3	2.3×10 <sup>15</sup>	27.7	62
Serpens MMS3	8.22	0.51	7.0±0.19	2.1	10.2	2.0×10 <sup>15</sup>	7.5	50
L673-SMM2	6.93	0.50	8.4±0.14	0.53	33.3	7.2×10 <sup>14</sup>	11.3	76
L1157	2.71	0.56	8.6±0.15	1.6	13.4	8.5×10 <sup>14</sup>	16.0	87
CB230	2.78	0.47	6.5±0.22	1.1	16.9	6.1×10 <sup>14</sup>	4.8	36

Note. — The NH<sub>3</sub> properties of each source are tabulated. The  $V_{lsr}$  and FWHM linewidth are taken from the position of peak intensity. The statistical uncertainty in the linewidth is less than 0.01 km s<sup>-1</sup>; however, the linewidth varies across the envelope. The optical depth,  $T_{ex}$ , column density are measured at the NH<sub>3</sub> emission peak except. The envelope mass is computed by summing the column density over the entire emitting region and assuming a constant NH<sub>3</sub> abundance of 1.0×10<sup>-8</sup> relative to H<sub>2</sub>; regions of bad data toward edges are masked out of the measurement. The optical depths, column densities, and masses should only be regarded as accurate within factors of a few owing to systematic errors in calculation of optical depth and excitation temperature. The masses from NH<sub>3</sub> also appear to be overestimating the actual envelope masses, compared to the 8μm and submillimeter dust masses; thus, the NH<sub>3</sub> abundance relative to H<sub>2</sub> could be larger than assumed.

<sup>a</sup>NH<sub>3</sub> lines in these sources are optically thick making mass and column density measurements uncertain.

<sup>b</sup>The radii quoted are the radius of a circle which encompasses the detected regions of the envelope above the 3σ level in the integrated intensity map. Note that these radii will not reflect the dimensions of the entire core in most cases because they are highly influenced by the primary beam, uv-coverage, and sensitivity.

<sup>†</sup>Intensity quoted is summed over the main NH<sub>3</sub> lines and multiplied by the channel velocity width.  $\sigma_I = \sigma_T N_{ch}^{1/2} \Delta v$  where  $N_{ch}^{1/2}$  is the number of channels in the summed velocity range and  $\Delta v$  is the channel width;  $N_{ch}$  can be calculated from the information given in the table.  $\sigma_I$  is the statistical uncertainty and does not take into account the ~10% absolute calibration uncertainty.

Table 5.9. Single-Dish Velocity Gradients

Source	Gradient <sup>†</sup> (10000AU) (km s <sup>-1</sup> pc <sup>-1</sup> )	Gradient Fit <sup>†</sup> 1D (km s <sup>-1</sup> pc <sup>-1</sup> )	Gradient Fit 2D (km s <sup>-1</sup> pc <sup>-1</sup> )	Gradient PA 2D (°)	Gradient PA - Outflow PA (°)
Perseus 5	-	-	-	-	-
IRAS 03282+3035	1.13±0.2	1.31 ±0.004	4.6±0.04	301±0.5	1
HH211-mm	7.2±0.3	6.9±0.03	4.2±0.07	31±0.9	85
L1521F	0.26±0.13	0.13±0.002	0.76±0.02	239±1.8	31
IRAS 04325+2402 <sup>a</sup>	3.1±0.11	5.2±0.01	3.5±0.01	79±0.3	59
L1527	2.7±0.29	2.2±0.01	2.2±0.02	114±0.5	24
RNO43	2.5±0.9	2.2±0.1	3.3±0.4	280±4.6	80
HH270 VLA1	0.98±0.2	0.88±0.004	1.4±0.04	166±1.3	74
IRAS 16253-2429	0.8±0.18	1.2±0.002	1.7±0.04	311±1.3	69
L483	3.7±0.24	3.6±0.01	2.2±0.02	66±0.4	36
Serpens MMS3	1.5±0.24 <sup>b</sup>	1.4±0.01 <sup>b</sup>	1.1±0.01	307±0.6	53
HH108IRS	0.64±0.24	2.0±0.004	1.2±0.03	96±2.1	68
HH108MMS	1.7±0.13	1.6±0.004	2.0±0.05	67±1.6	62
L673-SMM2	-	-	1.0±0.02	100±2.1	10
L1152 <sup>a</sup>	1.7±0.42	2.7±0.004	3.2±0.04	145±0.7	80
L1157	0.9±0.084	0.9±0.003	0.69±0.01	303±1.4	27
CB230	2.4±0.094	3.2±0.01	2.3±0.2	281±1.0	79
L1165	1.5±0.63	2.5±0.01	2.8±0.1	154±2.7	71

Note. — The kinematic properties of each source are tabulated. The uncertainty in gradient PA is statistically small; however, it is subject to systematics resulting from the spatial distribution of data points. The outflow position angles are given in Table 1.

<sup>†</sup>Gradients are measured normal to the outflow.

<sup>a</sup>Gradients are measured from center of the core as the protostars are located at the edge.

<sup>b</sup>Gradient was measured along the the velocity gradient, shifted slightly from being normal to the outflow.

Table 5.10. Interferometric Velocity Gradients

Source	Gradient Fit <sup>†</sup> 1D (km s <sup>-1</sup> pc <sup>-1</sup> )	Gradient Fit 2D (km s <sup>-1</sup> pc <sup>-1</sup> )	Gradient PA 2D (°)	Gradient PA - Outflow PA (°)	Single-Dish PA - Int. PA (°)	Region Fit 1D, 2D (")
IRAS 03282+3035	0.94±0.003	8.7±0.01	294±0.04	9	7	30>R≥10, all
Perseus 5 - N <sub>2</sub> H <sup>+</sup>	13.1±0.05	8.6±0.1	147±0.8	66	-	10≥R, 10≥R
Perseus 5 - NH <sub>2</sub> D	12.4±0.06	17.4±0.13	125±0.4	43	-	30>R, 30>R
HH211-mm	8.9±0.02	6.6±0.03	26±0.3	89	5	20>R, 20>R
L1521F	9.5±0.02	5.7±0.01	41±0.2	41	161	30>R, all
L1527-CARMA	12.1±0.14	13.5±0.2	36± 0.7	54	78	15≥R, 20>R
L1527-VLA	12.2±0.13	15.2±1.7	212±4.6	58	98	15≥R, 20>R
RNO43	10.7±0.09	15.9±0.04	262±0.14	62	18	20≥R≥7, 15>R
HH270 VLA1	2.4±0.06	6.0±0.03	162±0.2	77	4	20>R, all
IRAS 16253-2429	4.1±0.02	3.5±0.06	279±1.0	79	33	30>R, 20>R
L483	11.1±0.16	9.3±0.03	45±0.2	57	21	20>R≥10
Serpens MMS3	14.1±0.14 <sup>b</sup>	-	-	-	-	+30≥R≥+5
HH108IRS	14.0±0.07	15.1±0.05	140±0.1	68	44	+30>R>-10, +25>R>-5
HH108MMS	2.7±0.02	2.3±0.7	90±0.1	40	22	15≥R, all
L1152 <sup>a</sup>	6.5±0.010	6.3±0.01	114±0.1	69	30	25>R, 25>R
L1157-PdBI	6.2±0.01	-	-	-	-	20>R, ...
L1157-CARMA	4.8±0.02	10.5±0.03	179±0.1	29	124	20>R, 25>R
L1157-VLA	3.5±0.01	3.5±0.06	260±0.9	70	43	20>R, 25>R
CB230	11.3±0.03	3.2±0.1	278±1.3	82	4	15>R, 20>R
L1165	11.1±0.03	11.2±0.1	120±0.4	75	34	20>R, 10≥R

Note. — Same as Table 9, but for the interferometer data.

<sup>†</sup>Gradients are measured normal to the outflow.

<sup>a</sup>Gradients are measured from center of the core as the protostar is located at the edge.

<sup>b</sup>Gradient was measured along the the velocity gradient, shifted slightly from being normal to the outflow.

Table 5.11. 3mm Continuum Fluxes

Source	RA (J2000)	Dec (J2000)	$S_\nu$ (mJy)
Perseus 5	03:29:51.876	31:39:05.7	4.0±1.0
HH211	03:43:56.78	32:00:49.8	43.4±2.0
L1527	04:39:53.86	26:03:09.5	32.6±6.0
HH270VLA1	05:51:34.64	02:56:45.8	6.3±1.0
RNO43	05:32:19.39	12:49:40.8	9.4±3.5
IRAS 16253-2429	16:28:21.42	-24:36:22.1	1.8±1.0
HH108MMS	18:35:46.46	-00:32:51.2	10.3±2.3
HH108IRS	18:35:42.14	-00:33:18.5	35.7±4.9
L1165	22:06:50.46	59:02:45.9	12.1±1.7
L1152	20:35:46.22	67:53:01.9	15.2±2.8
L1157-PdBI	20:39:06.25	68:02:15.9	37.5±6.1
L1157-CARMA	20:39:06.22	68:02:16.05	55.1±8.3

Note. — The 3mm continuum fluxes for sources observed with CARMA and the PdBI. The flux is measured from the naturally weighted continuum image in a box centered on the source with dimensions four times the size of the FWHM listed in Tables 3 and 5. The errors on the measured fluxes are statistical only and do not consider the 10% absolute calibration error. The difference in continuum flux between the CARMA and PdBI observations can be attributed to the CARMA observations including shorter uv-spacing data from CARMA E and D-arrays as compared to D-array at the PdBI.

## CHAPTER 6

# Velocity Gradients in Non-Axisymmetric Envelopes, Infall or Rotation?

### 6.1 Introduction

The protostellar collapse process results in the formation of a protostar(s) and disk via a complex interplay between infall and rotation. Several theories describing the collapse process have been developed over the years, the first by Larson (1969) and Penston (1969) (hereafter LP) which detailed the gravitational collapse of a non-rotating, uniform density sphere, forming a protostar and surrounding envelope. Later, Shu (1977) developed the inside-out collapse model, with a non-rotating singular isothermal sphere (SIS) as the initial condition. Infall solutions for spherical clouds with initially uniform rotation were later developed by Cassen & Moosman (1981); Terebey et al. (1984). During the collapse of a rotating cloud (assuming no additional forces), the angular momentum is conserved, leading to the formation of a protostellar disk.

Attempts have been made to characterize core rotation on 0.05 to  $\sim 0.5$  pc scales using the dense gas tracers  $\text{NH}_3$  and  $\text{N}_2\text{H}^+$  (Goodman et al., 1993; Caselli et al., 2002; Tobin et al., 2011). The angular momentum of dense cores and collapsing envelopes is important for understanding the sizes of protostellar disks and the ability of the core to fragment. Velocity gradients are clearly observed; however, increasing spatial resolution appears to reveal that velocity gradients are systematically underestimated, as evidenced by the progression of average gradients increasing from Goodman et al. (1993) ( $1 \text{ km s}^{-1}$ ) to Caselli et al. (2002) ( $2 \text{ km s}^{-1}$ ) with  $90''$  and  $54''$  resolutions respectively. Tobin et al. (2011) (hereafter Chapter 5) then found a slightly larger average gradient of ( $2.3 \text{ km s}^{-1}$ ) with  $27''$  resolution. On smaller scales, Volgenau

et al. (2006) and Chen et al. (2007) examined the kinematic structures down to  $\sim 1000$  AU scales, only finding evidence of rotation in a few cases. In contrast, the interferometric data presented in Tobin et al. (2011) found that most envelopes had ordered velocity gradients which *could* be interpreted as rotation. Several studies have also found the possible signatures of rotation on sub-1000 AU scales from high-velocity molecular line wings in interferometric data (Brinch et al., 2007; Lee et al., 2009; Tobin et al., 2011).

Observationally constraining the infall process has received considerable attention over the years. The most convincing signature of infall is the inverse P-Cygni line profiles observed toward NGC 1333 IRAS4 (Di Francesco et al., 2001). Subsequent follow-up observations indicate that the infall detected is likely being observed at larger-scales (i.e. outer envelope) and not necessarily in the inner envelope (Jørgensen et al., 2007). Further evidence of infall is found in the blue-asymmetry of optically thick line-profiles (Zhou et al., 1993; Myers et al., 1995). These infall data are interpreted as being consistent with the inside-out collapse model. However, these signatures of infall are uncertain due to abundance effects and that the molecular lines used are also often found in outflows.

An assumption of axisymmetry is usually made in the interpretation of optically thick line profiles as infall and velocity gradients as core rotation.  $8\mu\text{m}$  shadow images of protostellar envelopes viewed against the Galactic background in *Spitzer Space Telescope* imaging showed that envelopes around Class 0 protostars are often highly asymmetric and filamentary (Tobin et al., 2010b, hereafter Chapter 4). The single-dish and interferometric maps of  $\text{N}_2\text{H}^+$  and  $\text{NH}_3$  presented in Chapter 5 closely map to the extinction structures shown in Chapter 4. While velocity gradients in the majority of systems were found to be normal to the outflow, the magnitude of the velocity gradients and the asymmetric nature of many envelopes lead to the suggestion that the velocity gradients observed may not solely originate from core rotation.

To explore the nature of envelope velocity structure in more detail, I am presenting further analysis of the interferometric  $\text{N}_2\text{H}^+$  ( $J = 1 \rightarrow 0$ ) and  $\text{NH}_3$  (1,1) observations from Chapter 5 taken with CARMA, the Plateau de Bure Interferometer, and

the Very Large Array (VLA)<sup>1</sup>. The details of the observations, data reduction, and analysis were given in Chapter 5 and will be omitted here for brevity. The sample to be analyzed in this chapter are a subset of the sources from Chapter 5 and listed in Table 6.1. These sources are chosen because they have the most favorable envelope morphologies, inclination angles, and velocity fields, making them ideal for comparisons to models. These data are used to construct channel maps and position-velocity (PV) diagrams taken across the equatorial plane of the envelopes (normal to the outflow), probing the kinematics of the envelopes from 1000 AU out to  $\sim 10000$  AU. PV diagrams simplify the data by collapsing one dimension, making analysis and comparison to models easier. The observed PV diagrams will be compared to schematic kinematic models derived from the rotating collapse solution. This chapter is organized as follows: Section 6.2 briefly describes the model, Section 6.3 describes the observational results from the channel maps and PV diagrams compared to the models, and Section 6.4 discusses the results.

## 6.2 Kinematic Models

Given the complex morphological and kinematic structure of the envelopes discussed in Chapters 4 and 5, it is not clear that the conventional wisdom of interpreting velocity gradients as purely rotation is correct. Figure 6.1 illustrates the expected velocity structure observed for infall and/or rotation in a spherical/axisymmetric system and a filamentary system. In both cases, uniform rotation alone will yield a linear velocity gradient across the envelope, as shown by Goodman et al. (1993). Then, global infall in the absence of rotation will simply increase the linewidth of the axisymmetric system. However, in the filamentary envelope, infall alone produces a velocity gradient which will appear similar to rotation at large-scales. Furthermore, if both infall and rotation are present, one can still differentiate the rotation from infall at large-scales in the axisymmetric system. On the other hand, in a filamentary system, the infall and rotation velocities are entangled with each other. Therefore,

---

<sup>1</sup>The National Radio Astronomy Observatory is a facility of the National Science Foundation operated under cooperative agreement by Associated Universities, Inc.

if envelopes are often non-axisymmetric as indicated in Chapter 4, then the angular momentum cannot be well-determined. Upper limits of rotation are also uncertain because the combined infall and rotation velocities can increase or decrease velocity gradients depending on envelope orientation and rotation direction.

Figure 6.1 does show that there could be smaller-scale velocity features which could enable differentiation between axisymmetric and filamentary envelope structures. In an infalling filament, the velocities on opposing sides of the envelope increase toward the red or blue, while an axisymmetric envelope will have velocities increasing toward both the red and blue on opposing sides of the envelope. Therefore, the small-scale kinematic structure that could be observed with interferometers may enable differentiation between axisymmetric and filamentary envelopes. Note that filamentary envelopes are likely more complex and not perfectly linear in the plane of the sky as shown for the model; however, this is a useful starting point for investigating their kinematic structure.

### 6.2.1 Rotating Collapse Model

Given the multitude of velocity structures that might be found in protostellar envelopes as illustrated in Figure 6.1, a model of the expected velocity structures that could be observed in a multitude of viewing geometries is a critical tool. The rotating collapse model (Ulrich, 1976; Cassen & Moosman, 1981; Terebey et al., 1984, hereafter CMU model) will be used to compare with the observations. While this model is simplistic, it is well-understood and commonly used; the velocity structure can be described with only a few free parameters. The infalling gas in the CMU model follows ballistic trajectories for constant angular momentum around a central gravitating mass. In the case of the rotating collapse model by Terebey et al. (1984), there is an inner infalling region inside within a radius of  $R_{inf} = c_s \times t$ . Outside this region, the envelope is not infalling and is assumed to have uniform rotation in their model. Within the infalling region, the angular momentum is roughly constant out to  $R_{inf}/2$ ; therefore, the CMU velocity field reasonably describes the infalling region of the envelope out to this limit.

The velocity components of the infalling, rotating gas are given by the following relations (Ulrich, 1976)

$$v_r = - \left( \frac{GM}{r} \right)^{1/2} \left( 1 + \frac{\cos \theta}{\cos \theta_0} \right)^{1/2} \quad (6.1)$$

$$v_\phi = \left( \frac{GM}{r} \right)^{1/2} \left( 1 - \frac{\cos \theta}{\cos \theta_0} \right)^{1/2} \left( \frac{\sin \theta_0}{\sin \theta} \right) \quad (6.2)$$

$$v_\theta = \left( \frac{GM}{r} \right)^{1/2} (\cos \theta_0 - \cos \theta) \left( \frac{\cos \theta_0 + \cos \theta}{\cos \theta_0 \sin^2 \theta} \right)^{1/2}, \quad (6.3)$$

describing particles in parabolic motion. The angle  $\theta_0$  is the angle between the orbital plane and the rotation axis, while  $\theta$  is the angle from the rotation axis to the particle. For simplicity, the velocities are only considered for motion nearly in the equatorial plane ( $\theta_0 \sim 89^\circ$ ), making  $v_\theta \sim 0$ . Note that the term  $\cos \theta / \cos \theta_0$ , appearing in both  $v_r$  and  $v_\phi$  will go to zero as  $\theta_0 \rightarrow \theta$ .

The analytic nature of the the CMU model makes it ideal for comparison to well-ordered kinematic data. The only free-parameters of the CMU velocity field are the total angular momentum and the central object mass. The total angular momentum is not explicitly defined in Equations 6.1 through 6.3, but following Hartmann (2009)

$$\frac{r}{R_C} = \frac{\sin^2 \theta_0}{1 - \frac{\cos \theta}{\cos \theta_0}} \quad (6.4)$$

where  $R_C$  is the centrifugal radius defined as

$$R_C = \frac{R_0^4 \Omega^2}{GM} \quad (6.5)$$

which can be derived from conservation of angular momentum, by rewriting the smaller-scale velocity in terms of  $R_C$ .  $R_0$  is the radius at which the material started at with angular velocity  $\Omega$ . The angle terms in Equations 6.2 can then be rewritten in terms of  $R_C$  linking the total angular momentum of the system to the rotation velocity.

To calculate the velocities that would be observed in a PV plot across the equatorial plane, the velocities in the  $r$ ,  $\phi$ , and  $\theta$  directions must be projected along a line of sight. For simplicity, the line of sight is defined to be the  $y$ -axis at  $z = 0$ , which makes

$$v_{los} = v_r(\sin \theta \sin \phi_0) + v_\theta(\cos \theta \sin \phi_0) + v_\phi(\cos \phi_0) \quad (6.6)$$

where  $\phi_0$  is rotation angle of the envelope with respect to the plane of the sky, measured counterclockwise from the  $x$ -axis. Note that a complete exploration of the different envelope velocity structures should ideally be run through a multi-dimensional molecular line radiative transfer code to compare in detail to observations; however, the emission lines of  $\text{NH}_3$  and  $\text{N}_2\text{H}^+$  are generally optically thin and detected from large-scales down to radii as small as  $\sim 1000$  AU (Lee et al., 2004, Chapter 5). In this context, simply drawing the velocities of the particle orbits should be valid since all material along the line of sight can be traced.

For the axisymmetric case, the infall streamlines are computed every 15 degrees in the  $\phi$  direction to sample the entire envelope. The left panel of Figure 6.2 shows the infall streamlines on large-scales and the middle panels show a zoom-in on the inner 1000 AU. The projected velocities versus  $x$ -axis position are used to construct simple PV plots from the individual envelope streamlines, shown in the right panel of Figure 6.2. A fiducial central object mass of  $0.5 M_\odot$  is assumed in these models, as well as only comparing velocities for inclinations of  $90^\circ$ . This simplification is made because most of the observed systems in Chapter 5 have inclinations of  $i \geq 60^\circ$ , given their outflow cavity morphologies from Chapter 4 compared to Whitney et al. (2003c).

To approximate a filament, only three streamlines are plotted on either side of the protostar, such that the narrow filamentary envelope is spanned by only  $30^\circ$  in azimuth at large-scales. The geometry of the infall streamlines is shown in the top left and middle panels of Figure 6.3. The PV plots are then constructed in the same manner as the axisymmetric case, which are shown in the right panels of Figure 6.3. Notice that the region of velocity space enclosed by the filament model is smaller than the axisymmetric case; the velocity streamlines plotted in the filament model

represent a subset of those plotted for the axisymmetric model. Then the effects of viewing the filamentary envelope at  $\phi_0 = \pm 30^\circ$  rotation angles in the plane of the sky are shown the middle and bottom rows of Figure 6.3. Substantially different velocity structures are evident in the filamentary PV plots, especially when rotated within the plane of the sky, as compared to Figure 6.2. This shift is *not* due to rotation; rather it is due to the infall velocities being projected along the line of sight. *The simple filament model shows that the envelope morphology can significantly impact the observed kinematic structure.*

### 6.3 Observational and Model Results

The protostellar systems to compared with the models have simple morphological structure and/or a well-ordered kinematic structure. These features are important because the interpretation of the velocity structures is made more complicated by the often filamentary and complex envelope structures (Chapters 4 & 5). I will examine channel maps and PV diagrams of four protostellar systems in an attempt to better understand the dynamical processes behind the observed kinematic structure. I will attempt to fit the data using PV plots of the simplistic axisymmetric or filamentary collapse models derived from the CMU rotating collapse model. This is not an attempt to quantitatively fit these models to the data, but rather to illustrate how the data are schematically described by the models.

#### 6.3.1 L1527

L1527 is a relatively nearby Class 0/I protostar in Taurus ( $d \sim 140$  pc) and it has been well-studied in this thesis. While the envelope was found to be asymmetric in the  $8\mu\text{m}$  extinction image in Chapters 2 and 4, with more material on one side than the other. However, the envelope and outflow cavity structure as a whole is not as dramatically complex as some other cases. The  $\text{N}_2\text{H}^+$  integrated intensity is shown in the upper left panel of Figure 6.4. Like many of the envelopes observed in Chapter 5, the  $\text{N}_2\text{H}^+$  emission exhibits a central depletion relative to the outer envelope.

In addition to the molecular line data, the radius of the disk is well known to

be  $\sim 200$  AU from the Gemini observations shown in Chapter 3. This enables the expected envelope rotation rate to be characterized using Equation 6.5. I assume that angular momentum is conserved and that the material currently arriving on the disk fell in from 5000 AU. If the Shu (1977) SIS model applies, then the mass of the infalling region plus the core would be  $\sim 0.5 M_{\odot}$ . The corresponding rotation rate for  $R_C = 200$  AU is  $\Omega \sim 8 \times 10^{-14} \text{ s}^{-1}$  or  $\sim 2.5 \text{ km s}^{-1} \text{ pc}^{-1}$ , which is consistent with the large-scale velocity gradient measured in Chapter 5. One would then expect that L1527 would be found to have a well-ordered velocity field on small-scales with a velocity structure consistent with producing a  $\sim 200$  AU disk.

However, looking at the  $\text{N}_2\text{H}^+$  channel maps, the kinematic structure on small-scales is not so well-defined. On scales  $>30''$  there is a blue-shifted clump north of the protostar and a red-shifted clump south of the protostar. The channel maps on large-scales agree with the single-dish velocity gradient. However, on scales  $\sim 10''$  there is a compact blue-shifted clump south of the protostar and a compact red-shifted clump north of the protostar. The opposite orientation of the red and blue-shifted emission at large and small-scales means that the kinematic structure is not coherent throughout the envelope and this was noted to be a velocity gradient reversal in Chapter 5. Despite the expectation for L1527 to represent a nearly “ideal” system, the kinematic structure is clearly more complex than would be expected for an axisymmetric system undergoing rotating collapse. Alternatively, the density structure could also be quite clumpy which could make an ordered kinematic structure appear complex.

### 6.3.2 L1157

L1157 is located in Cepheus at a distance of  $\sim 300$  pc and is another example of a seemingly simple protostellar system. The envelope of L1157 is highly flattened in  $8\mu\text{m}$  extinction, as well as  $\text{N}_2\text{H}^+$  and  $\text{NH}_3$  emission. The  $\text{N}_2\text{H}^+$  integrated intensity map is shown in the upper left panel of Figure 6.5. Furthermore, the envelope is much more likely to be a filament than an axisymmetric sheet (Chapter 4), due to the very thin vertical extent of the envelope. Thus, L1157 may be well-described by an axisymmetric filament, one of the ideal cases shown in Figure 6.1. Thus, on

small-scales, rotation or infall in a filamentary envelope would produce high-velocity features on opposing sides of the envelope with opposite velocities.

The channel maps in Figure 6.5 show several things happening in this system. In the top and bottom rows, there is higher-velocity  $\text{N}_2\text{H}^+$  emission north and south of the protostar extended along the outflow. This emission was attributed to outflow interactions with the envelope in Chapter 5. In the middle panels, there is highly-peaked emission from the inner envelope on  $\pm 5''$  scales present in all the channels. However, on scales  $> 7''$  it is seen that the east side of the envelope comes into view at blue-shifted velocities and the west side at red-shifted velocities. This traces a clear velocity gradient at large-scales in L1157 which may be attributed to rotation or projected infall. Note that the extension of  $\text{N}_2\text{H}^+$  emission southeast of the protostar traces emission from the outflow cavity wall and also appears to reflect outflow entrainment.

Now looking at the PV plot in Figure 6.6, there is high-velocity emission due to from the outflow-envelope interaction extending toward red-shifted velocities on both sides of the envelope, coincident with the  $\text{N}_2\text{H}^+$  emission peaks. Thus, any indication of line broadening due to rotation or infall at small-scales is masked by the outflow effects. On scales  $> 7''$  in Figure 6.6, the envelope velocities are nearly constant with a systematic  $\sim 0.1 \text{ km s}^{-1}$  velocity shift between either side of the envelope, as seen in the channel maps. The larger-scale features, with their nearly constant velocity, are quite similar to the filament model seen in the bottom right panel of Figure 6.3. At the same time, the velocity structure is dissimilar to uniform rotation and the axisymmetric infall model. A filament model has been overlaid on the data in the PV plot in Figure 6.6, showing that the fit is reasonable, except in the inner envelope where the kinematic structure is not accurately probed. The envelope is rotated with respect to the plane of the sky by  $\phi_0 = 15^\circ$  and has a centrifugal radius of 100 AU; these parameters are also listed in Table 6.2.

### 6.3.3 L1165

L1165 is also located in the Cepheus region and the protostar is forming within a larger-scale filamentary structure. The  $\text{N}_2\text{H}^+$  emission on small scales, shown in the upper left panel of Figure 6.7, traces a structure extended normal to the outflow, peaking just southeast of the protostar. The velocity structure of L1165 is first examined in the  $\text{N}_2\text{H}^+$  channel maps shown in Figure 6.7. The channel maps show that there is a clear velocity gradient normal to the outflow direction across the protostar. The velocity on the northwest side of the protostar is blue-shifted, with nearly constant velocity. The emission then becomes red-shifted on the southeast side of the envelope, with the highest velocity emission near the protostar. There is evidence of some higher-velocity blue-shifted emission adjacent to the protostar on the northwest side in the channel maps, but it is not as definitive as the higher-velocity red-shifted emission.

The PV diagram in Figure 6.8 shows that the  $\text{N}_2\text{H}^+$  emission northwest of the protostar is not only at a roughly constant velocity, but also has a very narrow linewidth. The lines only broaden near the protostar; most of the region with the broad linewidth is southeast of the protostar, near the  $\text{N}_2\text{H}^+$  peak. Southeast of the peak linewidth, the line rapidly becomes narrow again, while becoming more blue-shifted at the same time, approaching a velocity similar to the opposite side of the envelope. The channel maps show that the higher velocity emission is unlikely to be outflow related due to its location next to the protostar, in the direction orthogonal to the outflow. The velocity structure in Figure 6.8 is also dissimilar from what would be expected for axisymmetric infall and uniform rotation. Therefore, the filamentary model better describes the observed velocity structure. The velocities of the filamentary model are overlaid in Figure 6.8, showing that it is able to approximate the observed velocity structure, though the fit is not ideal. The model is turned  $15^\circ$  within the plane of the sky and has a centrifugal radius of 10 AU (Table 6.2).

As Figures 6.7 and 6.8 show,  $\text{N}_2\text{H}^+$  is only able to trace emission down to within  $\sim 1200$  AU of the protostar. A special feature found in L1165 is that  $\text{HCO}^+$  ( $J = 1 \rightarrow 0$ ) emission is able to trace small-scale kinematics in the inner envelope. The

high-velocity emission of  $\text{HCO}^+$  is shown in Figure 6.9. The red and blue-shifted components are extended normal to the outflow at radii of  $3''$  (600 AU) from the protostar. This emission lies inside the broadest  $\text{N}_2\text{H}^+$  emission, suggesting that it traces smaller-scale kinematic structure, in agreement with the small-scale model predictions. Furthermore, location of the blue and red-shifted high-velocity emission is consistent with what is expected for a filamentary envelope (Figure 6.3).

Chapter 5 suggested that if half of the  $\text{HCO}^+$  emission were from rotation and half from infall, then the combined protostar and disk masses would be  $\sim 0.5 M_\odot$ . If it is assumed that material falling onto a  $R \sim 600$  AU disk began infalling from 5000 AU, the angular velocity is calculated to be  $\Omega(5000 \text{ AU}) = 1.4 \times 10^{-13} \text{ s}^{-1}$  or  $4.26 \text{ km s}^{-1} \text{ pc}^{-1}$ , by applying Equation 6.5. This predicted velocity gradient, assuming that centrifugally supported motion is being traced on small-scales, is twice as large as the  $2.2 \text{ km s}^{-1} \text{ pc}^{-1}$  velocity gradient fit to the single-dish data in Chapter 5. Higher-resolution data are necessary to better constrain whether or not the  $\text{HCO}^+$  emission reflects rotationally supported motion on 600 AU scales. If material is not rotationally supported until smaller-scales, then the predicted angular velocity could be in better agreement with the single-dish velocity gradient.

#### 6.3.4 CB230

CB230 was classified as a one-sided envelope in Chapter 4, given its asymmetric distribution of  $8\mu\text{m}$  extinction; this was also reflected in the single-dish  $\text{N}_2\text{H}^+$  map shown in Chapter 5. On smaller scales, probed by  $\text{NH}_3$  in the upper left panel of Figure 6.10. The envelope is still slightly asymmetric to the west, but the small-scale envelope emission as a whole is well-ordered. There is also a depression in the  $\text{NH}_3$  emission in the inner envelope, coincident with the protostar. This effect was attributed to destruction of  $\text{NH}_3$  in the inner envelope in Chapter 5. The velocity structure of the  $\text{NH}_3$  emission is shown by channel maps in Figure 6.10. Because the main  $\text{NH}_3$  (1,1) lines are a pair separated by  $0.2 \text{ km s}^{-1}$ , the last three panels in the middle row are blends of blue and red-shifted emission, while the rest of the plots reflect mostly unblended emission. The channel maps show that there is a clear,

well-ordered velocity gradient across the envelope from east to west. The emission in the channel maps tends to avoid the location of the main protostar, which is seen as the deficit of emission in the integrated intensity map

The structure of the emission is examined more closely in the PV diagram shown in Figure 6.11. The PV diagram, in contrast to the channel maps, is derived from  $\text{NH}_3$  satellite emission lines that are separated by  $\sim 0.4 \text{ km s}^{-1}$ . This makes the emission appear more distinct than if the PV diagram were plotted using the main  $\text{NH}_3$  lines. The PV plot and channel maps show that the emission on the east and west sides of the envelopes has a rather constant velocity and there is an abrupt shift from blue to red-shifted emission starting at the location of the protostar. The constant velocity emission is dissimilar from what would be expected for uniform rotation and/or the axisymmetric infall model. While a measure of the small-scale velocities is missing, the emission on scales  $> 1000 \text{ AU}$  is most consistent with the infalling filament and I have overlaid a model that reasonably describes the data in the PV plot. The model plotted in Figure 6.11 is rotated by  $\phi_0 = -15^\circ$  and has  $R_C = 10 \text{ AU}$ . The inability to trace kinematics on small-scales with  $\text{NH}_3$  is due to inner envelope chemistry which tends to destroy both  $\text{NH}_3$  and  $\text{N}_2\text{H}^+$ , see Section 5.4.5.

## 6.4 Discussion

All the objects discussed in this paper have velocity gradients at both large and small-scales normal to the outflow direction. The direction of the jet and outflow is thought to correspond to the rotation axis of the protostar and disk (e.g. Shu et al., 1987). Since circumstellar disks form in the inner envelope due to conservation of angular momentum, it has been natural to interpret large-scale velocity gradients that are normal to the outflow as rotation (e.g. Goodman et al., 1993; Caselli et al., 2002; Belloche et al., 2002; Belloche & André, 2004; Chen et al., 2007, and Chapter 5). However, it was shown in Chapter 4 that envelopes are often asymmetric and filamentary and Chapter 5 showed that the large-scale kinematics are often quite complex. These factors, along with the schematic arguments shown in Figure 6.1 make it uncertain whether or not velocity gradients in these envelope reflect rota-

tion. The qualitative arguments shown in Figure 6.1 are reinforced by the models of axisymmetric and filamentary collapse shown in Figure 6.2 & 6.3.

The interferometric PV diagrams and channel maps of these systems reveal small-scale kinematic detail invisible in single-dish data, but are also sensitive to emission on size scales between 1000 and 10000 AU. On this scale, differences between the various model PV diagrams shown in Figures 6.2 and 6.3 become apparent. Despite their asymmetric structure, the sources presented in this chapter represent some of the most well-ordered systems kinematically and morphologically from Chapter 5. Therefore, the dynamical processes giving rise to the kinematic structure should be able to be determined.

#### 6.4.1 Velocity Gradients as Rotation

It was shown in Chapter 5 that the envelopes often have substantial velocity gradients ( $\sim 2.3 \text{ km s}^{-1} \text{ pc}^{-1}$ ) out to 10000 AU and beyond, measured by single-dish mapping. The majority of the envelopes in the sample also had velocity gradients that were within  $45^\circ$  of normal to the outflow direction, reinforcing an interpretation as rotation. However, if the large-scale velocity gradients are interpreted as rotation, the inferred centrifugal radii of this infalling material is  $\sim 1400$  AU by applying Equation 6.5. This assumes that the material from 10000 AU falls all the way in to  $R_C$ , with a  $1.0 M_\odot$  central object. This is substantially larger than the size of a reasonable circumstellar disk ( $\sim 250$  AU Andrews & Williams, 2007; Andrews et al., 2009; Williams & Cieza, 2011). The wide range of gradients observed indicates that some envelopes could have considerably larger centrifugal radii. The unrealistically large centrifugal radii implied by the velocity gradients may indicate that there is another velocity component contributing to the velocity gradient. However, the data presented are of sufficient resolution and quality for calculations of the centrifugal radius at points across the equatorial plane of the envelope, independent of fitting linear velocity gradients.

Using the interferometer and single-dish data, I have calculated  $R_C$  versus radius from the observed velocities, assuming a central object mass of  $0.5M_\odot$  and that

the observed velocities reflect rotation. Since this calculation does not depend on a constant angular velocity, it is valid for any type of rotation curve. The velocities of the interferometer data were shown to be approximately constant from the inner envelope out to large-scales. Therefore, if the line-center velocities reflect rotation, then it must be a differential rotation curve; this is to be expected if the molecular line emission is within the infalling region of the envelope. The centrifugal radii calculated from the velocity distributions observed with the interferometer and single-dish data are shown in Figure 6.12. The plots of  $R_C$  versus  $R$  show that inside of  $\sim 5000$  AU the centrifugal radii have reasonable values which are below 1000 AU. However, on scales greater than 5000 AU, the centrifugal radii are in excess of 1000 AU. If these large centrifugal radii are correct, then this would imply substantial fragmentation on large-scales during the collapse phase. Furthermore, the fragmentation and disk growth should occur rapidly since the free-fall time at these densities ( $\sim 10^6 \text{ cm}^{-3}$ ) is of order  $10^4$  yr. However, the velocity gradients may have a contribution from infall velocities rather than simply reflecting pure rotation.

#### 6.4.2 Velocity Gradients from Projected Infall?

Since the centrifugal radii are so large, contributions to the line-center velocity field, in addition to rotation should also be considered. Figure 6.1 shows that if an envelope is filamentary rather than spherical, then a component of infall motion could be present in the velocity field. Therefore, if an envelope is non-axisymmetric or simply filamentary, a velocity gradient normal to the outflow does not necessarily imply rotation. This is reinforced by Figure 6.1 and the models shown in Figure 6.3. The models demonstrate that the radial motion of a globally infalling filamentary envelope can produce detectable velocity shifts, even with only  $\phi_0 = 30^\circ$  rotation with respect to the plane of the sky. If the envelope is only marginally resolved (as in the single-dish observations), such a velocity shift would likely present itself as a linear gradient in single-dish data.

The PV plots for CB230, L1157, and L1165 enable the kinematic structure of the dense gas to be examined between  $\sim 1000$  and  $\sim 10000$  AU. CB230, L1157, and

L1165 all have velocities that are approximately constant outside the inner envelope region. This observation is *inconsistent* with uniform rotation, which is expected if the observations are tracing the infalling region of the envelope. The PV structures also disagree with what would be expected from axisymmetric collapse (Figure 6.2), but are in reasonable agreement with the predicted kinematic structure for an infalling filament, as shown in Figure 6.3. The resemblance of the PV plots to the predictions of the infalling filament model, as well as the filamentary morphology of the envelopes, leads me to suggest that the principal dynamic process producing the velocity gradients is infall at large scales and not rotation.

The results from the analysis of these data strongly suggest that many of the large-scale velocity gradients observed in Chapter 5 and in other studies result from a combination of infall and rotation velocities rather than rotation alone. This is based on most envelopes having  $> 1M_{\odot}$  of dust and gas within a 0.05 pc radius (Chapter 4), implying that they are gravitationally bound (Chapter 5). Evidence for large-scale infall may be seen in the star-less core L1544 (Tafalla et al., 1998) and it is also seen in simulations of cores fragmenting from a large-scale molecular cloud (Smith et al., 2011). *The possibility of projected infall makes the true rotation velocities difficult to disentangle in protostellar envelopes with complex morphological structure, limiting the ability to definitively measure angular momentum at large-scales.*

### 6.4.3 Linewidth Constraints on Infall

Another piece of evidence for large-scale infall is the observed linewidth in the envelopes. The  $\text{N}_2\text{H}^+$  and  $\text{NH}_3$  linewidths in protostellar envelopes are often observed to be about a factor of two or three larger than expected for purely thermal linewidths ( $0.13 \text{ km s}^{-1}$  for  $\text{N}_2\text{H}^+$  and  $0.22 \text{ km s}^{-1}$  for  $\text{NH}_3$ ) for  $T = 10 \text{ K}$  gas (e.g. Caselli et al., 2002; Chen et al., 2007, Chapter 5). Infall motions themselves on large-scales, in an axisymmetric envelope, would cause substantial line broadening ( $\sim 0.5 \text{ km s}^{-1}$ ) due to the superposition of radially infalling material along the line of sight (Figure 6.2). The line broadening generated by the infalling motions of filamentary envelopes in Figure 6.3 is often just  $0.2 \text{ km s}^{-1}$  from 1000 AU out to 10000 AU, which is consis-

tent with what is observed in Chapter 5. Such line broadening is observed toward smaller-scales in the pre-stellar core L1544 (Tafalla et al., 1998). Thus, global infall of axisymmetric or non-axisymmetric protostellar envelopes could naturally give rise to the observed line broadening and it would not be necessary to invoke a turbulent, non-thermal component to explain the observed linewidths.

## 6.5 Summary and Conclusions

I have presented an analysis of the likely dynamical processes giving rise to the observed kinematic structure in protostellar envelopes, based on the interpretation of interferometric  $\text{N}_2\text{H}^+$  and  $\text{NH}_3$  channel maps and position-velocity diagrams. To better interpret the observations, I have formulated an analytic model which approximates a filamentary envelope structure based on the rotating collapse model (Ulrich, 1976; Cassen & Moosman, 1981; ?). I have calculated a set of models for comparison to the data, using the analytic velocity structure for the radial and azimuthal velocity components. I have attempted match these models to the observations in order to determine the likelihood of rotation or infall producing the observed velocity gradients in axisymmetric or filamentary protostellar envelopes. The PV diagrams constructed from the infalling axisymmetric and filamentary models are generally distinct from each other on scales between 1000 and 10000 AU. The models of filamentary collapse rotated with respect to the plane of the sky, show that infall motions along the long-axis of a protostellar envelope can produce systematic velocity gradients, without the need for significant rotation at large-scales. These velocity shifts when viewed at low resolution in single-dish measurements would give the appearance as a small, approximately linear velocity gradient.

The velocity structures of the envelopes presented are inconsistent with being in uniform rotation and tend to have constant velocity outside the inner envelope. If the envelope velocities reflected rotation, then the centrifugal radii on calculated on scales larger than 5000 AU would be  $> 1000$  AU. I therefore suggest, rather, a scenario in which the envelopes are in a state of global collapse, and the projection of the infall velocities along the likely filamentary envelopes is the dominant component

of the velocity distributions observed in the PV plots, while rotation is subordinate. This scenario is consistent with the predictions of the filamentary collapse model, an extension of the CMU rotating collapse model, toward a dominant central mass.

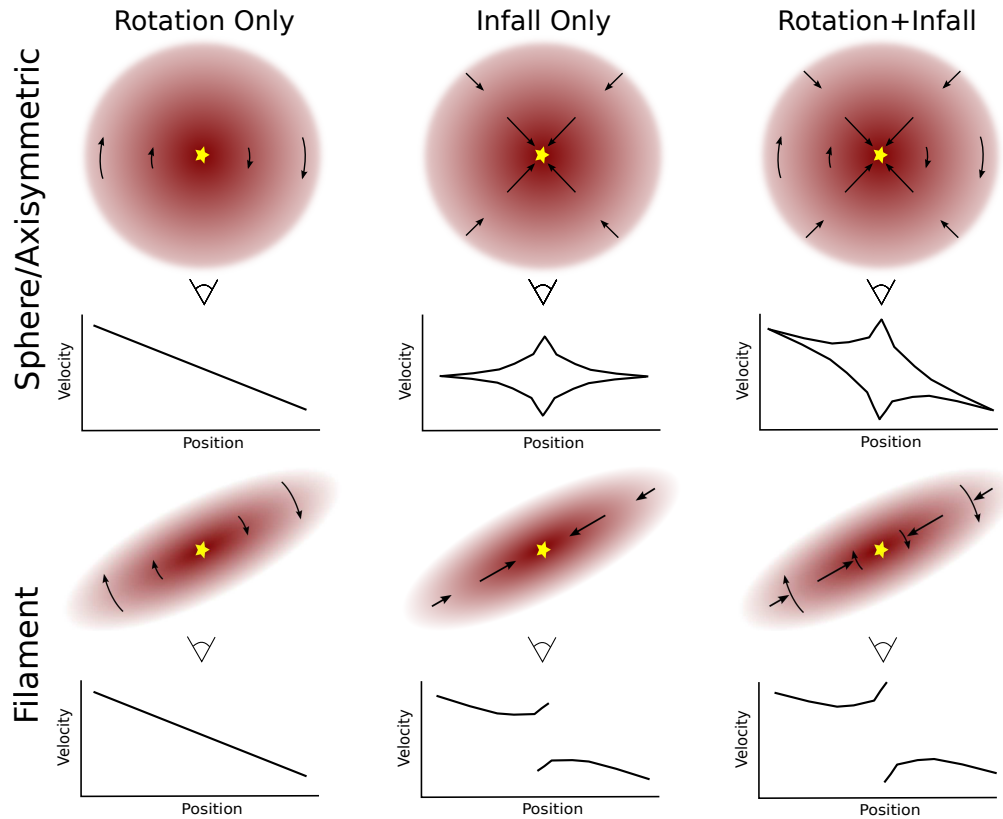


Figure 6.1 These plots schematically show the velocity structure expected to be observed from the dynamical processes of rotation, infall, and their combination for particular envelope morphologies. The top row demonstrates spherical/axisymmetric envelopes and the bottom row demonstrates filamentary envelopes, with schematic position-velocity diagrams below each drawing. The plots illustrate that solid-body rotation in an axisymmetric envelope (*top left*) will show a linear velocity gradient and infall alone (*top center*) only increases linewidth. The convolution of these processes is shown in the *top right* panel. A filament also shows a linear velocity gradient for uniform rotation (*bottom left*); however, infall along a filament turned toward the line of sight would generate an approximately linear velocity structure in the absence of rotation (*bottom middle*). When these process are convolved in the *bottom right* panel, the two processes are difficult to separate.

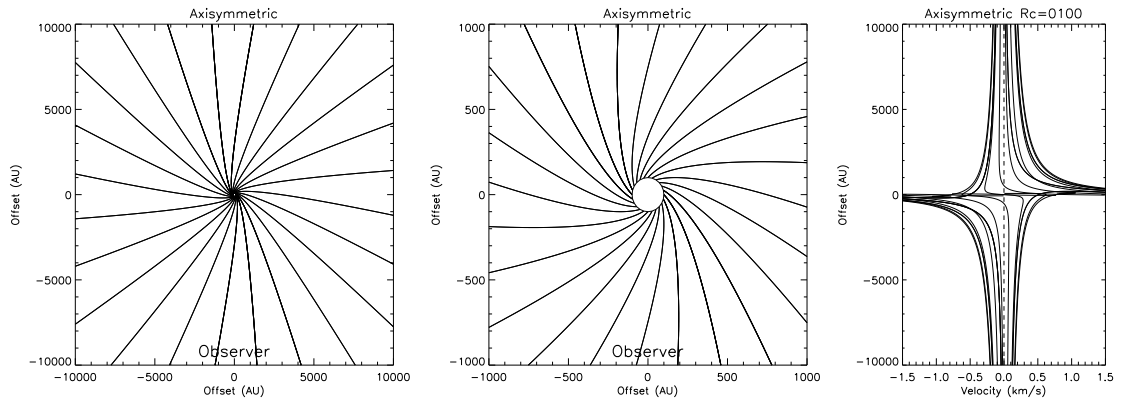


Figure 6.2 Plots of infall streamlines and projected velocities for an axisymmetric envelope with  $R_C=100$  AU, The *left panel* shows the streamlines out to 10000 AU while the *middle panel* zooms in on the inner 1000 AU. The circle at the center represents the edge of the circumstellar disk forming at  $R_C$ . The right panel shows the predicted PV structure for the axisymmetric envelope.

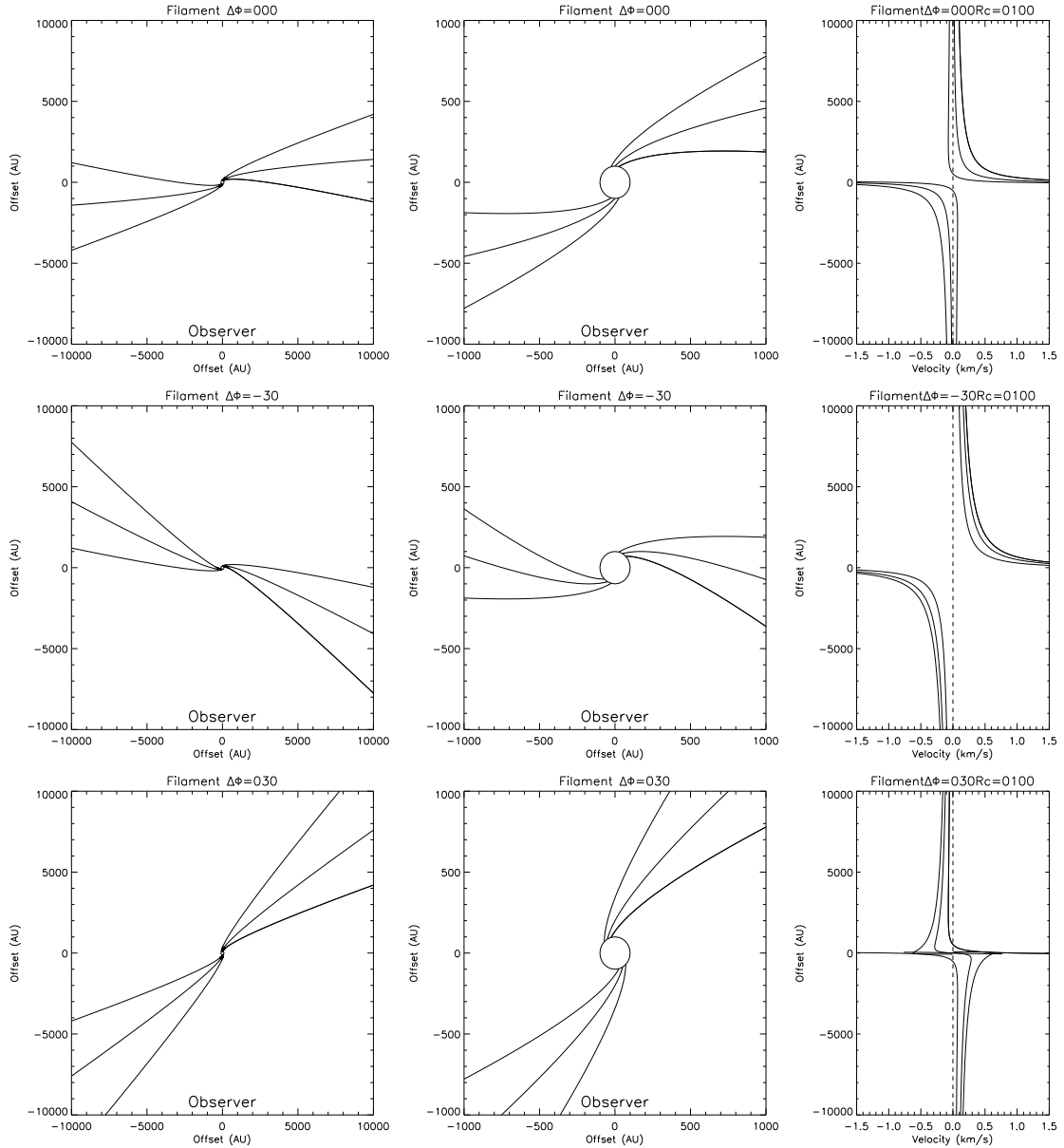


Figure 6.3 Plots of infall streamlines for a filamentary envelope with  $R_C=100$  AU. From top to bottom, filamentary envelopes are shown with rotation with respect to the plane of the sky at angles of  $\phi_0 = 0, -30, \text{ and } 30^\circ$ . The *left panel* shows the streamlines out to 10000 AU while the *middle panel* zooms in on the inner 1000 AU. The circle at the center represents the edge of the circumstellar disk forming at  $R_C$ . The *right panel* show the PV structure of the filamentary streamlines. The filamentary envelopes at a particular rotation angle can be thought of as showing a selected portion of the axisymmetric PV diagram.

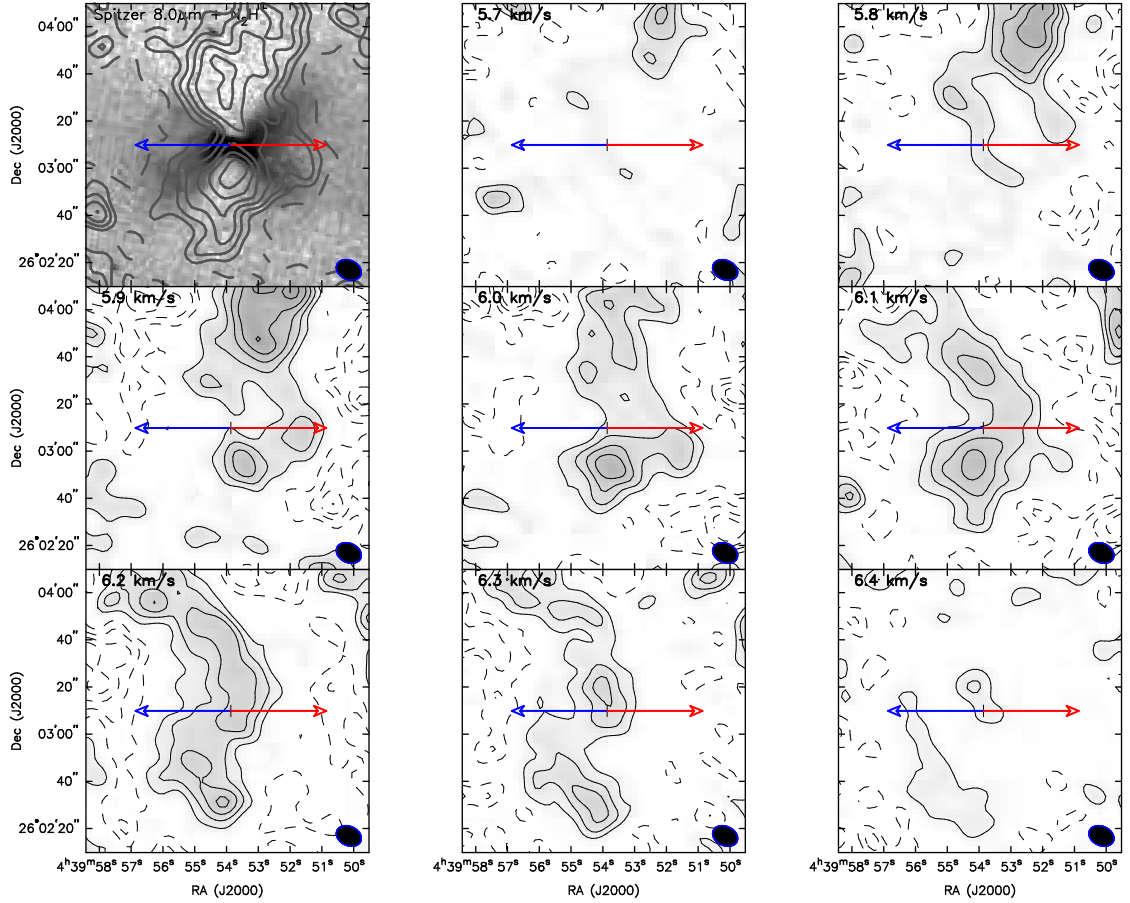


Figure 6.4 L1527 – Channel maps of the isolated  $N_2H^+$  ( $JF_1F = 101 \rightarrow 012$ ) line; the blue and red arrows mark the outflow direction and the cross marks the location of the protostar. These channel maps show both large and small-scale features in the  $N_2H^+$  emission from L1527. On large-scales a clump  $\sim 30''$  north of the protostar becomes visible at blue-shifted velocities, then at smaller scales another blue-shifted clump becomes visible at  $\sim 10''$  south of the protostar. At red-shifted velocities, there is a similar pattern with a red-shifted clump  $\sim 30''$  south of the protostar and another  $\sim 10''$  north of the protostar. Thus, the velocity gradients on large and small-scales have the opposite directions. The contours in the integrated intensity map start at  $\pm 3\sigma$ , increasing in increments of  $3\sigma$  and  $\sigma = 0.022 \text{ K km s}^{-1}$ ; contours in the channel maps start at and increase in increments of  $\pm 3\sigma$ , where  $\sigma = 0.1 \text{ K}$ .

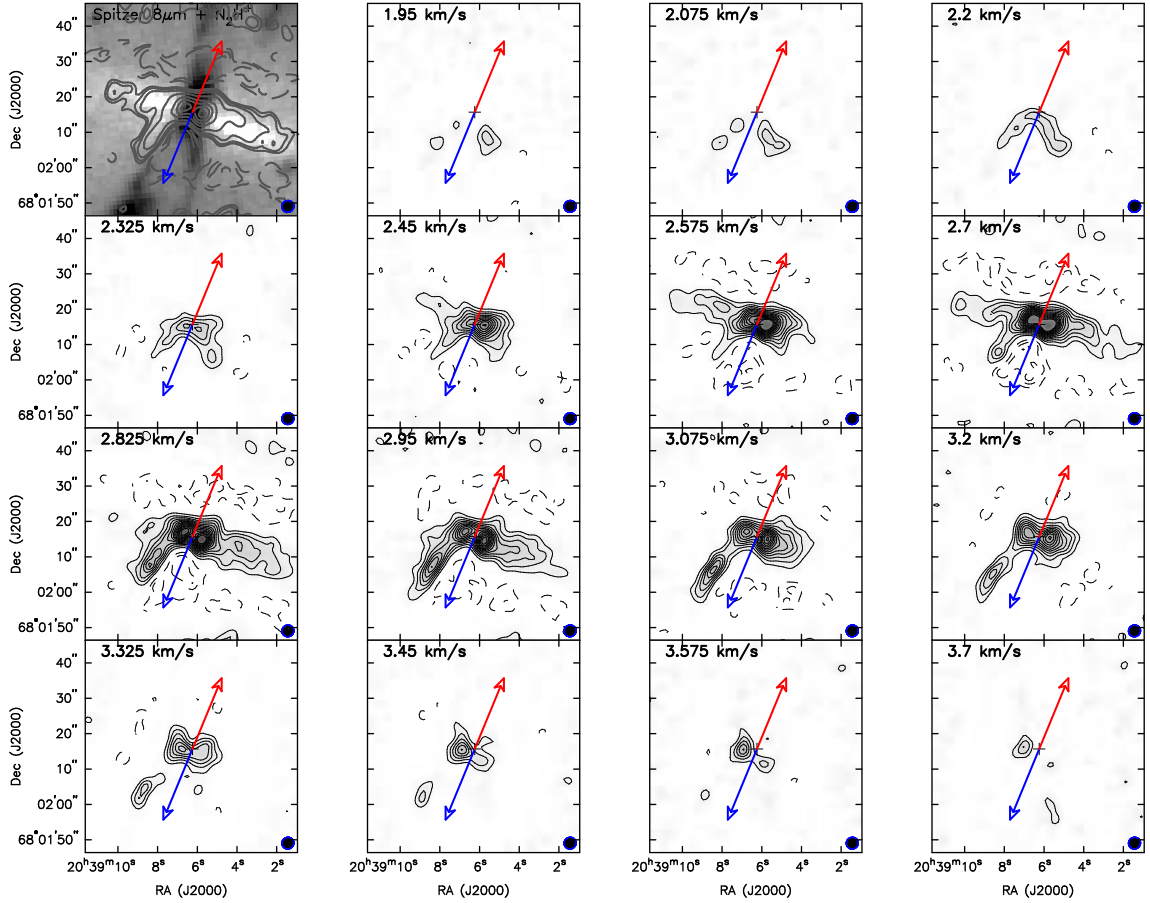


Figure 6.5 L1157– Channel maps of the isolated  $N_2H^+$  ( $JF_1F = 101 \rightarrow 012$ ) line; the blue and red arrows mark the outflow direction and the cross marks the location of the protostar. The higher and lower velocity data in the top and bottom rows mainly trace the likely outflow entrained material, while the middle two rows primarily reflect emission due to envelope kinematics. Note the velocity gradient of the large-scale material from  $2.45 \text{ km s}^{-1}$  to  $3.075 \text{ km s}^{-1}$ . The large-scale emission on the east and west sides of the envelope has a rather constant velocity as previously shown in Figure 6.6. The extension of  $N_2H^+$  emission to the south traces an outflow cavity wall whose kinematics also reflect some outflow entrainment. Contours start at  $\pm 3\sigma$  increase by  $\pm 3\sigma$  intervals, where  $\sigma=0.08 \text{ K}$ . The contours in the integrated intensity map are  $\pm 6, 9, 15, 30, 60\sigma, \dots$ , where  $\sigma=0.02 \text{ K km s}^{-1}$ .

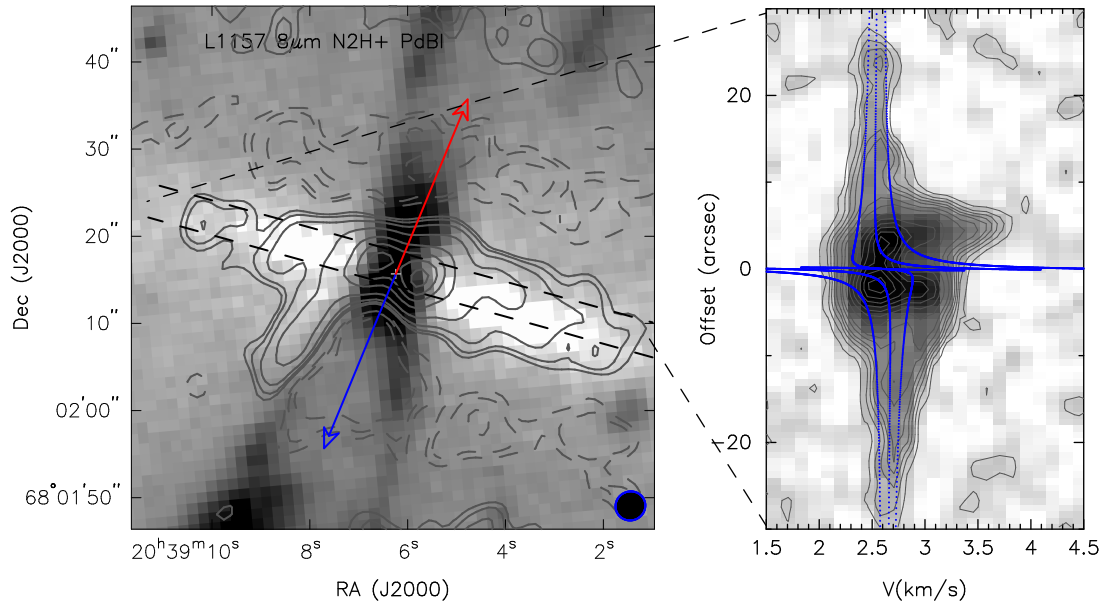


Figure 6.6 L1157– The *left panel* shows the IRAC  $8\mu\text{m}$  image with PdBI  $\text{N}_2\text{H}^+$  integrated intensity contours overlaid of the isolated  $\text{N}_2\text{H}^+$  line ( $JF_1F = 101 \rightarrow 012$ ). The dashed lines mark the regions where the position-velocity cut was taken and point to respective ends of the PV plot in the *right panel*. The position of the protostar/continuum source is marked with a white cross. The position-velocity cut is shown for the isolated  $\text{N}_2\text{H}^+$  line, showing that the two lumps of  $\text{N}_2\text{H}^+$  emission are directly associated with regions of increased linewidth, likely due to outflow effects. Outside of this region, the linewidth becomes fairly narrow in the outer envelope with constant velocity. The contours in the integrated intensity map are  $\pm 6, 9, 15, 30, 60\sigma, \dots$ , where  $\sigma = 0.02 \text{ K km s}^{-1}$ ; the contours in the PV diagram are  $\pm 3\sigma$  and in increments of  $3\sigma$  where  $\sigma = 0.17 \text{ K}$ .

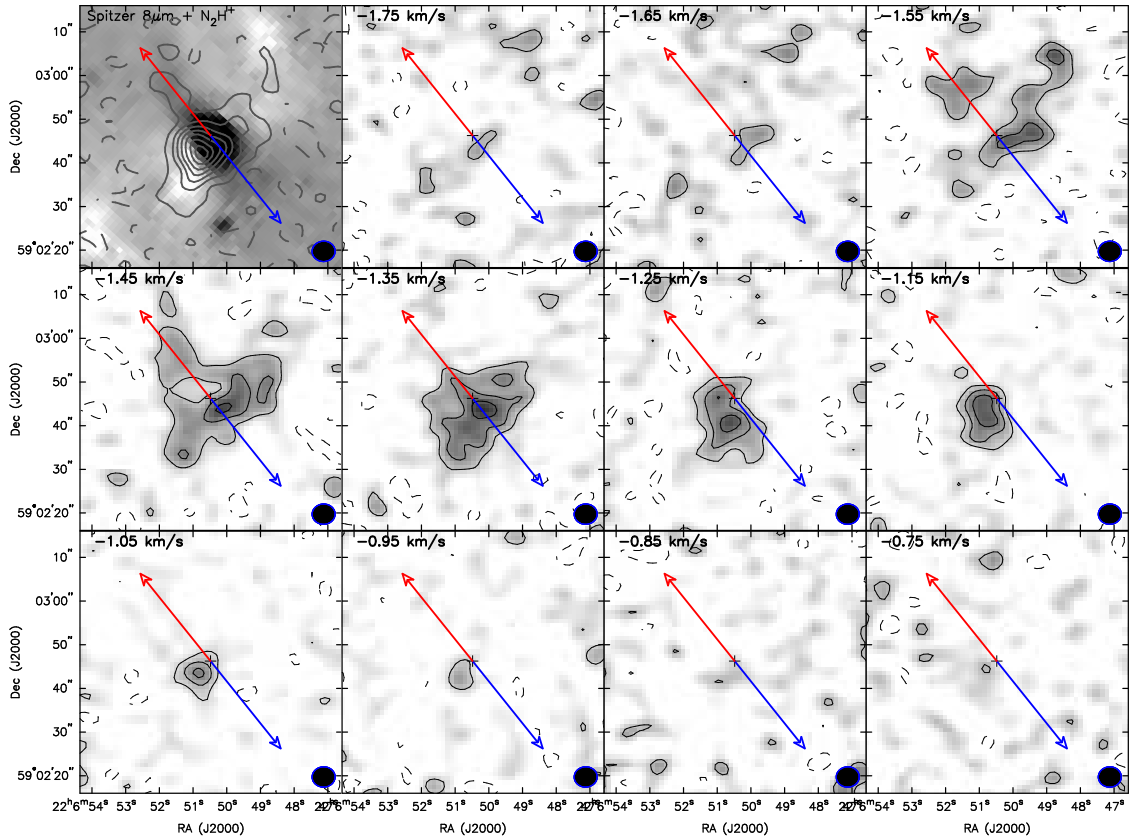


Figure 6.7 L1165– Channel maps of the isolated  $N_2H^+$  ( $JF_1F = 101 \rightarrow 012$ ) line; the blue and red arrows mark the outflow direction and the cross marks the location of the protostar. There is a rather well-behaved global velocity structure in L1165 from blue-shifted northwest of the protostar and red-shifted to the southeast. There does not appear to be significant outflow effects on the kinematic structure. There is also higher velocity red-shifted emission apparent on small-scales near the protostar, but very little blue-shifted emission with higher velocities. The contours in the integrated intensity map are  $\pm 2.5, 3, 6\sigma, \dots$ , where  $\sigma = 0.207 \text{ K km s}^{-1}$ .

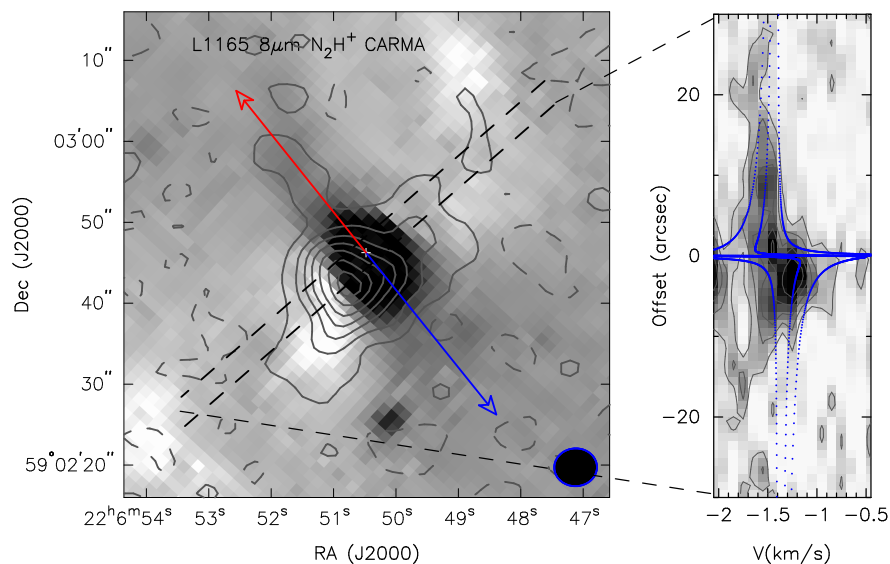


Figure 6.8 L1165– The *left panel* shows the IRAC  $8\mu\text{m}$  image with CARMA  $\text{N}_2\text{H}^+$  integrated intensity contours overlaid. The dashed lines mark the regions where the position-velocity cut was taken and point to respective ends of the PV plot in the *right panel* showing the  $\text{N}_2\text{H}^+$  ( $JF_1F = 122 \rightarrow 011$ ) transition. The position of the protostar/continuum source is marked with a white cross. Northwest of the protostar the lines tend to be more narrow than on the southeast side of the protostar where the  $\text{N}_2\text{H}^+$  emission is both broad and red-shifted. The contours in the integrated intensity map are  $\pm 2.5, 3, 6\sigma, \dots$ , where  $\sigma = 0.207 \text{ K km s}^{-1}$ ; the contours in the PV diagram are  $\pm 3\sigma$ , increasing in increments of  $3\sigma$  where  $\sigma = 0.225 \text{ K}$ .

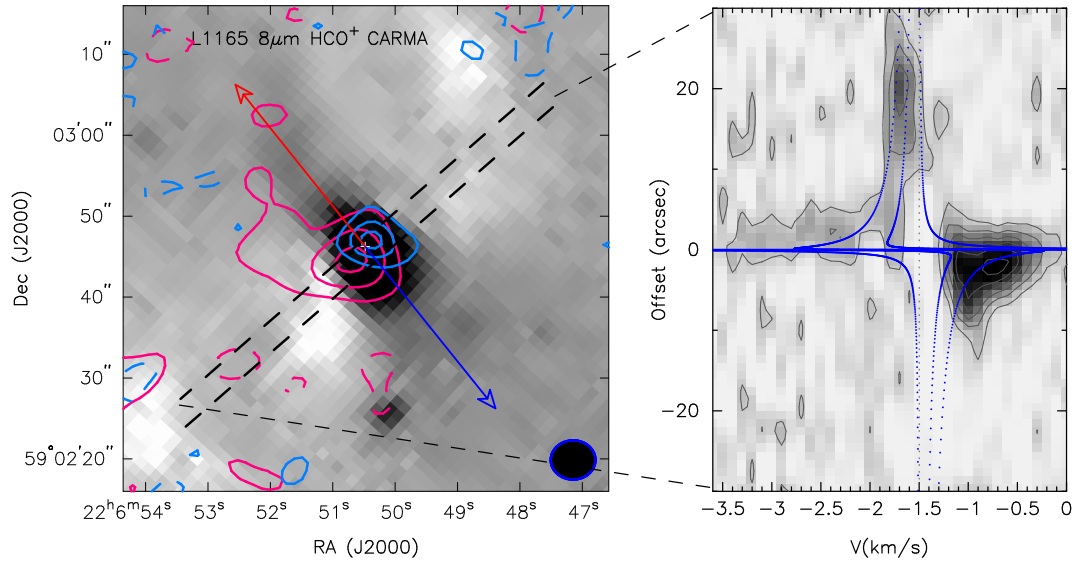


Figure 6.9 L1165– The *left panel* shows the IRAC  $8\mu\text{m}$  image with CARMA  $\text{HCO}^+$  ( $J=1\rightarrow 0$ ) blue and red-shifted emission, summed over  $-3.5$  to  $-2$   $\text{km s}^{-1}$  and  $-1.0$  to  $0$   $\text{km s}^{-1}$ , plotted as blue and red contours respectively. The contours levels are 3, 6, and  $8.25\sigma$  ( $\sigma=0.175$  K) for the blue-shifted emission and 3, 9, and  $18\sigma$  ( $\sigma=0.212$  K) for the red-shifted emission. The blue and red-shifted emission from  $\text{HCO}^+$  is located symmetrically about the protostar, normal to the outflow. The dashed lines mark the regions where the position-velocity cut was taken and point to respective ends of the PV plot in the *right panel*. The position of the protostar/continuum source is marked with a white cross. The position-velocity cut shows that the blue and red-shifted emission traces higher velocity material and there is a slight gradient of material going to higher velocity closer to the continuum source. The line center velocity of  $-1.5$   $\text{km s}^{-1}$  is plotted as the dotted black line. The PV plot contours start at  $3\sigma$  and increase in  $3\sigma$  intervals ( $\sigma=0.2$ ).

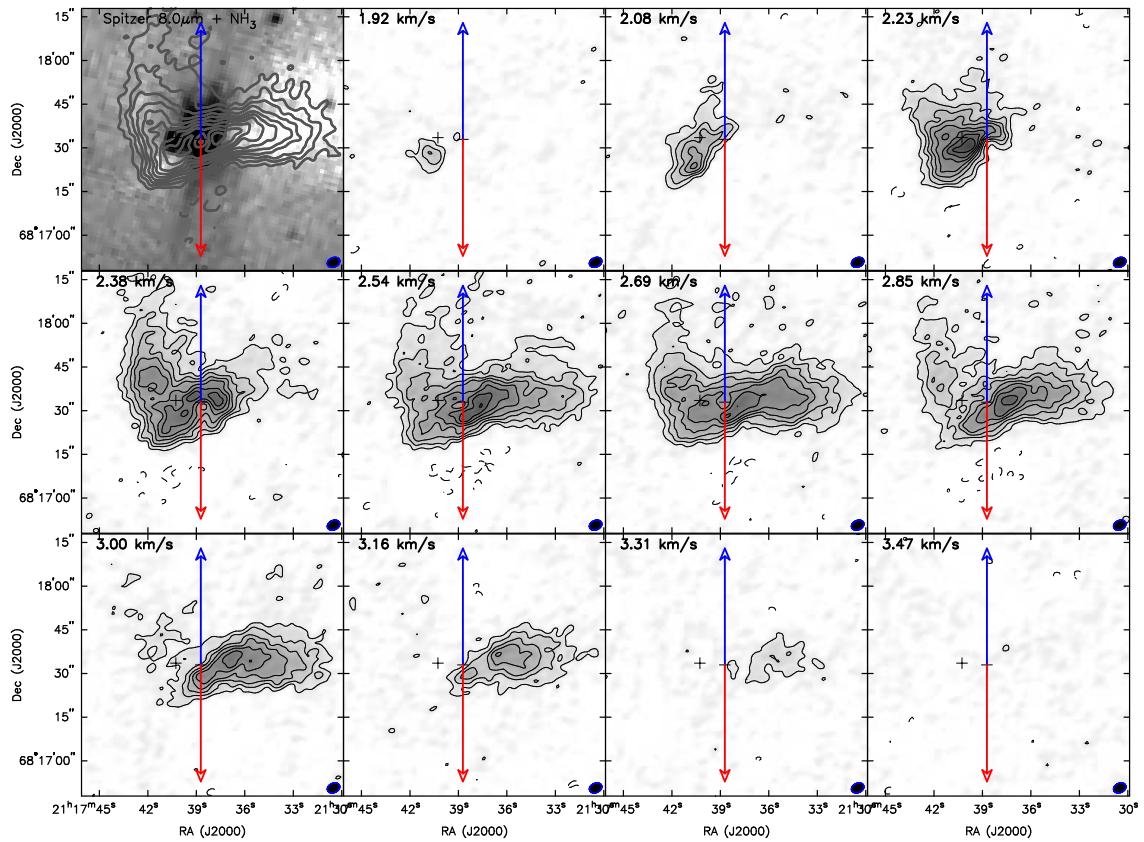


Figure 6.10 CB230– NH<sub>3</sub> integrated intensity map of the main NH<sub>3</sub> (1,1) lines (*upper left*) and channel maps of the two main NH<sub>3</sub> (1,1) lines are shown in the rest of the panels. The protostars are marked with crosses and the outflow direction is drawn from the main protostar. The emission between 2.54 and 2.85 km s<sup>-1</sup> consists of blended emission from both lines, while the remaining emission is mostly free of blending. The channel maps show a clear velocity gradient across the source, appearing normal to the outflow. Notice how the emission tends to avoid the location of the main protostar, owing to destruction of NH<sub>3</sub> near the protostar. The contours in the integrated intensity map start at  $\pm 3\sigma$ , increasing in increments of  $3\sigma$  and  $\sigma=0.195$  K km s<sup>-1</sup>.

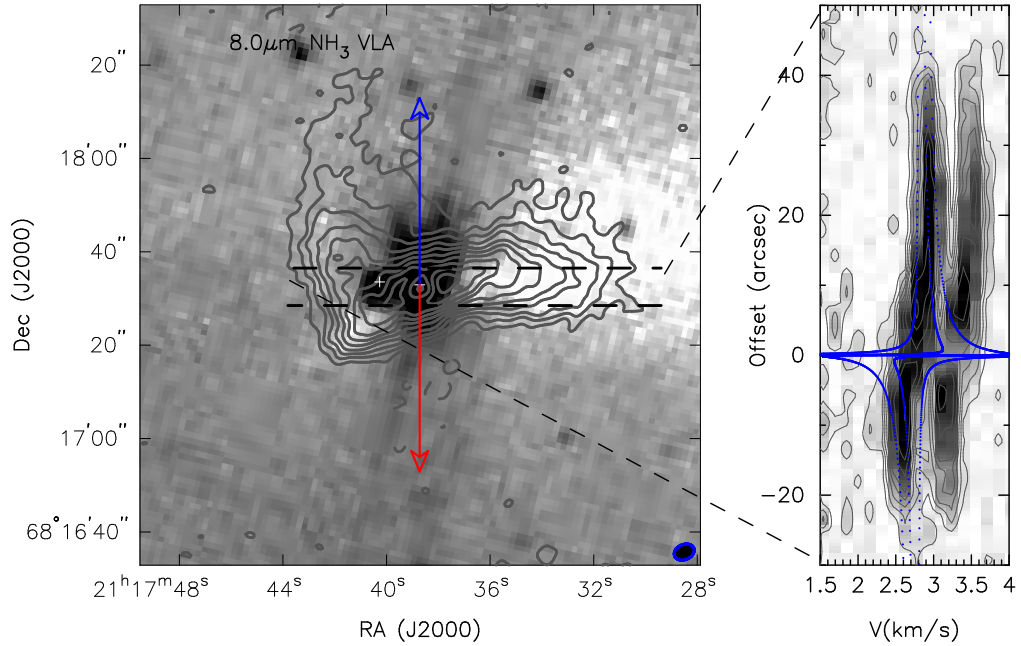


Figure 6.11 CB230– Same as Figure 6.6 but with VLA  $\text{NH}_3$  (1,1) observations and the secondary source is also marked with a white cross. The PV diagram in the *right panel* appears different from those constructed from  $\text{N}_2\text{H}^+$  because the  $\text{NH}_3$  emission consists of two blended hyperfine lines; the  $\text{NH}_3$  satellite lines with greater separation are shown in the PV plot rather than the more blended main lines. The line-center velocity from the  $\text{NH}_3$  emission traces a velocity gradient similar to the single-dish data; however, the shift from red to blue-shifted emission is quite abrupt. The transition region starts at the protostar and does not finish until  $+10''$ . The  $\text{NH}_3$  linewidth does not show much detail other than having its peak coincident with the highest intensity  $\text{NH}_3$  emission. The contours in the integrated intensity map start at  $\pm 3\sigma$ , increasing in increments of  $3\sigma$  and  $\sigma=0.195 \text{ K km s}^{-1}$ ; the contours in the PV diagram start at  $\pm 3\sigma$ , increasing in increments of  $3\sigma$  and  $\sigma=0.11 \text{ K}$ .

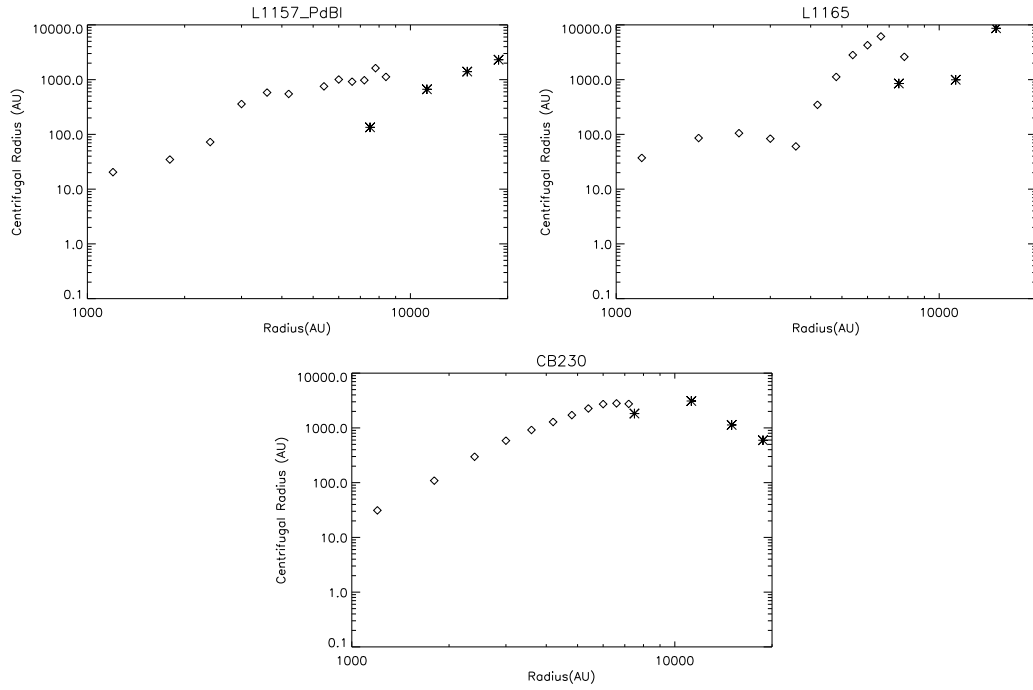


Figure 6.12 Plot of centrifugal radius ( $R_C$ ) versus radius for L1157, L1165, and CB230 assuming the observed velocities reflect rotation.  $R_C$  is calculated from the observed line-center velocities from Chapter 5 and converted to a centrifugal radius using the relation  $R_C = R^2(V - V_{lsr})^2/GM$  (Equation 6.4), where  $M = 0.5 M_\odot$  is assumed. The small points are the calculation from the interferometer data and the large points at large radii are from the single-dish data (Chapter 5)

Table 6.1. Source Properties

Source	RA (J2000)	Dec (J2000)	Distance (pc)	Mass $_{8\mu m}$ ( $M_{\odot}$ ) ( $r < 0.05 \text{ pc}$ )	Mass $_{submm}^*$ ( $M_{\odot}$ )	$L_{bol}$ ( $L_{\odot}$ )	$T_{bol}$ (K)	Morphological Classification	Outflow PA ( $^{\circ}$ )	References (Dist., $M_{ref}$ , $L_{bol}$ , $T_{bol}$ )
L1527	04:39:53.86	+26:03:09.5	140	0.8	2.4	0.9	56	One-sided	90	7, 3, 5, 9
L1157	20:39:06.25	+68:02:15.9	300	0.86	2.2	3.0	29	Flattened	150	4, 3, 2, 9
CB230	21:17:38.56	+68:17:33.3	300	1.1	1.1	7.2	69	One-sided	0	4, 8, 2, 9
L1165	22:06:50.46	+59:02:45.9	300	1.1	0.32	13.9	46	Irregular	225	4, 6, 6, 1

Note. — Properties of sources observed in the single-dish and/or interferometric sample. The  $8\mu m$  extinction masses are taken within 0.05 pc of the protostar and note that some of the masses have been rescaled to account for a different distance estimate as compared to Chapter 4. Positions are reflect the coordinates of the  $24\mu m$  point source from *Spitzer* data or the 3mm continuum continuum position for protostars observed with CARMA. References: (1) Chapter 5, (2) Enoch et al. (2009), (3) Shirley et al. (2000), (4) Kirk et al. (2009), (5) Tobin et al. (2008), (6) Visser et al. (2002), (7) Loinard et al. (2007), (8) Kauffmann et al. (2008), (9) Froebrich (2005).

\*Mass was computed with sub/millimeter bolometer data assuming an isothermal temperature.

Table 6.2. Model Parameters

Source	Distance (pc)	Model	$R_C$ (AU)	$R_{inf}$ (AU)	Proj. Angle ( $^\circ$ )
L1527	140	-	-	-	-
L1157	300	Filament	100	-	15
CB230	300	Filament	10	-	-15
L1165	300	Filament	10	-	15

Note. — Parameters of models which appear to describe the PV data. All models assume a  $0.5 M_\odot$  central object.

## CHAPTER 7

### Summary and Conclusions

In this thesis, I have presented new results on the structure and kinematics of the dense envelopes around protostars. These results challenge the simple models of protostellar collapse and envelope kinematics. Moreover, this thesis has revealed critical new details on the initial conditions of star formation. I will outline the specific results of this thesis in more detail and how they have improved our understanding of the star formation process.

#### 7.1 Initial Conditions of Core/Envelope Formation

The  $8\mu\text{m}$  extinction mapping of protostellar envelopes represent a new way to probe protostellar envelope structure with good sensitivity from large-scales down to  $\sim 1000$  AU. Using this method, I found that the densest parts of protostellar envelopes are often highly non-axisymmetric with a preference for filamentary envelopes. I was able to distinguish between filamentary and flattened, sheet-like envelopes by fitting the vertical structure of the envelope, orthogonal to the long-axis. Flattened sheets would need to be much more vertically extended for the observed column densities. The structures seen in the extinction maps are often not strongly reflected in the dust emission maps, an effect that likely results from the temperature weighting of thermal dust emission and limited sensitivity of ground-based observations to extended structures. The  $8\mu\text{m}$  extinction also indicates that there is substantial mass surrounding these envelopes on 0.1 pc scales, enough for the system to be gravitationally bound at this scale.

The often complex morphology of protostellar envelopes sheds light on the initial

conditions of star formation. The complexities are found on  $\sim 0.05$  pc scales and persist down to  $\sim 1000$  AU. These structures are not the result of outflow effects on the envelope, because the envelopes tend to be extended away from the outflow cavities and the outflows are well collimated. The observed envelope structures strongly indicate that the initial conditions of star formation are likely non-equilibrium. Furthermore, these findings may be at odds with magnetically controlled star formation, which would enable the formation of more axisymmetric systems. These envelopes appear to require rapid collapse of cores formed in turbulent molecular clouds. Collapse must be rapid (roughly on the free-fall timescale) to preserve and enhance whatever non-axisymmetry the parent cores had initially. Thus, the highly non-axisymmetric envelopes may result from the collapse of a modestly asymmetric pre-stellar core.

The non-axisymmetric envelope structure may have further implications for the subsequent evolution of the forming protostellar systems. The likelihood for fragmentation during collapse can be enhanced by non-axisymmetric of the infalling envelope; therefore, the systems that are not currently binary could form companions later on. In addition, the complex envelopes could be feeding mass to the disks asymmetrically. This could perturb the disks and possibly trigger fragmentation of the disk: a possible method for explaining close binary systems. Lastly, infall from the envelopes which are not aligned normal to the outflow could lead to the angular momentum vector of the disk changing with time, causing warping of the disk and significant outflow precession.

The location of protostars in relation to the larger-scale structure indicates that gravitational focusing may play a role in determining the location of where stars form in a cloud (Burkert & Hartmann, 2004). Protostars are often located at the ends of larger-scale structures or at bends or kinks within large-scale filaments. This further indicates that star formation is gravity driven and that the shape of the initial cloud has much to do with where stars will form.

## 7.2 Infall and Rotation in Protostellar Systems

I found that ordered velocity fields are often present on large and small-scales in most protostellar envelopes from single-dish and interferometric observations of  $\text{NH}_3$  and  $\text{N}_2\text{H}^+$ . The average velocity gradient found at large-scales ( $\sim 10000$  AU) is  $\sim 2.3 \text{ km s}^{-1} \text{ pc}^{-1}$ , with a range between  $0.13$  and  $7 \text{ km s}^{-1} \text{ pc}^{-1}$ . At small-scales ( $\sim 4000$  AU) the average gradient is  $8.6 \text{ km s}^{-1} \text{ pc}^{-1}$  with a range between  $0.9$  and  $14 \text{ km s}^{-1} \text{ pc}^{-1}$ . Both the velocity gradients and linewidths are consistent with the envelope being gravitationally bound. On scales of  $\sim 1000$  AU, I found that  $\text{N}_2\text{H}^+$  and  $\text{NH}_3$  often become depleted in the protostellar envelopes, making these tracers ineffective at probing sub-1000 AU kinematics. However, in the cases of L1165 and RNO43,  $\text{HCO}^+$  ( $J = 1 \rightarrow 0$ ) was able to be used to trace inner envelope kinematics on scales of  $\sim 600$  AU. The velocities of the gas are consistent with free-fall motion, but the spatial location of the high-velocity features is consistent with rotation.

The velocity gradient directions are generally consistent from large to small-scales, suggesting that the same dynamical process is producing the gradients at all scales. Moreover, it was also found that the velocity gradients directions are predominantly within  $45^\circ$  of normal to the outflow direction, which may suggest that the gradients reflect rotation. On the other hand, the strong asymmetric nature of the envelopes, the magnitude of the velocity gradients, and the complexity of the velocity fields on large and small-scales leads me to suggest that the observed velocity gradients probably do not reflect pure rotation in most cases. I suggest, rather, that a component of infall projected along the line of sight is entangled with whatever amount of rotation is present, producing velocity gradients that are inherently complex.

Using the interferometer data, we have made a comparison of the observed position-velocity structure to several possible kinematic models. Many protostars have emission at a roughly constant velocity out to large-scales from the inner envelope. This is contrary to what is expected from uniform rotation, but is consistent with infall at large-scales either due to projection effects, and/or enclosed mass growing linearly with radius. Furthermore, one protostellar system has a velocity gradient reversal

going from large to small-scales, a strong indicator of envelope asymmetry and that infall can manifest itself in the velocity field. Some protostars in the sample do, however, have a velocity structure most consistent with uniform rotation and show small-scale velocity line wings only on one side of the protostar, indicating non-axisymmetric kinematic (possibly infalling) structure on  $\sim 1500$  AU scales. These small-scale kinematic features appear to reflect gravitationally dominated motion, likely originating from a combination of infall and rotation in most cases. Rotation will only greatly differentiate itself from infall in non-axisymmetric systems on the smallest scales ( $< 1000$  AU) as infalling material approaches the centrifugal radius. Thus, the high-velocity emission found in  $\text{HCO}^+$  for two sources may reflect motion that is nearly rotationally supported.

To summarize, the possibility of projected infall effects in the velocity field makes determination of rotation velocities difficult. Depending on projection effects, the infall and rotation velocities could increase or decrease the velocity gradient from what rotation alone would yield. Assuming random projection angles of a filamentary envelope in the plane of the sky, an upper limit could be an overestimate in 50% of systems. These possibilities strongly indicate that the conventional wisdom of assuming velocity gradients trace pure rotation may not be correct and previous determinations of angular momentum on large-scales should be regarded with due caution, especially when used to constrain theory or as an initial condition for simulations. However, there is hope that angular momentum can be determined from the innermost regions of protostellar envelopes on sub-1000 AU scales where the rotation velocities are expected to be as large as the infall velocities. These values could then be related back to the observations on larger-scales to check for consistency.

### **7.3 Outflows Effects on Envelope Kinematics**

Most envelopes do not appear to show significant effects of the outflow in the  $\text{NH}_3$  and  $\text{N}_2\text{H}^+$  kinematics. On large-scales, no envelopes appear to have bulk motion effects (line-center velocity) induced by the outflow. Linewidth effects are found on larger scales in the single-dish data for a few systems; however, the lack of a velocity shift at

line-center indicates that only a small amount of mass is involved. On small-scales, however, a few sources appear to have significant outflow effects on the line-center velocities. These are some of the most heavily obscured sources in the mid-infrared, without well developed scattered light cavities. Thus, the outflow may still be in the midst of its initial break-out from the envelope in these select cases.

One remarkable case of possible outflow-envelope interaction is found in the inner envelope of L1157. The  $\text{N}_2\text{H}^+$  emission shows broad line wings extending to  $\sim 1 \text{ km s}^{-1}$  away from line center, located at  $\sim 1000 \text{ AU}$  from the protostar. In contrast, CO observations in outflows typically have emission velocities on the order of 10s of  $\text{km s}^{-1}$  (Arce & Sargent, 2006). This broad  $\text{N}_2\text{H}^+$  line emission is extended in directions along the blue and red-shifted outflow, an indication that the outflow may be entraining some envelope material. If envelope material is being entrained on small-scales, only a small amount ( $\sim 0.04 M_\odot$ ) is being carried and the outflow does not appear to be stopping infall.

Given that the structure of most envelopes does not lend them to being significantly influenced by the outflow, I suggest that the apparent cavity widening with source age (Arce & Sargent, 2006) may be due the result of the envelope collapse itself rather than outflow sculpting. Since the envelopes tend to be filamentary, it seems quite unlikely that the outflow could halt the infall process with most material arriving to the disk normal to it. The possible ineffectiveness of outflows shutting off infall may enable the competitive accretion process to take place (Bonnell et al., 1998) by not clearing the regions surrounding protostars.

## 7.4 Constraints on Protostellar Structure from Radiative Transfer Modeling

I constructed a detailed model of the L1527 protostellar system using the CMU rotating collapse model with the Monte Carlo radiative transfer code developed by Whitney et al. (2003c). Despite the obvious complexities of this system, I was able to fit the near to mid-infrared images, mid-infrared IRS spectrum, and full SED. This

model was then further refined to reflect the high-resolution structure observed with Gemini in L'-band, which strongly indicates that a large, highly-flared circumstellar disk is present around the protostar. The disk appears as a compact, bipolar scattered light structure in the L' images and is a point source in the *Spitzer* images. The highly flared nature of the disk is also responsible for creating the large apparent separation between the outflow cavities due to its shadow.

The high degree of flaring is not surprising since material is still thought to be landing on the disk from the envelope, but a radius of  $\sim 200$  AU is perhaps larger than expected, given that L1527 is a Class 0 protostar. Disks are thought to start small and grow as material falls-in from larger radii. The large disk could mean that disks quickly grow in radius or that L1527 is more evolved than its Class 0 designation implies; however, this system has characteristics of both Class 0 and Class I sources.

The Gemini image is the first resolved image of a disk in scattered light around a Class 0 protostar and the first direct evidence for large disks around such a young protostar. There are observations of many other Class 0 protostars showing point-like features in the mid-infrared, similar to L1527 (Seale & Looney, 2008). Therefore, protostellar disks may frequently reveal themselves in mid-infrared scattered light if the envelope optical depth toward  $R_C$  is low enough in the near to mid-infrared.

Despite the fact that envelopes are generally non-axisymmetric and the model is axisymmetric, the parameters derived from modeling the free-fall collapse region of the envelope likely have some generic applicability. This is because all protostellar systems should have a phase of free-fall collapse on to the protostar and disk with similar density profiles in the collapsing region. Furthermore, attempting to use non-axisymmetric models to derive physical parameters is a slippery slope, since the number of free parameters increases, making the model less unique than the axisymmetric case. Thus, modeling with axisymmetric structures is likely to yield more meaningful results than a more complex model, so long as the limitations of how well the model describes the physical structure are understood.

I showed that simultaneous image and SED modeling of protostars is useful in exploring the physical parameters of protostellar systems. The modeling of L1527

illustrates the importance of considering all the observable data in order to construct the most realistic model. Only fitting the SED could lead to an unphysical model, if the parameter space is not adequately defined. The resolved imaging greatly helps in defining the proper parameter space by constraining the inclination and outflow opening angles, which strongly affect emission in the near to mid-infrared. The observed outflow cavity surface brightness required that larger dust grains with higher mid-infrared albedo ( $1\mu\text{m}$  vs.  $0.25\mu\text{m}$  radius dust grains) be used to model the protostellar envelope and that the wall of the protostellar disk at the dust destruction radius be very bright in the mid-infrared. Furthermore, it was necessary for the dust grains in the disk to be the same as those found in the envelope ( $a_{max}=1\mu\text{m}$ ), rather than a dust model with larger grains ( $a_{max}=1\text{mm}$ ), otherwise the SED could not be fit. Thus, protostellar disks are likely populated with small, only slightly larger than interstellar dust grains, without significant grain-growth or settling, consistent with the thick dark lane separating the disk upper layers.

The physical parameters derived from the SED and image modeling are similar to previous studies; the primary improvement of our work is a better quantification of the detailed envelope and outflow cavity structure. The envelope infall rate found from the modeling is  $\dot{M}_{env} \sim 1 \times 10^{-5} M_{\odot} \text{ yr}^{-1}$ , typical for a Class 0/I object. However, this infall rate is substantially larger than the disk accretion rate onto the protostar as inferred from the bolometric luminosity  $\dot{M}_{acc} \sim 3 \times 10^{-7} M_{\odot} \text{ yr}^{-1}$ . The inequality of  $\dot{M}_{env}$  and  $\dot{M}_{acc}$  implies that mass should be building up in the disk, possibly leading to accretion outbursts (Zhu et al., 2009).

## 7.5 Future Work

As is the case with most research, at least as many questions have been raised as I have been able to answer in this thesis. Some of these questions need new and/or higher fidelity observations to answer, while others need more careful comparison to numerical simulations. The Atacama Large Millimeter Array (ALMA) and the Expanded Very Large Array (EVLA) are coming online now and will enable the new paths of research that have been motivated by this thesis. ALMA is a completely new

facility dedicated to millimeter-wave astronomy and will be comprised of 66 antennas, yielding a factor of 10 - 100 improvement in resolution and sensitivity over current facilities. The EVLA, on the other hand, is an upgraded VLA with greatly expanded bandwidth and improved receivers. Also, the James Webb Space Telescope (JWST) will be launched in the latter half of the decade and will enable observations in the near and mid-infrared with unprecedented resolution and sensitivity.

This thesis has motivated the need to study the kinematic structure of the inner envelope on sub-1000 AU scales. The conventional dense gas tracers ( $\text{N}_2\text{H}^+$  and  $\text{NH}_3$ ) disappear on scales less than 1000 AU, due to chemical processes catalyzed by the evaporation of CO in the inner envelope. Thus, molecular line tracers such as  $\text{HCO}^+$  and HCN may be abundant in the inner envelope, and their kinematics likely reflect the more dynamic environment closer to the protostar with high-velocity emission. In order to better understand the dynamic environment of the inner envelope, more protostars which exhibit high-velocity emission consistent with rotation/infall must be found. This could be done with single-dish radio telescopes (GBT at 3mm and IRAM 30m at 1mm), or any of the current interferometers. The protostars currently without the high-velocity emission in the  $\text{HCO}^+$  or HCN should be revisited, observing other molecular transitions that are likely present in the inner envelope as well as higher excitation transitions of  $\text{HCO}^+$  and HCN. Going further, those protostars with detected high-velocity emission in the inner envelope will need to be observed at higher resolution with ALMA in order to resolve the emitting regions of these lines and trace material flowing down on to the disk. Such a study would greatly enhance our knowledge of how disks are built from the infalling envelope.

Disks around the Class 0 protostars themselves have yet to be characterized, while the more evolved disks around Class II objects have been studied a great deal. The high-resolution  $L'$ -band imaging for L1527 demonstrates that it is possible to directly probe the disk properties through both mid-infrared imaging and sub/millimeter continuum observations. The sizes and rotation rates of protostellar disks will yield direct constraints of the angular momentum of infalling gas onto the disk and the mass of the protostar. The rotation rates of protostellar disks require the sensitivity and an-

gular resolution of ALMA to observe molecular isotopologues which will be optically thin through the dense protostellar envelope. Multi-band sub/millimeter continuum observations at high resolution with ALMA and EVLA will enable the determination of the radial and vertical density structure of the protostellar disks. This structure can be related back to the density structure of the infalling envelope and can indicate if the disk is likely to fragment. Furthermore, high-resolution ground and space-based near and mid-infrared observations can independently constrain the vertical height and radii of edge-on Class 0 disks, complementing the sub/millimeter studies of emission from the disk midplane. Such observations would motivate questions to be answered with JWST.

In the absence of new observations, the data collected for this thesis still have significant scientific potential. Given that the kinematic data are not wholly described by the simplistic models employed in Chapter 6, a logical course of work would be to compare the observed velocity structures to those found in simulations. Numerical simulations of core formation from a large-scale molecular cloud will likely have more complex velocity structures than the simplistic models employed. Moreover, rotation and infall velocities can be separated in the simulated data to understand the dominant physical process that produces the velocity structure in the simulated protostellar envelopes. A comparison of the relatively large sample presented in this thesis to simulations could yield statistically meaningful results on the dominant dynamical processes producing velocity gradients in envelopes.

There is also the potential to study the absolute abundance of  $\text{N}_2\text{H}^+$  and  $\text{NH}_3$  across the protostellar envelopes at high resolution by combining the single-dish and interferometer data. Combined with the  $8\mu\text{m}$  extinction observations, the abundance ratio of  $\text{N}_2\text{H}^+$  relative to  $\text{H}_2$  can be compared to predictions of chemical models for a large sample of envelopes with different luminosities. A comparison of  $\text{NH}_3$  and  $\text{N}_2\text{H}^+$  abundances in a number of systems may enable the formation process of  $\text{NH}_3$  to be better constrained.

The outflow effects on the velocity structure of some protostellar envelopes also deserve further investigation. The impact of the outflow on the envelope of these sys-

tems should be quantified in order to characterize the effects the outflows have on the protostellar envelopes during the earliest phase of protostellar evolution. Comparison of the outflow energy from CO observations to the momentum flux needed to entrain the  $\text{N}_2\text{H}^+$  would quantify how much force the outflow can put on the outflow cavity walls with the oblique incident angles. This could be used to quantify the likelihood of the outflow cavity widening on its own.

## BIBLIOGRAPHY

- Adams, F. C., Lada, C. J., & Shu, F. H. 1987, *ApJ*, 312, 788
- Adams, F. C. & Shu, F. H. 1986, *ApJ*, 308, 836
- Aikawa, Y., Ohashi, N., Inutsuka, S., Herbst, E., & Takakuwa, S. 2001, *ApJ*, 552, 639
- Andre, P., Ward-Thompson, D., & Barsony, M. 1993, *ApJ*, 406, 122
- Andrews, S. M. & Williams, J. P. 2005, *ApJ*, 631, 1134
- Andrews, S. M. & Williams, J. P. 2007, *ApJ*, 659, 705
- Andrews, S. M., Wilner, D. J., Hughes, A. M., Qi, C., & Dullemond, C. P. 2009, *ApJ*, 700, 1502
- Anglada, G., Rodriguez, L. F., Torrelles, J. M., Estalella, R., Ho, P. T. P., Canto, J., Lopez, R., & Verdes-Montenegro, L. 1989, *ApJ*, 341, 208
- Arce, H. G. & Sargent, A. I. 2005, *ApJ*, 624, 232
- Arce, H. G. & Sargent, A. I. 2006, *ApJ*, 646, 1070
- Arce, H. G., Shepherd, D., Gueth, F., Lee, C., Bachiller, R., Rosen, A., & Beuther, H. 2007, *Protostars and Planets V*, 245
- Arquilla, R. & Goldsmith, P. F. 1986, *ApJ*, 303, 356
- Bachiller, R. 1996, *ARA&A*, 34, 111
- Bacmann, A., André, P., Puget, J., Abergel, A., Bontemps, S., & Ward-Thompson, D. 2000, *A&A*, 361, 555
- Ballesteros-Paredes, J., Hartmann, L., & Vázquez-Semadeni, E. 1999, *ApJ*, 527, 285
- Ballesteros-Paredes, J., Klessen, R. S., Mac Low, M., & Vazquez-Semadeni, E. 2007, *Protostars and Planets V*, 63
- Barsony, M., Wolf-Chase, G. A., Ciardi, D. R., & O'Linger, J. 2010, *ApJ*, 720, 64
- Basu, S. & Ciolek, G. E. 2004, *ApJ*, 607, L39

- Basu, S., Ciolek, G. E., Dapp, W. B., & Wurster, J. 2009, *New Astronomy Rev.*, 14, 483
- Basu, S. & Mouschovias, T. C. 1994, *ApJ*, 432, 720
- Bate, M. R. 2000, *MNRAS*, 314, 33
- Bate, M. R. & Bonnell, I. A. 1997, *MNRAS*, 285, 33
- Bate, M. R., Bonnell, I. A., & Bromm, V. 2003, *MNRAS*, 339, 577
- Becklin, E. E. & Neugebauer, G. 1967, *ApJ*, 147, 799
- Beichman, C. A., Myers, P. C., Emerson, J. P., Harris, S., Mathieu, R., Benson, P. J., & Jennings, R. E. 1986, *ApJ*, 307, 337
- Belloche, A. & André, P. 2004, *A&A*, 419, L35
- Belloche, A., André, P., Despois, D., & Blinder, S. 2002, *A&A*, 393, 927
- Bence, S. J., Richer, J. S., & Padman, R. 1996, *MNRAS*, 279, 866
- Benson, P. J., Caselli, P., & Myers, P. C. 1998, *ApJ*, 506, 743
- Benson, P. J. & Myers, P. C. 1989, *ApJS*, 71, 89
- Bergin, E. A., Alves, J., Huard, T., & Lada, C. J. 2002, *ApJ*, 570, L101
- Bergin, E. A. & Tafalla, M. 2007, *ARA&A*, 45, 339
- Bertin, E., Mellier, Y., Radovich, M., Missonnier, G., Didelon, P., & Morin, B. 2002, in *Astronomical Society of the Pacific Conference Series*, Vol. 281, *Astronomical Data Analysis Software and Systems XI*, ed. D. A. Bohlender, D. Durand, & T. H. Handley, 228–+
- Bevington, P. R. 1969, *Data reduction and error analysis for the physical sciences*, ed. Bevington, P. R.
- Bodenheimer, P. 1995, *ARA&A*, 33, 199
- Bok, B. J., Cordwell, C. S., & Cromwell, R. H. 1971, in *Dark nebulae, Globules and Protostars*, ed. B. T. Lynds, 33–+
- Bonnell, I. & Bastien, P. 1993, *ApJ*, 406, 614
- Bonnell, I. A. & Bate, M. R. 1994, *MNRAS*, 269, L45
- Bonnell, I. A., Bate, M. R., & Zinnecker, H. 1998, *MNRAS*, 298, 93
- Bontemps, S., Andre, P., Terebey, S., & Cabrit, S. 1996, *A&A*, 311, 858

- Boss, A. P. 1995, in *Revista Mexicana de Astronomia y Astrofisica Conference Series*, Vol. 1, *Revista Mexicana de Astronomia y Astrofisica Conference Series*, ed. S. Lizano & J. M. Torrelles, 165–+
- Boss, A. P. 2002, *ApJ*, 568, 743
- Bottinelli, S., et al. 2010, *ApJ*, 718, 1100
- Bourke, T. L. 2001, *ApJ*, 554, L91
- Bourke, T. L., Hyland, A. R., Robinson, G., James, S. D., & Wright, C. M. 1995a, *MNRAS*, 276, 1067
- Bourke, T. L., Hyland, A. R., Robinson, G., James, S. D., & Wright, C. M. 1995b, *MNRAS*, 276, 1067
- Bourke, T. L., et al. 2006, *ApJ*, 649, L37
- Brinch, C., Crapsi, A., Jørgensen, J. K., Hogerheijde, M. R., & Hill, T. 2007, *A&A*, 475, 915
- Burkert, A. & Bodenheimer, P. 1993, *MNRAS*, 264, 798
- Burkert, A. & Hartmann, L. 2004, *ApJ*, 616, 288
- Burrows, C. J., et al. 1996, *ApJ*, 473, 437
- Butler, M. J. & Tan, J. C. 2009, *ApJ*, 696, 484
- Calvet, N. & Gullbring, E. 1998, *ApJ*, 509, 802
- Calvet, N., Hartmann, L., Kenyon, S. J., & Whitney, B. A. 1994, *ApJ*, 434, 330
- Cambrésy, L. 1999, *A&A*, 345, 965
- Caselli, P., Benson, P. J., Myers, P. C., & Tafalla, M. 2002, *ApJ*, 572, 238
- Caselli, P., Walmsley, C. M., Tafalla, M., Dore, L., & Myers, P. C. 1999, *ApJ*, 523, L165
- Cassen, P. & Moosman, A. 1981, *Icarus*, 48, 353
- Chandler, C. J. & Richer, J. S. 2000, *ApJ*, 530, 851
- Chapman, N. L. & Mundy, L. G. 2009, *ApJ*, 699, 1866
- Chen, H., Myers, P. C., Ladd, E. F., & Wood, D. O. S. 1995, *ApJ*, 445, 377
- Chen, X., Launhardt, R., & Henning, T. 2007, *ApJ*, 669, 1058
- Chiang, H., Looney, L. W., Tassis, K., Mundy, L. G., & Mouschovias, T. C. 2008, *ApJ*, 680, 474

- Chiang, H., Looney, L. W., Tobin, J. J., & Hartmann, L. 2010, *ApJ*, 709, 470
- Chini, R., Ward-Thompson, D., Kirk, J. M., Nielbock, M., Reipurth, B., & Sievers, A. 2001, *A&A*, 369, 155
- Ciolek, G. E. & Basu, S. 2006, *ApJ*, 652, 442
- Cohen, M. 1973a, *MNRAS*, 161, 85
- Cohen, M. 1973b, *MNRAS*, 161, 97
- Connelley, M. S., Reipurth, B., & Tokunaga, A. T. 2008, *AJ*, 135, 2526
- Crapsi, A., Caselli, P., Walmsley, C. M., Myers, P. C., Tafalla, M., Lee, C. W., & Bourke, T. L. 2005, *ApJ*, 619, 379
- Crapsi, A., Caselli, P., Walmsley, C. M., Tafalla, M., Lee, C. W., Bourke, T. L., & Myers, P. C. 2004, *A&A*, 420, 957
- Crutcher, R. M., Hakobian, N., & Troland, T. H. 2009, *ApJ*, 692, 844
- Crutcher, R. M., Wandelt, B., Heiles, C., Falgarone, E., & Troland, T. H. 2010, *ApJ*, 725, 466
- D'Alessio, P., Calvet, N., & Hartmann, L. 2001, *ApJ*, 553, 321
- D'Alessio, P., Calvet, N., Hartmann, L., Franco-Hernández, R., & Servín, H. 2006, *ApJ*, 638, 314
- D'Alessio, P., Canto, J., Calvet, N., & Lizano, S. 1998, *ApJ*, 500, 411
- Danby, G., Flower, D. R., Valiron, P., Schilke, P., & Walmsley, C. M. 1988, *MNRAS*, 235, 229
- Delamarter, G., Frank, A., & Hartmann, L. 2000, *ApJ*, 530, 923
- Di Francesco, J., Johnstone, D., Kirk, H., MacKenzie, T., & Ledwosinska, E. 2008, *ApJS*, 175, 277
- Di Francesco, J., Myers, P. C., Wilner, D. J., Ohashi, N., & Mardones, D. 2001, *ApJ*, 562, 770
- Dickman, R. L. 1978, *ApJS*, 37, 407
- Djupvik, A. A., André, P., Bontemps, S., Motte, F., Olofsson, G., Gålfalk, M., & Florén, H. 2006, *A&A*, 458, 789
- Draine, B. T. & Lee, H. M. 1984, *ApJ*, 285, 89
- Duchêne, G., et al. 2010, *ApJ*, 712, 112

Dullemond, C. P., Dominik, C., & Natta, A. 2001, *ApJ*, 560, 957

Dunham, M. M., Evans, N. J., Terebey, S., Dullemond, C. P., & Young, C. H. 2010, *ApJ*, 710, 470

Dunham, M. M., et al. 2006, *ApJ*, 651, 945

Dzib, S., Loinard, L., Mioduszewski, A. J., Boden, A. F., Rodríguez, L. F., & Torres, R. M. 2010, *ApJ*, 718, 610

Eiroa, C., Miranda, L. F., Anglada, G., Estalella, R., & Torrelles, J. M. 1994, *A&A*, 283, 973

Elmegreen, B. G. 2000, *ApJ*, 530, 277

Enoch, M. L., Evans, N. J., Sargent, A. I., & Glenn, J. 2009, *ApJ*, 692, 973

Enoch, M. L., Glenn, J., Evans, N. J., Sargent, A. I., Young, K. E., & Huard, T. L. 2007, *ApJ*, 666, 982

Enoch, M. L., et al. 2006, *ApJ*, 638, 293

Evans, N. J., et al. 2009, *ApJS*, 181, 321

Evans, N. J. 1999, *ARA&A*, 37, 311

Evans, N. J., et al. 2003, *PASP*, 115, 965

Fatuzzo, M. & Adams, F. C. 2002, *ApJ*, 570, 210

Fazio, G. G., et al. 2004, *ApJS*, 154, 10

Fűrész, G., Hartmann, L. W., Megeath, S. T., Szentgyorgyi, A. H., & Hamden, E. T. 2008, *ApJ*, 676, 1109

Fűrész, G., et al. 2006, *ApJ*, 648, 1090

Fiedler, R. A. & Mouschovias, T. C. 1992, *ApJ*, 391, 199

Flaherty, K. M., Pipher, J. L., Megeath, S. T., Winston, E. M., Gutermuth, R. A., Muzerolle, J., Allen, L. E., & Fazio, G. G. 2007, *ApJ*, 663, 1069

Foster, P. N. & Chevalier, R. A. 1993, *ApJ*, 416, 303

Frerking, M. A., Langer, W. D., & Wilson, R. W. 1982, *ApJ*, 262, 590

Froebrich, D. 2005, *ApJS*, 156, 169

Fuller, G. A., Lada, E. A., Masson, C. R., & Myers, P. C. 1995, *ApJ*, 453, 754

Fuller, G. A. & Wootten, A. 2000, *ApJ*, 534, 854

- Furlan, E., et al. 2008, ApJS, 176, 184
- Galli, D., Lizano, S., Shu, F. H., & Allen, A. 2006, ApJ, 647, 374
- Galli, D. & Shu, F. H. 1993, ApJ, 417, 220
- Girart, J. M., Estalella, R., Anglada, G., Torrelles, J. M., Ho, P. T. P., & Rodriguez, L. F. 1997, ApJ, 489, 734
- Goldsmith, P. F. 1987, in *Astrophysics and Space Science Library*, Vol. 134, *Interstellar Processes*, ed. D. J. Hollenbach & H. A. Thronson Jr., 51–70
- Goldsmith, P. F. & Langer, W. D. 1999, ApJ, 517, 209
- Goodman, A. A., Barranco, J. A., Wilner, D. J., & Heyer, M. H. 1998, ApJ, 504, 223
- Goodman, A. A., Benson, P. J., Fuller, G. A., & Myers, P. C. 1993, ApJ, 406, 528
- Gramajo, L. V., Whitney, B. A., Gómez, M., & Robitaille, T. P. 2010, AJ, 139, 2504
- Gueth, F. & Guilloteau, S. 1999, A&A, 343, 571
- Gueth, F., Guilloteau, S., & Bachiller, R. 1996, A&A, 307, 891
- Haisch, K. E., Lada, E. A., & Lada, C. J. 2001, ApJ, 553, L153
- Hartmann, L. 1998, *Accretion Processes in Star Formation* (Accretion processes in star formation / Lee Hartmann. Cambridge, UK ; New York : Cambridge University Press, 1998. (Cambridge astrophysics series ; 32) ISBN 0521435072.)
- Hartmann, L. 2002, ApJ, 578, 914
- . 2009, *Accretion Processes in Star Formation: Second Edition*, ed. Hartmann, L. (Cambridge University Press)
- Hartmann, L., Ballesteros-Paredes, J., & Bergin, E. A. 2001, ApJ, 562, 852
- Hartmann, L., Boss, A., Calvet, N., & Whitney, B. 1994, ApJ, 430, L49
- Hartmann, L., Calvet, N., Allen, L., Chen, H., & Jayawardhana, R. 1999, AJ, 118, 1784
- Hartmann, L., Calvet, N., & Boss, A. 1996, ApJ, 464, 387
- Hartmann, L., Megeath, S. T., Allen, L., Luhman, K., Calvet, N., D'Alessio, P., Franco-Hernandez, R., & Fazio, G. 2005, ApJ, 629, 881
- Harvey, P. M., et al. 2006, ApJ, 644, 307
- Heitsch, F. & Hartmann, L. 2008, ApJ, 689, 290
- Heitsch, F., Hartmann, L. W., & Burkert, A. 2008a, ApJ, 683, 786

- Heitsch, F., Hartmann, L. W., Slyz, A. D., Devriendt, J. E. G., & Burkert, A. 2008b, *ApJ*, 674, 316
- Heitsch, F., Mac Low, M., & Klessen, R. S. 2001, *ApJ*, 547, 280
- Heitsch, F., Slyz, A. D., Devriendt, J. E. G., Hartmann, L. W., & Burkert, A. 2006, *ApJ*, 648, 1052
- Henriksen, R., Andre, P., & Bontemps, S. 1997, *A&A*, 323, 549
- Herbig, G. H. & Jones, B. F. 1983, *AJ*, 88, 1040
- Hernández, J., et al. 2007, *ApJ*, 662, 1067
- Hirota, T., Honma, M., Imai, H., Sunada, K., Ueno, Y., Kobayashi, H., & Kawaguchi, N. 2011, *PASJ*, 63, 1
- Ho, P. T. P., Barrett, A. H., & Martin, R. N. 1978, *ApJ*, 221, L117
- Ho, P. T. P. & Townes, C. H. 1983, *ARA&A*, 21, 239
- Hogerheijde, M. R. & Sandell, G. 2000, *ApJ*, 534, 880
- Hogerheijde, M. R., van Dishoeck, E. F., Blake, G. A., & van Langevelde, H. J. 1998, *ApJ*, 502, 315
- Houck, J. R., et al. 2004, *ApJS*, 154, 18
- Hsu, W., Hartmann, L., Heitsch, F., & Gómez, G. C. 2010, *ApJ*, 721, 1531
- Huard, T. L., Sandell, G., & Weintraub, D. A. 1999, *ApJ*, 526, 833
- Hunt, L. K., Mannucci, F., Testi, L., Migliorini, S., Stanga, R. M., Baffa, C., Lisi, F., & Vanzi, L. 1998, *AJ*, 115, 2594
- Indebetouw, R., et al. 2005a, *ApJ*, 619, 931
- Indebetouw, R., et al. 2005b, *ApJ*, 619, 931
- Jeans, J. H. 1902, *Royal Society of London Philosophical Transactions Series A*, 199, 1
- Johnstone, D., Fiege, J. D., Redman, R. O., Feldman, P. A., & Carey, S. J. 2003, *ApJ*, 588, L37
- Johnstone, D., Rosolowsky, E., Tafalla, M., & Kirk, H. 2010, *ApJ*, 711, 655
- Jørgensen, J. K. 2004, *A&A*, 424, 589
- Jørgensen, J. K., et al. 2007, *ApJ*, 659, 479
- Jørgensen, J. K., et al. 2006, *ApJ*, 645, 1246

- Jørgensen, J. K., van Dishoeck, E. F., Visser, R., Bourke, T. L., Wilner, D. J., Lommen, D., Hogerheijde, M. R., & Myers, P. C. 2009, *A&A*, 507, 861
- Kauffmann, J., Bertoldi, F., Bourke, T. L., Evans, N. J., & Lee, C. W. 2008, *A&A*, 487, 993
- Kenyon, S. J., Brown, D. I., Tout, C. A., & Berlind, P. 1998, *AJ*, 115, 2491
- Kenyon, S. J., Calvet, N., & Hartmann, L. 1993a, *ApJ*, 414, 676
- Kenyon, S. J., Whitney, B. A., Gomez, M., & Hartmann, L. 1993b, *ApJ*, 414, 773
- Keto, E. & Rybicki, G. 2010, *ApJ*, 716, 1315
- Kim, S.-H., Martin, P. G., & Hendry, P. D. 1994, *ApJ*, 422, 164
- Kirk, J. M., et al. 2009, *ApJS*, 185, 198
- Klessen, R. S. & Burkert, A. 2000, *ApJS*, 128, 287
- Klessen, R. S. & Burkert, A. 2001, *ApJ*, 549, 386
- Klessen, R. S., Heitsch, F., & Mac Low, M. 2000, *ApJ*, 535, 887
- Koda, J., Sawada, T., Wright, M. C. H., Teuben, P., Corder, S. A., Patience, J., Scoville, N., Donovan Meyer, J., & Egusa, F. 2011, *ApJS*, 193, 19
- Kratter, K. M., Matzner, C. D., Krumholz, M. R., & Klein, R. I. 2010, *ApJ*, 708, 1585
- Krumholz, M. R., Matzner, C. D., & McKee, C. F. 2006, *ApJ*, 653, 361
- Kunz, M. W. & Mouschovias, T. C. 2009, *ApJ*, 693, 1895
- Lada, C. J. 1987, in *IAU Symp. 115: Star Forming Regions*, ed. M. Peimbert & J. Jugaku, 1–17
- Lada, C. J. 2006, *ApJ*, 640, L63
- Lada, C. J., Lada, E. A., Clemens, D. P., & Bally, J. 1994, *ApJ*, 429, 694
- Ladd, E. F., Adams, F. C., Fuller, G. A., Myers, P. C., Casey, S., Davidson, J. A., Harper, D. A., & Padman, R. 1991, *ApJ*, 382, 555
- Larson, R. B. 1969, *MNRAS*, 145, 271
- Larson, R. B. 1981, *MNRAS*, 194, 809
- Launhardt, R., Nutter, D., Ward-Thompson, D., Bourke, T. L., Henning, T., Khanzadyan, T., Schmalzl, M., Wolf, S., & Zylka, R. 2010, *ApJS*, 188, 139

- Launhardt, R., Sargent, A., & Zinnecker, H. 2001, in *Astronomical Society of the Pacific Conference Series*, Vol. 235, *Science with the Atacama Large Millimeter Array*, ed. A. Wootten, 134–+
- Lee, C., Hirano, N., Palau, A., Ho, P. T. P., Bourke, T. L., Zhang, Q., & Shang, H. 2009, *ApJ*, 699, 1584
- Lee, J., Bergin, E. A., & Evans, N. J. 2004, *ApJ*, 617, 360
- Li, A. & Draine, B. T. 2001, *ApJ*, 554, 778
- Li, Z. & Nakamura, F. 2004, *ApJ*, 609, L83
- Lin, C. C., Mestel, L., & Shu, F. H. 1965, *ApJ*, 142, 1431
- Loinard, L., Rodríguez, L. F., D’Alessio, P., Wilner, D. J., & Ho, P. T. P. 2002, *ApJ*, 581, L109
- Loinard, L., Torres, R. M., Mioduszewski, A. J., & Rodríguez, L. F. 2008, *ApJ*, 675, L29
- Loinard, L., Torres, R. M., Mioduszewski, A. J., Rodríguez, L. F., González-Lópezlira, R. A., Lachaume, R., Vázquez, V., & González, E. 2007, *ApJ*, 671, 546
- Looney, L. W., Mundy, L. G., & Welch, W. J. 2000, *ApJ*, 529, 477
- Looney, L. W., Tobin, J. J., & Kwon, W. 2007, *ApJ*, 670, L131
- Lovas, F. J. 1992, *Journal of Physical and Chemical Reference Data*, 21, 181
- Low, F. J. & Smith, B. J. 1966, *Nature*, 212, 675
- Luhman, K. L. 2008, *Chamaeleon*, ed. Reipurth, B., 169–+
- Lynds, B. T. 1962, *ApJS*, 7, 1
- Mac Low, M. & Klessen, R. S. 2004, *Reviews of Modern Physics*, 76, 125
- Machida, M. N., Tomisaka, K., Matsumoto, T., & Inutsuka, S. 2008, *ApJ*, 677, 327
- Markwardt, C. B. 2009, in *Astronomical Society of the Pacific Conference Series*, Vol. 411, *Astronomical Data Analysis Software and Systems XVIII*, ed. D. A. Bohlender, D. Durand, & P. Dowler, 251–+
- Martin, R. N. & Barrett, A. H. 1978, *ApJS*, 36, 1
- Maury, A. J., André, P., Hennebelle, P., Motte, F., Stamatellos, D., Bate, M., Bellocche, A., Duchêne, G., & Whitworth, A. 2010, *A&A*, 512, A40+
- McCaughrean, M. J., Rayner, J. T., & Zinnecker, H. 1994, *ApJ*, 436, L189

McClure, M. 2009, ApJ, 693, L81

McKee, C. F. & Ostriker, E. C. 2007, ARA&A, 45, 565

Meadows, V. S., et al. 2004, ApJS, 154, 469

Meakin, C. A., Biegging, J. H., Latter, W. B., Hora, J. L., & Tielens, A. G. G. M. 2003, ApJ, 585, 482

Mendoza V., E. E. 1966, ApJ, 143, 1010

Men'shchikov, A., et al. 2010, A&A, 518, L103+

Menten, K. M., Reid, M. J., Forbrich, J., & Brunthaler, A. 2007, A&A, 474, 515

Menten, K. M., Serabyn, E., Guesten, R., & Wilson, T. L. 1987, A&A, 177, L57

Mestel, L. & Spitzer, L. 1956, MNRAS, 116, 503

Mink, D. J. 1999, in Astronomical Society of the Pacific Conference Series, Vol. 172, Astronomical Data Analysis Software and Systems VIII, ed. D. M. Mehringer, R. L. Plante, & D. A. Roberts, 498–+

Motte, F. & André, P. 2001, A&A, 365, 440

Mouschovias, T. C. 1979, ApJ, 228, 475

Mouschovias, T. C. 1991, ApJ, 373, 169

Muzerolle, J., Calvet, N., Hartmann, L., & D'Alessio, P. 2003, ApJ, 597, L149

Myers, P. C., Adams, F. C., Chen, H., & Schaff, E. 1998, ApJ, 492, 703

Myers, P. C., Bachiller, R., Caselli, P., Fuller, G. A., Mardones, D., Tafalla, M., & Wilner, D. J. 1995, ApJ, 449, L65+

Myers, P. C. & Benson, P. J. 1983, ApJ, 266, 309

Myers, P. C., Fuller, G. A., Goodman, A. A., & Benson, P. J. 1991, ApJ, 376, 561

Neugebauer, G., et al. 1984, ApJ, 278, L1

Noriega-Crespo, A., et al. 2004, ApJS, 154, 352

Offner, S. S. R. & Krumholz, M. R. 2009, ApJ, 693, 914

Ohashi, N., Hayashi, M., Ho, P. T. P., & Momose, M. 1997, ApJ, 475, 211

O'Linger, J., Wolf-Chase, G., Barsony, M., & Ward-Thompson, D. 1999, ApJ, 515, 696

- Osorio, M., D'Alessio, P., Muzerolle, J., Calvet, N., & Hartmann, L. 2003, *ApJ*, 586, 1148
- Ostriker, E. C., Stone, J. M., & Gammie, C. F. 2001, *ApJ*, 546, 980
- Padgett, D., et al. 2006, in *Bulletin of the American Astronomical Society*, Vol. 38, *Bulletin of the American Astronomical Society*, 947–+
- Padgett, D. L., Brandner, W., Stapelfeldt, K. R., Strom, S. E., Terebey, S., & Koerner, D. 1999, *AJ*, 117, 1490
- Padoan, P., Juvela, M., Goodman, A. A., & Nordlund, Å. 2001, *ApJ*, 553, 227
- Padoan, P. & Nordlund, Å. 2002, *ApJ*, 576, 870
- Penston, M. V. 1969, *MNRAS*, 144, 425
- Pineda, J. E., Goodman, A. A., Arce, H. G., Caselli, P., Foster, J. B., Myers, P. C., & Rosolowsky, E. W. 2010, *ApJ*, 712, L116
- Pogge, R. W., et al. 1998, in *Society of Photo-Optical Instrumentation Engineers (SPIE) Conference Series*, Vol. 3354, *Society of Photo-Optical Instrumentation Engineers (SPIE) Conference Series*, ed. A. M. Fowler, 414–418
- Pollack, J. B., Hollenbach, D., Beckwith, S., Simonelli, D. P., Roush, T., & Fong, W. 1994, *ApJ*, 421, 615
- Pudritz, R. E. & Norman, C. A. 1983, *ApJ*, 274, 677
- Rafikov, R. R. 2005, *ApJ*, 621, L69
- Rafikov, R. R. 2007, *ApJ*, 662, 642
- Ragan, S. E., Bergin, E. A., & Gutermuth, R. A. 2009, *ApJ*, 698, 324
- Ragan, S. E., Bergin, E. A., Plume, R., Gibson, D. L., Wilner, D. J., O'Brien, S., & Hails, E. 2006, *ApJS*, 166, 567
- Raghavan, D., McAlister, H. A., Henry, T. J., Latham, D. W., Marcy, G. W., Mason, B. D., Gies, D. R., White, R. J., & ten Brummelaar, T. A. 2010, *ApJS*, 190, 1
- Reach, W. T., et al. 2005, *PASP*, 117, 978
- Rebull, L. M., et al. 2007, *ApJS*, 171, 447
- Reipurth, B., Raga, A. C., & Heathcote, S. 1996, *A&A*, 311, 989
- Reipurth, B., Yu, K. C., Heathcote, S., Bally, J., & Rodríguez, L. F. 2000, *AJ*, 120, 1449

- Rich, J. W., de Blok, W. J. G., Cornwell, T. J., Brinks, E., Walter, F., Bagetakos, I., & Kennicutt, R. C. 2008, *AJ*, 136, 2897
- Rieke, G. H. & Lebofsky, M. J. 1985, *ApJ*, 288, 618
- Rieke, G. H., et al. 2004, *ApJS*, 154, 25
- Robitaille, T. P., Whitney, B. A., Indebetouw, R., & Wood, K. 2007, *ApJS*, 169, 328
- Robitaille, T. P., Whitney, B. A., Indebetouw, R., Wood, K., & Denzmore, P. 2006, *ApJS*, 167, 256
- Rodríguez, L. F., Reipurth, B., Raga, A. C., & Cantó, J. 1998, *Rev. Mexicana Astron. Astrofis.*, 34, 69
- Román-Zúñiga, C. G., Lada, C. J., Muench, A., & Alves, J. F. 2007, *ApJ*, 664, 357
- Rydbeck, O. E. H., Sume, A., Hjalmarsen, A., Ellder, J., Ronnang, B. O., & Kollberg, E. 1977, *ApJ*, 215, L35
- Ryden, B. S. 1996, *ApJ*, 471, 822
- Sault, R. J., Teuben, P. J., & Wright, M. C. H. 1995, in *Astronomical Society of the Pacific Conference Series*, Vol. 77, *Astronomical Data Analysis Software and Systems IV*, ed. R. A. Shaw, H. E. Payne, & J. J. E. Hayes, 433–+
- Schöier, F. L., van der Tak, F. F. S., van Dishoeck, E. F., & Black, J. H. 2005, *A&A*, 432, 369
- Scholz, A., Wood, K., Wilner, D., Jayawardhana, R., Delorme, P., Caratti O Garatti, A., Ivanov, V. D., Saviane, I., & Whitney, B. 2010, *MNRAS*, 409, 1557
- Seale, J. P. & Looney, L. W. 2008, *ApJ*, 675, 427
- Shirley, Y. L., Evans, N. J., Rawlings, J. M. C., & Gregersen, E. M. 2000, *ApJS*, 131, 249
- Shu, F., Najita, J., Ostriker, E., Wilkin, F., Ruden, S., & Lizano, S. 1994, *ApJ*, 429, 781
- Shu, F. H. 1977, *ApJ*, 214, 488
- Shu, F. H., Adams, F. C., & Lizano, S. 1987, *ARA&A*, 25, 23
- Shu, F. H., Ruden, S. P., Lada, C. J., & Lizano, S. 1991, *ApJ*, 370, L31
- Simon, R., Jackson, J. M., Rathborne, J. M., & Chambers, E. T. 2006, *ApJ*, 639, 227
- Skrutskie, M. F., et al. 2006, *AJ*, 131, 1163

- Smith, R. J., Glover, S. C. O., Bonnell, I. A., Clark, P. C., & Klessen, R. S. 2011, MNRAS, 411, 1354
- Snell, R. L., Loren, R. B., & Plambeck, R. L. 1980, ApJ, 239, L17
- Spitzer, L. 1968, Dynamics of Interstellar Matter and the Formation of Stars, ed. Middlehurst, B. M. & Aller, L. H. (the University of Chicago Press), 1–+
- Stanke, T., Smith, M. D., Gredel, R., & Khanzadyan, T. 2006, A&A, 447, 609
- Stark, D. P., Whitney, B. A., Stassun, K., & Wood, K. 2006, ApJ, 649, 900
- Sterzik, M. F., Durisen, R. H., & Zinnecker, H. 2003, A&A, 411, 91
- Strom, S. E., Strom, K. M., Brooke, A. L., Bregman, J., & Yost, J. 1972, ApJ, 171, 267
- Stutz, A. M., Rieke, G. H., Biegging, J. H., Balog, Z., Heitsch, F., Kang, M., Peters, W. L., Shirley, Y. L., & Werner, M. W. 2009, ApJ, 707, 137
- Swift, J. J. & Welch, W. J. 2008, ApJS, 174, 202
- Tafalla, M., Mardones, D., Myers, P. C., Caselli, P., Bachiller, R., & Benson, P. J. 1998, ApJ, 504, 900
- Tafalla, M., Myers, P. C., Caselli, P., & Walmsley, C. M. 2004, A&A, 416, 191
- Tafalla, M., Myers, P. C., Mardones, D., & Bachiller, R. 2000, A&A, 359, 967
- Tan, J. C., Krumholz, M. R., & McKee, C. F. 2006, ApJ, 641, L121
- Tanner, J. D. & Arce, H. G. 2011, ApJ, 726, 40
- Tannirkulam, A., Harries, T. J., & Monnier, J. D. 2007, ApJ, 661, 374
- Tassis, K. & Mouschovias, T. C. 2007, ApJ, 660, 370
- Terebey, S., et al. 2009, ApJ, 696, 1918
- Terebey, S., Shu, F. H., & Cassen, P. 1984, ApJ, 286, 529
- Thompson, A. R., Moran, J. M., & Swenson, G. W. 2001, Interferometry and Synthesis in Radio Astronomy, 2nd Edition, ed. Thompson, A. R., Moran, J. M., & Swenson, G. W., Jr.
- Tobin, J. J., Hartmann, L., Calvet, N., & D'Alessio, P. 2008, ApJ, 679, 1364
- Tobin, J. J., Hartmann, L., Chiang, H., & Looney, L. W. 2011, ApJ
- Tobin, J. J., Hartmann, L., Furesz, G., Mateo, M., & Megeath, S. T. 2009, ApJ, 697, 1103

- Tobin, J. J., Hartmann, L., & Loinard, L. 2010a, *ApJ*, 722, L12
- Tobin, J. J., Hartmann, L., Looney, L. W., & Chiang, H. 2010b, *ApJ*, 712, 1010
- Tobin, J. J., Looney, L. W., Mundy, L. G., Kwon, W., & Hamidouche, M. 2007, *ApJ*, 659, 1404
- Tohline, J. E. 1981, *ApJ*, 248, 717
- Tohline, J. E. 2002, *ARA&A*, 40, 349
- Tsitali, A. E., Bourke, T. L., Peterson, D. E., Myers, P. C., Dunham, M. M., Evans, N. J., & Huard, T. L. 2010, *ApJ*, 725, 2461
- Tuthill, P. G., Monnier, J. D., & Danchi, W. C. 2001, *Nature*, 409, 1012
- Ulrich, R. K. 1976, *ApJ*, 210, 377
- van der Blik, N. S., et al. 2004, in *Society of Photo-Optical Instrumentation Engineers (SPIE) Conference Series*, Vol. 5492, *Society of Photo-Optical Instrumentation Engineers (SPIE) Conference Series*, ed. A. F. M. Moorwood & M. Iye, 1582–1589
- Vázquez-Semadeni, E., Kim, J., Shadmehri, M., & Ballesteros-Paredes, J. 2005, *ApJ*, 618, 344
- Velusamy, T. & Langer, W. D. 1998, *Nature*, 392, 685
- Visser, A. E., Richer, J. S., & Chandler, C. J. 2002, *AJ*, 124, 2756
- Volgenau, N. H., Mundy, L. G., Looney, L. W., & Welch, W. J. 2006, *ApJ*, 651, 301
- Vorobyov, E. I. 2009, *ApJ*, 692, 1609
- Walch, S., Naab, T., Whitworth, A., Burkert, A., & Gritschneider, M. 2010, *MNRAS*, 402, 2253
- Walker, C. K., Lada, C. J., Young, E. T., Maloney, P. R., & Wilking, B. A. 1986, *ApJ*, 309, L47
- Ward-Thompson, D., Scott, P. F., Hills, R. E., & Andre, P. 1994, *MNRAS*, 268, 276
- Watson, A. M. & Stapelfeldt, K. R. 2007, *AJ*, 133, 845
- Weingartner, J. C. & Draine, B. T. 2001, *ApJ*, 548, 296
- Whitney, B. A. & Hartmann, L. 1993, *ApJ*, 402, 605
- Whitney, B. A., Wood, K., Bjorkman, J. E., & Cohen, M. 2003a, *ApJ*, 598, 1079
- Whitney, B. A., Wood, K., Bjorkman, J. E., & Wolff, M. J. 2003b, *ApJ*, 591, 1049

- Whitney, B. A., Wood, K., Bjorkman, J. E., & Wolff, M. J. 2003c, ApJ, 591, 1049
- Whittet, D. C. B., Gerakines, P. A., Hough, J. H., & Shenoy, S. S. 2001, ApJ, 547, 872
- Wilkin, F. P. & Stahler, S. W. 2003, ApJ, 590, 917
- Willing, B. A. & Lada, C. J. 1983, ApJ, 274, 698
- Williams, J. P. & Cieza, L. A. 2011, ArXiv e-prints
- Womack, M., Ziurys, L. M., & Wyckoff, S. 1992, ApJ, 387, 417
- Wood, K., Smith, D., Whitney, B., Stassun, K., Kenyon, S. J., Wolff, M. J., & Bjorkman, K. S. 2001, ApJ, 561, 299
- Wood, K., Wolff, M. J., Bjorkman, J. E., & Whitney, B. 2002, ApJ, 564, 887
- Ybarra, J. E., Barsony, M., Haisch, K. E., Jarrett, T. H., Sahai, R., & Weinberger, A. J. 2006, ApJ, 647, L159
- Young, K. E., et al. 2006, ApJ, 644, 326
- Yun, J. L. 1996, AJ, 111, 930
- Zhou, S. 1992, ApJ, 394, 204
- Zhou, S., Evans, N. J., Koempe, C., & Walmsley, C. M. 1993, ApJ, 404, 232
- Zhou, S., Evans, N. J., & Wang, Y. 1996, ApJ, 466, 296
- Zhu, Z., Hartmann, L., & Gammie, C. 2009, ApJ, 694, 1045